DEPOSITION-PATTERNING OF LEAD ZIRCONATE TITANATE (PZT) USING ELECTROHYDRODYNAMIC ATOMIZATION

DONGYANG SUN

A thesis submitted for the degree of

Doctor of Philosophy

Mechanical Engineering

University College London

2008

ProQuest LLC
789 East Eisenhower Parkway
P.O. Box 1346
Ann Arbor, MI 48106-1346

Declaration

I, Dongyang Sun, confirm that the work presented in this thesis is my own. Where information has been derived from other sources, I confirm that this has been indicated in the thesis.

Dongyang Sun

Abstract

This research develops a novel processing technique, namely electrohydrodynamic atomization, for forming lead zirconate titantate (PZT) in various structures.

The capability to process PZT materials is crucial due to the demand in applications of sensors, capacitors and actuators. Structures from continuous films to columnar structures and track-structures need to be fabricated with high effectiveness, low cost and high accuracy. This study focused on investigating a new deposition-patterning technique to fabricate such versatile material. Electrohydrodynamic atomization is a novel processing technique which makes use of electric field induced flow (electrohydrodynamics) to deposit and pattern pre-designed structures.

This research is comprised of three parts. In the first part, the properties of 0.6 mol/L PZT sol was studied, which include density, electrical conductivity, viscosity and surface tension. Then the sol was placed in a furnace and heat-treated and the ideal sintering temperature was determined. After that, the electrohydrodynamic atomization process was successfully utilized for spraying 0.6 mol/L PZT sol in the cone-jet mode. Important spraying parameters such as applied voltage, flow rate and distance between the needle and substrate were examined. The mode selection map for this sol was constructed from 5×10^{-12} m^3 s^{-1} up to the critical flow rate point above which the cone-jet mode is not obtainable. The PZT particles were deposited on metallic substrates and heat-treated at 650°C. Microstructure of the deposit was studied. Nano-structured PZT particles were observed under the microscope and the average size of these spherical particles was approximately 100nm.

Secondly, the influence of concentration of sprayed sol on the as-deposited structures was investigated. Continuous PZT films were obtained using 0.06 mol/L sols while columnar PZT structures which are used to form 1-3 composites were produced using 0.6 mol/L sols. The reason for this feature was discussed considering the droplets of different sizes and their evaporation. The growth of PZT columns was studied by observing the cross-sectional structures at 10s, 20s, 40s, 60s, 180s and 330s. The affect of substrate temperature on the columnar structure was also analyzed by studying the density of the columns. A 1-3 composite was produced by infiltrating photoresists into columnar structures. The dielectric properties of such composite and the continuous film were investigated.

Thirdly, PZT track-structures were produced by electrohydrodynamic printing. Cracks within the printed structures were eliminated by adding polyvinylpyrrolidone (PVP) to 0.6 mol/L PZT sol. Different volume ratios from 1:1 to 1:4 were used when mixing PZT and PVP solutions. The microstructure of the PZT tracks printed using different solutions were investigated using optical microscope. The content of residual PVP polymer was examined and it elucidated that PVP was completely removed after heat treatment at 650°C.

Table of Contents

List of Figures

List of Tables

Acknowledgements

I am indebted to many people who provided assistance to me in numerous ways during my PhD work. This thesis would not have been possible without their supports.

I would like to take this opportunity to express my special gratitude and deep respect to my supervisor, not only an internationally known researcher, but also a sincere friend, Professor Mohan Edirisinghe, Chair of Biomaterials, University College London. Thank you for providing me the opportunity and financial assistance for this study. I could not have imagined having a better mentor for my PhD, and without your genuine, professional and personal advice I would never have completed it.

I would like to thank Department of Mechanical Engineering, University College London and Department of Materials, Queen Mary, University of London for proving me the opportunity and facilities to pursue my PhD degree.

I sincerely thank Dr. Robert Dorey and Dr. Sophie Rocks of Cranfield University, who not only have helped me by providing materials and analyzing experiment results, but also have given me precious suggestions for my study.

Many people have provided vast technical supports and essential information for my research. I would like to take this opportunity to thank Dr. William Suen, Mr. Terry Dyer, Mr. Kevin Reeves, Dr. Steve Firth, Dr. Zofia Luklinska, Mr. Vince Ford, Mr. John Caulfield and all those people who have helped me. Thank you very much for your constructive advice and support.

I would like to say thank you to my wife, Tianyao Xu, for your persistent encouragement and support. I am proud and happy to stay with you for ever.

It is with endless love that I thank my parents, Mr. Sun Tao and Mrs. Yang Junru, for giving me selfless care and help. An appreciation also gives out to all my relatives for their constant support. I love you for ever.

Last but not least, I would like to be graceful to my research group members for their cordial advice and help. It is a great pleasure to work with them and the time we spent is never forgettable.

Thank you all!

Publications and Conference Presentations

The following publications and conference presentations have resulted from this work:

Sun, D., Rocks, S. A., Edirisinghe, M. J., Dorey, R. A., & Wang, Y. 2005, "Electrohydrodynamic deposition of nanostructured lead zirconate titanate", *Journal of Nanoscience and Nanotechnology*, vol. 5, no. 11, pp. 1846-1851.

Rocks, S., Wang, D., **Sun, D.**, Jayasinghe, S., Edirisinghe, M., & Dorey, R. 2007, "Direct writing of lead zirconate titanate piezoelectric structures by electrohydrodynamic atomisation", *Journal of Electroceramics*, vol. 19, no. 4, pp. 287-293.

Sun, D., Rocks, S. A., Wang, D., Edirisinghe, M. J., & Dorey, R. A. 2008, "Novel Forming of Columnar Lead Zirconate Titanate Structures", *Journal of the European Ceramic Society*, doi:10.1016/j.jeurceramsoc.2008.05.034.

Sun, D., "Processing of Lead Zirconate Titanate by Electrohydrodynamic Atomization", oral and poster presentation in *Gordon Research Conference*, Massachusetts, USA, July 2005.

CHAPTER 1 Introduction

1.1 Electrohydrodynamic atomization

Electrohydrodynamic atomization (alternatively called electrospraying) is a well known processing technique which relies on the elongation of the liquid formed at the outlet of a capillary to a jet that subsequently breaks up into droplets by means of electrohydrodynamic force. This phenomenon was reported as early as in the 18^{th} century until a solid scientific description of it as a technical process was given in early 1900s (Zeleny 1914). Since then many researchers have contributed to the understanding of this process (Ganan-Calvo *et al.* 1993; Taylor 1964) and nowadays it has become a well-established procedure for processing materials for a range of applications (Chen *et al.* 1996; Edirisinghe & Jayasinghe 2004; Jayasinghe & Edirisinghe 2004; Miao *et al.* 2001).

Several spray modes can be classified depending on the geometrical forms of the meniscus near the needle exit and/or jet generated after that. It was firstly proposed by Cloupeau *et al.* (1990) and developed by Jaworek *et al.* (1999a). The major spray modes include dripping, micro-dripping, spindle, unstable/stable cone-jet and multi-jet mode, in which a different droplet sizes distribution and a different spatial aerosol distribution (spray pattern) can be obtained. These modes are determined by various factors which include the physical properties of the sprayed liquid (e.g. density, viscosity, electrical conductivity and surface tension), the capillary diameter and the processing parameters (e.g. liquid flow rate and applied voltage). Amount those spray modes, the stable cone-jet mode is of highly interest and has been

intensively developed by many researchers (Hartman *et al.* 1999a).

In the stable cone-jet mode, the electric field induces a surface charge in the sprayed liquid. The surface charge is accelerated by the electric field and this acceleration and the electrical stress in the liquid surface transform it in a conical shape, which is known as Taylor cone (Meesters *et al.* 1992). At the cone apex, a jet with a high charge density is generated which can break up into a number of primary main droplets with a mono-disperse size distribution. The major advantages of the cone-jet mode spraying are its stability and capability of generating droplets of micrometer or sub-micrometer size which are nearly monodispersed (Cloupeau & Prunetfoch 1994).

Spraying in the cone-jet mode can be utilized as a deposition process in which a continuous and stable aerosol stream containing monodispersed droplets transports through the environment and deposits on the substrate; this process is called electrohydrodynamic deposition. This technique can be utilized to generate functional ceramic thin/thick films using sol precursors with the advantage of a simple setup, ambient atmosphere operation, wide choice of precursors, relatively high film-growth rate and large deposition area (Chen *et al.* 1996a).

Alternatively, utilizing the focused jet generated in the cone-jet mode, another electrohydrodynamic atomization derived technique can be developed, which is named electrohydrodynamic printing. This versatile printing technique has been studied by many researchers (Gupta *et al.* 2007; Jayasinghe, Edirisinghe, & De Wilde

2002; Rocks *et al.* 2007; Wang *et al.* 2007). Unlike electrohydrodynamic deposition, the printing process manifests by the deposition of droplet/relics very close to the break-up of the jet. The spraying distance for the former process is generally >10mm while for the printing process it is less than 1mm. Apart from that, a point-like needle is also utilized as a ground electrode during the process in order to focus the sprayed droplets after break-up (Jayasinghe & Edirisinghe 2004). Accordingly, the deposit can be generated in small features rather than a large area. This and the cooperation with x-y motion controller system enable the printing process to generate materials of high resolution in various complex 2D/3D structures.

As a well-known functional ceramic, PZT has been developed for numerous applications such as thin/thick films for capacitors, columnar structures for piezoelectric composites and micro-sized features for microelectromechanical systems (MEMS) (Alguero *et al.* 2001; Muralt 1997; Scott *et al.* 1992). In this research, the two electrohydrodynamic atomization derived techniques, deposition and printing, will be investigated and developed for the generation of PZT materials in different structures.

1.2 Aim and objectives of the research

The primary objective of this research is to develop electrohydrodynamic atomization technique in order to utilize it to process functional ceramic PZT in various structures. Two derived techniques, electrohydrodynamic deposition and printing, are aimed to be investigated and developed so that both PZT films can be deposited and simple

structures (e.g. track-structure) can be printed. To achieve these objectives, several works in different stages are necessary to achieve, which are arranged into three different chapters as follows.

Initially, a low toxicity PZT sol is prepared and developed and the properties of such solution (e.g. density, viscosity, electrical conductivity and surface tension) are studied to verify that it is compatible with the electrohydrodynamic atomization technique. A study of heat treatment on the PZT sol is carried out so that an ideal sintering temperature can be revealed and subsequently utilized in other experiments. Then the prepared PZT sol is to be subjected to electrohydrodynamic atomization to spray small droplets. The cone-jet mode in this technique is suitable for the deposition and patterning process due to its advantages mentioned above, thus the stable cone-jet mode map of the prepared PZT sol is necessary to be constructed in which the regime with the specific flow rate and applied voltage to obtain cone-jet mode can be identified. Once the processing parameters for the cone-jet mode are clarified, the sprayed PZT particles can be collected on a substrate and characterized after heat treatment.

Secondly, PZT films are aimed to be deposited directly on titanium/platinum coated silicon wafer for electrical applications. By adjusting the parameters in the electrohydrodynamic deposition process, such as spraying distance, flow rate and applied voltage, concentration of the sol and the substrate temperature, a suitable processing scenario for the generation of PZT thin/ thick film and columnar structure

can be obtained. Some of the electrical properties of generated PZT samples are to be investigated so that the processing details can be developed in order to improve those properties. This part of work is an important section for this research, as all the technical parameters and factors investigated in this chapter are related to the structures of the obtained PZT sample, and partially, determine the quality of the sample that is utilized as a functional component. Any relationship between the processing parameters and the deposited structures is necessary to be explored so that a consummate processing technique can be developed to fabricate such material.

As mentioned above, electrohydrodynamic atomization can also be utilized to pattern track-structures by using a point ground electrode and short spray distance. Therefore, as the third part of this research, such a novel printing technique is developed so that a dense PZT track-structure can be generated without faults (e.g. cracking). This is an important step on the way to developing this technique for the manufacture of complex three-dimensional MEMS components. In order to eliminate cracking and scattering within the printed structures after heat treatment, a polymer, namely polyvinylpyrrolidone (PVP), is designed to incorporate with the PZT sol that is used to print track-structures. Microstructure of the printed track is to be investigated so that the improvement by such polymer can be identified. The removal of PVP polymer after heat treatment is vital in order to obtain a single phase PZT structures. Residual PVP in the structures at different temperature level is to be detected by means of TGA/DTA and FTIR analysis methods.

The objectives for each chapter are all serving for the primary aim of this research; that is developing electrohydrodynamic atomization technique to process functional ceramic PZT. The compact works in each chapter is related to each other so that this research project can be carried out systematically and effectively.

1.3 Structure of the thesis

Based on the aim and objectives of this research, the works were successfully done during the PhD work. This thesis is a summary of the accomplished work in the past and the structure of which is described as follows.

Chapter 1 mainly introduces the core processing technique of this project, electrohydrodynamic atomization and its two derived process: deposition and printing. The fundamental theories of these processes are briefly reviewed. The aim and objectives of this research are elucidated. The structure of this thesis is illustrated and finally the scope of this research is mentioned.

Chapter 2 is devoted to a critical literature review of the relevant knowledge of this research. The information of PZT material is introduced systematically from crystal structure and property to processing and application. Electrohydrodynamic atomization technique is intensively reviewed and the mechanism of cone-jet mode is particularly discussed. The two techniques, deposition and printing, are also described by comparing with other relevant processing techniques.

Chapter 3 gives a detailed description of the experimental work in this research. It includes the introduction of the materials used in this research. The preparations of the materials (e.g. PZT sol, PVP solution) are also introduced. The device configuration of electrohydrodynamic atomization is particularly described and the details of each device used are explained. Methods and equipments used for the characterization of PZT material are also described and finally the electrohydrodynamic printing system is introduced in details.

Chapter 4 elucidates the work of characterization and electrohydrodynamic atomization of PZT sol. In this chapter, the first part is concerning the preparation of propanol-based PZT sol and the study of its properties such as density, viscosity, electrical conductivity, surface tension and yield. Heat treatment of such solution is also introduced and the suitable sintering temperature is discussed. The second part of this chapter is concerning electrospraying of PZT sol. A mode selection map was constructed and the process parameters to obtain stable cone-jet mode, such as flow rate, applied voltage and spray distance were also identified. Nanostructured PZT particles were generated using electrohydrodynamic atomization in the cone-jet mode on a metallic surface. The heat-treated samples were then examined using the electron scanning microscope and X-ray diffraction and spherical nanoparticles were observed, of which the diameter is approximately 100nm.

Chapter 5 focuses on the formation of columnar PZT structures and continuous PZT films using electrohydrodynamic deposition. The research in this part reveals that the

as-deposited structures are highly dependant on the concentration of sprayed sol. By varying the sol concentration from low to high, a transition from continuous film to columnar structure can be observed. The mechanism of this feature is discussed and 0.6M and 0.06M PZT sol are identified as the suitable solution for forming columnar structure and continuous film using this technique. The development of columnar PZT structure was investigated by observing the cross-sectional structure of the samples of different deposition time, followed by heat treatment, disclosing a 3-stage growth process for these structures. Consequently, a 1-3 composite was produced by infiltrating photoresists into the columnar PZT structures and the relative permittivity and dissipation factor of such composite were measured. The relative permittivity of the PZT columnar material is calculated by modelling the structures as a PZT and a polymer capacitor connected in parallel in the PZT/polymer composite. The cross-sectional microstructure of the continuous PZT film obtained using 0.06M sol were also investigated, revealing a high process efficiency of electrohydrodynamic deposition technique when compared with the sol gel spin coating process. The XRD pattern of such film was also obtained and discussed. The frequency variation of the relative permittivity and the dissipation factor of the PZT film were illustrated and these particular values at 50 kHz were compared with the ones of the columnar PZT structures.

Chapter 6 demonstrates the work on generating PZT track-structures on Ti/Pt coated silicon wafer using electrohydrodynamic printing technique. PVP polymer was incorporated with 0.6M PZT sol in order to eliminate the crack formation within the

printed structure. 1:1 to 1:4 volume ratios of PZT and PVP solutions were prepared and used during the printing process. The generated track-structures after heat treatment reveal that the incorporation of PVP polymer into PZT sol is effective to eliminate the crack formation within the printed structure and an improved definition of track border can be observed at the same time. The PVP polymer can be removed at approximately 450°C during the heat treatment, which is concluded from TGA/DTA and FTIR results. Larger volume shrinkage can be observed in the structure obtained from PVP content-rich solutions, which reveals the presence of an upper limit of the incorporated PVP solution. This is because the excessive volume shrinkage may also induce the cracks after heat treatment.

Chapter 7 makes comprehensible conclusions based on the research described in **Chapter 4**, **5** and **6**. The limitation and challenges for some works and their possible future plans are also described. Finally, some recommendations for developing electrohydrodynamic atomization technique are given.

1.4 Benefits of the research

The most important benefit of this research is that, first of all, the author has gained a capability of analyzing and solving academic problems in a scientific and logical manner. Through the use of numerous laboratory equipments for various experimental procedures, the author has become much confident in interacting with the research environment.

On scientific contribution aspect, this research is of great value to micro-fabrication of functional ceramic PZT. The work in this project has revealed that the two technologies, sol gel method and electrohydrodynamic atomization, are fundamentally compatible and the combination of them has developed as a novel technique to process functional materials. This results in a significant step towards realizing a production process capable of fulfilling an imperative requirement within the multidisciplinary MEMS community (micro or submicro-scale two and three dimensional structures) produced at low temperature, thus allowing the incorporation of low temperature substrates and metallic circuit elements (e.g. platinum). Beside of it, other technologies requiring ceramics that is to be incorporated with metal elements and the production of structured ceramic components would also benefit from this new technology, which include micro-fuel cells, micro-fluidics, wear and thermal barrier coatings.

The finding of the effect of precursor concentration on the as-deposited structures has unearthed a new application of the electrohydrodynamic atomization technique. The generation of columnar PZT structure utilizing this technique has a considerable impact on the processing of 1-3 piezoelectric composites. This process can be improved to realize the fabrication of feature-controlled piezoelectric composites in micrometer or submicrometer scale.

Incorporation of polymer material into the sol solution has further improved the sol gel solution method of ceramic processing. Elimination of cracks and improvement of

the printed structure definition using such a method can assist to minimize the printed structure size, which is vital for the next generation of MEMS. This polymer-assisted method may also have effects on other sol gel processing techniques, such as spin coating and dip coating.

Finally, the development of such low temperature fabrication technology for obtaining ceramic micro-scale features such as columnar structures, continuous films and printed track-structures may also contribute to other fields where small scale discrete ceramic components are required.

CHAPTER 2 Literature Review

2.1 Dielectric, piezoelectric, pyroelectric and ferroelectric phenomenon

Dielectric materials do not conduct electricity and as such are of critical importance as capacitive elements in electronic applications such as capacitors and insulators. In contrast to electrical conductivity, which involves long-range motion of charge carriers, the dielectric response results from the short-range motion of these charge carriers under the influence of an externally applied electric field. The application of an electric field to such material will result in a separation of its charges. This separation of charge is called polarization and the dielectric is then polarized. Piezoelectrics, pyroelectrics and ferroelectrics are always dielectrics which may undergo comparable mechanism.

2.1.1 Dielectric polarization

When an electric field E is applied to two parallel plates, charges will be accumulated on each one (**Figure 2.1a**). Therefore the total surface charge density induced by E is given by the dielectric displacement factor D, which is defined as the charges per unit area, is

$$D = \varepsilon_0 E \qquad \textit{Equation 2.1}$$

where ε_0 is the permittivity of free space. If a dielectric material is inserted between the plates, its positive charges will undergo a small displacement in the direction of the field and the negative charges in the opposite direction (**Figure 2.1b**). These are defined as dipoles and the term dipole moment μ is the charge on the dipole q times

the distance of separation of the charges d, the total dipole moment is then

$$\mu = \sum q_n \cdot d_n \qquad \textit{Equation 2.2}$$

This moment is very small since charges in insulators are strictly bound and not free. The small moments are aligning with the directions opposite the external electric field, which results in the appearance of electric charges on the surface of the dielectric material. This phenomena is called dielectric polarization, and the value of polarization P is

$$P = \frac{\mu}{V} \qquad \textit{Equation 2.3}$$

where V is the volume of the material. Therefore, the dielectric displacement factor D becomes

$$D = \varepsilon_0 \cdot E + P \qquad \textit{Equation 2.4}$$

Within the parallel plates, the applied electric field is uniform, which induces uniform polarization. Therefore, P is proportional to the electrical field E by

$$P = \chi \cdot \varepsilon_0 \cdot E \qquad \textit{Equation 2.5}$$

where χ is called dielectric susceptibility. Thus,

$$D = \varepsilon_0 \cdot E + \chi \cdot \varepsilon_0 \cdot E = \varepsilon_0 \cdot (1+\chi) \cdot E \qquad \textit{Equation 2.6}$$

Substitute D and E by $\frac{Q}{A}$ and $\frac{U}{d}$, gives

$$\frac{Q}{A} = \varepsilon_0 \cdot (1+\chi) \cdot \frac{U}{d} \qquad \textit{Equation 2.7}$$

where Q is the charge produced and U is the voltage that produces electric field with distance d and A is the area of the parallel plates. As a result, the capacitance, which is defined as charge produced per unit voltage, is equal to

$$C = \frac{Q}{U} = \varepsilon_0 \cdot (1+\chi) \cdot \frac{A}{d} \qquad \textit{Equation 2.8}$$

This is the prototype of a typical capacitor. The term $(1+\chi)$ is defined as relative

permittivity or dielectric constant ε_r. ε_r is a property of the dielectric material, and could characterise how much electric energy that a dielectric can store under certain electric field.

There are several types of polarization in dielectrics. They are atomic/electronic, ionic, orientation and interfacial polarizations. The schematic diagram for each type of polarization is shown in **Figure 2.2**. Atomic polarization is a small displacement of the electrons in an atom relative to the nucleus. Ionic polarization involves the relative displacement of the cation and anion sub-lattice when applying an electric field on the dielectric. Dipolar polarization happens in materials such as water, since the directions of the molecules are re-orientated by the applied electric field. And finally, the interfacial polarization means when the charges have a limited transport by the electric field, they might be stopped at certain barriers, which includes grain boundary or phase boundary, as a result the charges are polarized within that region.

2.1.2 Relaxation effect and dielectric loss

When a dielectric is experienced on an a.c. field, polarizations alternate in sympathy with the applied field. However due to the inertia of charges, polarization does not alternate instantaneously with the electric field but in a certain time. When the frequency is higher than a point, the dipoles cannot keep up with the field and the alternation of the polarization will lag behind the field and this corresponds to a reduction of it which appears in measurements as a reduction in the permittivity of the material. Ultimately, as the frequency increases the dipole will barely have started to

move before the field reverses, which implies that the field produces no polarization of dielectric at such a high frequency. This process is called relaxation and the frequency beyond which the polarization no longer follows the field is called the relaxation frequency.

Considering the various mechanisms of polarization in dielectrics, the relationship between the dielectric constant ε_r and frequency over the entire spectrum for a hypothetical material can be illustrated in **Figure 2.3**. It is apparent that ε_r decreases with the frequency increasing, although it has peaks around 10^{13} Hz and 10^{15} Hz which is due to the resonance of the atomic and electric polarization. Across the whole frequencies, the interfacial polarization is the slowest process as it involves the diffusion of charges through a resistive material and it cannot exist over 100 Hz. The orientation polarization, which refers to actual reorientation of groups of ions forming dipoles, could not exist over the radio frequency (10^4 Hz) as the inertia of these groups is also considerable. Since ion and atom/electron are rather small, their relaxation time is short, and they could exist over high frequencies around optical range. However, for ultrahigh frequencies over 10^{16} Hz, none of the polarisation type could exist and the dielectric constant is approximately equal to one.

When a capacitor with an ideal dielectric is experienced to an a.c. field, it undergoes charge and discharge following the alternative voltage. The phase diagram of the relationship between the current through the circuit and the applied voltage is shown in **Figure 2.4a**. In this case, the current leakage is zero and there is no power

dissipated in the form of heat. However, there are no perfect dielectrics in reality, where conductivity is not present. For any real dielectric material, the resultant total current density flowing through a dielectric when experienced to an a.c. field can be expressed as

$$j(t) = \frac{\partial D(t)}{\partial t} + \sigma E(t) \qquad \textit{Equation 2.9}$$

where the current density is contributed by the dielectric loss due to movement or rotation of the atoms or molecules in the material by an alternating electric field and the conduction loss from the dc conductivity of σ of the material. The dc conductivity in materials can be divided into band conduction and dc hopping conduction. The former is present in the absence of defects and impurities, which is determined by the band structure of the material. The latter one takes place via defects or impurities which form potential wells (traps or localized states) that are favourable for charge carriers (electrons, holes and ions) to hop (Tuncer *et al.* 2002).

As a result, for real dielectrics, the current-voltage phase diagram is different from the one for ideal dielectrics, in which the current and voltage vectors are not by 90° but with an angle (90-δ) degree (**Figure 2.4b**). The current I contains two components, I_c, which is the capacitance current corresponding to the current in ideal capacitors; I_i, which is in the same direction of voltage, leads to the power loss in the form of heat.

Therefore, $\tan\delta$, alternatively named loss tangent, is defined as dissipation factor or loss factor, which is a measure of the energy dissipated in the dielectric in unit time when an electric field acts on it.

2.1.3 Piezoelectric, pyroelectric and ferroelectric materials

The symmetry of the material, whether it is a single crystal, a thin film, a polycrystalline or an amorphous material, affects its properties (Damjanovic 1998). This can be demonstrated by examples of 32 crystal point groups (**Figure 2.5**). Amount these 32 classes, 11 of them possess a centre of symmetry and are non-polar, which means that when an external force applied, only symmetrical ionic displacements induced so that there is no net change in dipole moment. The other 21 crystal classes are non-central symmetric, in which 20 of them are piezoelectric, with the only exception of point group 432 possessing symmetry characteristics in the cubic system. Piezoelectric materials are a class of materials which can be polarized by an electric field or by application of a mechanical stress. Subsequently, half of these 20 classes are pyroelectric, which exhibit a permanent polarization even in the absence of applied force. This permanent polarization is called spontaneous polarization, P_s. In pyroelectric materials, change in temperature can cause change in polarization due to thermal expansion. A subgroup of pyroelectric is a very special category of material called ferroelectric. Ferroelectric materials are polar materials that possess two or more orientations of spontaneous polarization which can be switched between orientations by an external electric field (Chiang *et al.* 1996).

2.1.4 Piezoelectricity

Piezoelectricity is an electro-deformation phenomenon basically derived from the

Greek word 'piezein' for 'press' with the term 'pressure electricity'. It was originally discovered by Pierre and Jacque Curie in 1880 (Busch 1987), who found that electric charges developed on the surface of quartz and other crystals when they were mechanically stressed. Simply, piezoelectricity can be described as follows: the development of an electrical charge (voltage) under the application of a mechanical force (**Figure 2.6a, b**); or conversely, the deformation (strain) of a material when exposed to an applied electric field (**Figure 2.6c, d**). The mechanism of piezoelectricity is the separating of the centre of gravity of the positive charge and negative charge in non-symmetric crystals, by the application of external force, producing a dipole moment (Anderson *et al.* 1990).

If X is defined as mechanical stress and S is defined as mechanical strain, **Figure 2.6** can be depicted relating the polarisation P to stress X and strain S to electric field E by

$$\left(\frac{\partial P}{\partial X}\right)_E = \left(\frac{\partial S}{\partial E}\right)_X = d \qquad \textit{Equation 2.10}$$

where suffix E indicates the electric field is held as constant (**Figure 2.6a, b**) and suffix X refers that the stress is held as constant (**Figure 2.6c, d**). Thus, d is defined as piezoelectric coefficient. Consider the linear and shear stress along each of the three axes, there are six possibilities and polarization along each axis is

$$P_i = \sum_j d_{ij} X_j (i = 1,2,3; j = 1,2,3,4,5,6) \qquad \textit{Equation 2.11}$$

Alternatively, the strains produced by the electric field is

$$S_j = \sum_i d_{ij} E_i (i = 1,2,3; j = 1,2,3,4,5,6) \qquad \textit{Equation 2.12}$$

where d_{ij} is the piezoelectric coefficient with the directions of each component. There are 18 values of this coefficient of which 15 are independent. The number of

non-zero coefficients amongst those 15 depends on the symmetry of the crystal.

Piezoelectric materials can be used as transducers that transmit into and receive ultrasound energy from the surrounding medium and so are generating and experiencing hydrostatic pressure changes. The corresponding coefficient, namely hydrostatic coefficient d_h, is a measure of the effectiveness of the material as a transmitter and defined as

$$d_h = d_{33} + 2 \cdot d_{31} \qquad \textit{Equation 2.13}$$

where d_{31} is the coefficients relating the field along the polar axis to the strain perpendicular to it and d_{33} is the corresponding coefficient for both strain and field along the polar axis (Burianova *et al.* 2004).

2.1.5 Pyroelectric effect

Pyroelectric effect, which can be observed in pyroelectric materials, is defined as the change of the vector of spontaneous polarization with temperature:

$$p_i = \frac{\partial P_{s,i}}{\partial T} = \frac{D_i}{\Delta T} \qquad \textit{Equation 2.14}$$

where p_i is defined as pyroelectric coefficient, P_s is spontaneous polarisation, T is temperature and D_i is the surface charge density.

2.1.6 Ferroelectricity

A ferroelectric material is a subgroup of pyroelectric materials which possesses at least two equilibrium orientations of the spontaneous polarization vector in the

absence of an external electric field and the spontaneous polarization vector can be switched between their orientations by an electric field. Many ferroelectric materials undergo a structure phase transition from a high-temperature paraelectric phase into low-temperature ferroelectric phase. Some materials even undergo several phase transitions into successive ferroelectric phases. The temperature of the first phase transition into ferroelectric phase is called Curie point T_c. The symmetry of the paraelectric phase is always higher than the ferroelectric phase and the transition into which usually leads to strong anomalies in the dielectric, elastic, thermal and other properties of the material (Damjanovic 1998). In order to minimize the electrostatic energy of depolarizing fields and the elastic energy associated with mechanical constraints during the phase transition, the spontaneous polarization is not uniformly aligned throughout the material, but with the formation of randomly orientated regions within which the polarizations are uniformly aligned. The regions with uniformly oriented spontaneous polarization are called ferroelectric domain and the region between two domains is called domain wall. The walls which separate domains with oppositely orientated polarization are called 180° walls and those which separate regions with mutually perpendicular polarization are called 90° walls.

The most important characteristic of ferroelectric materials is that the spontaneous polarisation can be reoriented by applying a strong electric field. This process is called poling. The consequence of domain-wall switching is the occurrence of the ferroelectric hysteresis loop. A typical hysteresis loop is shown in **Figure 2.7** and was explained by many researchers (Damjanovic 1998; Lohse *et al.* 2001). At small

value of the electric field, the polarization increases linearly with the field amplitude (segment AB). In this region, the field is not strong enough to switch domains with the unfavourable direction of polarization. When the electric field is increased continuously, the polarization of domain with an unfavourable direction of polarization will start to switch in the direction of the field, which results a sharp rising of polarization. However, the response is strongly non-linear in this region (segment BC). Once all the domains are aligned (point C), the ferroelectricity behaves linearly again (segment CD). When the electric field is decreasing, some domains will back-switch, but the polarization is non-zero when the field is reduced to zero (point E). A reversed electric field must be applied in order to reach a zero polarization state (point F). Further increase of the field in the negative direction will cause a new alignment of dipoles and saturation (point G). The electric field is then reduced to zero and reversed to complete the cycle. The value of the polarization at zero fields (point E) is called remnant polarisation, P_r. The field necessary to bring the polarization to zero is called the coercive field, E_c.

A hysteresis loop can reflect the value of polarization, which is the true measurement of the degree of ferroelectricity (Jaffe 1971). The coercive field, spontaneous and remnant polarization and shape of the loop may be affected by many factors including the thickness of the film, the presence of charged defects, mechanical stresses, preparation conditions, and thermal treatment (Demartin & Damjanovic 1996; Klissurska *et al.* 1995; Li *et al.* 2007; Tagantsev *et al.* 1995).

2.2 Lead zirconate titanate (PZT) solid solution system

Lead zirconate titanate (PZT) solid solution system is the major material investigated in this project. It is a well-known piezoelectric ceramic with wide range of applications. In this section, the crystal structure, properties and applications of PZT material are reviewed.

2.2.1 Historical development of PZT

Ferroelectric ceramics were born in the early 1940s with the discovery of the phenomenon of ferroelectricity as a source of the unusually high dielectric constant in ceramic barium titanate capacitors. In 1950s, the solid solution system lead zirconate titanate $Pb(Zr_x, Ti_{1-x})O_3$ ($x = 0 \sim 1$) was firstly investigated in Japan (Shirane & Suzuki 1952) and developed in piezoelectric applications by Jaffe (1954), after which PZT has been largely supplanted for transducer applications (Berlincourt 1959, 1960). It is because PZT compounds (a) possess higher electromechanical coupling coefficients than $BaTiO_3$, (b) have higher T_c values, which permit higher temperatures of operation or higher temperatures of processing during the fabrication of devices, (c) can be easily poled, (d) possess a wide range of dielectric constants, (e) are relatively easy to sinter at lower temperatures than $BaTiO_3$, and (f) form solid-solution compositions with many different constituents, thus allowing a wide range of achievable properties (Haertling 1999).

2.2.2 Perovskite structure

Many piezoelectric materials, such as $BaTiO_3$ and PZT, crystallize in the perovskite

structure (Izyumskaya *et al.* 2007; Kipkoech, Azough, & Freer 2005), which is referred from the mineral perovskite $CaTiO_3$. The perovskite compound is in ABO_3 structure, in which A and B are representing two cations of considerably different size. The perovskite structure of $BaTiO_3$ is shown schematically in **Figure 2.8 a**. It is evident that the structure is based on a cubic close-packed assembly of composition AO_3 with the A ion (Ba^{2+}) coordinated with 12 oxygen ions and B ion (Ti^{4+}) in the octahedral site. Above Curie temperature (T_c) of $BaTiO_3$, the unit cell is cubic. Below T_c, the structure transforms from a non-ferroelectric cubic to a ferroelectric tetragonal phase, realised by a small displacement of B ion in the octahedral site, as shown in **Figure 2.8 b**. The octahedron for B ion is larger than necessary, as it is expanded by the larger A ion neighbours. When the temperature goes through T_c, B ion can move towards one of the six directions within the octahedron, resulting a slightly change of the lattice parameter. This displacement produces a permanent electrical dipole, i.e. spontaneous polarization. The directions along which the polarization will develop depend on the electrical and mechanical boundary conditions imposed on the sample (Damjanovic 1998). In order to minimize the energy associated with these conditions, the spontaneous polarizations uniformly orientate in many domains of which the directions are separated by 180° and 90°, leading a zero net polarization.

There are also lower temperature transformation occurs in $BaTiO_3$, which is shown in **Figure 2.9**. Below 0°C the unit cell is orthorhombic and below -80°C it is rhombohedral with the polar axis along a body diagonal. Both of these two structures are ferroelectrics.

PZT possesses perovskite structure too. Within the unit cell, the A ion (Ba^{2+}) is replaced by Pb^{2+}, and both Ti^{4+} and Zr^{4+} are randomly distributed over B sites of octahedrons in the perovskite structure. The structure formation of PZT at room temperature depends on the ratio of Ti^{4+} and Zr^{4+} and can be depicted in the PZT phase diagram, which was firstly set up by Jaffe (1971).

2.2.3 Morphotropic phase boundary

Lead zirconate titanate is a solid solution of lead titanate ($PbTiO_3$) and lead zirconate ($PbZrO_3$), which are soluble in all proportions. A schematic presentation of $PbZrO_3$-$PbTiO_3$ phase diagram is shown in **Figure 2.10**, which was described and analysed by many pioneers (Damjanovic 1998; Noheda *et al.* 2000). The x axis shows the compositions, which are abbreviated by $100x/100(1-x)$ indicating the Zr/Ti ratio in the solid solution in % while the y axis shows the temperature. The structure of the high-temperature phase is cubic, which is non-ferroelectric (paraelectric). When the temperature goes down, titanium-rich compositions transform into tetragonal perovskite structures. Substitution of Zr^{4+} for Ti^{4+} in $PbTiO_3$ reduces the phase transform temperature and changes the symmetry of tetragonal structure which ultimately transforms to another ferroelectric phase of rhombohedral. At low Ti content (x>95%), the structure is orthorhombic with a small field of stability of a tetragonal phase near 240°C. Both of these two phases are anti-ferroelectrics. The rhombohedral phase actually divides into two phases with a transition from a high-temperature rhombohedral phase to a low-temperature rhombohedral phase with

the roughly x value between 5% and 35%, as shown in the graph.

It is obvious that a boundary near the centre of the phase diagram, by which the tetragonal and rhombohedral phases are separated, is nearly independent of temperature. This boundary is called morphotropic phase boundary, which in short is MPB. It is reported that the piezoelectric coefficients, pyroelectric coefficient, dielectric constant and remanent polarization of PZT material reach a peak with the composition in the region near MPB (Jaffe 1971). One of the reasons can be explained by the ease with which domains may be reoriented near MPB. At the boundary of rhombohedral and tetragonal phases, the free energy of these two phases is equal and it is possible that the electrical poling field may easily switch between tetragonal and rhombohedral domain states. In tetragonal structure, there are six equivalent polar axes giving six domain states while in rhombohedral phase, the polar axis is along the body diagonal of the cubic state, giving eight possible domain states. As a result, there are effectively 14 possible directions along which polarization may be reoriented by the poling field, leading to a large remnant polarization for the compositions near MPB, which is also supportive of the increase of piezoelectric coefficients (Damjanovic 1998). The current understanding is that MPB is not a sharp boundary but a temperature-dependent compositional range where tetragonal and monoclinic phases coexist. The enhanced electrical properties can be rationalised in terms of large ionic displacements associated with electrical or mechanical stress induced rotation of the monoclinic polar axis (Moulson & Herbert 2003).

For the application point of view, the most interesting composition of PZT is near MPB. Many researches are based on the composition in this region (Du *et al.* 1998; Suzuki *et al.* 1999). PZT ceramics are always used with a dopant, a modifier, or other chemical constituent to improve and optimize their basic properties for specific applications (Haertling 1999). Donor dopants, which are those of higher charge than that of the ions replaced and acceptor dopants, which are those of lower charge than the replaced ions are commonly used for PZT doping. In order to maintain electrical neutrality, the donor dopants are compensated by cation vacancies while the acceptor dopants are compensated by oxygen vacancies.

2.2.4 Bulk and thin film PZT

2.2.4.1 Bulk PZT

By far, bulk materials are still dominating in numerous applications of ferroelectric ceramics due to their simplicity, compact size, low cost and high reliability (Haertling 1999). Bulk PZT ceramics are traditionally made from powder formulated from individual oxides. This process is called mixed-oxide powder process. The main stages of this process include powder preparation, calcination, ball milling, forming and sintering. This traditional technique is explained by many excellent researchers (Moulson & Herbert 2003; Haertling 1999). The process starts from the selection of individual oxide powders with the desired composition and mixed in a slurry form. Distilled water is always used to solute the oxide from a cost and environmentally preferred standpoint. The mixed powders are then calcined at the temperature of several hundred degrees below the sintering point. In this stage, a high-temperature

solid state chemical reaction happens so that a desired composition forms. Ball milling is necessary for calcined materials in order to produce the required chemical homogeneity. A common method is to use a plastic-lined mill with high-density media (alumina or zirconia balls) and a non-polar, powder soluble milling liquid, such as distilled water or ethanol. Depending on the particular powder characteristics, milling times may very from 2hrs to 16hrs. The milled powders are then thoroughly dried, mechanically broken up, homogenised in a V-blender, and stored for the next stage.

There are a variety of forming methods that have been successfully applied to compact the powders to a specific form or shape prior to densification, amount which cold pressing in a steel mod is a common one. Other methods include extrusion, slip casting, tape casting, roll compaction, screen printing, and injection molding etc. The subsequent step is sintering, which makes the pressed powders into a pore-free, fully dense ceramic element. The sintering temperature for PZT ceramic is reported to be over 1200°C. However, in order to reduce the volatilization of lead during this stage, excess lead oxide is used when mixing the powders. Other sintering techniques include hot isostatic pressing and vacuum sintering and so on. The final steps after sintering are (1) slicing of the slug, (2) lapping of the slices, (3) polishing of the plates for electrooptic elements, (4) electroding, and (5) evaluation of the parts for further assembly to components.

2.2.4.2 PZT thin film

Although most of the ferroelectric applications are based on bulk materials, a trend

toward thin films for some applications has developed and is steadily increasing in intensity due to the continuing drive to greater miniaturization and integration of bulk component. Thin films are layers which are in micrometer and sub-micrometer level in thickness deposited on substrates. Like bulk materials, thin films possess a given set of properties relatable to their composition and microstructure; but unlike the bulks, they possess another set of properties derived from their proximity to and interaction with the supporting substrate, such as diffusion (forming buffer layers), epitaxy, and internal stresses and so on. These factors commonly control the total behaviour of the film. It is reported that PZT films have been widely investigated for direct integration onto silicon based devices due to the fast development of MEMS (Choi *et al.* 2005; Duval *et al.* 2003; Muralt 2000b).

There are many apparent advantages of thin films when compared with bulk components, such as smaller size, less weight, and easier integration, aside from which they offer additional benefits including (1) lower operating voltages, (2) size and weight compatibility with integration trends, (3) better processing compatibility with silicon technology, (4) ease of fabrication, and (5) lower costs through integration. Moreover, the sintering and crystallization temperatures of the film are usually hundreds of degrees centigrade lower than that for bulks, and this can often be the dominating factor in a successful design and application. Take PZT as an example, typical sintering conditions for conventional PZT are over 1200°C for 3 to 5hrs (Chen *et al.* 2007), while for thin film produced by sol gel method, it is reported that the temperature is below 700°C (Dorey, Stringfellow, & Whatmore 2002).

2.2.4.3 Bulk and thin film PZT applications

The applications for ferroelectric ceramics are manifold and pervasive, covering all areas of our workplaces, homes, and automobiles. Many general category applications for bulk PZT and thin film PZT are given in **Figure 2.11**. Some of the traditional applications are more appropriate for bulk materials, which are typically divided into two categories: piezoelectric generators and piezoelectric motors. The piezoelectric generator is working with the phenomenon whereby electrical charge (polarization) is generated from a mechanical stress. Devices with this principle include hydrophones, microphones, gas igniters and sensors and so on. Conversely, the piezoelectric motors are working associated with the mechanical movement generated by the application of an electrical field. Examples include actuators, micropositioners, ultrasonic motors etc. Moulson *et al.* (2003) have summarised the details of those applications from principle to manufacturing.

Some applications are appropriate for both bulk and thin film materials, within which dielectric capacitors must be introduced exclusively since it is such an important component integrating in a wide range of electronic devices. $BaTiO_3$ was historically the first composition used for dielectric capacitors and afterwards PZT, especially PZT thin film, was reported to be processed as dielectric capacitors by many techniques (Asano *et al.* 2003; Dimos & Mueller 1998).

At the bottom of **Figure 2.11**, there are several applications which are exclusively

designed for thin films. One of the good examples is non-volatile memories. PZT thin films are now replacing the conventional SiO_2 capacitors in the computer memory application. The higher dielectric constant can reduce the size of the component thus increase the density of capacity memories on a given substrate wafer. The operating voltage will also be decreased when applying ferroelectric thin films into memory system.

2.2.5 PZT/polymer composites

PZT/polymer composites have been developed principally because their properties offer advantages for sonar and medical ultrasonic imaging technologies over those of PZT alone. Composite technology in general sets out to combine materials in such a way that the properties of the composite are the optimum for a particular application. The mechanical, thermal and electrical properties are determined by the choice of component, the amount of them and the connectivity in which how the components (ceramic and polymer) are interconnected. When a second phase is introduced in a material, there are 10 connectivity patterns ranging from 0–0 which is unconnected three-dimensional checkerboard pattern to 3–3 which is interpenetrating pattern in which both phases are three-dimensionally self-connected. Some of these connectivity patterns are particularly well suited for decoupling the longitudinal and transverse piezoelectric effects, so that materials will significantly enhance piezoelectric properties. A good example is 1-3 composites.

Figure 2.12 shows the model of a 1-3 composite and its cross-section graph. It

consists of piezo-ceramic rods extending from electrode to electrode and embedded in a polymer. The rods have one-dimensional connectivity and the polymer has three-dimensional connectivity. In this design, PZT is embedded in polymers that can bear the force of vibrating PZT in the x-y layer. As a result, the negative coefficient d_{31} is significantly reduced and a high hydrostatic coefficient d_h (defined in *Equation 2.13*) can be obtained. 1-3 composites are successfully exploited in sonar system, which include sound navigation and ranging (Asano *et al.* 2003; Marin-Franch *et al.* 2004; Ting 1992). They are also utilized in some other applications such as medical imaging technologies and non-destructive testing (Asano *et al.* 2003; Benjamin 2002; Tseng *et al.* 2003). These diagnostic tools are widely used by physicians due to their ability to produce real-time, high-resolution, and three-dimensional images of internal soft body tissue without the use of potentially hazardous ionizing radiation. The process utilizes an electromechanical transducer operating in the pulse-echo mode to transmit ultrasonic pulses into the body and to receive the faint echoes produced by the reflections from internal structures (Janas & Safari 1995).

The traditional fabrication of 1-3 composites is based on 'dice and fill' process due to its simplicity. A piezoelectric ceramic plate is diced by diamond machining into an array of square-section column standing on the un-diced base of the plate. The structure is then infiltrated with the chosen polymer after which the base is removed away to produce composites. The size of the ceramic rod is reported to be 100 μm (Moulson & Herbert 2003). The diamond machining is progressively slower when

making fine structures which may also be damaged during processing. Other means of performing the dicing operation have been investigated, which include laser cutting (Eyett *et al.* 1987; Ohara *et al.* 1994) and ultrasonic machining (Ohara *et al.* 1993). In laser cutting, ceramic discs are mounted on a laser cutter. Laser beams ranging from 5μm to 500μm are scanned across the ceramic transversely and vertically, followed by the incorporation of polymers. In ultrasonic cutting, the ceramic discs are cut by steel saw blades through a combination of ultrasonic vibration, abrasives and pressure. In 'dice and fill' process, the rod size is highly depend on the accuracy of the cutter, therefore fine-scale structure needs more accurate cutting tools which are always expensive. Also, cutting is a time-consuming process resulting the limitation of less efficiency of the process.

Fine-scale arrays can also be produced by injection-molding process, which is schematically shown in **Figure 2.13**. In this process, PZT powders are injected into a mold to form the desired structure and then heat-treated to remove binder and sintered, after which the mold is removed. The rod size was reported to be 50μm with various shapes and spacings (Moulson & Herbert 2003). The injection molding process is simple and therefore in high efficiency. However, the limitation of it is the lengthy process of forming the mold. The process shows promise for manufacturing a large number of samples, but not for rapid prototyping of research samples.

Bhatti *et al.* (2001) reported that an array of pillars can be formed by direct ink-jet printing with a PZT ink. The components of the ink are PZT powders, acrylic

dispersant and PVB binder and an ethanol-propanol mixture as the solvent. The structure is printed by a color-jet printer and a multi-layer printing process is necessary when producing thicker structures. In that work, the author reported that 1000 layers were printed in 12ks and the structure thickness is about 400 μm.

In this project, it has been discovered that micrometer PZT columnar structures can be formed by electrohydrodynamic deposition when a precursor with adjusted concentration is used. Details will be discussed in **Chapter 5**.

2.3 Typical processing techniques for PZT films

The last two sections have introduced the properties of functional materials (e.g. PZT) and their versatile applications in capacious fields, which have witnessed a considerable scientific and industrial interest in the area of developing film processing techniques for these materials. Various methods have been developed, which can be utilized to process films of micro- or nano-dimensions with a precisely controlled structures. These methods commonly comprise three basic steps: generation of the coating precursors at the source; transport from the source to the substrate; and nucleation and growth of the coating at the substrate. Considering the working principles, commonly used techniques can be classified into three major groups, which include physical vapor deposition (PVD), chemical vapor deposition (CVD) and sol gel method. In this section, typical methods in each group and their apparatus used are introduced and compared.

2.3.1 Physical vapor deposition process

Physical vapor deposition processes comprise a class of deposition techniques in which one or all constituents of the deposit are generated from a solid source by heat induced vaporization or momentum transfer processes. These include sputtering, pulsed-laser deposition and electron-beam evaporation and so on.

2.3.1.1 Sputtering deposition process

The basic sputtering deposition involves removal of atoms from the surface of a material by energetic ion bombardment and collection of the sputtered species on a solid surface (substrate). The working principles are described schematically in **Figure 2.14**. A target, compromising of the material to be processed, is placed at a negative potential of a power supply of which the voltage range is from a few hundred volts to a few kilovolts. At a critical value of the chamber pressure (1×10^{-3} Torr to -1 Torr), the applied voltage strikes a discharge in the vicinity of the target material. The target, because of its negative potential, is bombarded by the ions present in the plasma. In situations when the gas ions are sufficiently heavy, the bombardment of the target leads to sputtering of the target surface by a momentum transfer process, as shown in **Figure 2.15.** These sputtered atoms collide with the substrates to be coated and form an extremely adherent coating. When the ions collide with the target surface, electrons can be emitted too. These light and negatively charged electrons are affected by the combination of electrostatic and magnetic forces when they leave the surface and execute cycloidal motion around the magnetic field lines. When the electrons have sufficient energies, the gas atoms can be ionized and these ions can collide with

the target material again so that a continuous sputtering process can be sustained. Inert gas argon is commonly used as the sputtering gas which is pumped into the working chamber because of its higher atomic number and non-reactivity.

The sputtering rate is proportional to the number of ions striking the target material, which can be increased by increasing the ion density in the vicinity of the target. One of the methods for such propose is to apply magnetron field and this modified sputtering process is known as magnetron sputtering (Rossnagel & Hopwood 1994). If the target material is electrically conductive, a d.c. voltage can be used for the generation of plasma. However, when the target is a non-conductive material (e.g. oxide) on which the charges are easily built-up, an RF potential must be applied where the sign of the anode-cathode bias is varied at a high rate (Adachi *et al.* 1986).

The advantages of a sputtering process are as follows. Firstly, various materials can be processed such as metal oxide, carbides, nitrides, metals and metal alloys especially of which are with high melting temperatures. Secondly, high density and adhesive films can be deposited on the substrates with high reproducibility of layer properties. Moreover, the deposition rate is stable with high thickness uniformity and large deposit scale (Kukla 1997).

When multicomponent materials are used as targets, especially for the deposition of ferroelectric films using oxide in complex composition, the sputtering process is difficult to control the composition of the deposit, which leads to off-stoichiometry in

the film. This has been quoted as a major disadvantage of sputtering process when compared with other techniques (Jayadevan & Tseng 2002). This matter can be improved by sputtering the constituent components in a reactive sputtering mode. A modified process has been developed making use of a rotating target assembly (Nielsen *et al.* 1998). The system can hold different component oxide targets or elemental targets in a controlled partial pressure of oxygen. For example, for deposition of $BaTiO_3$ films, BaO and TiO_2 can be used as the targets. During deposition, these two targets are connected to the power supply with a pulse unit connecting in series, so that the targets can be sputtered according to different compositions. This modified process can also be utilized to fabricate multilayer structures in which layers with different materials are stacked (Jia, Chang, & Anderson 1995).

2.3.1.2 Pulsed laser deposition

Pulsed laser deposition is one of the physical vapor deposition techniques, which can produce single and multi layer films of a wide range of target materials on various substrates (Jayadevan & Tseng 2002). This technique involves ablating the target material by focusing a laser source for a short pulse of about 30s followed by deposition on the heated substrate. A schematic diagram representing the laser ablation deposition process is shown in **Figure 2.16**. An excimer laser beam is induced and specified through an attenuator and a pair of expanding/collimating lenses, and subsequently focused on the surface of the target. The laser beam is rastered during ablation by means of using a programmable kinematic mount for the

last mirror of the optical train. The rotating target holder is capable to hold several targets and position them to the laser beam in order to fabricate the desired multilayered hetero-structures without breaking vacuum. The substrate to be coated is facing the target and placed on a heated substrate holder which is subjected to a high oxygen background pressure in order to produce oxide films when such structures are processed.

The factors that influence the characteristics of the deposited film may vary, which include flux distribution during ablation, background gas pressure, target to substrate distance, laser energy and wavelength, and target substrate geometry arrangement (Jayadevan & Tseng 2002). Pulsed laser deposition is extensively used for the fabrication of ferroelectric/conductive oxide hetero-structures for capacitor applications. An example of such structures is PZT/$La_{0.5}Sr_{0.5}CoO_3$ (LSCO), where LSCO is a conductive oxide layer that deposited as the electrodes (Auciello *et al.* 1998).

The major advantages of this processing technique include 1) it is easy to generate stoichiometric films after deposition; 2) the applying of oxygen in high content during the deposition is suitable for crystallization of oxide films; 3) high deposition rate; 4) relatively low substrate temperature. The disadvantages of this technique are that it is not suitable for large scale deposition and the high capital cost makes it difficult to be used in commerce (Auciello *et al.* 1998; Kidoh *et al.* 1991; Verardi *et al.* 2000).

2.3.2 Chemical vapor deposition

The constituents of the precursors for most of the ceramics exist in the form of heavy molecular gases or volatile liquids such as halides, hydrides and hydrocarbons. Chemical vapor deposition (CVD) is a processing technique involving the dissociation and/or chemical reactions of such reactants in an activated environment such as thermal, photon or plasma excitation, followed by the formation of a stable solid product. Depending on different energy sources or different precursors, CVD can be categorized into various methods such as thermally assisted CVD, plasma assisted CVD, photon assisted CVD and metalorganic CVD (MOCVD) (Choy 2003).

2.3.2.1 Thermally assisted CVD process

Thermally assisted CVD is a conventional CVD process in which the chemical reactions are initiated by thermal energy (heated substrate) in a reactor using inorganic chemical precursors. The thermal energy can be in the form of RF heating, infrared radiation or resistive heating. The schematic diagram of conventional CVD process is shown in **Figure 2.17**, which was described by Choy (2003). A wide range of oxides, borides, silicides, nitrides and carbides have been deposited by the thermally assisted CVD process. Some of the typical reactions are given below:

$$Si(CH_3)Cl_3(g) \rightarrow SiC(s) + 3HCl(g)$$

$$2Al(CH_3)_3(g) + 9O_2(g) \rightarrow Al_2O_3(s) + 6CO(g) + 9H_2O(g)$$

$$SnCl_4(g) + O_2(g) \rightarrow SnO_2(s) + 2Cl_2(g)$$

The high substrate temperatures have both advantages and adverse effects on the properties of the films. On the one hand, this high temperature promotes the growth of

a dense and well crystallized structure with the minimum of impurities trapped in. On the other hand, this high deposition temperature may have adverse effects in situations where the substrate is susceptible to temperature and can induce irreversible structural/electrical changes. This is frequently encountered while depositing dielectric films on previously processed electronic devices. According to this, the deposition process should be carried out at low temperature environment in which plasma or photon can be utilized to assist the deposition process.

2.3.2.2 Plasma assisted CVD process

Plasma assisted CVD, which is also known as glow discharge CVD, is a modernized CVD process using electron energy (plasma) as the activation method to enable deposition to occur at a low temperature. The commercial plasma reactor was first developed in 1970s for the deposition of Si_3N_4 passivation layers (Rosler 1991). The basic design of a plasma CVD reactor is shown schematically in **Figure 2.18**. It mainly consists of two parallel plates one of which is connected to a d.c. or RF power supply and the other is a heated substrate holder. As shown in the graph, the constituent gases are delivered into the reaction chamber through region 1; consequently, the reactant gases are excited by the plasma near region 2; and finally, thin film is deposited at heated substrate which is immersed in the plasma (region 3). During this process, the applied electrical power at a sufficiently high voltage to the reactant gas results in the breaking down of the gas and generates discharge plasma consisting of electrons, ions and electronically excited species. The molecules in the reactant vapor are ionized and dissociated by electron impact, and hence generating

chemically active ions and radicals that undergo the heterogeneous chemical reaction at or near the heated substrate surface and deposit as a thin film. The gas pressure and the frequency of the applied electrical power are determined by the conditions under which the plasma can be sustained.

In order to avoid the ion bombardment of the growing film in the plasma, this process can be modified to generate plasma away from the deposition zone, which can avoid damaging the films caused by energetic ions and electrons in the plasma. This is known as remote plasma assisted CVD. The design and development of such modified process have been described by many other researchers (Lucovsky *et al.* 1989; Richard *et al.* 1985; Tsu & Lucovsky 1987).

The main advantage of plasma assisted CVD process is that the deposition can occur at relatively low temperatures on large areas. The ion bombardment can substitute for the higher deposition temperature to obtain the required film density. This low temperature deposition is suitable for applications in which temperature-sensitive substrates are used. One of the most common examples utilizing such technique is the growth of silicon nitride using SiH_4 and NH_3 gases (Budhani *et al.* 1987; Smith *et al.* 1990). The disadvantages of this process are first of all, the high ion energy plasma produced may damage the film and also some fragile substrates (e.g. silicon wafer) by strong ion bombardment and needs to be avoided by means of placing the substrate away from the plasma (remote process); secondly, this process is in demand of high vacuum to generate plasma, which requires a more sophisticated reactor, and thus it is

more expensive than the conventional CVD system (Choy 2003).

2.3.2.3 Photo assisted CVD process

Although plasma assisted CVD can deposit films in lower temperature substrate, ion bombardment of the growing films and fragile substrates may restrict the applications of such technique. Photo assisted CVD can be utilized to avoid this matter. It is a process that relies on absorption of light to raise the substrate temperature which causes thermal decomposition of the precursor in the gas phase and the decomposed intermediate products undergo subsequent heterogeneous chemical reactions on the substrate surface to form the desired film. The design of photo assisted CVD is slightly different to the thermally heated reactor in the conventional CVD. A transparent window is used in the deposition chamber for optical access, through which the excitation wave can be transmitted and focused on the substrate (Allen 1981). The selected area is scanned by the laser or projection imaging transmitted through the chamber window, which provides localized surface heating on the substrate and achieves sufficiently high transient temperatures that are required for vapor decomposition. The light sources used in the process can be various, which include arc lamp, CO_2 lasers, Nd-YAG lasers, excimer lasers and argon ion lasers (Mayo 1986). The laser wavelength is commonly selected from the near ultraviolet through to the infrared in order to give photon energy greater than the band gap of the substrate so that it is highly absorbing in the substrate for photo-thermal deposition and no absorption in the vapor phase. Beside those, the visible range wavelength is also used (Choy 2003).

The advantages of photo assisted CVD are as follows. Firstly, it can be performed at atmospheric or reduced pressure (e.g. 0.01–1 atm), which is different from plasma assisted CVD where a vacuum environment is compulsory. Secondly, localized deposition, selected area deposition or patterned films can be achieved by rastering a focused laser on localized area or image projection of a pattern. Moreover, performed at low excitation energies (typically <5 eV), photo assisted CVD process can avoid the ion bombardment damage of film and substrate that is encountered in plasma assisted CVD (Choy 2003). However, the disadvantage of this process is that the poor dissociation efficiency of the precursors induced by the photon may reduce the deposition rates.

2.3.2.4 Metalorganic chemical vapor deposition

Metalorganic chemical vapor deposition (MOCVD) is a variant of CVD process, which has been classified according to the use of metalorganics as precursors. The phase metalorganic is defined as the compound containing metal atoms bonded to organic radicals. MOCVD process involves decomposition or pyrolysis reactions of metalorganic precursors and other gases in a CVD reactor, to produce a nonvolatile solid deposited on a suitably placed substrate. Superior to halides, hydrides or halohydrides that are always used as reactant precursors in conventional CVD, metalorganic precursors have lower decomposition or pyrolysis temperatures, which enable MOCVD process to perform at a lower deposition temperature. A comparison has been demonstrated by Choy (2003), which is shown in **Table 2.1**.

The apparatus design of MOCVD is comparable with the one of conventional CVD, as the underlying operation principles are the same. However, modified precursor delivery techniques are incorporated with the standard design and described by many researchers (Foster *et al.* 1995; Gao *et al.* 1993). Utilizing these techniques, MOCVD can be used to deposit amorphous, epitaxial and polycrystalline films of a wide range of materials, such as semiconducting material, ferroelectric material, dielectric material and superconducting material (Choy 2003).

Table 2.1 *Comparison of MOCVD and conventional CVD for forming GaAs*

Precursor	Process conditions	Reaction
Metalorganic	600-800°C (0.1-1 atm)	$(CH_3)_3Ga + AsH_3 \rightarrow GaAs + 3CH_4$
Halide	800°C (reduced pressure)	$Ga + AsCl_3 + 1.5H_2 \rightarrow GaAs + 3HCl$

The advantages of MOCVD are 1) simplified apparatus when compared with plasma/photo assisted CVD processes; 2) the process can be performed at relatively low temperature and ambient or reduced pressure; 3) films in various forms can be generated (e.g. amorphous, epitaxial and polycrystalline); 4) relatively high deposition rate and large deposition scale (Peng & Desu 1994). However this process also has limitations. Firstly, metalorganic precursors are commonly very expensive compared to halides, hydrides, and halohydrides that used in conventional CVD process and they are not widely available in commerce for some coating systems, which need to be synthesized specifically for certain applications. Secondly, metalorganics are normally very reactive and hence they are difficult to purify, which is not suitable

when process high quality semiconductor materials (Choy 2003).

2.3.3 Sol gel method

The sol gel process is originally discovered by Ebelmen in which under the influence of humidity, a silicon alkoxide solution changed from a clear liquid into a transparent solid that heated to form silicon dioxide (Reuter 1991). Nowadays, sol gel method has become a common approach for the preparation of glasses and ceramics thin films, especially ferroelectric oxide (Livage *et al.* 1988). The method consists of three steps: 1) making a homogeneous precursor solution of the desired metal component; 2) the sol is deposited on the substrate and undergoes hydrolysis under controlled conditions to produce a gel containing the hydrated metal oxide; 3) the gel is then dried, compacted, and sintered to produce a ceramic or glassy material at a temperature much lower than that required by the conventional melting process.

In the solution preparation step, the precursor containing the desired metal ions present as alkoxides, metalorganics or inorganic salts is dissolved in a suitable solvent to form the sol solution. Alcohol is commonly used as the solvent and acetic acid, used as the catalyst, is also dissolved into the solution (Wu *et al.* 1998). The viscosity of the solution needs to be adjusted in order to obtain dense and homogeneous films after gelation (Jayadevan & Tseng 2002). This solution preparation route is also utilized to prepare precursors for other processing techniques. In this project, the PZT precursor used for electrohydrodynamic atomization is prepared following the sol gel solution preparation route. Details will be given in the following chapters.

In the gel formation step, the sol is initially deposited onto a substrate by dip coating or spin coating before it is gelled. In dip coating process, the substrate is normally withdrawn vertically from the coating bath at a constant speed. The sol is entrained on the substrate and splits from the liquid bath surface. In spin coating process, an excess of liquid is dispensed on the substrate which is subsequently spun up. Driven by centrifugal force, the liquid flows radially outward the edge and leaves as droplets. The left liquid with high resistance to flow will remain on the surface and form a thin film. After deposited on the substrate, the sol will transform to a semi-rigid gel as a result of evaporation and polymerization. This process is determined by the rate of hydrolysis, condensation, evaporation and also the electrostatic or steric interactions amount various groups present in the sol (Brinker *et al.* 1992).

Finally, the formed gel film needs to be subjected to heat treatment which is necessary for further decomposition of the organic compounds and crystallization of the desired material (Mackenzie & Xu 1997).

The advantages of the sol-gel process reside in the high purity of the metal alkoxide precursors, the homogeneity of the components at the molecular level, and the low processing temperature when compared with the powder processing method. These features are all of paramount importance in fabricating electronic ceramics (Bradley 1989). Moreover, this technique is also economically affordable due to the simple equipment needed for deposition (Jayadevan & Tseng 2002). The disadvantages of sol

gel method are: 1) it is difficult to control the chemical composition and eliminate the metastable phases; 2) the heat treated film is easily contaminated due to the presence of undecomposed groups in the gel (Jayadevan & Tseng 2002); 3) low processing efficiency and difficulty in obtaining thick films (3μm of critical thickness) (Tsaur *et al.* 2002).

2.4 Electrohydrodynamic atomization

In this section the emphasis is on understanding the various modes of electrohydrodynamic atomization, amongst which the mechanism of the stable cone-jet mode is described in details in order to explain why it is suitable for the electrohydrodynamic deposition and printing process. The influence of processing parameters (e.g. flow rate and applied voltage) and the physical properties of the sprayed precursor are also discussed considering the mode obtained under different conditions.

2.4.1 Spray modes in electrohydrodynamic atomization

As mentioned in **Chapter 1**, electrohydrodynamic atomization of liquids is a physical process induced by an electric force applied to the surface of a liquid which undergoes deformation to a meniscus at the outlet of a capillary and/or elongates to a jet which subsequently breaks up into droplets. Considering the geometric criteria characterizing the form of the meniscus and jet, the spray process can be classified into different modes. Many researchers have summarized the knowledge in the

subject of the spraying mode under different criteria, considering different influent parameters such as physical properties of the liquid (e.g. surface tension, density, conductivity and viscosity) and processing parameters (e.g. flow rate and applied voltage). (Cloupeau & Prunetfoch 1994; Grace & Marijnissen 1994; Hayati *et al.* 1987; Jaworek & Krupa 1999b; Shiryaeva & Grigorev 1995). In this section, the spraying mode present in this work where the PZT sol was used as the sprayed precursor have been summarized based on the theories published by those researchers. The different drop size and spatial distribution of the sprayed aerosol in different spraying mode have also been discussed.

2.4.1.1 Dripping mode

The dripping mode of electrospray is commonly obtained at lower applied voltage. It does not differ significantly from the dropping when no voltage is applied to the capillary. **Figure 2.19** shows the schematic diagram of the dripping mode and its real image captured by high speed camera. At the beginning, the liquid rises along the outer wall of the capillary and accumulates partly over the outlet section. Then the liquid is formed as regular spheres and detaches from the capillary as a drop when the gravity force and the electric force overcome the surface tension force. After the drop detachment, the meniscus contracts back to form a hemispherical-like meniscus.

In the dripping mode, the emission of droplets may occur at regular time intervals, without the creation of satellites, so that all the droplets have the same size. In general, droplet diameter remains greater than that of the capillary, thus leading to the

emission of large droplets at low frequencies. For a given flow rate, the maximum emission frequency may increase and the minimum droplet diameter may decrease significantly if the diameter of the capillary is reduced (Cloupeau & Prunetfoch 1990; Sato 1984). Since the time of the drop formation is much longer than the fall of the former drop, the droplet charge does not affect the drop formation. However, when the voltage increases the meniscus elongates and the drop becomes smaller with an increased emission frequency. This is attributed to two different reasons: one is the reduction in the surface tension of the liquid because of electric charges on the surface create an electrostatic pressure opposite to the capillary pressure; the other is the attraction of liquid towards plate due to the action of the electric field on the charges located at the end of the hanging droplet (Cloupeau & Prunetfoch 1990). For further increase of the applied voltage, the drop can be connected with the capillary by a thread, which subsequently breaks off as the drop falls down and a sibling can be generated from the thread.

2.4.1.2 Microdripping mode

The microdripping mode can be obtained when the electric force close to the capillary outlet is sufficiently high to keep a stable hemispherical or elliposoidal meniscus. **Figure 2.20** shows the schematic diagram of microdripping mode and its real image. It is different from the conventional dripping mode: firstly, the droplet, which is much smaller than the capillary diameter, is formed at the tip of the meniscus where the electric field is much stronger; secondly, the droplet is detached from the meniscus and does not undergo further disruption; thirdly, the meniscus has a highly variable

height and shape and does not contract after the droplet detachment; and moreover, the characteristic time that the liquid is provided to the capillary outlet is much longer than the time of the drop formation because of the higher electrical force, and no great fragment of liquid can be formed.

In the microdripping mode, the size of the droplets obtained can be ranged from a few micrometers up to approximately a hundred micrometers in diameter (Jaworek & Krupa 1999a). Additionally, it is of much interest that the emission in microdripping mode sometimes takes place at very regular time intervals, giving droplets of uniform size (Cloupeau & Prunetfoch 1990). It is also noticeable that the space charge formed by formerly generated droplets is too weak to affect the generation process, because the droplets are quickly removed by the electric field. However, when the flow rate and applied voltage increase, the space charge builds up by the charged droplets and gas ions, which may disturb the emission of regular drops. This means the microdripping and conventional dripping modes can be generated only in limited ranges of applied voltage and flow rate.

2.4.1.3 Spindle mode

The spindle mode is generated at high flow rate with sufficiently high electric field where the liquid is elongated in the direction of the electric field, taking the shape of a thick jet which detaches as a vast spindle-like fragment. **Figure 2.21** is the schematic diagram showing the spindle mode and its real image. This mode is different from (micro)dripping mode: 1) it is generated at higher voltage and such high voltage

detaches a fragment of liquid before a continuous jet is formed; 2) there is no regular droplet is ejected from the meniscus but only elongated fragments of liquid; 3) after detachment, the spindle can disrupt into several smaller droplets of different size due to the electric force; 4) the meniscus contacts to its initial shape after detachment and a new spindle-like fragment starts to be formed; and 5) the characteristic time that liquid is provided to the capillary is nearly equal to or shorter than the jet formation time.

The major droplets generated in this mode are commonly heterogeneous in size, with the diameters varying in the range from 300 to 1000μm, and siblings are smaller than 100μm. It has been reported that the main drops become greater and sibling droplets become smaller with increasing voltage (Jaworek & Krupa 1999a).

2.4.1.4 Multi-spindle mode

When the voltage in the spindle mode is increased, the spindle like jet detached from the capillary will become multiple, and this mode with multiple spindle-like jets is defined as multi-spindle mode. The schematic diagram of multiple spindle mode and its real image are shown in **Figure 2.22**. When illuminated continuously, the multi-spindle mode resembles to some extent the multijet mode (described in later section). However, they considerably differ from each other because the jet and drop formation is different (Jaworek & Krupa 1999b). In the multi-spindle mode, the liquid is not sprayed in the form of regular continuous thin jets, but only in the form of the spindle-like pieces of liquid which is comparable to the spindle mode. The jets are

ejected periodically from the fixed points at the circumference of the capillary. The meniscus at the outlet of the capillary is flat, and only one small piece of liquid, usually in the form of a short spindle-like jet, is ejected at an instant from a distinct point at the circumference of the capillary. After detachment the piece of liquid can disintegrate into a few smaller droplets, therefore several narrow streams around the capillary can be then observed. These streams of droplets, ejected periodically, seem to be distributed uniformly around the axis of the capillary.

As shown in **Figure 2.22**, only two such spindle-like jets are emitted symmetrically to the capillary axis, generally, and are at one plane with this axis. The streams are generated in both directions in a pulsating manner forming intermittent traces when illuminated continuously. Such droplet generation manner is caused by the space charge produced by the gaseous ions and the charged droplets. The space charge deforms the axisymmetrical structure of the meniscus of the issuing liquid repulsing it off the capillary axis (Jaworek & Krupa 1999b). When the applied voltage increases, the spray angle slightly increases due to repulsive electric forces. The number of emission points may also increase with the voltage increasing.

It has been reported that the droplets generated in multi-spindle mode are greater than in the multijet mode, but smaller than in the spindle mode, which are usually a few tens of μm in diameter (Jaworek & Krupa 1999a).

2.4.1.5 Unstable cone-jet mode

A transitional mode which lies between the spindle/multi-spindle mode and the stable cone jet mode (described in later section) can be observed under the condition of certain flow rate and applied voltage. It is an intermittent mode namely unstable (or intermittent) cone-jet mode (Jayasinghe & Edirisinghe 2004). In this mode, the liquid escapes the capillary in the form of a skewed cone and smoothly changes into a thin jet at the tip of it, which is similar to the configuration of cone-jet mode. However both the cone and the jet rotate regularly round the capillary axis, taking the shape of a fragment of a spiral. Compared with the spindle mode, the unstable cone-jet mode has a thinner jet of diameter smaller than 100μm of which the end part is winding round the mother spiral. The jet disintegrates into droplets due to repulsive electrostatic forces and possibly the centrifugal forces too.

The aerosol is sprayed into a cone of an elongated ellipsoidal base and an apex angle greater than 90°. With increasing voltage this apex angle becomes smaller and the diameter of the sprayed patterns on the collecting substrate is reduced. Moreover, the cone becomes shorter and the jet becomes longer and rotates faster with the voltage increasing, which is possibly due to the increased repulsive electrostatic force generated by the space charge that is induced by the sprayed droplets. It has been reported that the droplet can be generated in the unstable cone-jet mode with the size ranging from 25 to 60 μm (Jaworek & Krupa 1998).

2.4.1.6 Stable cone-jet mode

With the increased applied voltage, a stable cone-jet mode can be generated from the

intermittent cone-jet mode, which is shown in **Figure 2.23**. In this mode, the liquid forms a regular cone at the outlet of the capillary, which is known as Taylor cone (Taylor 1964). A stable thin jet of diameter ranging from a few micrometers up to a few tens of micrometers is formed at the tip of the cone, and flows along the capillary axis or deflects from it only on a small angle usually smaller than 10°. Unlike unstable cone-jet mode, the cone is axisymmetrical and both the cone and the jet at its initial fragment remain (Jaworek & Krupa 1999b). The jet undergoes instabilities at the bottom end, two types of which are known: varicose and kink. In the varicose instability case, the axis of the jet is not deflected and the jet disintegrates into equal droplets, which flow along the capillary axis. In the kink instability case, the end of the jet moves irregularly and breaks up into series of droplets due to electrical and inertial forces. An aerosol is spread out off the axis and forms a stable spray cone along the capillary axis with the apex angle of about 50° to 60°.

The fundamental advantages of the stable cone-jet mode are firstly, the cone and the jet remain stable and a steadily uniform spatial dispersion of the aerosol can be generated, which is suitable for the deposition and coating process; secondly, droplets break up at the jet end are homogeneous and the size from a few μm in diameter to several tens of μm can be obtained. The mechanism of the cone-jet mode will be discussed in detail in the later section.

2.4.1.7 Multijet mode

The multijet mode commonly develops from the cone-jet mode by increasing the

applied voltage. **Figure 2.24** shows the schematic diagram and the real image captured by high speed camera for the multijet mode. When the applied voltage increases in the cone-jet mode, the cone depth and the jet diameter become smaller until a critical level at which the Taylor cone becomes skewed, leading to a single jet at the rim. This situation is unstable and two or more jets can be formed symmetrically distributed on the rim of the capillary. The meniscus becomes perfectly flat with only short cones at the emission points. The jets disintegrate into small droplets due to kink instabilities, forming a fine mist around the capillary axis. Near the capillary, the aerosol does not fill the whole volume but is only dispersed in a few narrow streams which seem to be located uniformly around the axis.

The reason for the formation of multijet mode from stable cone-jet mode is the limited velocity of the jet formation as compared to the liquid velocity at the outlet of the capillary, resulting from the flow rate (Jaworek & Krupa 1999a). The number of the emission points increases with the increase in voltage and flow rate, which is also determined by the physical properties of the sprayed liquid. It has been reported that the droplets obtained in the multijet mode are smaller than a few micrometers in diameter (Jaworek & Krupa 1999b).

2.4.1.8 Corona discharge

When the electric field between the capillary and ground electrode becomes greater than the electrical breakdown threshold of the interfacial surface energy (surface tension) of liquid-surrounding air interface, corona discharge occurs and in this

situation none of the regular mode can be observed (Cloupeau & Prunetfoch 1989).

2.4.2 Mechanism of stable cone-jet mode

Amongst the spraying modes during electrohydrodynamic atomization, stable cone-jet mode is mostly utilized for this research due to it capability to generate mono-dispersed droplets over a wide size range (sub-micron to a hundred micron), which is suitable for the deposition and printing processing. Generally, in cone-jet mode an electrical field induces a surface charge in a liquid, which is accelerated by the electric field. The electric stresses in the droplet surface and this acceleration process transform the liquid in a conical shape. At the apex of the cone, a jet with a high charge density occurs which can break up into a number of primary main droplets with a narrow size distribution (and some secondary droplets). Therefore, this process can be classified into two stages: (1) liquid acceleration and cone forming and (2) the break-up of jet into droplets.

The liquid acceleration and the shape of the liquid cone process are result from the balance of several forces involved; these are liquid pressure, liquid surface tension, gravity and electric stresses in the liquid surface. Hartman has presented a Cone-Shape model, in which forces that have to be taken into account are illustrated. **Figure 2.25** shows these forces in the liquid cone schematically. Using this model it is capable to calculate the shape of the cone and jet, the surface charge on the jet, the electric fields in and outside the liquid cone, and the current through the liquid cone (Hartman *et al.* 1999b).

The second stage in the cone-jet mode is the break-up of the jet into droplets. The jet emerges at the apex of the cone is of higher charge density. Due to its charge and the acceleration of the liquid, the jet is axisymmetric unstable and subsequently breaks up into droplets. These are called varicose instabilities. At higher applied voltage and flow rate, the current through the liquid cone increases, which results in the surface charge on the jet increased. When this value is above certain value, the jet break-up will also be influenced by lateral instabilities of the jet, which are also called kink instabilities. When the influence of these kink instabilities increases, the produced size distribution of the main droplets will be wider (Hartman *et al.* 1999a).

Electrohydrodynamic atomization in cone-jet mode is the most important process in this project, in that the stable spatial dispersion of the monodispersed droplets is suitable for the deposition process. In the following chapters, the deposition and printing process based on this theory is developed and utilized for forming PZT material in different structures.

2.4.3 Parameters influencing electrohydrodynamic atomization

The relevant parameters in electrohydrodynamic atomization are vital in controlling such process. Many published works (Chen, Pui, & Kaufman 1995; Cloupeau & Prunetfoch 1989; Ganan-Calvo, Davila, & Barrero 1997; Hartman *et al.* 2000; Hohman *et al.* 2001; Kim & Turnbull 1976; Smith 1986) showed that physical properties of liquid (e.g. dc electrical conductivity, viscosity, surface tension and

density) and major processing parameters (i.e. applied voltage and flow rate), play an important role in achieving cone-jet mode electrospray.

The electrical conductivity of the liquid determines whether the liquid can be sprayed in the cone-jet mode: if the conductivity of the liquid is too low ($<10^{-10}$ S m^{-1}), the cone-jet mode is not attainable during spraying. The surface tension of the liquid is an important parameter since the applied electrical field must overcome the surface tension of the sprayed liquid in order to obtain cone-jet mode. Viscosity of the precursor influences the jet break-up process and consequently has a significant effect on the size of droplets produced. However, in most cases, the influence of viscosity on the droplet size is not considered because the precursors that used are of low viscosities (<100 mPa s) (Jayasinghe & Edirisinghe 2004). Increase in liquid density decreases the minimum flow rate required for cone-jet mode electrostatic atomization and it has also been reported that the density has an influence on droplet generation as it affects jet break-up (Hartman *et al.* 2000).

The processing parameters are also very important. If the flow rate is low (10^{-15} m^3 s^{-1}) the spraying process is unstable because the liquid cone relaxes to a droplet shape periodically. Above a minimum flow rate, droplet generation stabilizes and the size distribution of the droplets narrows. However, if the flow rate is increased above a critical value, the droplet size distribution becomes more polydisperse and the process becomes more unstable (Jayasinghe & Edirisinghe 2004). The varying applied voltage can change the spraying mode from dripping to multijet mode. And over high applied

voltage may induce corona discharge in which none of the regular spray modes can be observed.

2.5 Printing techniques for ceramic structures

Not only films, but also finer structures in micro and even nano scales of functional ceramics (e.g. PZT) are crucial for vast applications. Engineers are now targeting novel techniques to fabricate PZT structures in 10's to 100's micrometers, especially for MEMS (Dorey & Whatmore 2004). In this section, a series of printing technique for processing small scale ceramic structures will be introduced. Additionally, a novel printing technique, electrohydrodynamic atomization printing, which is relevant to this project, will also be introduced.

2.5.1 Historical develop of printing techniques

New methods with the capacity of fabricating materials at micro and nanoscale will drive scientific and technological advances in the areas of biology, chemistry, materials science, and physics. The broad diversity of potentially relevant materials, length scales, and architectures underscores the need for flexible patterning approaches. Typical examples are the fabrication of complex three-dimensional structures comprised of polymers (Sirringhaus *et al.* 2000), bioceramics (Roda *et al.* 2000) and functional ceramics (Cuk *et al.* 2000). These structures may find potential application as tissue engineering scaffolds (Griffith & Naughton 2002), drug-delivery devices (Li *et al.* 2003), sensors (Lee & Braun 2003), and MEMS (Jackman *et al.*

1998). Amongst those, MEMS are expected to be of great technological interest in the near future, which have applications in a diverse range of disciplines including medicine, communication, transport and leisure (Setter 2001).

At the heart of many MEMS is a functional ceramic component, such as PZT. However, the production of these MEMS ceramic components in small scale and complex structure poses a number of technological issues. Ceramic materials are brittle, hard and chemically inert which makes machining or etching them rather difficult, therefore the direct machining of ceramic component on desired structures is obviously impractical for complex fine scale structures in MEMS. Traditionally, the ceramic components were fabricated separately from the substrate and later boned to the substrate. The material can be injected or infiltrated into a pre-designed mold or mask, followed by a heat treatment to condense it into the designed structure, after which the sacrificial mould will be removed. This approach is limited in that fine scale components request complex geometric moulds which are also very complicated to fabricate. There is also a high degree of wastage associated with injection and infiltration, and the mould is normally not repeatable to use because it is commonly destroyed after being removed (Le Dren *et al.* 2000).

Recently, several strategies have emerged for precisely assembling complex three dimensional structures, amount which the direct writing technique offers the materials flexibility, low cost, and ability to construct arbitrary three dimensional structures required for advances across multidisciplinary boundaries (Lewis & Gratson 2004).

Direct writing technique is a solid freeform fabrication method that employs a computer-controlled translation stage, which moves a pattern-generating device, e.g. ink deposition nozzle or laser writing optics, to create materials with controlled architecture and composition. The technique can produce ceramic structures point-by-point, line-by-line, or plane-by-plane without the use of expensive tooling for prototypes (Tay *et al.* 2003). Several direct writing techniques are capable of patterning materials in three dimensions. These include dip-pen nanolithography, ink-jet printing, three dimensional printing, laser ablation and selective laser sintering. Recently, the electrohydrodynamic atomization derived printing technique, has been developed rapidly and generated great attentions of a number of researchers by means of its novel procedure and delicate patterns produced. In this section, all the methods mentioned above will be reviewed in details.

2.5.2 Dip-pen nanolithography

Lithographic methods are paramount for microfabrication, nanotechnology, and molecular electronics. These printing techniques often rely on patterning of a resistive film, followed by a chemical etch of the substrate (Piner *et al.* 1999). Lithography includes positive printing mode, which allows a material directly transport to the substrate and negative printing mode, which relies on scanning probe instruments, electron beams, or molecular beams to pattern substrates, using self-assembled monolayers (SAMs) and other organic materials as resist layers (Lercel *et al.* 1996; Perkins *et al.* 1996), that is, to remove material for subsequent processing or adsorption steps. However, the positive printing mode is more favored because it

allows small amounts of a molecular substance to a substrate in a nanolithographic fashion and does not rely on a resist, a stamp, complicated processing methods, or sophisticated noncommercial instrumentation (Piner *et al.* 1999).

In positive printing mode, there is a modified dip-pen technology called dip-pen nanolithography (DPN), which was firstly reported by Piner *et al.* DPN uses an atomic force microscope (AFM) tip as a "nib", a solid-state substrate (for example Au) as "paper", and molecules with a chemical affinity for the solid-state substrate as "ink". Capillary transport of molecules from the AFM tip to the solid substrate is used in DPN to directly "write" patterns consisting of a relatively small collection of molecules in submicrometer dimensions. **Figure 2.26** shows the schematic diagram of dip-pen nanolithography. When the AFM tip is close to the substrate, a narrow gap capillary will form between the tip and the substrate when it is conducted in air. This gap capillary condenses water from the ambient, which is a dynamic process and the water, which is depending on relative humidity and substrate wetting properties, can be transported from the substrate to the tip or vice versa (Piner & Mirkin 1997). In the latter case, metastable nanometer-length–scale patterns could be formed from very thin layers of water deposited from the AFM tip. As a result, when the proposed molecules are coated on the AFM tip, they can be delivered to the substrate through the water meniscus and anchor themselves to the substrate through chemisorption, resulting in a new type of nanolithography.

The resolution of DPN depends on several parameters. Firstly, the grain size of the

substrate affects DPN resolution because conventional writings are considerably affected by the texture of paper, so as DPN. Secondly, chemisorption and self assembly can be used to limit the diffusion of the molecules after deposition. Thirdly, the relative humidity plays an important role during DPN: on one hand, the structure of printed patterns are affected by the size of water meniscus that bridges the tip and substrate, which depends on relative humidity (Piner & Mirkin 1997); on the other hand, the relative humidity also affects the rate of molecular transport from AFM tip to the substrate, which can determine the resolution of the printing process. Fourthly, the humidity, temperature and reactivity of the ink will determine the spreading of the ink after depositing on the substrate, which will also affect the printing resolution. And finally, the tip-substrate contact time, radius of curvature of the probe and also the scan speed may influence DPN resolution. An example demonstrating the parameters affecting the printed structure is shown in **Table 2.2** (Piner *et al.* 1999).

Table 2.2 *Details of the structures processed by dip-pen lithography*

Printed line's width (nm)	Scanning time (s)	Relative humidity
30	300	34%
100	90	42%

DPN has been developed to pattern a variety of "ink–substrate" combinations. This technique is compatible with many materials (inks), from small organic molecules (Jung *et al.* 2003; Liu *et al.* 2002) to organic (Lim & Mirkin 2002; Maynor *et al.* 2002) and biological (Demers *et al.* 2002) polymers, and from colloidal particles (Ben Ali *et al.* 2002; Garno *et al.* 2003) to metal ions (Li, Maynor, & Liu 2001) and sols (Su *et al.*

2002). There are also a variety of substrates that DPN can pattern on which ranges from metals to insulators and even on top of functional monolayers that adsorbed on many surfaces. It has been also reported that DPN can be used to feed monomers to a living-polymerization reaction in a site-specific fashion thus opening the possibility of creating and screening combinatorial arrays of polymer features (Liu, Guo, & Mirkin 2003). Giner *et al.* (2004) have reviewed the various chemicals used and the systems in which they have been applied.

DPN is not only a 'single-pen' process, but also multiple. To increase the throughput and area accessible to scanning-probe techniques, researchers have been working on the development of parallel-probe cantilever arrays. Liu and co-workers have been designing MEMS-based parallel-probe DPN techniques (Zhang *et al.* 2002). The initial strategy of parallel-pen DPN is a passive probe array. In this case, the pens are not actuated independently but are simultaneously brought into contact with the surface and scanned together, which allows the duplication of a single pattern a number of times equal to the number of probes in the array (Wang *et al.* 2003). Consequently, independent control of each probe tip can be accomplished using piezoelectric, capacitive or thermoelectric actuation, which can lead to the bending of the probe. Using this approach, a number of complex patterns can be produced at high speed because the contact between the tip and the writing surface is independently controlled (Zou *et al.* 2003). Recently, researchers are working on integrating MEMS to DPN to realize the automation of tip coating and ink delivery. It is proposed that custom microfluidic systems will ultimately be used to control the inking of

individual cantilevers in a parallel probe array. As a result, the efficiency of dip-pen nanolithography will be considerably increased.

In summary, DPN is a unique scanning probe based lithographic tool for generating high-resolution patterns of chemical functionality on a range of surfaces. The combination of resolution, registration, and direct-write capability of DPN makes it a promising tool for patterning soft organic and biological nanostructures. However, the disadvantage of DPN is high cost and low operating speed. The devices and the AFM tip used in DPN are quit expensive. For example, NSCRIPTOR system for DPN costs more than $ 200k (Haaheim *et al.* 2005).

2.5.3 Three-dimensional printing

Three-dimensional printing (3DP) was developed at Massachusetts Institute of Technology, USA in early 1990s as a method to form powdered metals and ceramics into three dimensional structures (Sachs *et al.* 1992). The process involves computer controlled CAD model which moves a printing head to drop low viscosity binder onto a powder bed to locally fuse materials together in a desired pattern. After a two-dimensional layer was defined, an additional powder layer is spread across the bed surface and then patterned in order to realize three dimensional structures.

Figure 2.27 is the schematic presentation of the 3DP process. The process is operated in a container with a piston at the bottom. Initially, the desired powder is placed in the container and leveled by a roller to provide a thin layer. As an alternative to the roller,

mechanical, acoustic or ultrasonic vibration can be used to consolidate the powder bed (Tay *et al.* 2003). Consequently, a printing head moves across the powder in raster motion and prints a layer of binder selectively onto the loose power bed as defined by the CAD model. When printing on a metal powder bed, the spraying of the binder may cut a trench through the bed and redistributed the powder. As a result, 0.05% salt is always added into the metal powder and the powder bed is moistened to increase its cohesive strength. As the binder diffuses through the powder by capillary action, neighboring particles are pulled together by surface tension effects. When the printed layer is accomplished, the piston will lower the whole part in the container and the next power layer will be leveled and printed by the binders. This process will be repeated by lowering the piston incrementally until the desired thickness is obtained (**Figure 2.27 a**). The motion of the printing head will be changed by the CAD model if the pattern in x-y layer changed (**Figure 2.27 b**) and then the part will keep being built in z direction until the whole structure is completed (**Figure 2.27 c**). Consequently, the whole parts is oven cured and the non-formed excess dry powder will be removed by immersion in a liquid, such as water (Moon *et al.* 2000), without damage to the forming areas (**Figure 2.27 d**). Finally, the part will be sintered to achieve the desired density and strength.

The fluid dynamics involved in drop formation, wetting, and spreading play an important, and also limiting, role in defining the surface roughness and minimum size of the features (Lewis & Gratson 2004). Because of the initial droplet size and the propensity of droplets of the binders to spread both laterally and vertically within the

powder bed, it is reported that the minimum feature size is around 100μm (Moon *et al.* 2002).

The advantage of 3DP is that this process does not require high energy or involve any toxic materials and is relatively cheap and fast (Carrin 1997). The process can be adapted to suit a variety of powders and to generate the desired pore size and shape (Tay *et al.* 2003). Beside that, by using multiple printheads, additives may be deposited in a prescribed fashion to create gradients in composition. The fabrication of compositionally graded zirconia toughened alumina (ZTA) ceramic multilayers were achieved successfully by Yoo and his co-workers (Yoo *et al.* 1998).

Although 3DP was successfully applied to metal and ceramic powders to fabricate components, generation of structural parts is more challenging. Since fine powders are always used to improve sintering of the parts during the process, its high surface area decreased the powder flowability and therefore it is difficult to obtain layers of defect free powder. However, this can be improved by using intermediate isopressing or by modifying the binder or powders to obtain dense ceramic parts.

2.5.4 Ink-jet printing

Ink-jet printing is a well known technique which was firstly developed in 1960s (Heinzl & Hertz 1985). Direct ceramic ink-jet printing has recently emerged as an attractive technique for depositing minute quantities of material on surfaces with good spatial control (Calvert 2001). In this technique, small volumes of liquid ink from a

reservoir are ejected through a nozzle and dispensed onto the substrate. Ink-jet printing can be divided into two approaches: 1) continuous-ink-printer, in which the liquid is pumped through the nozzle to form a continuous jet of liquid; 2) drop-on-demand jet printer, in which small droplets are generated by applying an acoustic or thermal pulse. The liquid ink suspension are prepared by colloidal processing so that particles are well dispersed without agglomeration which is identified as the source of critical defects in ceramics (Lange 1984).

Figure 2.28 shows the schematic diagram of continuous-ink-jet printer designed by Song *et al.* (1999). Ceramic ink was pressurized using oxygen-free nitrogen so that it flowed to the print-head through an in-line filter. The filter contained a series of metal meshes with aperture sizes of 48, 34 and 26 mm and a 10 mm aperture size polymeric mesh. The liquid ink was then delivered from a pressurized reservoir through a 20-300 μm diameter nozzle. Just before the nozzle, a piezoelectric actuator superimposes a modulated pressure and, on leaving the nozzle, the stream breaks up at a matching frequency into a continuous series of equidistant, equal sized droplets. The droplets were charged simultaneously by the charging electrode having a voltage between 50 and 285 V. A detector in the charging electrode was used to determine whether effective charging of droplets was achieved. Charged droplets were deflected by high-voltage (18 kV) plates. The uncharged droplets were not deflected but collected through the return tube placed directly below the main jet. Not only this binary detection system, the continuous ink-jet printer can also be a multiple deflection system in which charged droplets are deflected by different amounts and

uncharged droplets are recirculated. This approach allows a single nozzle to print a small image (Le 1998). At the bottom, a substrate (acetate sheet) was attached to the sliding table which was fitted with a shaft encoder to provide registration for automatic multilayer printing. A portable hot-air blower was used to assist drying. Continuous printers have superior printing speed and can be used at a printhead-to-paper distance of 20-50 mm but tend to have a higher capital cost (Tay *et al.* 2003).

The drop-on-demand (DoD), or impulse ink-jet demand ink-jet printer system, is the most common reprographic jet printing method, developed to circumvent the limitations of continuous jet printing technology, such as start-up and shut-down requirements, complex charging and the need for ink recirculation. There are three main types: piezoelectric, thermal and electromagnetic (Tay *et al.* 2003). In the piezoelectric DoD ink-jet method, which is illustrated schematically in **Figure 2.29**, part of the chamber consists of a piezoelectric element, usually a polycrystalline ceramic **(a)**, which propagates an acoustic pressure wave towards the nozzle when excited by an electrical signal **(b)**. By overcoming the inertial and viscous pressure loss and the pressure associated with the surface tension in the ink meniscus, an ink droplet is formed at the nozzle and expelled **(c)**. The piezoelectrics are then reversed to let the ink refilled and repeat to the next cycle **(d)**. Droplets are ejected only when needed for printing and no ink recirculation pumps or gas pressure sources for the ink are needed; it has been report that this technique requires less hardware than a continuous ink-jet printer (Le 1998).

The thermal ink-jet printer uses a disposable ink-jet printhead, which contains ink reservoirs, electrical heating elements and the nozzle plate. **Figure 2.30** is the schematic diagram of thermal ink-jet printer. A droplet of ink is propelled from the nozzle when electrical heating causes a bubble of vapour to be formed by incipient boiling of the ink. The bubble collapses and capillary forces draw the ink from the reservoir for the process to begin again. The dimensional stability, accuracy and uniformity of the orifice as well as the firing signal profile influence jet performance (droplet frequency, volume and velocity) significantly. The mass and velocity of the droplet are also related to the geometrical parameters of the printhead and the physical properties of the ink (Le 1998). Compared with the continuous ink-jet method, drop-on-demand devices are less useful for printing on curved surfaces or where the ink droplet must traverse a long distance (Tay *et al.* 2003).

Inks play an important role during the ink-jet printing process. Compared with 3DP, the ceramic powder can be well dispersed in a liquid ink rather than placed as a powder bed, thus the agglomeration can be eliminated. Water and other solvent are always used for the ink preparation which depends on the application. Ideally, the liquid ink must be converted to a solid structure as quickly as possible by absorption, oxidation, evaporation, chemical reaction or radiation (such as ultraviolet, infrared or microwave) (Le 1998). The main properties defining ink behavior are viscosity, surface tension and electrical conductivity (Tay *et al.* 2003). Additionally, as the printer nozzles are small, it is important that particles agglomerates or entrained debris,

which may clog the nozzle, are removed upstream by an efficient filtration system. Protection of the nozzle is necessary so that the ink will not dry in the nozzle when the printer is not in operation. Tay *et al.* (2003) has summarized some of the key design parameters for the printer and ink, which is shown in **Table 2.3**.

Table 2.3 *Typical design parameters for continuous jet printer and drop-on demand jet printer (Tay et al. 2003)*

Parameter	Typical range
Continuous jet printer	
Nozzle diameter, μm	10–220
Operating frequency, kHz	17–1000
Charging voltage, V	100–300
Deflection voltage, V	1000–18 000
Ink pressure, kPa	0·5–150
Jet velocity, m s^{-1}	5–50
Ink viscosity, mPa s	1–20
Ink surface tension, mN m^{-1}	25–70
Ink conductivity, S m^{-1}	>0·2
Particle size, μm	<1
Drop-on-demand jet printer	
Nozzle diameter, μm	20–100
Droplet volume, pL	50–500
Operating frequency, kHz	3–25
Droplet velocity, m s^{-1}	3–15
Resolution, dots m^{-1}	7000–75 000

Ink-jet printing has already become a method of choice for generating polymer features as well as other materials such as ceramic powders, metal precursors and colloids on a number of different substrate (both rigid and flexible) (Geissler & Xia 2004). Ink-jet printing has vast of advantageous attributes: first, it is a contact-free technique; second, it is capable of providing high throughput, in particular when a large number of nozzles are used in parallel; third, it allows the simultaneous printing of different materials delivered from multiple nozzles and also, it provides good alignment capabilities and a precise control over the volume of deposited materials (Geissler & Xia 2004).

However, ink-jet printing also has limits. Firstly, the droplets obtained from ink-jet printing are directly related to the nozzle size as the droplet size is approximately twice the size of the nozzle diameter. Secondly, the substrate influence the spreading of the droplets after deposition (Noguera *et al.* 2005), which may limit the range of the substrate when processing complex features. Furthermore, the powder volume could be limited because nozzle blockage will be increased when using higher powder volume suspensions.

2.5.5 Laser ablation

As mentioned above, three-dimensional printing and ink-jet printing are both the direct writing techniques which involved a printhead to eject materials (either built ceramic powders or sacrificed polymer binders). Alternatively, this printhead can be replaced by a laser head and this process is called laser-writing techniques. Laser-writing technique is also a kind of direct writing techniques which creates patterned materials through ablation, selective laser sintering or reactive chemical process. The lasers used in the process includes ultraviolet, nanosecond pulsed, excimer, Nd−YAG lasers and some shorter pulse lasers (Lewis & Gratson 2004). Most of these approaches could generate complex structures with self-supporting features at resolutions comparable to those achieved by the processes discussed previously.

Laser ablation was firstly reported in early 1980s when a pulsed ultraviolet laser falls on the surface of an organic polymer to pattern the structures (Srinivasan & Braren

1989). It involves either directly removing or depositing material. In the first aspect, the material to be patterned is as the substrate and exposed to laser energy which is controlled by a CAD mode. The laser ablates off material in specified area until the desired features are written. It has been reported that multilayer microchangels have been fabricated with minimum diameter ~125μm in silicon using this technique (Lim *et al.* 2003). In the second aspect, the laser ablation is used to create coatings by ablating the coating material from a source and letting it deposit on the surface to be coated. This approach is developed by Chrisey and coworkers and named as matrix-assisted pulsed laser evaporation (MAPLE) (Chrisey *et al.* 2000). **Figure 2.31** shows the schematic diagram of MAPLE. In this process, a coated ribbon is used to be ablated by a laser and a substrate is placed in close proximity to the ribbon. The coating contains the material of interest embedded within a thermoplastic polymer matrix. As a pulsed laser scans across the coating ribbon interface, exposed areas absorb laser energy and undergo pyrolysis. The react area of the embedded material will then be propelled toward the substrate so that the patterns can be formed. This technique has been used to deposit a wide variety of materials, including metallic, ceramic, polymeric and even biological materials (Lewis & Gratson 2004), especially to manufacture several types of high temperature superconductor (Braccini *et al.* 2001).

The depth and width of the laser written area is determined by the optical property of the patterned material and the wavelength and the power of the used laser. It has been reported that the minimum printed feature size obtained by laser ablation is around

400nm in width and 10nm in height (Lewis & Gratson 2004).

The advantages of laser ablation technique include 1) no solvents are used, so it is environmentally friendly and operators are not exposed to chemicals, 2) it is relatively easy to automate by means of using the designed CAD mode, 3) the heating on the target is minimal, 4) the process is gentler than abrasive techniques, which is ideal for some delicate materials such as tooth enamel and carbon fibers.

However, compared with the ink-jet printing, the laser ablation can only produce two-dimensional layers or simple three-dimensional layers. Especially for MAPLE, the three-dimensional patterning becomes more difficult due to the requirement of an underlying substrate during the process. And also, the capital investment costs are obviously much higher because of the complex procedure to produce and control the lasers.

2.5.6 Selective laser sintering

Alike laser ablation, selective laser sintering is also a laser involved processing technique to print various material structures. However, unlike the ablation-off process in the former technique, selective laser sintering shares a common feature with 3DP in that a layer of powders is spread on a platform and the selected regions are bonded together. But while 3DP printing relies on binder deposition, selective laser sintering induces the desired powder by a laser scanning across the powders. Although the process is described as sintering, in many polymer and metal selective

sintering processes complete fusion occurs and the expression 'melting' or 'fusing' is more appropriate. This technique is invented by Deckard at the university of Texas at Austin in 1986 and was commercialized in 1990s (Bourell *et al.* 1992).

Figure 2.32 is the schematic presentation of selective laser sintering process. As shown in the graph, a thin layer of powder is spread out and leveled over the top surface of the building platform, a laser then selectively scans this layer to fuse the forming areas as designed by a CAD model and to leave the non-forming areas as supports for subsequent building. The working chamber is purged with inert gas and is often heated to raise the temperature of the uppermost layers of powder. This not only can reduce the additional laser energy required to heat the powder to its fusion temperature during fabrication but also may help to reduce residual stress development and to mitigate stresses that have been established. After one layer has been deposited and fused, an elevator platform lowers the part and the next layer of powder is deposited and fused, similar to the process in three-dimensional printing. When the shape is completely built, a heat treatment is conducted so that the fused part is formed with the desired structure and the un-fused part (loose powder) will be removed from the body. The removed loose powder may sometimes be recycled.

Parts processed by selective laser sintering are often porous and post-processing is necessary when strength is required in ceramic parts. Each material requires different heating and laser parameters, which can be predict from the devised process map (Beuth & Klingbeil 2001). In order to increase the final density of the ceramic or

metallic parts, both conventional sintering and isostatic pressing can be used. Additionally, the parts density can be improved by increasing the powder bed density. Numerous methods have been employed which include the use of spherical particles, bimodal size distributions of powder and agglomeration of fine powder and so on. Increasing the effectiveness of the powder distribution is also useful for increasing the powder bed density of which the methods include the use of electrostatic field, magnetic field and mechanical agitation of the powder and powder bed (Tay *et al.* 2003). The resolution of the structures processed by selective sintering is determined by the powder size, laser melting process and heat treatment, and it has been reported that the minimum feature size is about 100μm (Lewis & Gratson 2004).

Compared with 3DP method, selective laser sintering can process powders directly without the use of a sacrificial binder. However, low temperature fusion of a binder is always used to assemble the powder followed by pyrolysis and sintering steps, namely indirect selective laser sintering. The reason for the indirect approach is that laser sintering of high melting point ceramics requires a high level of laser energy and can create large thermal gradients, thermal shock and hence difficulty in forming a contiguous shape (Subramanian & Marcus 1995). This can be partially overcome by incorporating a second phase binder of lower melting point into the ceramic powder. The second phase binder can be an organic binder coated on the powder, an inorganic binder or a low melting point metallic binder (Tay *et al.* 2003).

The major advantage of selective laser sintering is that no support structure is needed

as the non-fused powder remains in place to act as a self support. Also, changing of materials is simpler than that in many liquid based techniques, considering the dry solid nature of the starting material (Tay *et al.* 2003).

The disadvantages of this process are firstly the laser print head are obviously more expensive than the ink nozzle print head in 3DP which may increase the capital of the process; secondly, the build time is rather long although many researchers have been investigating to minimize it (Pham & Wang 2000).

2.5.7 Electrohydrodynamic atomization printing

In the previous sections, the printing techniques using both ink-nozzle printhead and laser printhead were introduced. However, in terms of process capital, process efficiency, devices set-up and feature resolutions, all of these techniques have their drawbacks. Taking laser printing for example, the high level of laser used in the process demands high energy, which will increase the cost of the process so that a large amount of capital will be invested when it is applied for commercialization. When using ink-jet printing process, the relic size is closely related to the internal diameter of the nozzle. The droplets generated are approximately twice the nozzle diameter. Therefore to get small droplets, a fine nozzle is required making the passage of concentrated particulate suspensions extremely different and the deposition of droplet relics <100 μm in size virtually impossible. In 2002, Edirisinghe and coworkers developed another direct writing technique which is electrohydrodynamic atomization printing in both single (Jayasinghe, Edirisinghe, & De Wilde 2002) and

multiple (Jayasinghe & Edirisinghe 2003) needle configurations. This printing technique is an electrohydrodynamic atomization derived process which functions in conjunction with electrohydrodynamic forces to atomize the precursor into small droplets that deposit on the substrate to create high-resolution architectures. Jayasinghe *et al.* (2004) has used this technique for printing two-dimensional architectures using nanosuspensions with a significant reduction in scatter and thus much improved precision patterning capability.

Figure 2.33 shows the electrohydrodynamic atomization printing system (Jayasinghe, Edirisinghe, & De Wilde 2002). It composes of two parts: electrohydrodynamic atomization set-up and a two-dimensional printing device which consists of an x-y axis motion controller connected to a computer with a motion controlling software. Due to the superiority in generating monodispersed droplets of a few micrometers in size, electrohydrodynamic atomization operates in the cone-jet mode during the printing process (Chen, Pui, & Kaufman 1995) so that a structure with homogeneous feature size can be produced. The structure is collected on a substrate which is placed on the printing device with the distance between the nozzle and the substrate of 1mm or less (Wang, Jayasinghe, & Edirisinghe 2005a), because the area of the deposit is reversely proportional to the distance between the nozzle and the substrate (Chen *et al.* 1999a). A point-like ground electrode is also used to focus the sprayed patterns (Jayasinghe & Edirisinghe 2004), which is placed approximately 1mm below the substrate. The patterning is realized by moving the x-y motor under the designed CAD mode. The program is written into the software in advance and the motor runs in

the particular way while the nozzle is spraying constantly so that the structures can be patterned as desired.

A variety of materials have been processed utilizing this technique, which include silica (Wang *et al.* 2007), hydroxyapatite (Ahmad *et al.* In press) and polymeric materials (Gupta *et al.* 2007). Metallic nanoparticles (e.g. gold) can also be printed using this method, but require low loading-volumes to overcome conductivity constraints (Samarasinghe *et al.* 2006). Similar to electrohydrodynamic atomization, a precursor containing the desired materials is used during the printing process. The precursor can be formed by dissolving the nanoparticles in a proper solvent, of which ethanol is most suitable because of its fast evaporating rate. Sol gel solution is also used when a ceramic material is printed, which is followed by a necessary heat treatment in order to obtain crystallized structures. The substrates used in the printing process can also vary, from non-conductive glass to semiconductive silicon wafers.

Electrohydrodynamic atomization printing can produce three-dimensional structures by add-on fabrication. The principle of this process is that a two-dimensional pattern is created firstly, which serves as template for subsequent depositions steps. The patterning and deposition can be repeated layer-by-layer in a defined way to achieve the desired shape of a three-dimensional structure or lattice (Geissler & Xia 2004). Wang and the coworkers have printed complex three-dimensional structures by adding a stepper motor in z directions. The printing was repeated for 240 times and a zirconia walled structure with the height of 1mm was obtained (Wang, Jayasinghe, &

Edirisinghe 2005b).

Electrohydrodynamic atomization printing has numerous advantages and two major of which are: first, needles used in electrohydrodynamic atomization can be several hundred micrometers in size and this is almost ten times bigger than those used in ink-jet printing, which can prevent blockages and allow easier processing of viscous ceramic suspensions containing a high level of solid and/or fast evaporating liquids; second, despite the use of much coarser needles, the droplet size generated are much finer, usually by an order of magnitude compared with ink-jet printing (Jayasinghe & Edirisinghe 2002a).

In all, electrohydrodynamic atomization printing is a novel method immensely useful for the patterning of various materials. So far this process still has a great potential to develop and not only the nano-powder suspension, but also sol gel solution can be investigated using this printing process. In this project, the author and his coworkers focused on printing of ferroelectric ceramic lead zirconate titanate using sol gel solution. Processing parameters were investigated so that the track-structures were obtained. The problems encountered during this process were also investigated and all the details will be discussed in **Chapter 6**.

Figures

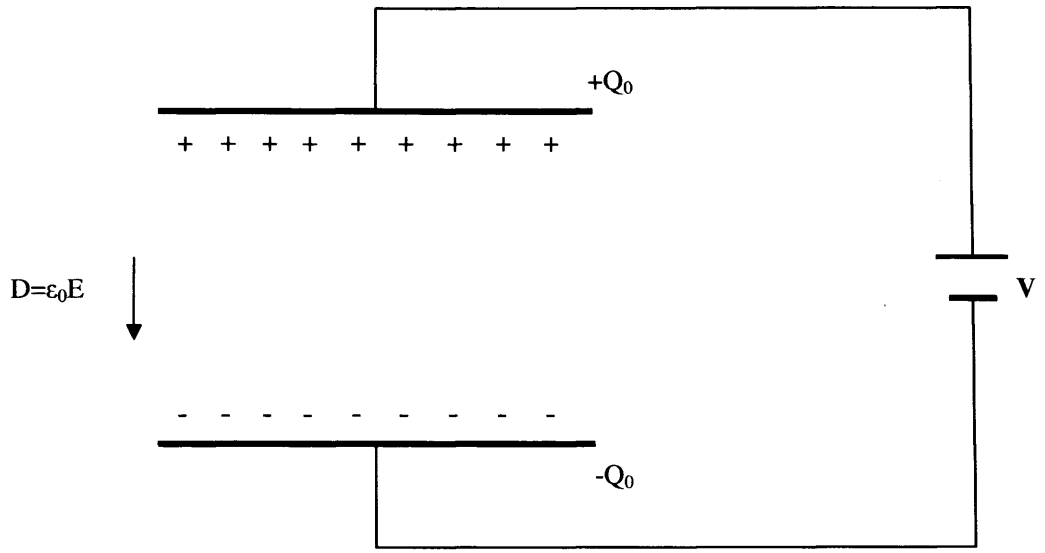

(a)

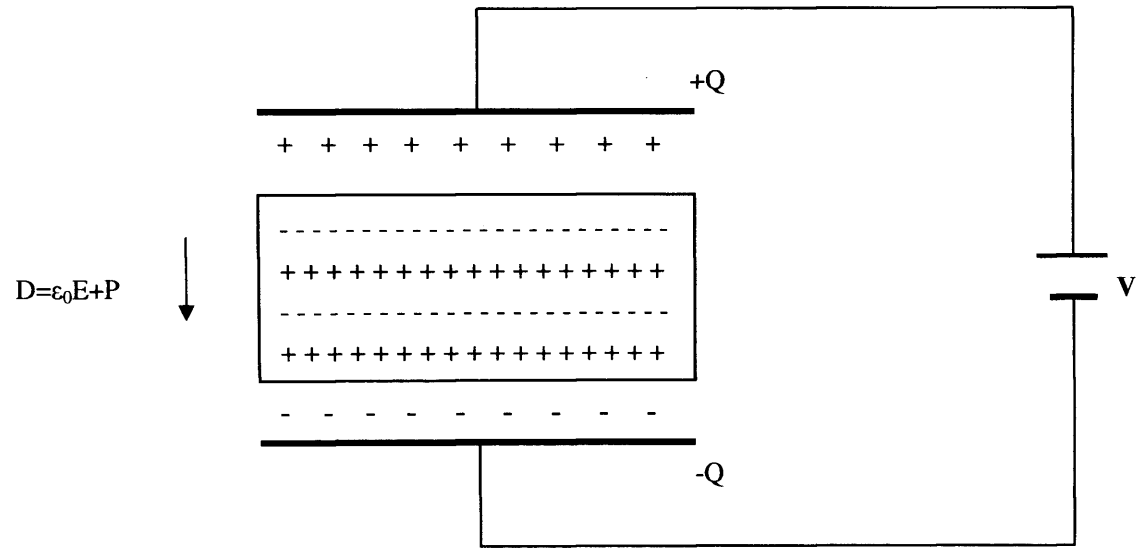

(b)

Figure 2.1 Schematic diagrams showing a parallel-plate capacitor of area *A* and separation of *d* **(a)** in vacuum attached to a voltage source, and **(b)** same as **(a)** except a dielectric is placed between the plates.

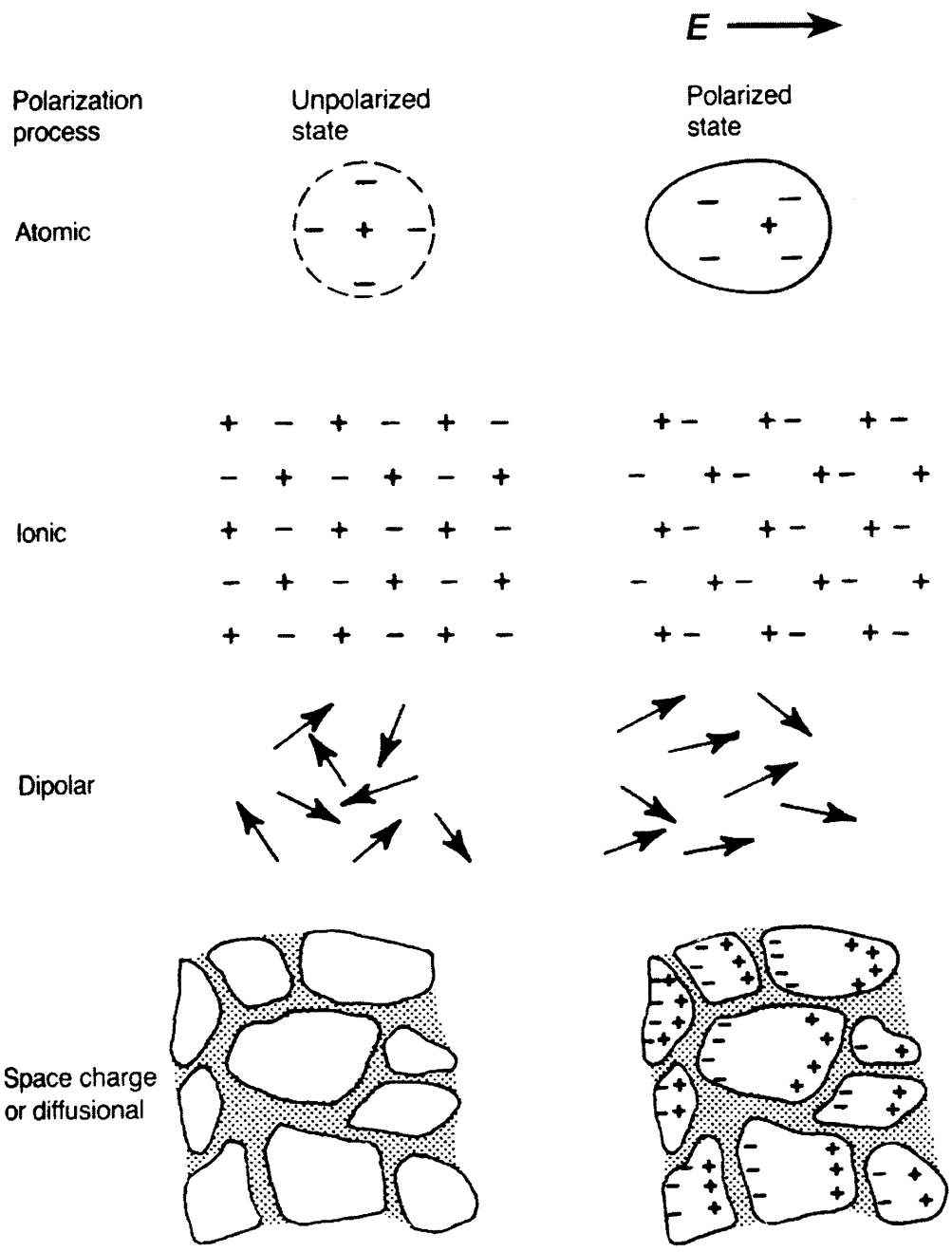

Figure 2.2 Schematic diagram of various polarization modes (Moulson & Herbert 2003).

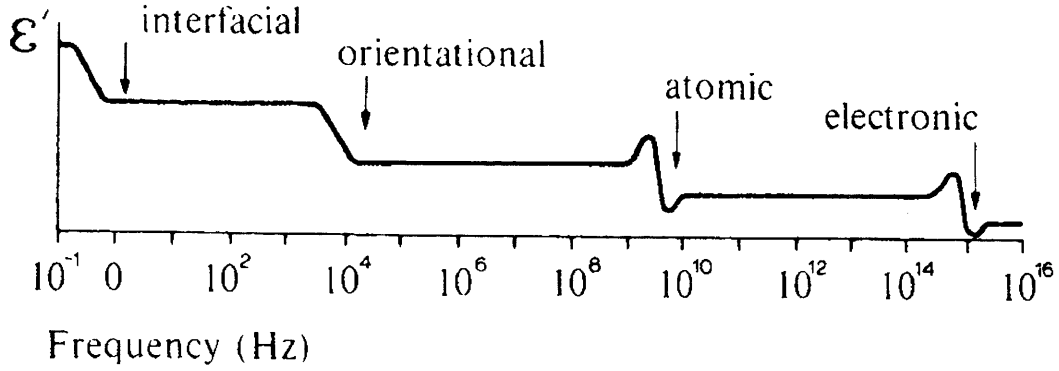

Figure 2.3 Frequency spectrum of relative permittivity for hypothetical material (Anderson *et al.* 1990).

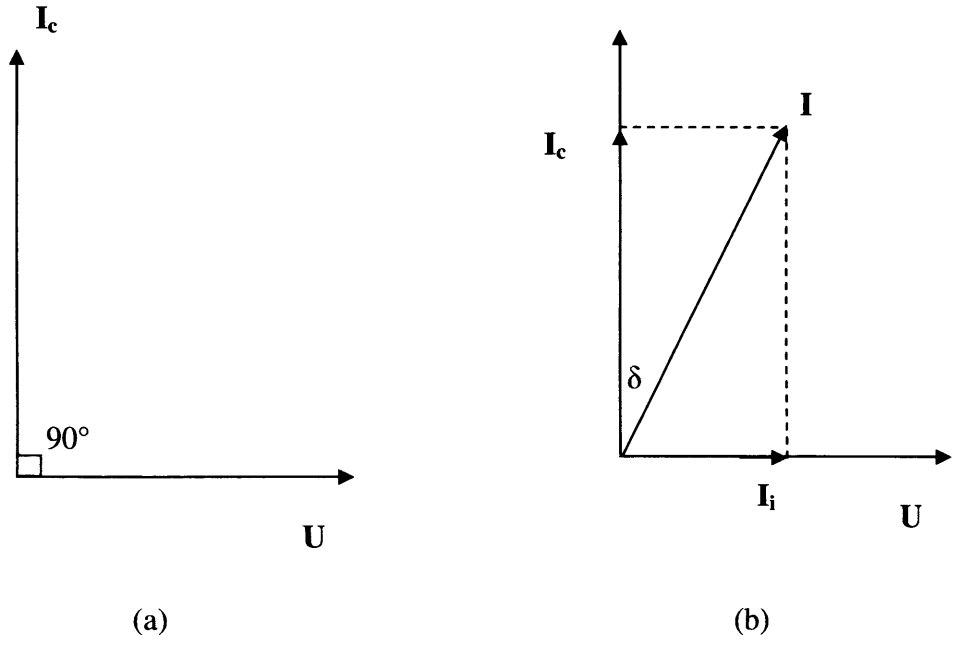

Figure 2.4 Applied voltage and current phase diagram of a capacitor experienced to an a.c. electrical field with **(a)** an ideal dielectric, and **(b)** a real dielectric.

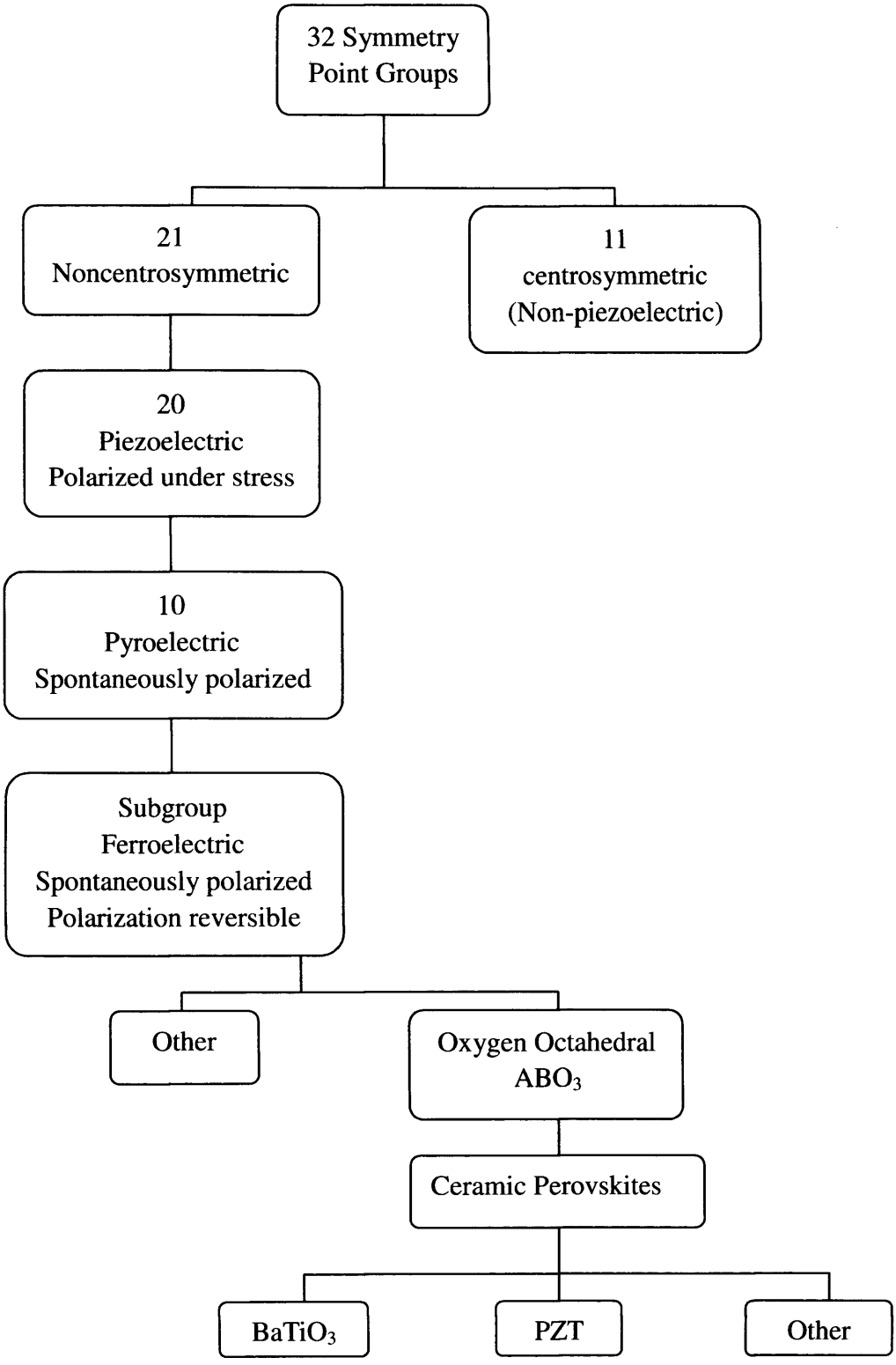

Figure 2.5 Interrelationship of piezoelectric and subgroups on the basis of symmetry.

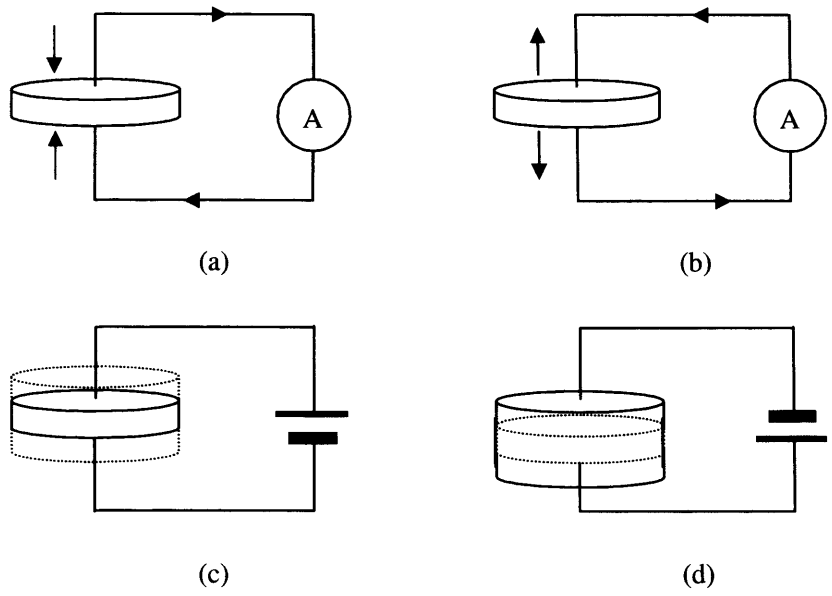

Figure 2.6 Piezoelectric effects: **(a)** and **(b)**, development of electrical charges under the application of mechanical forces; **(c)** and **(d)**, deformation of the material under the application of an electric field. The broken lines indicate the original dimensions.

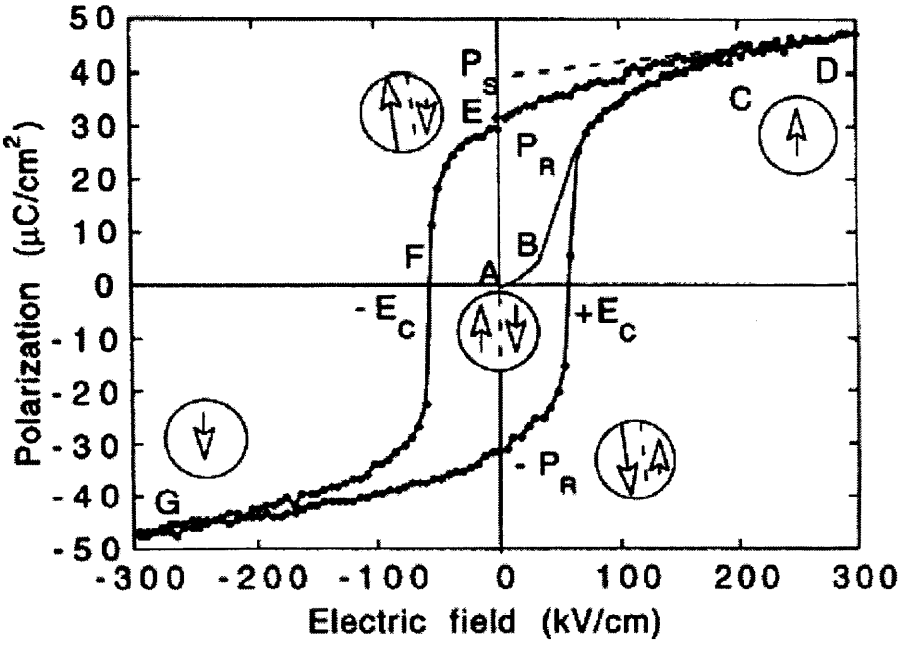

Figure 2.7 An example of ferroelectric P-E hysteresis loop of a typical ferroelectric material (Damjanovic 1998).

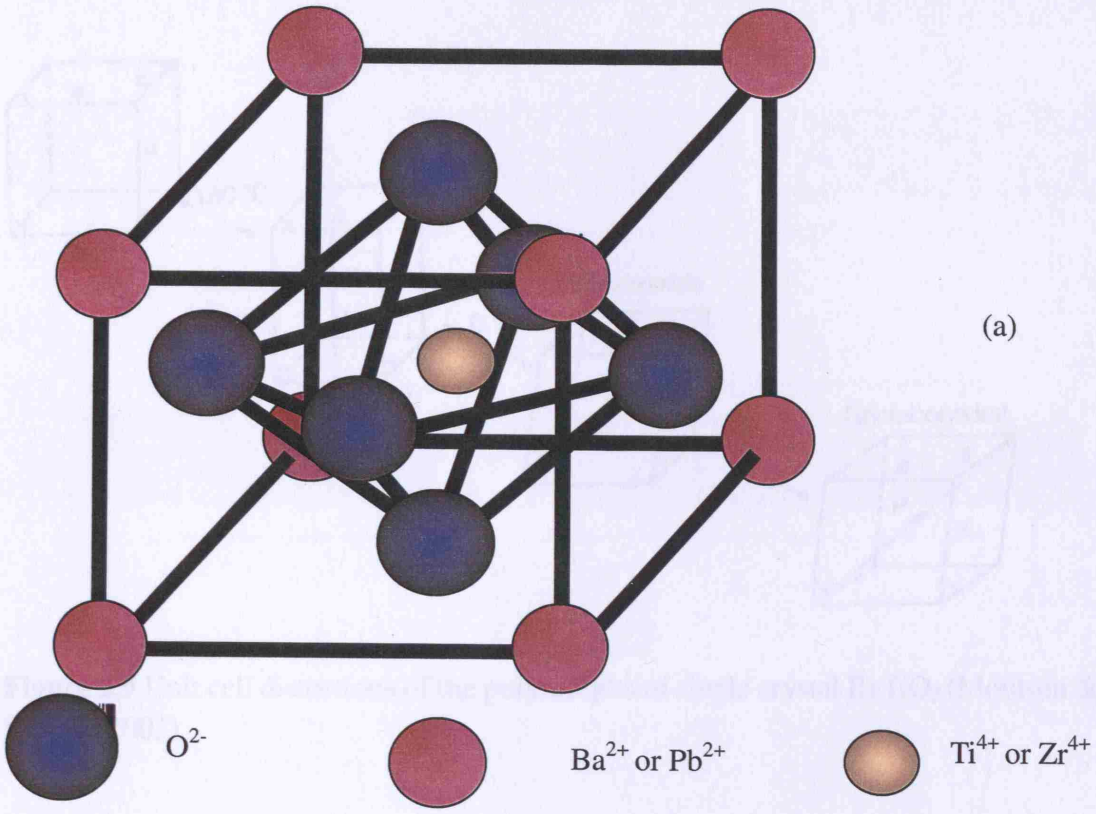

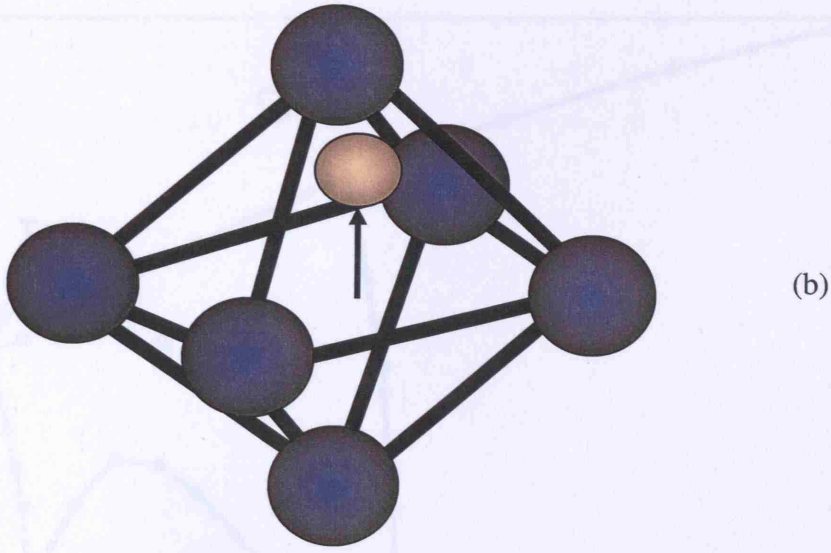

Figure 2.8 Schematic diagrams of **(a)** perovskite ABO_3 unit cell for $BaTiO_3$ or PZT and **(b)** a small displacement of B ion in the octahedral site.

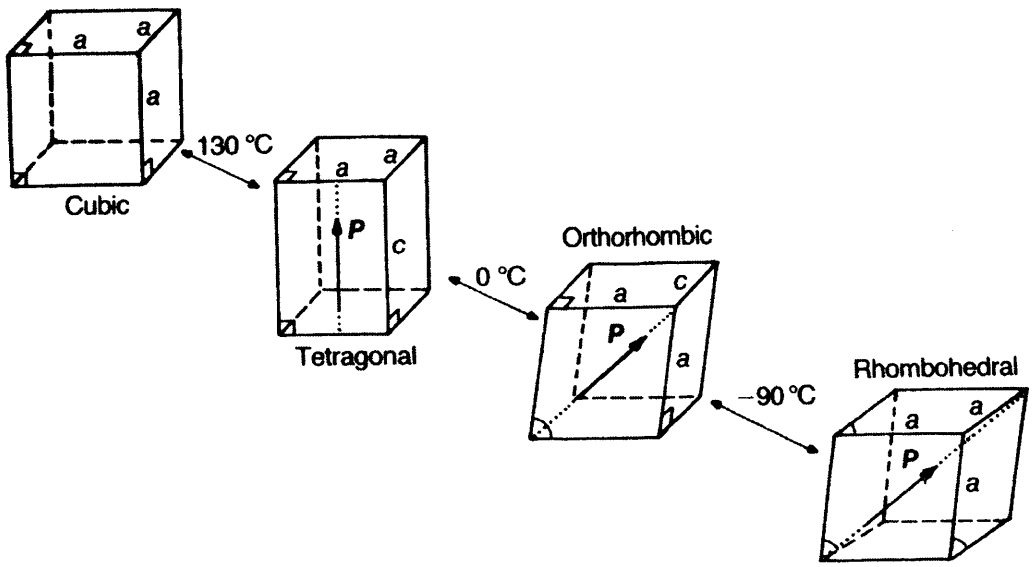

Figure 2.9 Unit cell distortions of the polymorphs of single crystal $BaTiO_3$ (Moulson & Herbert 2003).

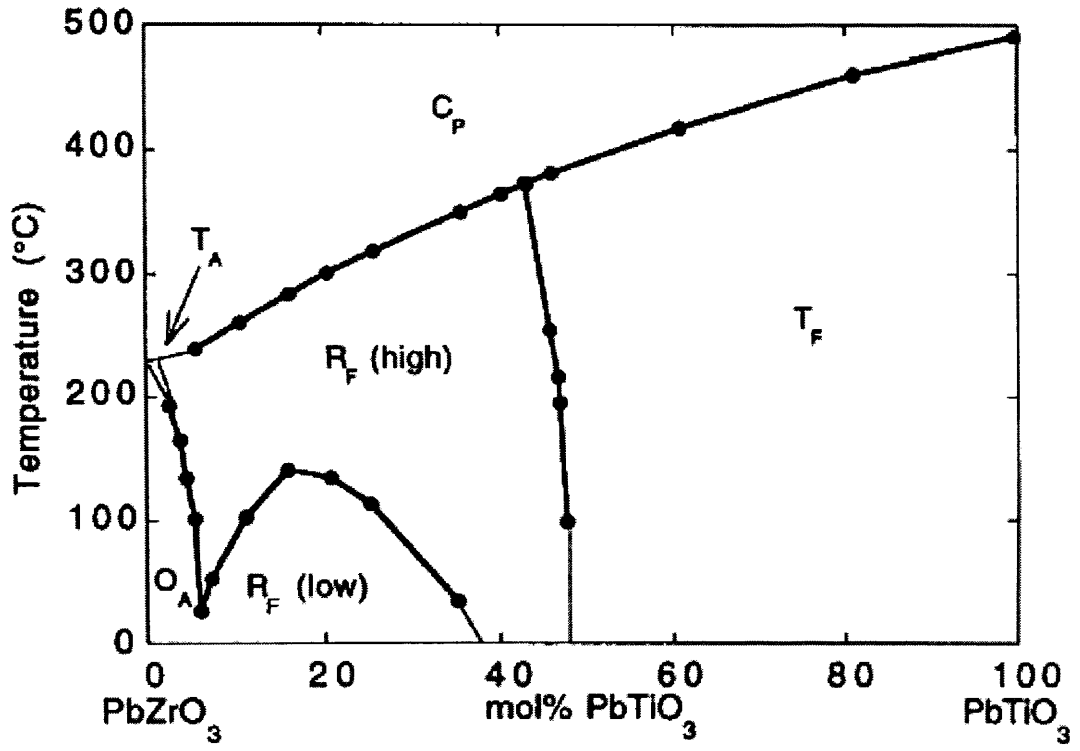

Figure 2.10 Schematic presentation of $PbZrO_3$-$PbTiO_3$ phase diagram (Damjanovic 1998).

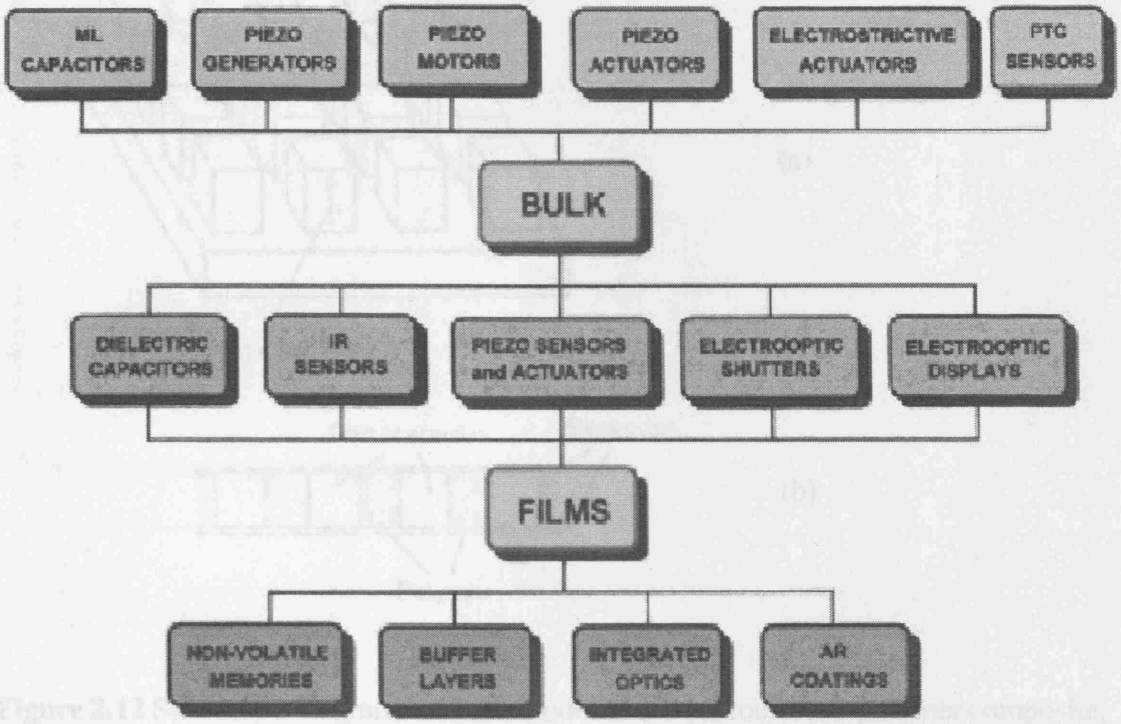

Figure 2.11 General category applications for bulk and thin film PZT materials (Haertling 1999).

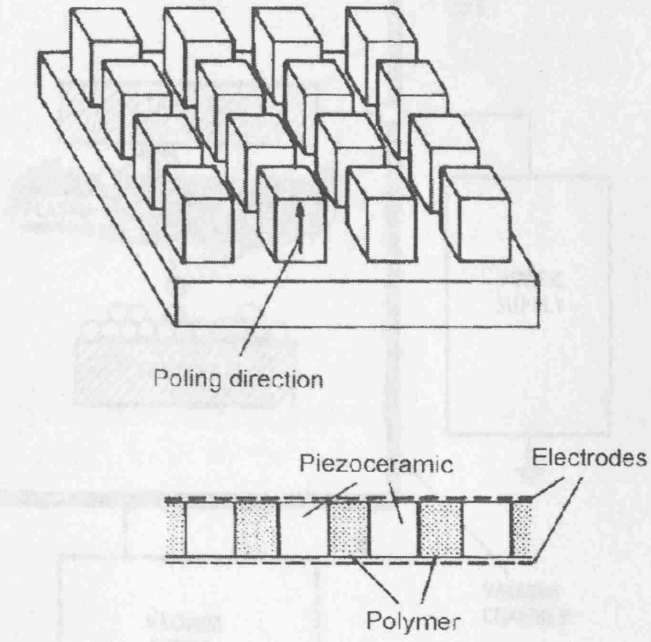

(a)

(b)

Figure 2.12 Schematic diagrams of **(a)** a model of 1-3 piezoelectric-polymer composite, and **(b)** its cross-sectional structure (Moulson & Herbert 2003).

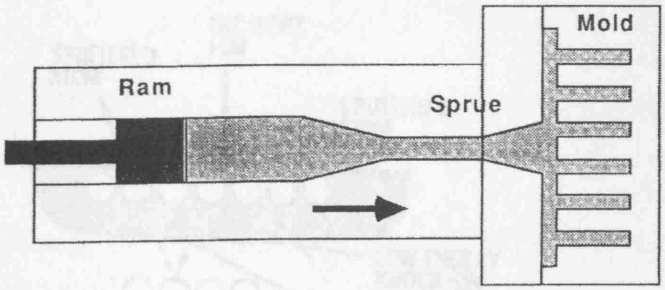

Figure 2.13 Schematic representation of injection-molding process for forming 1-3 composites (Janas & Safari 1995).

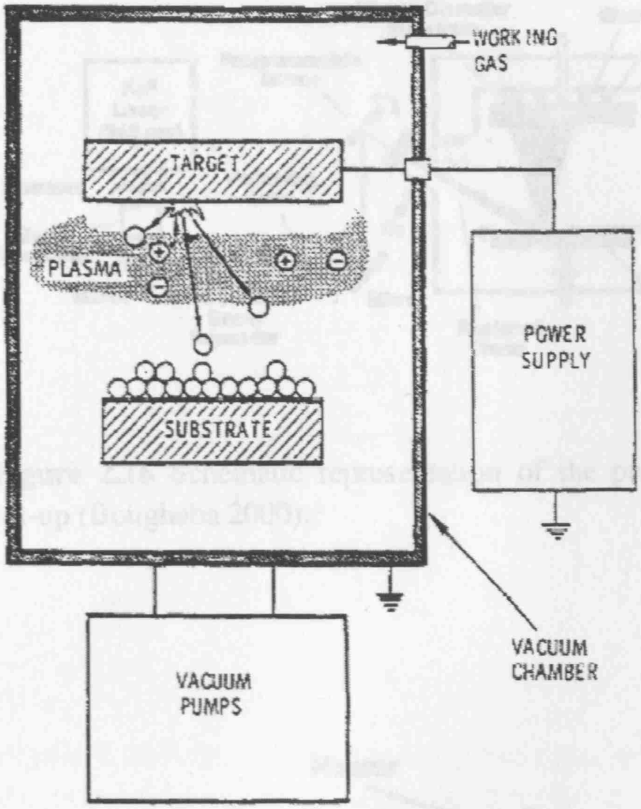

Figure 2.14 Schematic representations of sputtering deposition process (Kukla 1997).

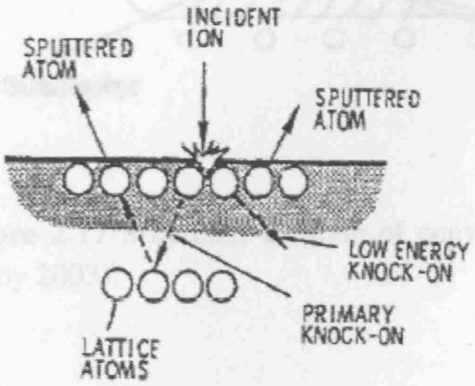

Figure 2.15 Schematic diagram showing momentum exchange processes that occur during sputtering (Kukla 1997).

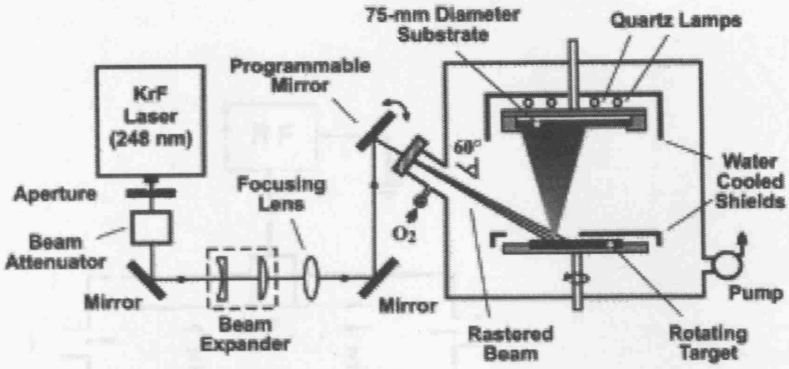

Figure 2.16 Schematic representation of the pulsed laser deposition experimental set-up (Boughaba 2000).

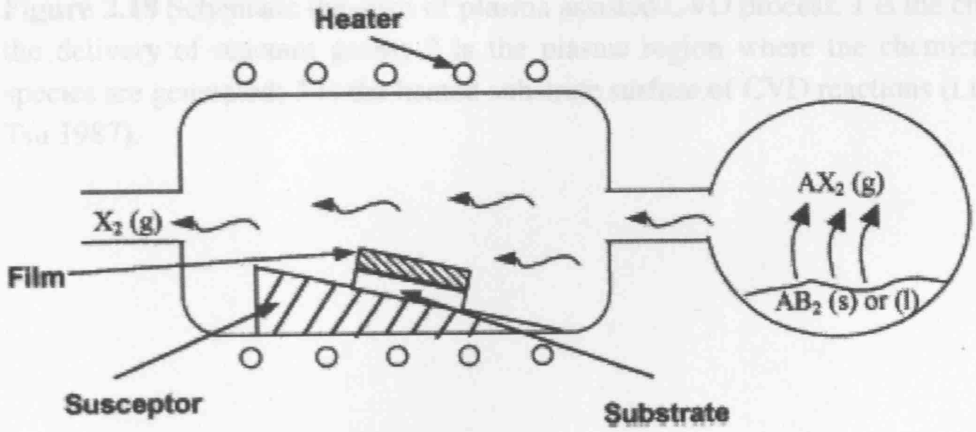

Figure 2.17 Schematic diagram of conventional chemical vapor deposition process (Choy 2003).

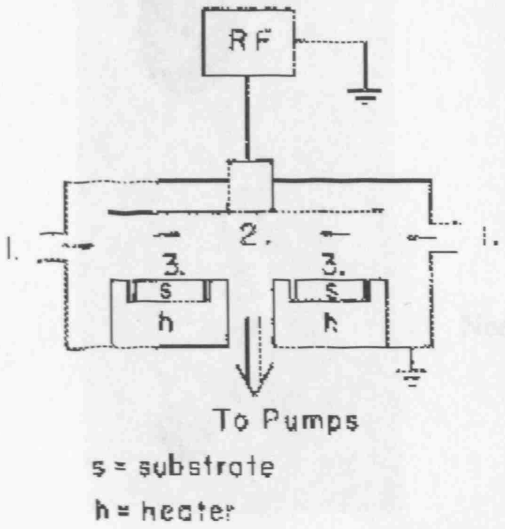

Figure 2.18 Schematic diagram of plasma assisted CVD process. 1 is the channels for the delivery of reactant gases; 2 is the plasma region where the chemically active species are generated; 3 is the heated substrate surface of CVD reactions (Lucovsky & Tsu 1987).

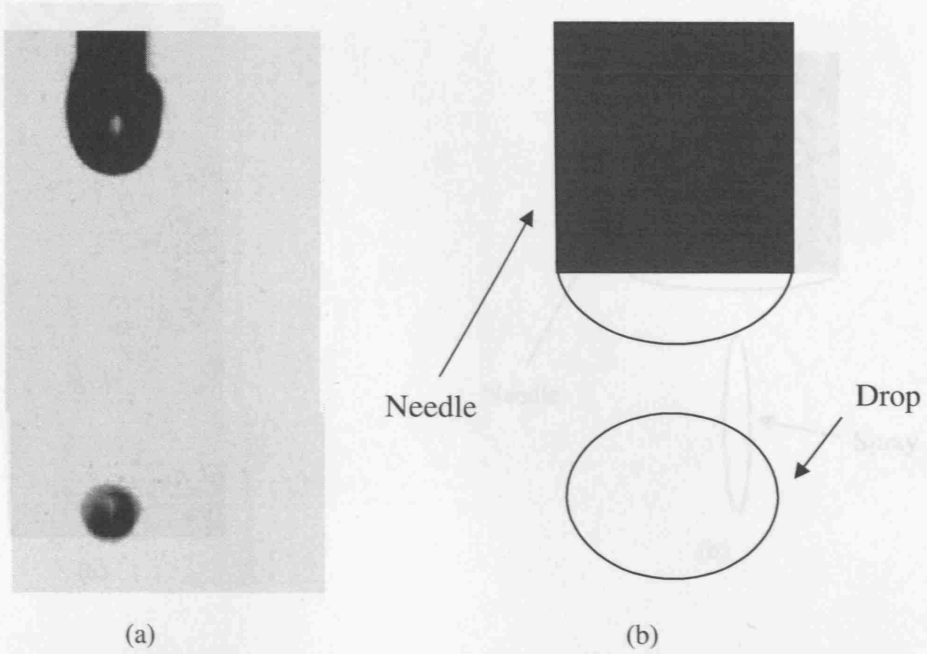

Figure 2.19 Dripping mode in electrohydrodynamic atomization **(a)** (Jaworek & Krupa 1999a) and **(b)** schematic illustration.

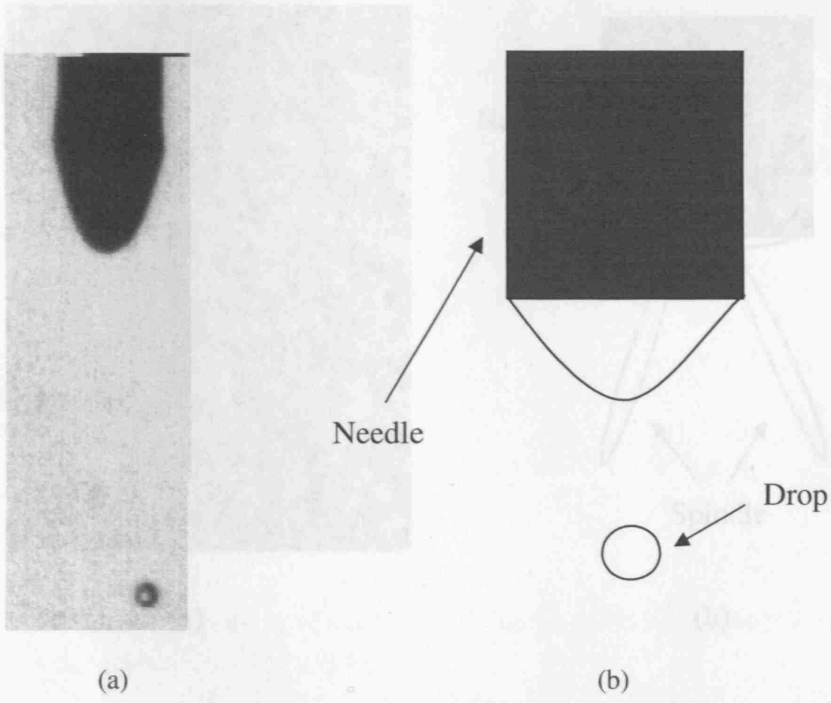

Figure 2.20 Microdripping mode in electrohydrodynamic atomization **(a)** (Jaworek & Krupa 1998) and **(b)** schematic illustration.

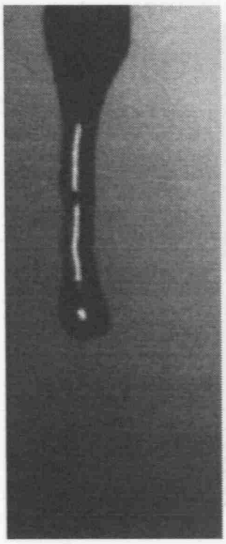

(a)

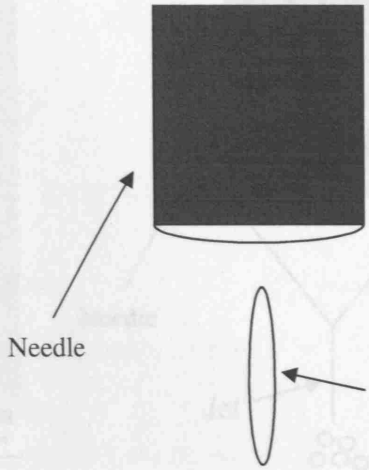

(b)

Figure 2.21 Spindle mode in electrohydrodynamic atomization **(a)** (Jaworek & Krupa 1999b) and **(b)** schematic illustration.

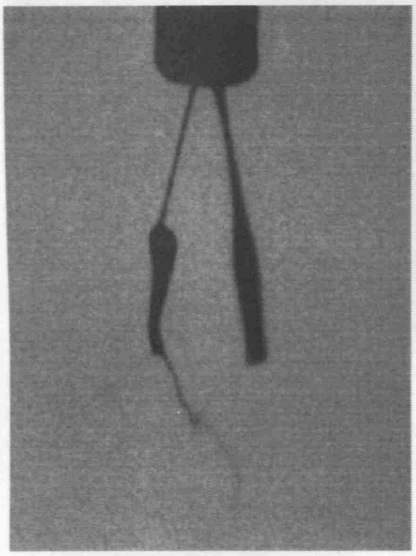

(a)

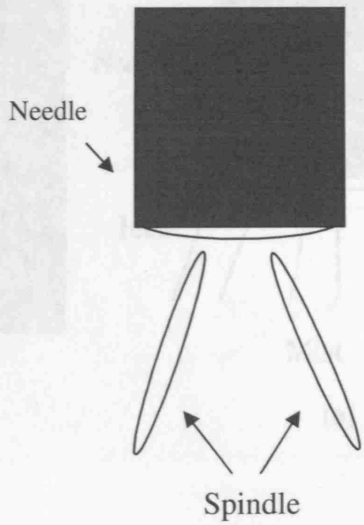

(b)

Figure 2.22 Multi-spindle mode in electrohydrodynamic atomization **(a)** (Jaworek & Krupa 1999b) and **(b)** schematic illustration.

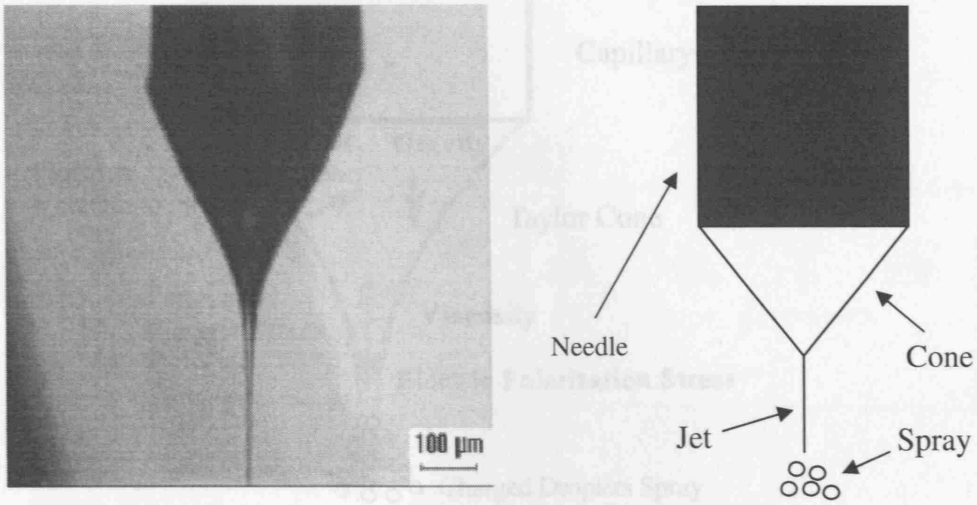

Figure 2.23 Stable cone-jet mode in electrohydrodynamic atomization **(a)** (Jayasinghe & Edirisinghe 2002b) and **(b)** schematic illustration.

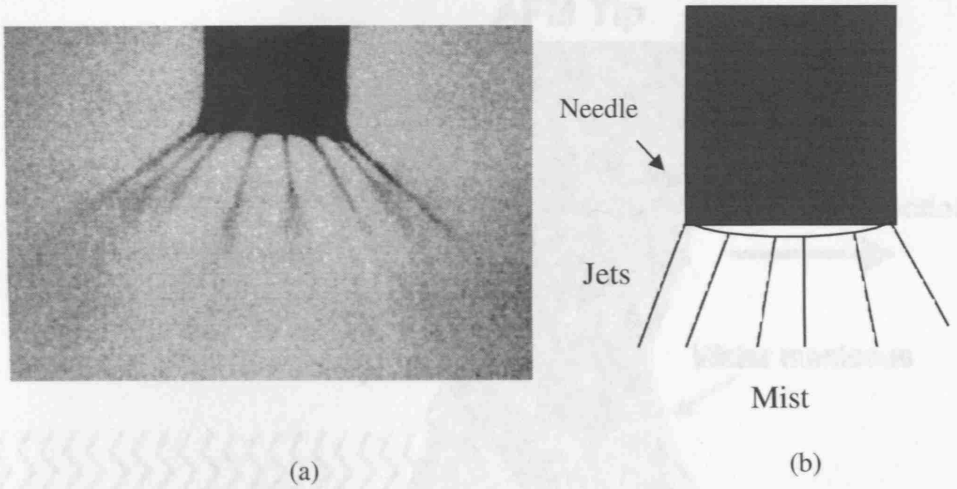

Figure 2.24 Multijet mode in electrohydrodynamic atomization **(a)** (Jaworek & Krupa 1998) and **(b)** schematic illustration.

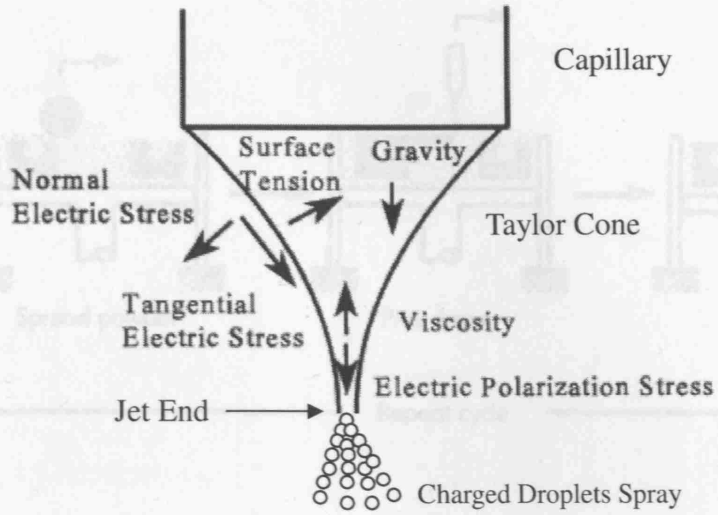

Figure 2.25 Schematic presentation of the forces acting on a Taylor cone (Hartman *et al.* 1999b).

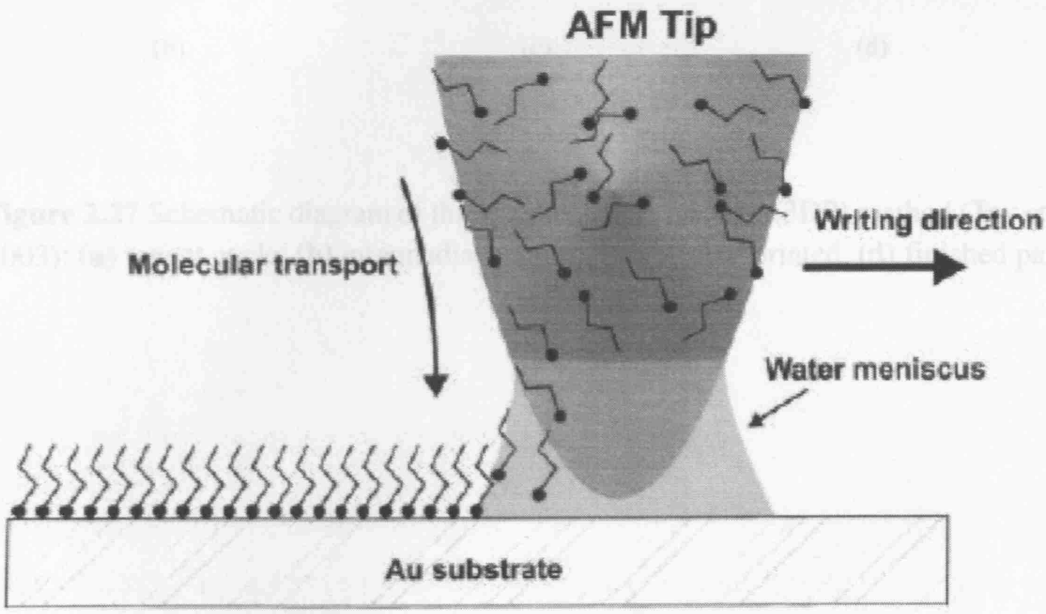

Figure 2.26 Schematic representation of DPN process. A water meniscus forms between the AFM tip coated with printed material and the Au substrate (Piner *et al.* 1999).

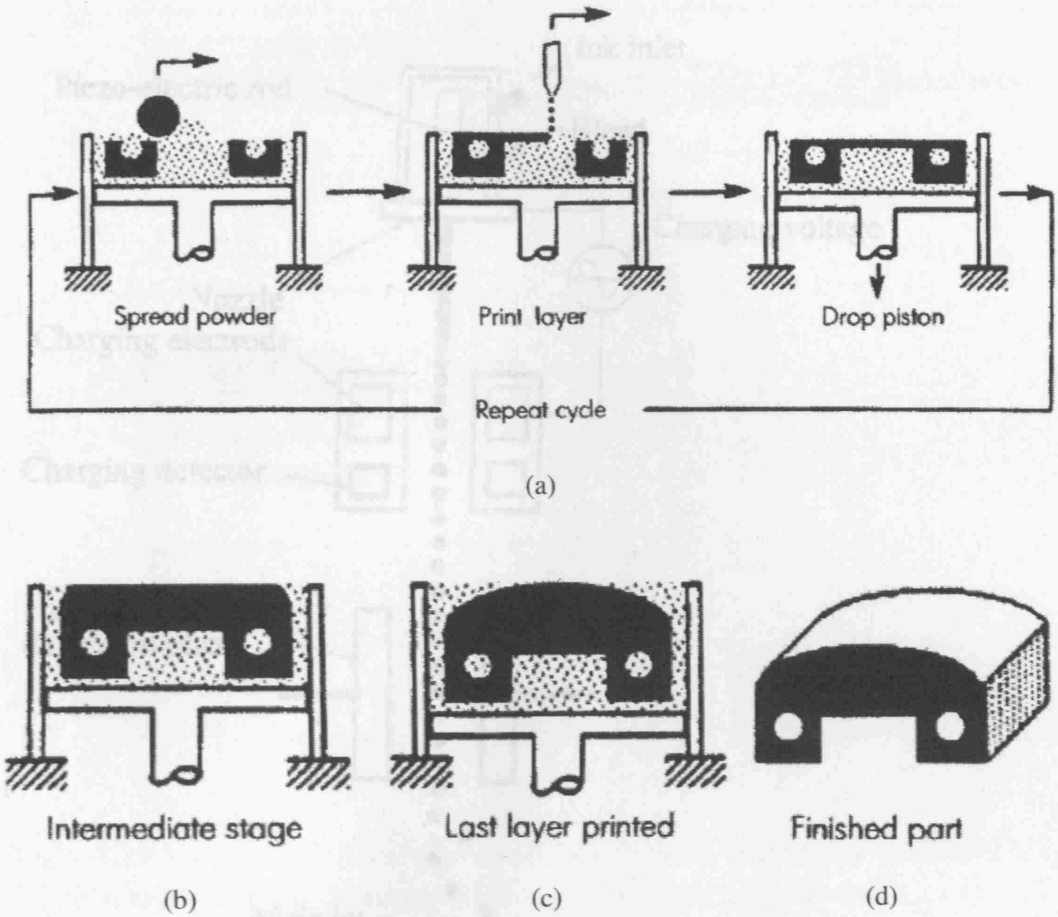

Figure 2.27 Schematic diagram of three-dimensional printing (3DP) method (Tay *et al.* 2003): **(a)** repeat cycle, **(b)** intermediate stage, **(c)** last layer printed, **(d)** finished part.

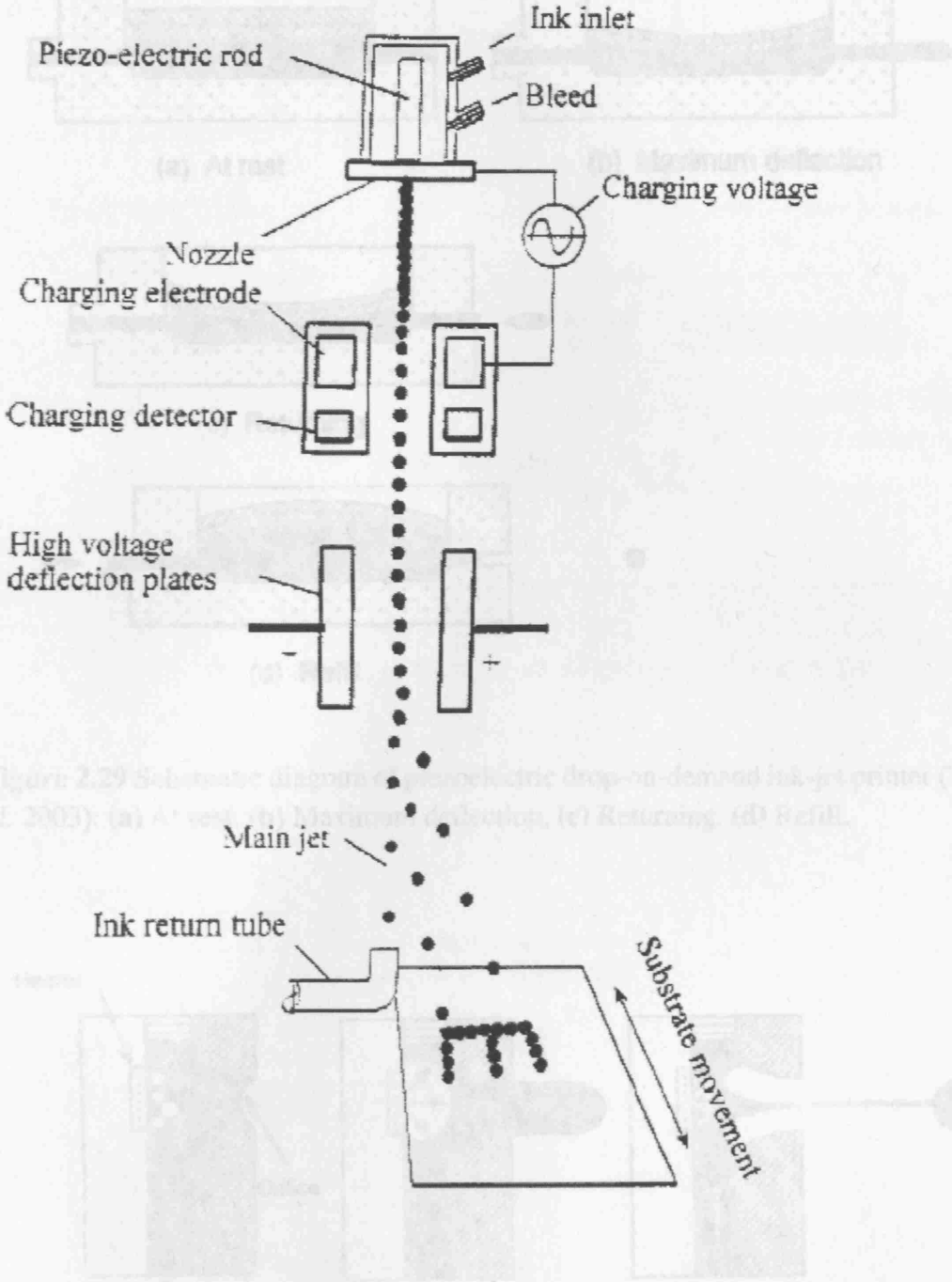

Figure 2.28 Schematic diagram of continuous-ink-jet printer designed by Song *et al.* (1999).

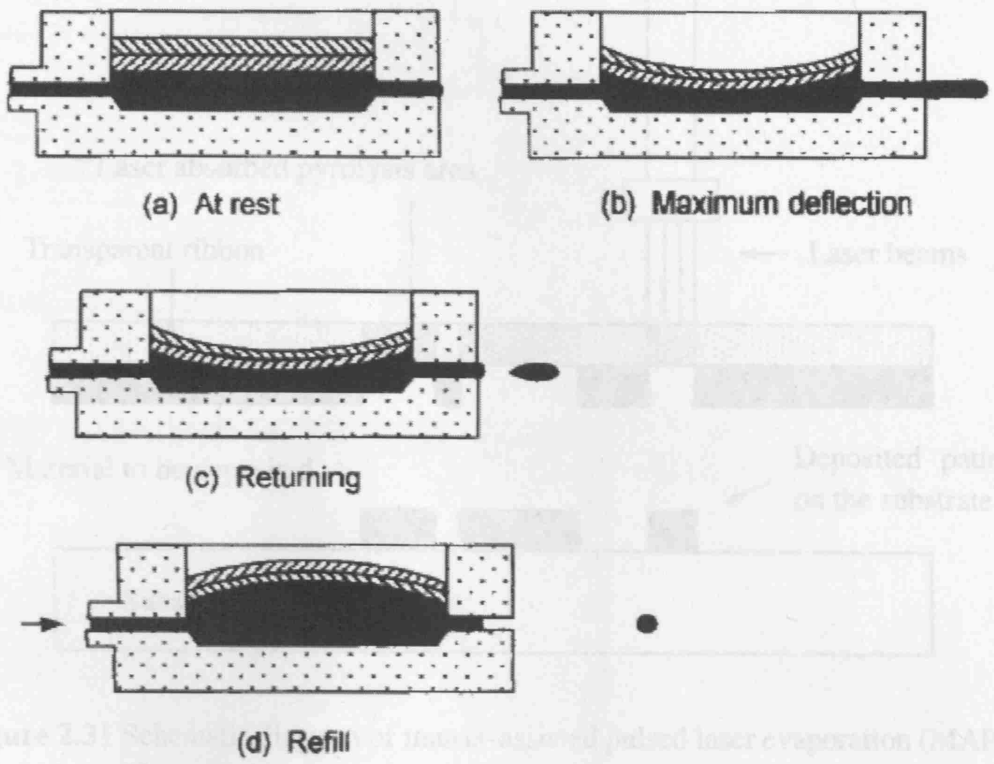

Figure 2.29 Schematic diagram of piezoelectric drop-on-demand ink-jet printer (Tay *et al.* 2003): **(a)** At rest, **(b)** Maximum deflection, **(c)** Returning, **(d)** Refill.

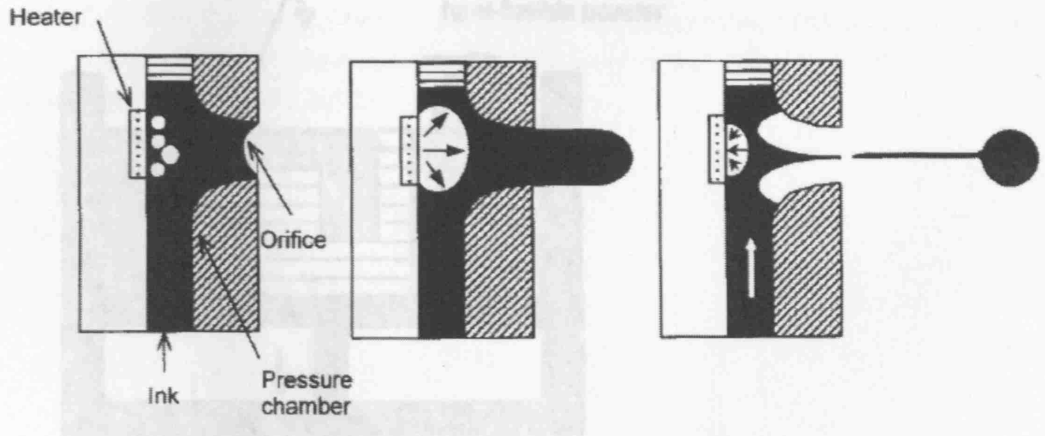

Figure 2.30 Schematic presentation of thermal ink-jet printer (Tay *et al.* 2003).

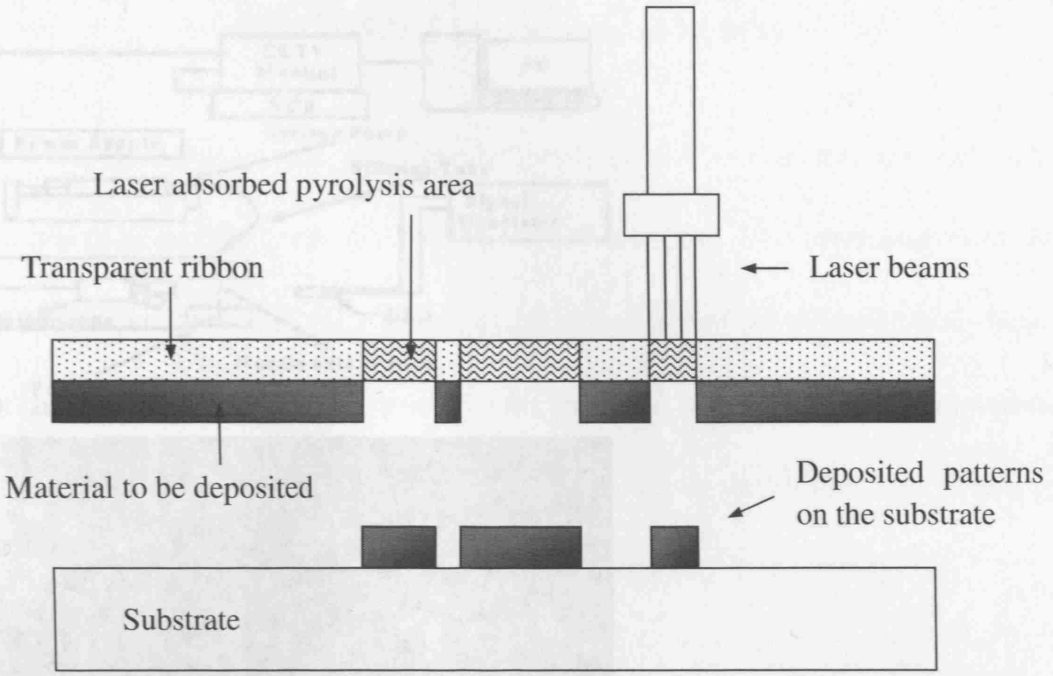

Figure 2.31 Schematic diagram of matrix-assisted pulsed laser evaporation (MAPLE), a variation of Laser Ablation.

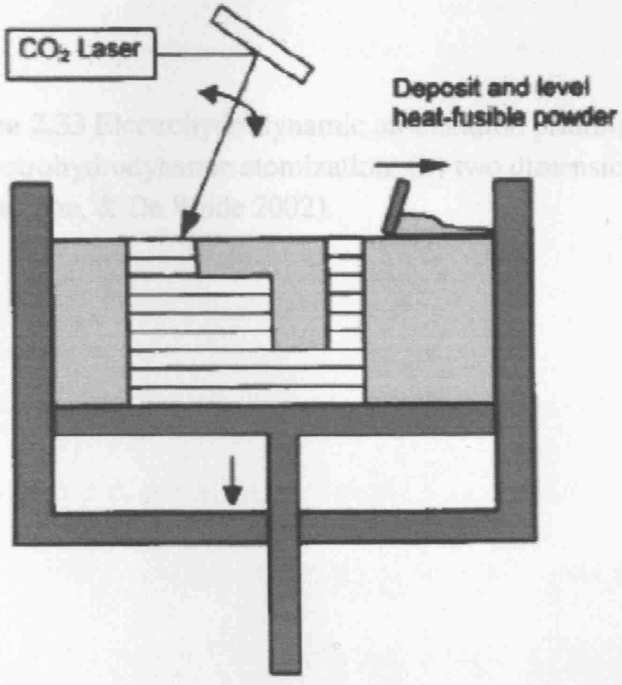

Figure 2.32 Schematic diagram of selective laser sintering process (Tay *et al.* 2003).

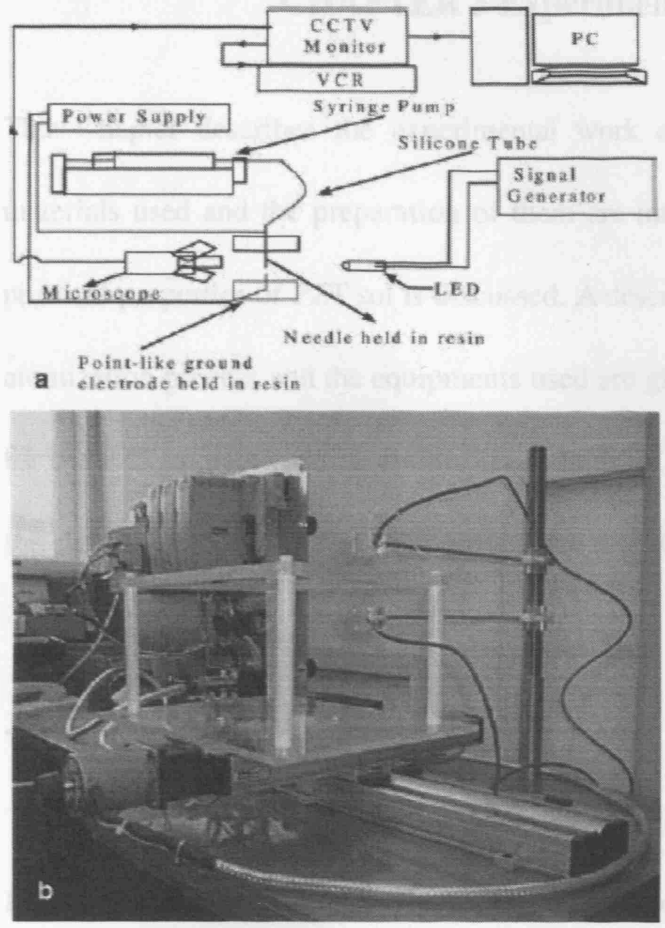

Figure 2.33 Electrohydrodynamic atomization printing system: **(a)** schematic diagram of electrohydrodynamic atomization, **(b)** two dimensional printing device (Jayasinghe, Edirisinghe, & De Wilde 2002).

CHAPTER 3 Experimental Details

This Chapter describes the experimental work carried out in this research. The materials used and the preparation of them are introduced. The investigation of the physical properties of PZT sol is discussed. A description of the electrohydrodynamic atomization process and the equipments used are given. The methods and equipments for the PZT characterization are also introduced in this chapter. Finally, the details of the electrohydrodynamic printing process are described.

3.1 Materials

The main material investigated in this project is lead zirconate titanate (PZT). The PZT sol containing the relevant materials is introduced. Other solutions and their preparation routes are also described. Substrate materials, such as copper discs and silicon wafer, are also introduced in details.

3.1.1 Acetic acid/1-propanol solvent

The solvent used for the synthesis of PZT sol and PVP solution, and the dilution of PZT sol is a mixed solution of acetic acid and 1-propanol. The acetic acid (Anala R, glacial, VWR, Lutterworth, UK) is in 100% purity. The density of it at 20°C is 1.05×10^{-3} kg m^{-3} and the molecular weight is 60.25 g/mol. The 1-propanol (GPR, Rectapur) is also supplied by VWR (Lutterworth, UK). The purity of it is >99% and the molecular weight is 60.10 g/mol. The acetic acid and the 1-propanol were mixed with the volume ratio of 11:10. The mixed solution was stirred for 24hours and sealed

in polyethylene (PE) bottles for the future use.

3.1.2 PZT sol

The PZT sol used in this research was synthesized by the collaborators in the Nanotechnology Centre, School of Applied Science, Cranfield University, who also provided the stoichiometric amount of each constituent (Dorey *et al.* 2002). A traditional sol gel solution route was used, which is presented in **Figure 3.1**. Titanium (IV) isopropoxide and zirconate (IV) propoxide were used as the starting reagents, which were mixed in a round bottle flask with magnetic stirrer and mixed for 300s in a nitrogen hood. The solution was then removed from the nitrogen hood and mixed with the glacial acetic acid/1-propanol solvent, followed by a stirring for 300s. Consequently, lead acetate trihydrate was added into the solution which was then stirred for 1800s until the material dissolved. Finally, the acetic acid/1-propanol solvent was added into the solution again to adjust the concentration of the sol to 0.6M. The sol was then stirred for 24hours before being sealed in 1ml plastic tubes for future use.

The 0.6M PZT sol prepared by the above route is transparent and with a light yellow colour. The chemical stoichiometric ratio of the PZT sol was $Pb_{1.10}\ Zr_x\ Ti_{(1-x)}\ O_3$, where x is 0.48 in the sol used in **Chapter 4** while in **Chapter 5** and **Chapter 6**, the x value in the compound is 0.5.

In order to study the effect of precursor concentration on the as-deposited structures

during electrohydrodynamic deposition, 0.6M PZT sol was diluted using the acetic acid/1-propanol solvent. The sol was diluted 2, 5, 10, 20 and 60 times to generate 0.3M, 0.12M, 0.06M, 0.03M and 0.01M PZT sol, respectively. The diluted solutions were stirred for 24hours and sealed and stored in PE bottles for the future use.

3.1.3 Polyvinylpyrrolidone (PVP) solution

In order to prepare PVP solution, polyvinylpyrrolidone powder was used, which is supplied by Sigma-Aldrich Company Ltd. (Gillingham, UK). The powder is in white colour with the molecular weight of 10,000g/mol. It was added into the acetic acid/1-propanol solvent and stirred until the material was completely dissolved. A light yellow colour solution was then obtained, of which the concentration was 0.01M. The solution was sealed in a PE bottle and kept stirred all the time in order to eliminate precipitation and sedimentation.

3.1.4 Preparation of PZT sol with PVP solution

The solution used for electrohydrodynamic printing in **Chapter 6** was prepared by mixing the produced PVP solution and 0.6M PZT sol. Four mixed solutions were obtained in which the PZT sol and PVP solution volume ratios were 1:1, 1:2, 1:3 and 1:4, respectively. The mixture was stirred for 24hours and stored in PE bottles.

3.1.5 Photoresist

The material used for processing 1-3 composites with generated PZT structures

(investigated in **Chapter 5**) was AZ 9260 thick film photoresist, which was supplied by Clariant Corporation, AZ Electronic Materials, U.S.A. The AZ 9260 photoresist is formulated with propylene glycol monomethyl ether acetate (PGMEA), which is in dark orange colour.

The preparation of 1-3 composites was carried out in a yellow light area. The photoresist was dropped onto the PZT columns using a plastic pipette. The sample was left for 300s until the photoresist was infiltrated into the entire columnar structure area and then placed into an oven (80°C) for 10800s to set the photoresist. Consequently, the solidified sample was taken out from the oven to cool down to the ambient temperature. The procedure was finalized by polishing the surface of the sample using silicon carbide grinding paper until the yellow colour PZT columns were exposed.

3.1.6 Ethanol

In this research, ethanol (BDH Laboratory Supplies, Poole, UK) was used as a standard material to calibrate the characterization devices. The properties of ethanol at the ambient temperature (22°C) are given in **Table 3.1**.

Table 3.1 *Properties of ethanol*

Density	790 kg m^{-3}	Electrical conductivity	4×10^{-5} S m^{-1}
Viscosity	1.3 mPa s	Surface tension	23 mM m^{-1}

3.1.7 Copper substrate

The copper substrate used in **Chapter 4** for deposition of nanostructured PZT was processed from a copper material which was obtained from the department workshop. The relevant properties of the copper material are shown in **Table 3.2**.

***Table 3.2** Properties of the copper material used as substrates**

Density	8960 kg m^{-3}	Electrical conductivity	59.6×10^6 S m^{-1}
Melting point	~ 1085°C	Thermal expansion	~ 17 μm m^{-1} K^{-1}

* The values are obtained at the ambient temperature

Both the circular and square substrates were prepared. The thickness of them is 2mm and the diameters are 28mm and 18mm, respectively. Consequently, the surfaces of the copper discs were polished using a selection of silicon carbide grinding papers (No.800, No.1200, No.2400 and No.4000). The components in both geometries were used in the electrospray process, on which the PZT deposits were collected.

3.1.8 Titanium/platinum coated silicon wafer

The substrates used in **Chapter 5** and **Chapter 6** are titanium (Ti)/platinum (Pt) coated silicon wafers. The silicon wafer is supplied by Si-Mat Silicon Materials, Germany. The specification of such material is shown in **Table 3.3**.

Table 3.3 Specification of silicon wafer

Type/Dopant	P / Bor	Thickness	525 +/- 25 μm
Orientation	<1 0 0>	Front surface	Polished
Resistivity	10-20 Ω cm	Back surface	Etched

The front surface of the wafer was coated with Ti and Pt by the collaborators in the Nanotechnology Centre, School of Applied Science, Cranfield University, UK. A Ti layer of approximately 8nm thick was sputter-coated on top of the silicon wafer, followed by a Pt layer of approximately 100nm thick coated using the similar method. Only the polished side of the silicon wafer was coated in such route with the other side left as-received. The produced Ti/Pt coated silicon wafer was connected to the ground potential and used as substrates in the work of **Chapter 5** and **Chapter 6**.

3.2 Study of PZT sol properties

The examined properties of PZT sol include density, viscosity, electrical conductivity and surface tension. The devices and the measuring procedures are introduced in this section. All the measurements were carried out at the ambient temperature and the equipments were calibrated using the standard ethanol (see section 3.1.6).

3.2.1 Density

The density of the PZT sol was measured using the well established standard density bottle method. The 10ml standard glass density bottle (VWR, Lutterworth, UK) was used. The mass of both the empty and the liquid-filled bottles were measured using a

precision weighing balance (AND GR-300 Analytical Balance, A & D Engineering, Inc., U.S.A.). The density of the sol was calculated by dividing the weight by the known volume of the density bottle. Mean of five consecutive measurements was calculated as the final result.

3.2.2 Viscosity

The viscosity of the liquid was measured using a U-tube viscometer (SC/542.20, Schott Instruments GmbH, Germany). The PZT sol was firstly filled into the U-tube until the standard level was submerged and then left for stabilization. A stop watch was used to record the time T taken by the sol solution to travel through the U-tube. The measurement was repeated for three times and a mean value of T was obtained.

The dynamic viscosity η or $d \cdot v$ can be calculated by *Equation 3.1* as below:

$$\eta = K(T - \theta)\rho \qquad \textit{Equation 3.1}$$

where K and θ are constants for each type of U-tube and in this work K is 1.0×10^{-7} m^2 s^{-2} and θ is 0.15s. ρ is the density of the examined PZT sol which can be obtained using a density bottle (described in section 3.2.1). The common unit of the resultant dynamic viscosity is mPa s.

3.2.3 Electrical conductivity

The electrical conductivity of 0.6M PZT sol was measured using Hi8733 conductivity probe meter. (HANNA instruments Ltd., Bedfordshire, UK). It comprises of a meter

panel and a conductivity probe; the meter panel is used to set the measurement range and read the result from a monitor while the probe is used to immerge into the examined liquid. The measuring range of this meter is 0.0 to 199.9 / 0 to 1999 μS/cm and 0.00 to 19.99 / 0.0 to 199.9 mS/cm, respectively. The resolution of the measured conductivity is 0.1 / 1 μS/cm and 0.01 / 0.1 mS/cm, respectively. The meter is always used at the ambient temperature.

The probe was calibrated using standard ethanol with known conductivity value. 0.6M PZT sol was contained in a cuvette where the probe was completely immersed for 10s so that the air bubbles can be dislodged. The conductivities of the diluted PZT sols, which were investigated in **Chapter 5**, were also measured using the same method. The probe was rinsed using distilled water and dried before an alternative solution was measured.

3.2.4 Surface tension

The surface tension of 0.6M PZT sol was measured using a Kruss Tensiometer K9 (Kruss GmbH, Germany) and the Du Nouy ring method was selected. The ring was fixed mechanically on the probe of the tensiometer and a glass container which contained the PZT sol was placed on the platform. The platform was firstly raised up so that the ring was completely immersed into the examined liquid. Subsequently, the platform was lowered gradually and the ring was detached from the liquid surface. The value can be read from a monitor, which increased first and suddenly dropped to zero when the ring was separated from the liquid completely. The maximum value

shown during this procedure is the surface tension of the examined liquid. Five consecutive values were measured and the average value was calculated as the final result. The ring was cleaned with distill-water and dried after each reading in order to minimize errors.

3.3 Equipments used for electrohydrodynamic atomization

The instruments set-up of electrohydrodynamic atomization is introduced in this section. The specification of each device/component used is introduced and the furnace, which was used for heat treatment of the sample, is also described.

3.3.1 Equipment configuration

The equipment set-up of electrohydrodynamic atomization was illustrated in **Figure 3.2**. A steel needle was held in resin and connected to the high voltage produced by a power supply. Silicone tubing was used to connect the inlet of the needle and a syringe where the sprayed sample was contained. The liquid is syringed out by a pump and passes through the needle where it can be deformed into different modes (detailed description in **Chapter 2**). A ring electrode with the diameter of 20mm was used as the ground electrode and placed below the needle exit. A high speed camera in conjunction with an optic fiber light source was used to record the scene of the spraying region and images can be interpreted using a connected computer where a program is installed.

3.3.2 Needle and ground electrode

The needle used in the set-up was supplied by Stanley Engineering Ltd., Birmingham, UK. The inner and outer diameters of the selected needle were 330μm and 640μm, respectively. The as-received needle was fixed in the resin, which was also connected with a copper wire for the connection of high voltage. The needle was cut in 15mm long from the resin and two ends of which were polished to be even.

Different ground electrodes were used in this research. In **Chapter 4**, a ring electrode with the diameter of 20mm was used so that the atomized droplets were capable of travelling through it and collected on the glass slide. In **Chapter 5**, a solid electrode was used during the electrohydrodynamic deposition process, on which a Ti/Pt coated silicon wafer was placed. In **Chapter 6**, an A4 paper which is fixed in the table frame was used to hold the silicon wafer substrate. However, a rod-like electrode, which was generated using a sharp tip needle, was used as the ground electrode.

3.3.3 Syringe pump

The pump used to eject the sol out of the syringe was a precision PHD syringe pump (Infuse/Withdraw PHD 4400 Hpsi Programmable Syringe Pump, Harvard Apparatus Ltd., UK). It employs a microcontroller that controls a small distance stepper motor. The motor drives a lead screw and a pusher block. Several operations can be selected via the keypad located on the pump, which included the pumping mode (infuse/defuse), the syringe mode (glass/plastic) and the value and the unit of the flow rate. In this work, 1ml plastic syringes (BD Plastipak^{tm}, VWR, Lutterworth, UK) were

used to fix on the pump and pushed in the infuse mode so that the liquid contained can be ejected out. The accuracy of the pump was calibrated using silicone oil-500 (VWR, Lutterworth, UK, density 971kg/cm^3). The liquid was ejected through the syringe with the flow rate of 10^{-10}m^3 s^{-1} and 5×10^{-11}m^3 s^{-1}. A balance (same as section 3.2.1) was used to weight the practical mass of the pumped liquid and the result was shown in **Table 3.4**. The theoretical mass was calculated according to the density of the silicone oil, the flow rate and the pumping time.

Table 3.4 *Practical and theoretical mass of pumped liquid and their deviations at different pumping times*

Pumping time (s)	Practical mass (g)	Theoretical mass (g)	Deviation (g)
1, Flow rate u=10^{-10}m^3 s^{-1}			
1034	0.0960	0.1004	0.0044
1987	0.1812	0.1929	0.0117
3027	0.2775	0.2939	0.0164
4291	0.4032	0.4167	0.0135
5657	0.5383	0.5493	0.0110
2, Flow rate u=5×10^{-11}m^3 s^{-1}			
688	0.0312	0.0334	0.0022
1433	0.0667	0.0696	0.0029
2433	0.1136	0.1181	0.0045
3992	0.1843	0.1938	0.0095
5979	0.2711	0.2903	0.0132

3.3.4 Power source

The high voltage involved in the process was generated using FC30 P4 120 Watt regulated high voltage DC power supply (Glassman Europe Ltd., Hampshire, UK). It provides a DC voltage to the connected needle so that an electric field can be obtained between the needle and the ground electrode. The output voltage range and the output

current range for this device are 0 to 30 kV and 0 to 4 mA, respectively. The operating temperature range is -20 °C to 50°C, and it is constantly at the ambient temperature for this research. This device also provides protections including fuses, surge-limiting resistors, low energy components and automatic current regulation that protects against all overloads.

3.3.5 High speed camera

In order to record the scene of the spraying region, a high definition digital camera (MOCAM-4000 high-speed b/w camera, Weinberger AG, Dietikon, Switzerland) was used in conjunction with an optical fiber light source. The camera contains a high-end CMOS sensor which can record ultra-high-speed phenomena. Its maximum resolution is 1,280 × 1,024 pixels and capturing speed range is 70 to 4,000 frames per second. The lens on the camera allows focusing on objects down to a few microns from a distance of approximately 5cm. A computer was connected to the high speed camera to interpret the image on the screen realised by running programmable software Mikrotron MotionBLITZ (v 3.0.7). The image size, capture speed can be changed using this software so that a proper image showing the spraying scene can be generated.

3.3.6 Heat treatment furnace

Heat treatment is necessary for the formation of perovskite PZT material from either the sol solution or the as-deposited structures. A laboratory chamber furnace (Lenton

Thermal Design Ltd., UK) was utilized to sinter PZT materials. The chamber with a capacity of approximately 5 liters was sealed by a lifting cover during the heating and the maximum temperature and output power of the furnace is 1600°C and 5 kW, respectively. The furnace is equipped with a microprocessor based temperature/programme controller (Eurotherm 2216) by which the target temperature and the heating ramp can be set and both the set value and actual furnace temperature can be displayed on the monitor.

Drying of as-deposited samples was carried out on a hotplate (VWR, Lutterworth, UK). The sample was firstly placed on the hotplate at the ambient temperature, followed by gradually increasing the surface temperature to 200°C for 120s. Consequently, the sample was naturally cooled to the ambient temperature.

3.4 Methods and equipments for PZT characterization

In this research, the PZT materials generated in various structures were characterized using different equipments. The details of these devices and the experimental methods are described briefly in this section.

3.4.1 TG/DTA analyzer

In **Chapter 4**, the weight loss and yield of the 0.6M PZT sol were measured using an STA-1500 thermal analysis system (Polymer Laboratories, Amherst, USA). Utilising this device, samples can be heated over a programmed temperature range (30°C to

1200 °C) and weight changes resulting from chemical reactions, decomposition and solvent/water evolution can be measured. The heating rate was set as 5°C min^{-1} in the flowing air (flow rate of the air was 150 ml min^{-1}).

In **Chapter 6**, the evaporation, decomposition and phase evolution behavior of the PZT/PVP (1:1 volume ratio) solution were investigated using a simultaneous thermal analyzer (NETZSCH STA 449 C Jupiter®, NETZSCH-Geratebau GmbH, Germany). The system is capable of performing both thermogravimetric analysis (TGA) and differential thermal analysis (DTA) at the same time. Apart from the TGA function, the high sensitivity DTA sensor in the system can detect endothermic and exothermic transitions related to evaporation, reaction kinetics, melting, decomposition effects, and phase transformation. A computer is used to plot the TGA and DTA data against the whole temperature range. The heating was operated at a constant rate of 10°C/min in flowing air of which the flow rate was 50 ml min^{-1}.

3.4.2 Optical microscopy

The droplets collected on microscope glass slides were examined using an optical microscope (Nikon ME600, Tokyo, Japan). The microscope was equipped with an incident illuminating unit in which the light can come from either sides of the specimen. When the droplets on the glass slide were examined (**Chapter 4**), the bottom light was used while when the columnar PZT structure (**Chapter 5**) and printed PZT track-structure (**Chapter 6**) were examined, the top light was used. Filters are fixed in the illuminating unit so that either the differential interference

contrast option or the dark field option can be selected. There are five objectives in this microscope including 5×, 10×, 20×, 50×, and 100× ones.

3.4.3 Scanning electron microscopy

The microstructures of the specimens generated in this research can be analysed at high magnification by secondary-electron imaging (SEI) using a scanning electron microscope (SEM, Jeol JSM 6300F, JEOL (UK) Ltd., Herts, UK). It is a high resolution SEM fitted with a field emission emitter, which can be operated at resolution of approximately 1.5 nm. The accelerating voltage is in 0.5 to 30 kV range and the working distance is varied between 15mm and 35mm.

When using SEM, gold or carbon coating is necessary for the ceramic samples so that the electrons involved can be released without being charged on the structure surface. In this experiment a thin gold layer of approximately 10nm thick was sputter-coated on the surface of the heat treated PZT sample before it was placed into the vacuum chamber.

An environmental scanning electron microscope (ESEM, Philips XL30, Philips Electronics UK Ltd., UK) was used to analyse the as-deposited PZT structures without heat treatment in **Chapter 4**. This versatile microscope with approximately 2nm ultimate resolution retains all advantages of a conventional SEM but removes the high vacuum constraint on the sample environment. Wet, oil bearing and insulating materials can be analysed in their natural state without modification or preparation.

Samples may also be examined in water vapour or other gasses such as CO_2 or N_2 at near atmospheric pressures (environmentally). In this work, the unsintered as-deposited PZT structures were in wet status, therefore ESEM can be utilised without prior specimen preparation or gold coating.

3.4.4 X-ray diffraction

X-ray diffraction (XRD) is a versatile technique that can be used to determine the spacing between the layers in a crystal structure and thus identify the present phase or phases. This application is based on the Bragg Equation,

$$n\lambda = 2d\sin\theta \qquad \textit{Equation 3.2}$$

where n is an integer, λ is the wave length of the X-rays, d is the planar spacing and θ is the angle of incidence between the X-ray beam and the lattice plane.

When using this technique, X-rays are incident on the parallel planes within the crystal and reflect. A detector scans the intensity of the reflections over the preset 2θ range. If the path difference of the reflected beams is an integer multiple of the wavelength, constructive interference will occur between them. Therefore, a trace of peaks with varying intensity at certain angles can be obtained over the entire 2θ range, thus the d spacing can be calculated by Bragg Equation so that the phase information can be identified.

In this research, two XRD diffractometers were used to detect the phase evolution of the PZT material after heat treatment. In **Chapter 4**, the perovskite phase

development of both PZT powder and the nanostructured deposit were analyzed using a Siemens D5000 diffractometer (Siemens Ltd., UK) using Cu Kα radiation. In **Chapter 5** and **6**, the deposited PZT structures after heat treatment were investigated using a Bruker D8 Discover diffractometer (Bruker AXS Ltd., UK) using Cu Kα radiation. Both devices were used for the detection of 2θ range from 20° to 60°.

3.4.5 Infrared spectroscopy

Vibration and rotation occurs in molecules because the chemical bond between atoms in the molecules works like a spring. Since atoms possess different shapes and size and the bonds between them have different strength and vibrating modes, the variations have characteristic frequencies, namely harmonic frequency. When supplied with energy, a molecule can alter its energy state and in doing so some energy is absorbed. The light source in the infrared range can be absorbed when its frequency matches the molecule's vibration, and thereafter exaggerates the molecule's movement. Utilizing an infrared spectrometer, the absorbed/unabsorbed energies can be distinguished and absorption peaks can be plotted along the whole infrared frequency range. This method of analyzing the vibration of a particular group is called infrared spectroscopy.

Infrared spectroscopy is used to analyse the composition of polymers in that the groups such as carbon-oxygen bond and carbon-hydrogen in polymers can only absorb light energy with specific frequencies. In **Chapter 6**, the PZT sol solution was incorporated with 0.01M PVP solution to generate track-structures by

electrohydrodynamic printing. The residual content of PVP material in the structure heated at different temperature level can be detected by infrared spectroscopy because the chemical bonds in PVP, such as C-N bond and C-H bond, vibrate in either stretching mode or bending mode, which can absorb the energy at certain frequencies.

In doing so, the samples heat-treated at different temperatures were analysed using a Fourier transform infrared (FTIR) spectrometer (Perkin-Elmer system 2000, PerkinElmer LAS Ltd., Beaconsfield, UK). 20 scans were carried out for data acquisition of the spectra which was analysed using a computer. The empty chamber was initially measured as a background reference. Nitrogen was used to purge the sample chamber during the measurement. Spectra were obtained between the wave numbers of 400-4000 cm^{-1}.

3.4.6 Electrical property measurement

The electrical properties of columnar PZT structures and continuous PZT films generated by electrohydrodynamic deposition were investigated. The columnar PZT structures were firstly fabricated as a 1-3 composite with polymer filled. Before measurement, gold layers were coated on the examined samples as top electrodes using vacuum evaporation (Edwards Evaporator E480). A series of circular electrodes were deposited with the diameter of approximately 740μm.

The relative permittivity and dissipation factor of the PZT/polymer composite was measured using a Wayne Kerr 6425 Precision Component Analyzer. This device is a

fast and accurate LCR meter that can measure a wide range of resistance, capacitance and inductance. There are 42 frequencies between 20 Hz - 300 kHz that can be set to test the sample and the working voltage is automatically altered subject to the measuring condition. In this work, C-D (Capacitance-Dielectric loss) measurement was selected. The probes were placed on both the top and bottom electrode, which was connected to the device using a four point method. The frequency was set as 50 kHz and the capacitance and dissipation factor values can be displayed in the monitor.

The frequency variation of the relative permittivity and the dissipation factor of the continuous PZT film were measured using a HP/Agilent 4294A Precision Impedance Analyzer. This device covers a broader test-frequency range of 40 Hz to 110 MHz. The testing DC bias range is from 0V to +/- 40V. An advanced calibration and error compensation function was pre-designed in the device in order to reduce measurement error factors during the testing. All the measurements were carried out at the ambient temperature.

3.5 Electrohydrodynamic printing devices

As an electrohydrodynamic atomization derived technique, electrohydrodynamic printing (utilized in **Chapter 6**) combines an advanced patterning controlled system with an electrohydrodynamic force to deposit materials from precursors. The complex structure patterning is realized by direct jet writing in the stable cone-jet mode where the deposit is collected on the substrate that is very close to the jet after break-up. The mechanism of the electrohydrodynamic force used to produce stable cone-jet from a

precursor is similar to the one in electrohydrodynamic atomization. The patterning controlled system has been developed by many researchers (Wang, Edirisinghe, & Jayasinghe 2006). In our experiment, this system has been modified, which include an x-y axis track device with stepper motors, motion controller system, limited sensors, table frame holder and motion controlling software. In this section, the devices used in this system are described in details and the procedure of printing process is also introduced.

3.5.1 Printing device configuration

The schematic diagram of printing device configuration is shown in **Figure 3.3**. The motion device was composed of an x-y axis track device with stepper motors and a z axis column where the needles fixed. A table frame was placed on the x-y axis device, on top of which the substrate collecting the printed patterns can be placed. A point-like ground electrode was also used which was aligned to the needle below the substrate. Stepper motors were fixed on the x-y axis device to realize the motion on the corresponding axis. A motion controller system was connected between the stepper motors and a computer in order to realize the programmable motion controlling via the motion planning software pre-installed in the computer. Two limited sensors were installed on the x-y axis track device to enhance the safety of the motion process.

During printing, both the needle and point-like ground electrode were connected to a power supply by which the electric field was generated between the needle and the

substrate. Silicone tubing was used to transport the liquid through and the spray-deposition procedure is similar to the one in the electrohydrodynamic atomization process (devices for such process has been omitted in **Figure 3.3**).

3.5.2 X-Y axis motion controller system

The x axis track is fixed on the base of the whole printing system, on which the y axis is mounted directly to keep the 2-axis in low profile. The moving distance for both tracks is 40mm. Two step motors are equipped at one end of each axis track with a ball screw pinch of 5mm. The motors employ incorporate mini-stepping technology (electrical sub-division of position) and are capable of dividing a complete 360° rotation to 4000 equivalent steps with a theoretical linear resolution of 2.5 μm.

The stepper motors are controlled by the motion controller system which is connected to a computer. Aided by a microprocessor in the system, the computer is capable to control the stepper motors through the pre-designed program.

The software used in the computer is called Motion Planner (version 4.3.1). It has a programming environment in which the codes to control the motion of the x-y axis can be designed and consequently download to the motion controller system. The Motion Planner also provides a platform on which the orders such as 'run' and 'stop' can be operated. The x-y axis track device is then driven by the stepper motors to follow the path of the co-ordinates given, thus enables printing.

3.5.3 Limit sensors

A travel limit sensor is fitted on each of the axis tracks to trigger the motion controller system when a respective carriage reaches a limit in any of the axis, which automatically enhances the safety during the operation.

3.5.4 Table and frame as a substrate holder

The table mounted on top of the x-y axis track device is made of Perspex, on top of which a frame is accommodated firmly using four stilts at each corner of the table. The substrate can be held tightly by the frame, of which the maximum dimension can be of A4 size.

3.5.5 Printing procedure for PZT track-structures

The PZT track-structures investigated in **Chapter 6** was printed in the following way. A program was initially designed to make the printing route as a single track and then return back to the origin. Then the precursor was electrohydrodynamic deformed in the cone-jet mode through the needle under certain flow rate and applied voltage conditions. Consequently, the motion controller system was started so that the substrate can move on the desired route and therefore the track-structure can be deposited on the substrate by the cone-jet mode jetting. The as-printed PZT structures were heat treated, as discussed in **Chapter 6**, followed by which the entire cycle of the electrohydrodynamic printing process was accomplished.

Figures

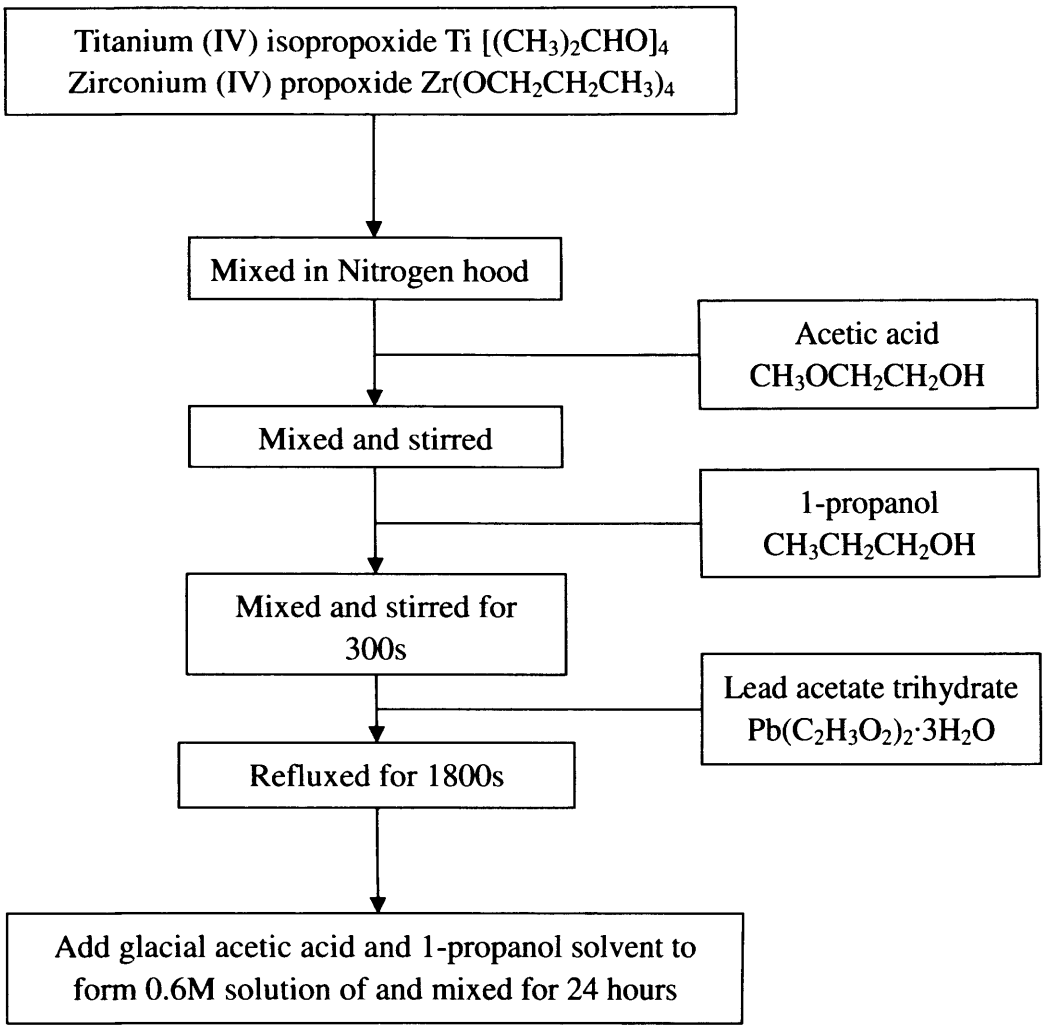

Figure 3.1 Preparation route of propanol-based 0.6M PZT sol using traditional sol gel solution method.

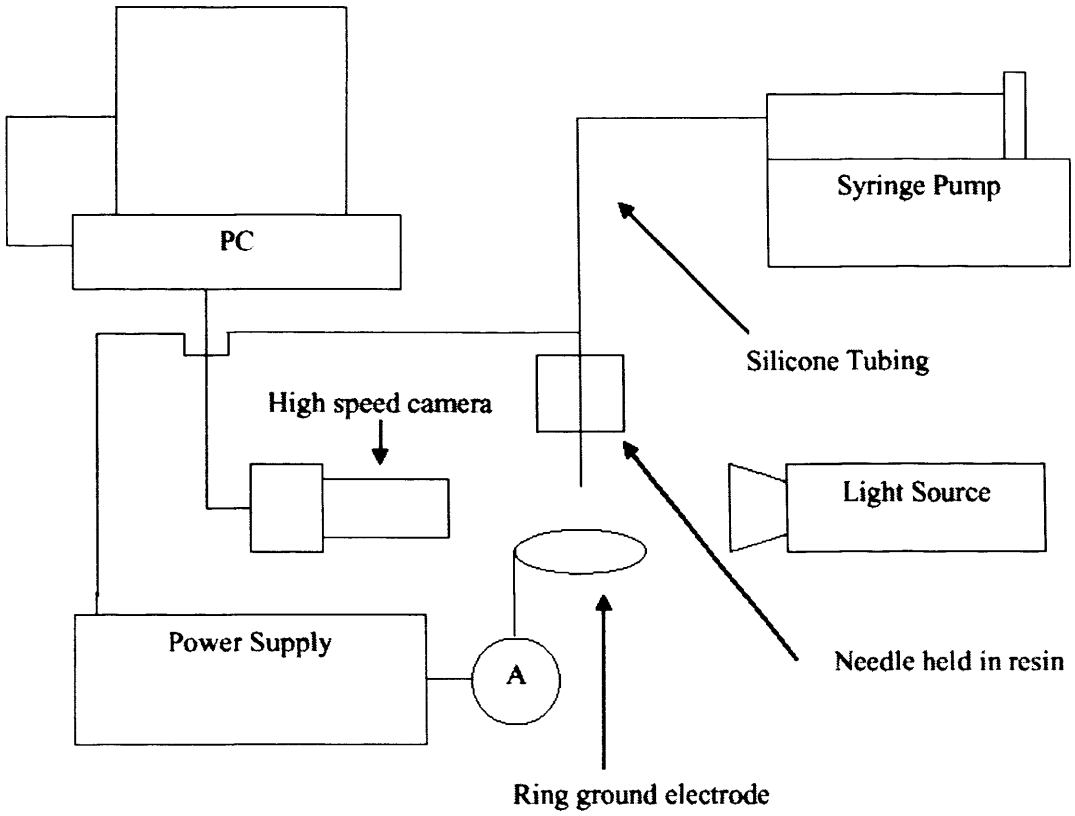

Figure 3.2 Schematic diagram of original electrohydrodynamic atomization equipment configuration showing the position of the electrodes, camera and light source.

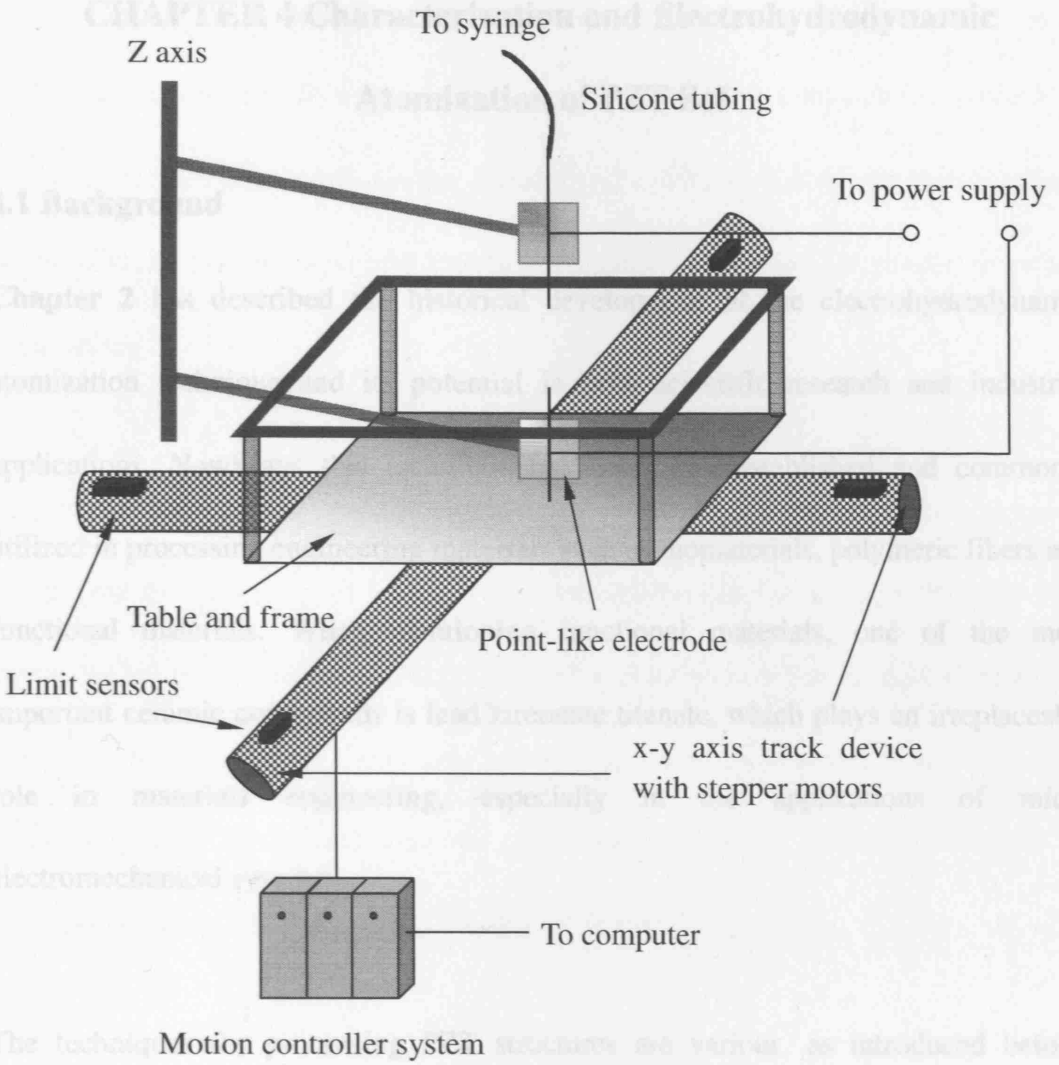

Figure 3.3 Schematic diagram of the printing device configuration, which works in conjunction with electrohydrodynamic atomization set-up.

CHAPTER 4 Characterization and Electrohydrodynamic Atomization of PZT Sol

4.1 Background

Chapter 2 has described the historical development of the electrohydrodynamic atomization technique and its potential in both scientific research and industrial applications. Nowadays this technique has been well established and commonly utilized in processing engineering materials such as biomaterials, polymeric fibers and functional materials. When mentioning functional materials, one of the most important ceramic compounds is lead zirconate titanate, which plays an irreplaceable role in materials engineering, especially in the applications of micro electromechanical systems.

The techniques for processing PZT structures are various, as introduced before. However, researchers are still investigating new techniques for processing micrometer or sub-micrometer PZT structures considering high efficiency, low cost, simple instrument set-up and low processing temperatures. Amongst those, the electrohydrodynamic atomization technique has generated considerable attentions of engineers in functional material forming area: both Wilhelm *et al.* (2005) and Nguyen *et al.* (2001) have done some research on utilizing electrohydrodynamic atomization to process ZrO_2 thin films; works on processing TiO_2 using electrohydrodynamic atomization have also been investigated by Nomura *et al.* (2003) and Chen and his coworkers (Chen *et al.* 1999b) who also have a published work on processing $LiCoO_2$ films using this technique (Chen *et al.* 1996b). However, works on processing of PZT

utilizing electrohydrodynamic atomization are very rare and this creates a great challenge and opportunity for the development of new PZT micro-device processing method. Therefore, research on the feasibility of utilizing the electrohydrodynamic atomization technique to process functional ceramic PZT using sol gel precursor has been started.

This chapter is an initial and fundamental part of this PhD project, which is aimed to investigate the feasibility of utilizing electrohydrodynamic atomization to form PZT structures using sol precursors. The result of it is important for the establishment of the electrohydrodynamic deposition technique to form columnar PZT structures and continuous PZT films and also the electrohydrodynamic printing technique to generate complex PZT structures (**Chapter 5** and **6**).

In this chapter, the precursor was prepared using a typical sol-gel method, and the properties of it, which determines the atomization mode during the electrospray process, were examined thereafter. The sol was placed in a furnace and heat treated at different temperatures in order to determine the ideal sintering temperature. The yield of the sol was also studied, which revealed the information on the evolution of the sol during heat treatment. The examined sol was then utilized for the electrospray process, in which a mode selection map was constructed considering the important processing parameters (e.g. flow rate, applied voltage and needle-substrate distance). After that the cone-jet mode can be obtained under certain conditions, which is ideal for the generation of droplets with mono-disperse size distribution. Such droplets generated

on the glass slide were investigated under the optical microscope. Consequently, the examined PZT sol was electrosprayed onto a copper substrate. Nano-structured PZT particles were obtained after heat treatment at the examined sintering temperature and these particles were investigated using scanning electron microscopy and X-ray diffraction.

4.2 Properties of PZT solution

4.2.1 PZT sol precursor

The solution used in this work is 0.6M PZT sol. The preparation route for 0.6M PZT was described in **Chapter 3**. The composition is $Pb_{1.1}\ Zr_{0.48}\ Ti_{0.52}\ O_3$ in this work. The 0.1 mol of extra lead in the composition is to compensate for the lead loss during the subsequent heat treatment. The ratio of Zr and Ti is approximately 1:1, which is near morphotropic phase boundary (MPB) in the PZT phase diagram. It has been discussed in **Chapter 2** that PZT is always used with the composition near MPB due to its peak value of dielectric, piezoelectric and ferroelectric properties.

4.2.2 Properties of PZT sol

The properties of 0.6M PZT sol were investigated using the methods mentioned in **Chapter 3**. The density, electrical conductivity, viscosity and surface tension of the sol are described in **Table 4.1**. Measuring equipment was calibrated and validated with data given by the supplier and reference book. Ethanol and silicone oil (**Chapter 3**) were used for the calibration.

Table 4.1 Properties of 0.6M PZT sol

Sol concentration mol L^{-1} (C)	Density kg m^{-3} (ρ)	Viscosity mPa s (η)	Surface tension mN m^{-1} (γ)	Electrical conductivity S m^{-1} (K)
0.6	1081	4.4	26	4.4×10^{-3}

As illustrated in **Table 4.1**, it is evident that the electrical conductivity is much higher than that of other suspensions used in the previous electrohydrodynamic atomization studies (Jayasinghe & Edirisinghe 2005), where alumina ink with ethanol solvent had an electrical conductivity of 0.043 mS m^{-1}. Due to the high electrical conductivity, the liquid could be easily charged during high electric field involved spraying process. The charged particles will be attracted to the ground electrode and this attraction between the particles and ground electrode is expected to provide a great degree of control of as-deposited PZT structures. This will be discussed in details in **Chapter 5**. The viscosity and surface tension values of the PZT sol are also smaller than that of silica nano-suspension from other studies (Jayasinghe, Edirisinghe, & Wang 2004). These smaller values of PZT sol needs relatively low electrical strength to balance the force near the capillary to produce electrohydrodynamic atomization and it can be predicated that the cone-jet mode in the electrospray process may be achieved in relatively low level of applied voltage for this PZT sol than for other liquids when flow rate is kept constant.

4.2.3 Yield of PZT sol

In order to investigate the evolution of the components in the PZT sol during heat

treatment, a thermogravimetric analyzer (TGA), which was described in **Chapter 3**, was used to study the weight loss of the solution and the yield of it. A sample of PZT sol was filled in the metallic holder which was placed in the device chamber. The temperature was increased from room temperature to 700°C at a constant heating rate of 5°C min^{-1} in air, the flow rate of which was set as 150 ml min^{-1}. The loss-on-ignition data of 0.6M PZT sol is shown in **Figure 4.1**. The data is expressed in terms of the % mass remaining of the initial mass of the solution between the temperature range of 100°C and 700°C.

As shown in the graph, the first considerable evaporation stage is at approximately 100°C. As the boiling point of 1-propanol is 97°C, the initial decrease in mass is due to the evaporation of propanol. The boiling point of acetic acid is 118°C, therefore it is likely that the majority of the solvent (propanol and acetic acid) was removed by point A (approximately 150°C). However the organic solvents can react to form esters, ethers, CO_2 and further alcohols and these compounds would react and be removed at higher temperatures (Nouwen *et al.* 1996). When the temperature increased, the loss due to the removal of these compounds increased, which is shown in segment A to B in the curve. Beyond point B, there is still some small mass loss which may be due to the further evaporation and decomposition of metal alcoxides, making up 31% of the original sol (segment B to C). At higher temperatures above 600°C (after point C), it is believed that the lead loss induced by high temperature is the main reason for the mass reduction in this range.

A plateau is reached at approximately 650°C around point C and the mass remaining is about 13 wt%. This result is comparable to a yield of 16 wt% obtained from another loss-on-ignition tests on the propanol-based PZT sol heated to 700°C with a ramp of 2 °C min^{-1}.The variation between the two yields may be due to the ageing of the sol and precipitation. The sol may precipitate when stored for long time and a small mount of solvent is always added to prevent PZT precipitation. This dilution procedure may be the reason for the yield decreases; however, 13 wt% is reasonable for the yield of 0.6M 1-propanal based PZT sol.

The loss of mass is due to the solvent evaporating off as well as lead being lost from the ceramic. The lead loss was estimated to be approximately 15 wt% following the comparison of the theoretical and actual mass yields of the propanol-based PZT sol. This is an important matter when processing compounds containing lead. Firstly, the loss of lead at high temperatures restricts the limit of the processing temperature, which makes it necessary to produce such compounds by low temperature processing methods. On the other hand, the loss of lead will change the composition and have a tendency to form a second phase called pyrochlore structure (Kwok & Desu 1992; Reading *et al.* 2002) rather than perovskite structure, resulting in lower dielectric, piezoelectric and ferroelectric properties (Moulson & Herbert 2003). The composition of pyrochlore phase is AB_2O_6, where A is a mixture of divalent ions. It is a paraelectric compound with low dielectric permittivity at room temperature. The structure contains corner-sharing MO_6 octahedra but with several different orientations. In order to inhibit the formation of pyrochlore, extra amount of lead

(approximately 10 wt%) was used in the original sol. In order to investigate the ideal sintering temperature for perovskite PZT crystallization with less lead loss due to the over high heating temperature, a series heating temperature were selected and the structures were analyzed using X-ray diffraction, which will be discussed in the next section.

4.3 Heat treatment of PZT sol

4.3.1 Heat treatment procedure of PZT sol

As mentioned above, heat treatment is necessary for the crystallization of PZT in desired perovskite structure. To determine the phase evolution, the sol samples were kept in a crucible, each covered with a lid and placed into the furnace. The heating ramp was 10°C min^{-1} and the heating temperatures were set at 600°C, 650°C, 700°C, 750°C, and 800°C, respectively, with the dwell time of 3600 s at each temperature. During heating to each temperature, an intermediate dwell time of 1800 s at 400°C was set in order to remove the organic solvent completely prior to crystallization. This procedure was carried out under the consideration of large mass reduction of the sol around this temperature (point B in TG curve). The samples were then furnace cooled to the ambient temperature. The powders were scraped off the crucible and ground into finer particles, and then investigated using an XRD diffractometer that was described in **Chapter 3**, using Cu Kα radiation.

4.3.2 Phase evolution of PZT

Figure 4.2 shows the XRD traces of the sol heated to different temperatures and held

at those temperatures for 3600s. The peaks in the curve reflect the close-packed layers in the perovskite structure, which are indicated by the Miller index (*h, k, l*). As shown in the graph, the material started to crystallize at 600°C, where the proper peaks according to the perovskite structure could be observed. From 650°C to 800°C, the pyrochlore phase is observed and becomes obvious over 750°C. It is believed that the over high sintering temperature facilitates the loss of lead, which may be the reason for the formation of pyrochlore phase. As the temperature increases, the (002/200) and (001/100) peaks begin to split, indicating that the tetragonal structure becomes prominent when the sintering temperature is higher (Zahi *et al.* 2003). Considering these matters, 650°C was selected as the heating temperature for PZT material. This temperature was also used as the sintering temperature for the reminder of the experiments (e.g. nanostructured PZT deposition on copper substrate) and other heat treatment processes discussed in **Chapter 5** and **6**.

4.3.3 Effect of heating duration

Although PZT material can be obtained after heat treatment at 650°C, there is still a slight amount of pyrochlore observed. It is assumed that 3600s holding duration is too long which may induce more lead loss, resulting in the formation of pyrochlore phase. In order to investigate the effect of holding duration, the PZT sol was heat treated at 650°C for less holding duration of 0s and 1200s. The samples were then analyzed by XRD which is similar to the previous experiment. The XRD result for these two samples is shown in **Figure 4.3**. The patterns indicate that the pyrochlore phase is prevalent in the sample sintered at 650°C without holding. When the sintering time is

increased, the pyrochlore phase decreases and the perovskite phase becomes more prominent. At 1200s it is evident that a larger proportion of the desired perovskite phase is present with a small amount of the pyrochlore phase. Compared with the result in **Figure 4.2** in which the samples were heated for 3600s, it is shown that for longer holding duration the pyrochlore phase starts to become more noticeable again as more lead is lost from the PZT structure. For that reason, holding duration of 1200s was used for the heat treatment process.

4.4 Electrohydrodynamic atomization of PZT sol

After investigation of PZT sol properties, the solution was utilized for the electrohydrodynamic atomization process. As mentioned in the previous chapters, electrohydrodynamic atomization in the cone-jet mode can be used to generate fine and homogeneous atomized relics. The effect of configuration and parameters of this process on different spray mode is analyzed and the ideal process parameters for the cone jet mode are discussed in this section

4.4.1 Electrospray configuration

The equipment used for electrohydrodynamic atomization was described in **Chapter 3**. In order to produce PZT relics from 0.6M PZT sol, the 330/640 μm (inner/outer) diameter needle that was held in epoxy resin was used. A ring-shaped ground electrode was used and placed 10mm below the needle exit. The functions of the ring-shaped ground electrode are first, to build up an electrical field between the

needle and ring for electrohydrodynamic atomization of PZT sol; second, to let the atomized relics pass through the ring and deposit on the glass slide that was placed right under the ring electrode.

4.4.2 Characteristics of cone and jet

Figure 4.4 shows the cone-jet mode in electrohydrodynamic atomization of 0.6M PZT sol. The important parameters set during the spraying to achieve this mode are given in **Table 4.2**.

Table 4.2 *Parameters to obtain the cone-jet mode*

Inner diameter of needle (μm)	Distance between needle and ground electrode(mm)	Applied voltage (kV)	Flow rate ($m^3 s^{-1}$)
330	10	4.4	1×10^{-10}

As shown in **Figure 4.4**, during spraying the cone-jet mode can be evidently observed. The liquid was ejected out of the needle and formed a cone near the exit under the balanced force of electrical field, gravity and surface tension etc. The cone then became a long and narrow jet followed by breaking up into droplets. The atomized relics have momentum moving towards the ground electrode so that the carried charges can be released. The big arrow in **Figure 4.4** indicates the position where the jet broke up into small relics. The diameters of the cone and jet in this mode were measured using image processing software (Image Pro-Express), which was calibrated using a standard image of known dimensions. The accuracy of measurement was limited by the maximum pixel of the images (1280×1024 pixels).

The approximate values of the cone depth, jet length and jet diameter are given in **Table 4.3**, where the cone depth is defined as the distance between the exit of the needle and the apex of the cone and the jet length is defined as the distance between the apex of the cone and the point where the jet breaks up.

Table 4.3 *Diameters of the cone and jet in the stable cone-jet mode*

Cone depth (μm)	Jet length (μm)	Jet diameter (μm)
~470	~50	~2

4.4.3 Droplet relics

The droplets/relics atomized from the cone-jet mode mentioned above were manually collected on a plain microscope glass substrate (75mm in length, 25mm in width and 1mm in thickness, provided by VWR, Lutterworth, UK). The glass slide was placed right under the ring electrode and fraction of the relics was deposited on it with the left attracted on the ring electrode. The droplets/relics were examined by optical microscope immediately after being collected on the glass slide, which is shown in **Figure 4.5**, in which the middle part of the deposit is focused. It is apparent that a near monodisperse droplet/relic size distribution was obtained, with an average diameter of approximately 1μm. This result well proves that the droplets achieved in cone-jet mode in electrohydrodynamic atomization are fine in scale, monodisperse in size distribution and homogeneous. Therefore, it is believed that electrohydrodynamic atomization in the stable cone-jet mode is suitable to deposit ceramic layers using PZT sol precursor, which is discussed in the later chapters.

4.4.4 Mode selection map and the effect of applied voltage and flow rate

Besides the stable cone-jet mode, there are some other modes in electrohydrodynamic atomization such as dripping, micro-dripping, unstable cone-jet and multi-jet mode, which is determined by the important parameters, i.e. applied voltage, flow rate and needle-substrate distance. In order to investigate the effects of these parameters, a map of the stable cone-jet mode for 0.6M PZT sol was constructed, which is shown in **Figure 4.6**. When constructing the map, the needle size and distance between the needle and substrate was selected as the ones of the work in the previous section and the ring electrode was placed by a solid metallic plate which was connected to the ground. The flow rate was varied between 5×10^{-12} m^3 s^{-1} and 1.2×10^{-10} m^3 s^{-1} and the applied voltage was adjusted to achieve the stable cone-jet mode.

As shown in the graph, the stable cone-jet mode can only be achieved when the flow rate and the applied voltage are in a distinctive regime. Otherwise, other modes such as unstable cone-jet mode or multi-jet mode are observed. The regime is closed at a critical flow rate point, above which the stable cone-jet mode is not obtainable. The other end of the regime (flow rate < 5×10^{-12} m^3 s^{-1}), which is displayed as a gray zone in **Figure 4.6,** is not clearly constructed. It is because of the limited measuring range and accuracy of the pump.

When compared the values in **Table 4.2**, the two parameters are not in the stable cone-jet mode regime obtained in this section (the values in **Table 4.2** are displayed as

a circular point in **Figure 4.6**). The variation is reasonable because the previous values were obtained using a ring electrode and this cone-jet mode map was constructed by using a solid plate electrode. This result provides evidence that the geometry of the ground electrode affects the forming of the stable cone-jet mode and it also elucidates that the cone-jet mode map can only be validated when other parameters such as apparatus configuration and the distance between the needle and substrate are initially fixed.

At each particular flow rate within the regime, the presence of lower and upper limits of the applied voltage is evident, between which the cone-jet mode is achievable. When the flow rate reduced, the upper and lower applied voltage limits were also reduced. It implies that at low flow rate the cone-jet mode can be obtained under lower applied voltage. The reason can be explained as follows. When the flow rate is increased, the liquid mass flowing per unit time also increases, resulting in a higher force due to the fluid dynamics. This increased force has to be counter-balanced by a higher electric strength near the needle exit for the forming of the stable cone-jet mode. As a result, the applied voltage for obtaining the cone-jet mode increases with the increase of the flow rate.

When varying the applied voltage between the upper and lower limit at a particular flow rate in the stable cone-jet mode regime, the mode does not change. However, the geometry of the cone changes significantly when the applied voltage is varied. This was investigated by observing the cone-jet mode at a constant flow rate with different

applied voltages, which is shown in **Figure 4.7**. As the voltage increased, the dimension of the jet did not change considerably but the cone was found to turn shallower and the cone depth was found to become smaller. Although the cone geometry was changed by the varied applied voltage, it was still in the stable cone-jet mode. The approximate cone depth under each applied voltage was measured by the same procedure in section 4.4.2 and is given in **Table 4.4**.

Table 4.4 *Cone depth of 0.6M PZT sol under different applied voltage*

Applied voltage (kV)	4.2	4.5	4.8	5.1
Cone depth (μm)	407	388	311	232

4.5 Generation of nano-structured PZT on metallic substrates

As proved above, electrohydrodynamic atomization is applicable to 0.6M PZT sol and the stable cone-jet mode is achievable under certain applied voltage and flow rate. In this part, copper discs were used as substrates to collect the PZT deposit sprayed in the stable cone-jet mode. Using the investigated sintering temperature, the deposit on the metal substrate was heat treated and nano-structured PZT was generated. Studies on this structure are also discussed in this section.

4.5.1 Spray-deposition process parameters

The configuration of the equipment used for collecting the sprayed PZT samples on the substrate is similar to that used in the previous section with the exception that the ring ground electrode was placed by a copper disk which was connected to the ground

potential. The reason for using the copper disk rather than the ring is that: firstly, when using the ring electrode, highly charged particles due to higher electrical conductivity of 0.6M sol are attracted to the ring electrode in a large portion without passing through it and depositing on the substrate; secondly, the highly conductive metal disk can be used as ground electrode by which a stable electrical field can be generated between the needle and substrate, which is profitable for the stable cone-jet mode formation.

Copper substrates in both circular and square geometries were used in order to investigate their effect on the deposit geometry. The distance between the needle and substrate was approximately 10 mm and the flow rate and the applied voltage used for deposition were 5×10^{-11} m^3 s^{-1} and 4.1 kV, respectively. For each sample, the spray-deposition was carried out for 900s. Subsequently, the substrate with the deposit were placed in the furnace and heated at 650°C, which followed the same temperature profile used in the work of the sol sample (see section 4.3).

4.5.2 Geometry of the PZT deposit

Following removal of the ring electrode, the droplets from 0.6M PZT sol were successfully deposited onto a copper substrate connected to earth without scattering to the vicinity. **Figure 4.8** shows the PZT deposit on copper substrate after heating at 650°C. The deposit adhered well on the copper substrate and was in a circular pattern. Varying the shape of the substrate from circular (**Figure 4.8a**) to square (**Figure 4.8b**) did not affect the geometry of the deposit of which the area was constant. It is

believed that the circular shape of the deposits shown in **Figure 4.8** is determined by the conical shape of the spray cone which is defined schematically in **Figure 4.9**. As shown in the graph, α is the angle of spray cone and H is the distance between the needle exit and substrate. Using simple geometric analysis, Chen *et al.* (1999a) have shown that the coverage area (A) is related to α and H by the equation:

$$A = \pi\left[H \tan\left(\frac{\alpha}{2}\right)\right]^2 \qquad \textit{Equation 4.1}$$

For this work H = 10 mm and the deposit area (A) is approximately 113 mm^2, the spray angle is calculated as 62°. It has also been reported that the angle of spray cone is a function of flow rate and it is different from the angle at the cone tip (indicated by β in **Figure 4.9**) which is approximately 80° in this experiment.

4.5.3 Characterization of the PZT deposit

4.5.3.1 Surface morphology

When observed, some uneven cracking is evident on the deposit surface. This observation may be caused by the differential thermal expansion behaviour of the PZT layer and substrate. This cracking is also present on samples that have not undergone any heat treatment, suggesting that the evaporation of the solvent from the PZT sol at room temperature may also have an effect. Cracking is not acceptable when producing PZT films for capacitor application since the top and bottom electrodes will be conductive when coated on the PZT films. An alternative route, which is a repeat process with a reduced spray time followed by a drying procedure, can be utilized to eliminate cracking. This modified spray process was successfully applied to deposit PZT on Pt/Ti/Si substrate and a continuous layer was obtained. Details will be

discussed in **Chapter 5**.

4.5.3.2 Microstructure

In order to investigate the microstructure of the sprayed PZT, the surface of the heat-treated deposit on the copper substrate was sputter coated with gold and studied using SEM (**Chapter 3**). The unsintered sample was left uncoated and observed in the environmental SEM which was also described in **Chapter 3**.

Figure 4.10 shows the microstructure of the PZT layer deposited on the copper substrate as analyzed using the microscopes. Comparing the unsintered PZT layer with the one sintered at 650°C, the two structures show uniform PZT nano-particles of approximately 100 nm in size. These spherical nano-particles are not seen in thin films deposited using a spin-coating method in other works and therefore can be considered to be characteristic of electrohydrodynamic atomization deposition. In order to analyze these particles, the ceramic powders deposited by electrohydrodynamic atomization were scraped off before and after they have been heat treated and then ball-milled to obtain the particles. The size of these particles was analyzed and the values are shown in **Table 4.5**.

Table 4.5 *Particle sizes of sintered and unsintered PZT deposited using electrohydrodynamic atomization*

Unsintered particle size (nm)	Standard deviation (nm)	Sintered particle size (nm)	Standard deviation (nm)
2618	158	701	17

It is clear that both the unsintered and sintered particle sizes are greater than the one suggested by the micrographs. It suggests that a degree of agglomeration remains even after ball-milling. The larger sizes observed in the unsintered system compared to the sintered system are probably a result of the softer agglomerates, which are not as easily broken up by ball-milling. The primary particle size is hardly observed in sintered systems following ball-milling due to the fusion of the nano-particles. Indeed, the PZT nano-particles in the sintered material do appear to have fused together forming larger particles, this may be the reason of great difference between the two values.

4.5.3.3 Phase detection of heat-treated PZT deposit

Figure 4.11 shows the XRD pattern of the deposited PZT on copper substrate after heating to 650°C. Apart from the peaks for the substrate (indicating as S in the graph), the main phases were perovskite PZT, although there was still a peak for pyrochlore present in the result. The pyrochlore phase is known to disappear when the PZT film is heated to the correct temperature for the correct period of time. However, if the optimum time at the sintering temperature is exceeded, the lead lost from the PZT will cause the pyrochlore phase to reform (Chen & Chen 1998), therefore the holding time needs to be reduced to 1200s for the subsequent experiments in order to reduce the content of pyrochlore phase. Additionally, it is deemed that the spherical particles obtained using the electrohydrodynamic atomization method have a large surface area and this may increase the amount of lead loss from the material, which would also promote pyrochlore phase reformation.

4.6 Summary

The work described in this chapter has led to two specific contributions with respect to the electrohydrodynamic atomization technique. Firstly, the properties of 0.6M PZT sol were studied and the yield of the sol and the ideal sintering temperature were obtained. Secondly, the electrohydrodynamic atomization was successfully utilized to spray and deposit 0.6M PZT sol on copper substrate. The affect of applied voltage, flow rate and distance between the needle and substrate on the geometric change of cone and jet were examined and the mode selection map was constructed considering these analyses. The deposited PZT on copper substrate followed by heat treatment at 650°C was investigated in terms of deposit geometry, surface morphology, microstructure and phase formation. Scanning electron microscopy shows that discrete nano-particles are formed during the electrohydrodynamic atomization. These spherical nano-particles are approximately 100 nm in diameter and believed to be characteristic of electrohydrodynamic atomization deposition. However, the XRD pattern of the heat-treated PZT specimen shows both pyrochlore and perovskite structures are present. The heating duration should be reduced in order to eliminate pyrochlore. Based on these findings, the electrohydrodynamic deposition technique can be established for forming the columnar PZT structures and continuous PZT films using different concentration precursors, which is essentially introduced in the next chapter. The copper substrates are replaced by semiconductor silicon wafers on which the generated PZT structures can be used for necessary electrical applications.

Figures

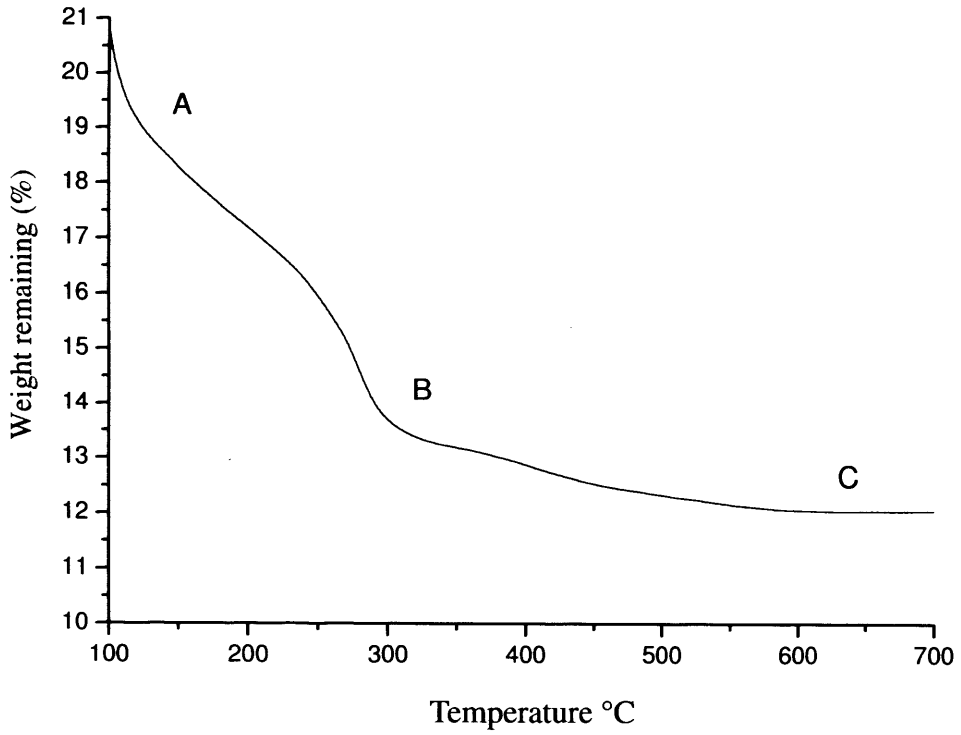

Figure 4.1 Thermogravimetric trace of propanol-based 0.6M PZT sol showing the percentage of initial mass remaining. The majority of the propanol and acetic acid solvents are removed by 150°C (A), but organic matter still remains until (B), the final PZT yield is achieved at 650°C (C).

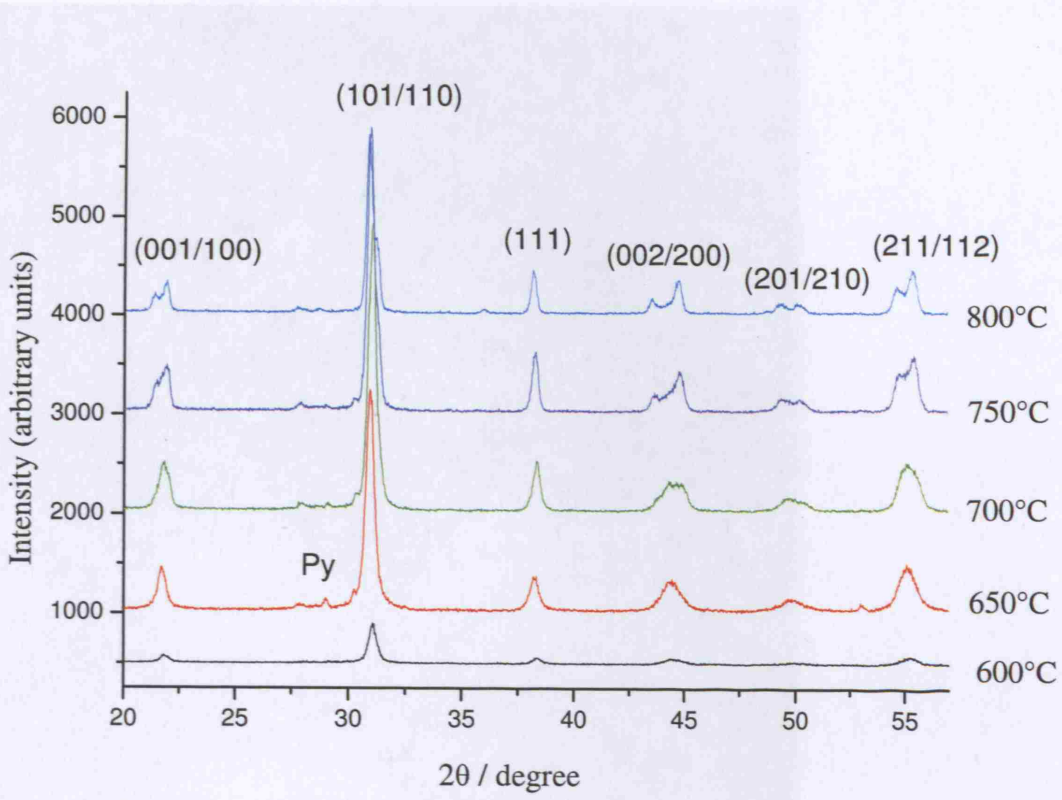

Figure 4.2 X-ray diffraction patterns of PZT material obtained from the sol heated to 600°C, 650°C, 700°C, 750°C and 800°C for 3600 s. *h k l* index for perovskite phase was manifested. The pyrochlore phase is represented by Py.

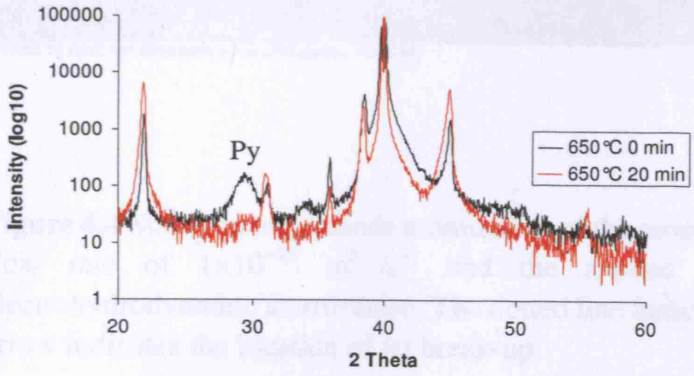

Figure 4.3 XRD patterns of propanol-based 0.6 M PZT sol heat-treated at 650°C for 0s and 1200s. Besides the main peaks of perovskite phase, the pyrochlore (Py) phase is indicated.

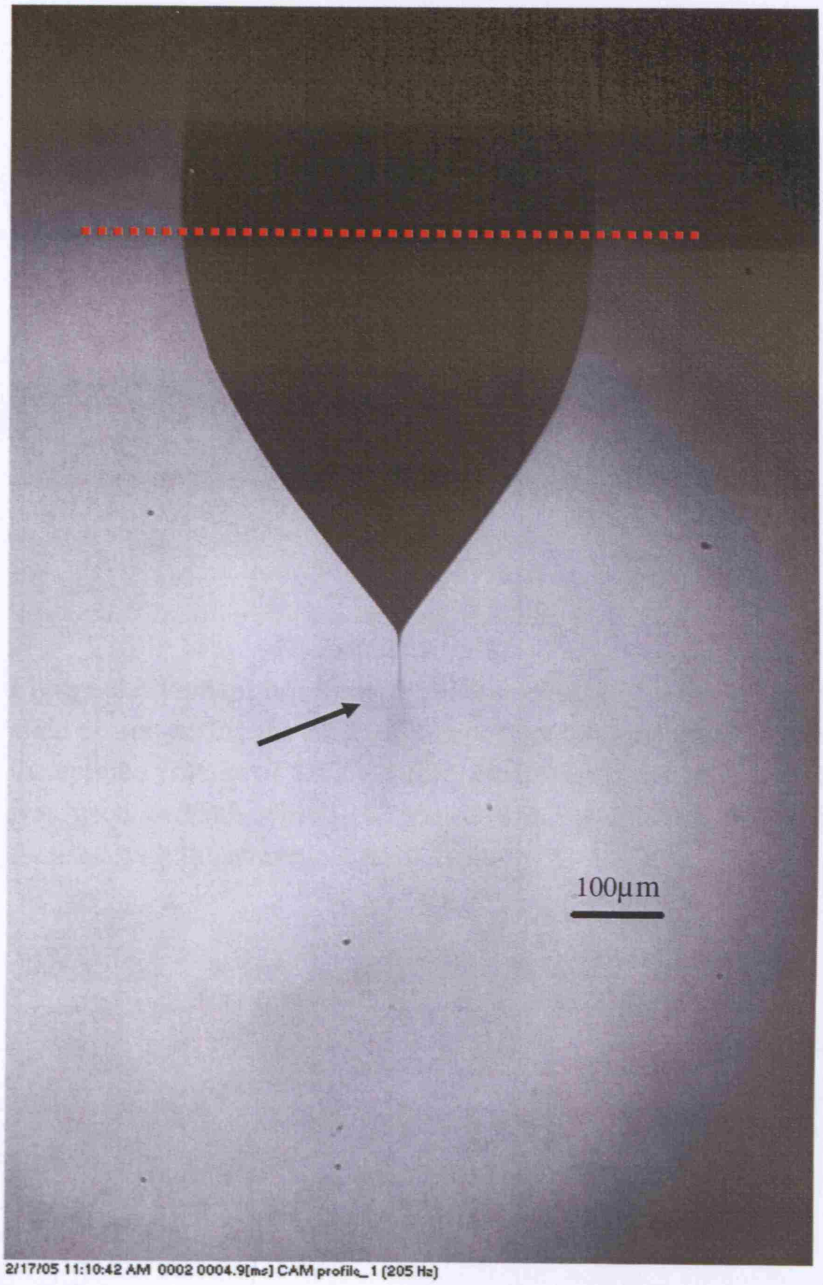

Figure 4.4 Stable cone-jet mode atomization of the propanol-based 0.6M PZT sol at the flow rate of 1×10^{-10} m^3 s^{-1} and the applied voltage of 4.4 kV during electrohydrodynamic atomization. The dotted line indicates the needle exit and the big arrow indicates the location of jet break-up.

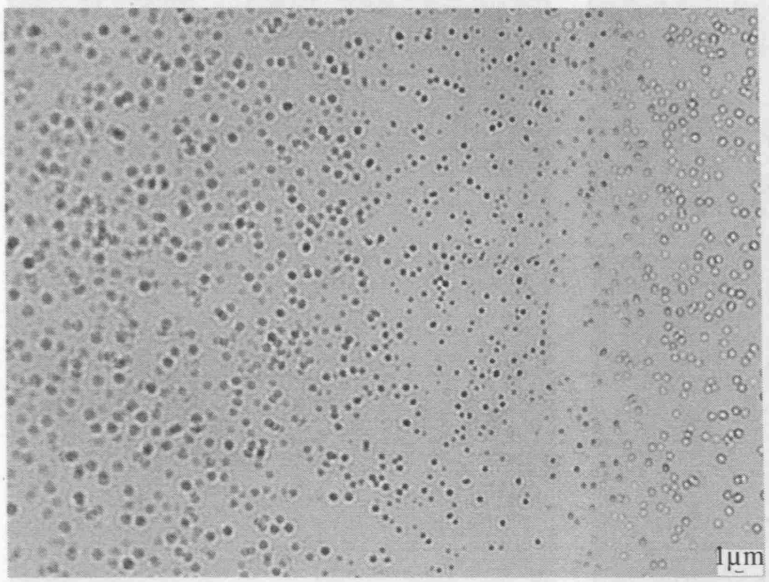

Figure 4.5 Optical micrographic observations of relics of droplets collected on glass slide on subjecting the PZT sol to cone-jet mode at the flow rate of 1×10^{-10} m^3 s^{-1} and the applied voltage of 4.4 kV during electrohydrodynamic atomization. A ring electrode was used beneath which the glass slide was placed. The relics in the center were focused with the average size of 1μm.

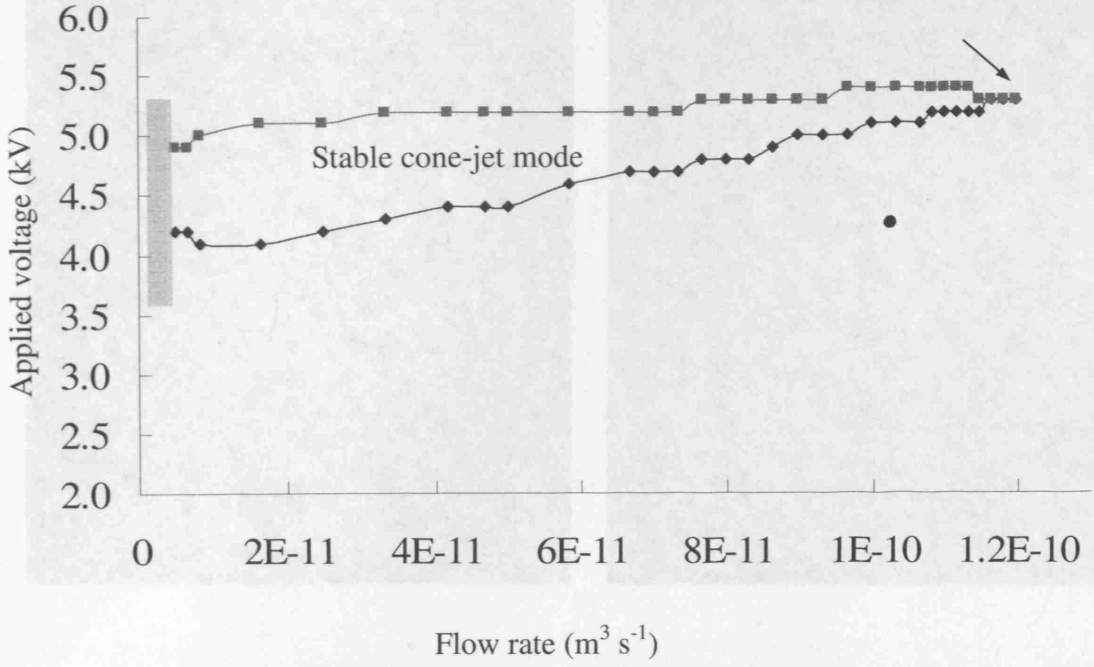

Figure 4.6 Map of the stable cone-jet mode during electrohydrodynamic atomization of 0.6M PZT sol. The arrow indicates the critical point above which the cone-jet mode is not obtainable. The gray bar illustrates the unknown mode zone due to the device limits. The values obtained in **Table 4.2** (indicated by a circular point) are out of this stable cone-jet regime, which is due to the different configuration of the ground electrodes.

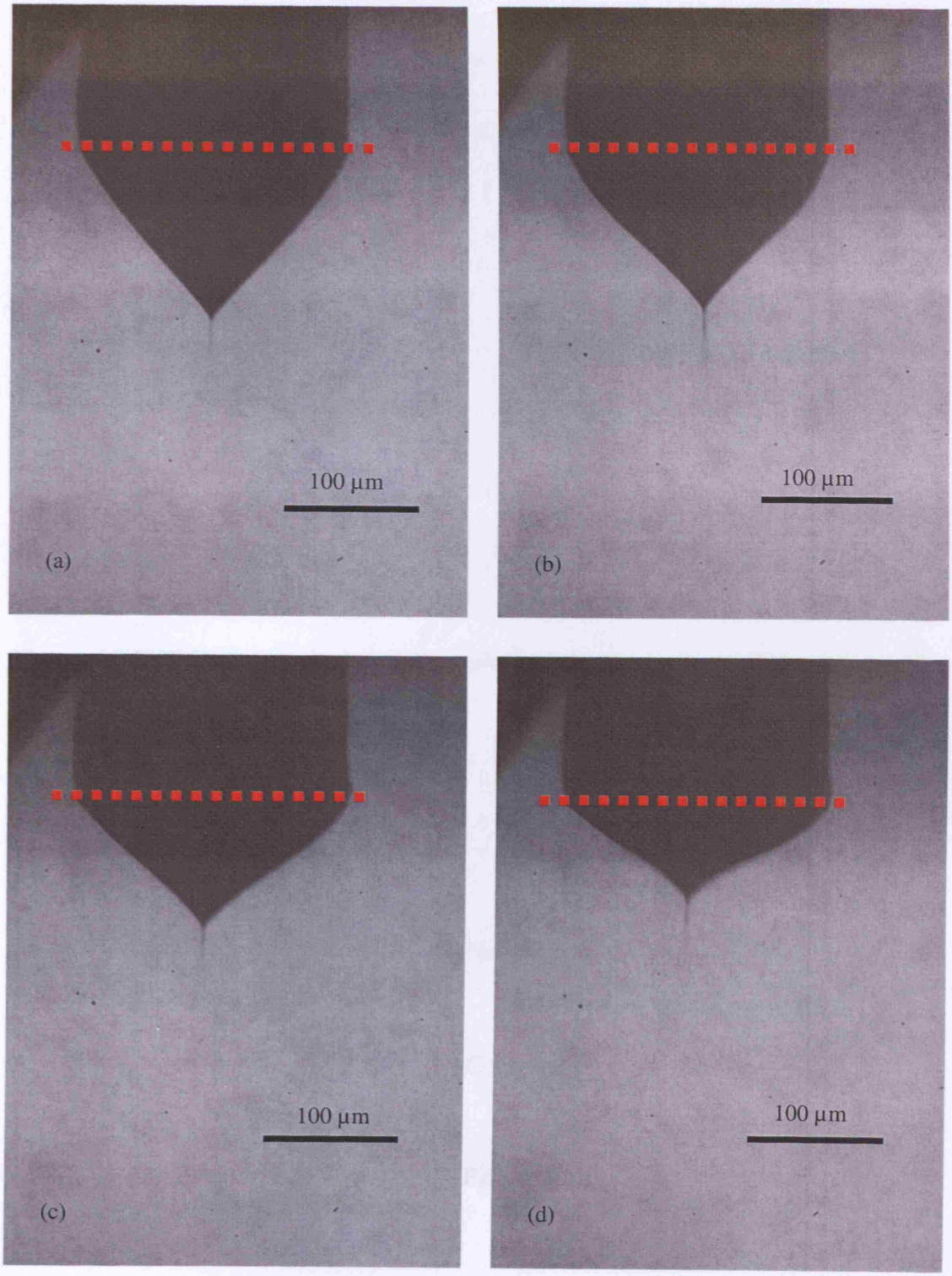

Figure 4.7 Stable cone-jet mode of 0.6M PZT sol at a constant flow rate of 5.0×10^{-11} m^3 s^{-1} and the applied voltages of **(a)** 4.2 kV, **(b)** 4.5 kV, **(c)** 4.8 kV and **(d)** 5.1kV. The dotted line indicates the needle exit where the liquid was deformed to be a cone.

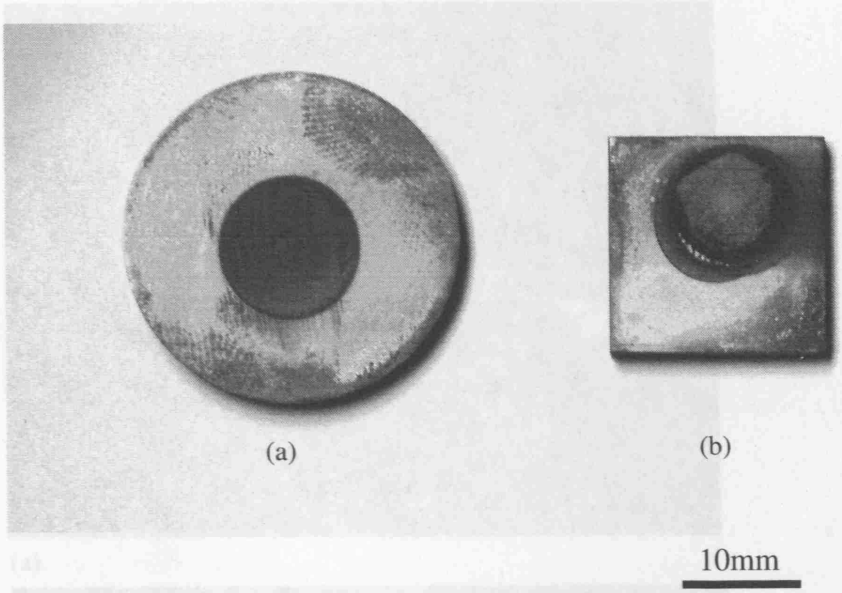

Figure 4.8 PZT films deposited on **(a)** circular and **(b)** square copper disks showing the size and shape of the deposit obtained.

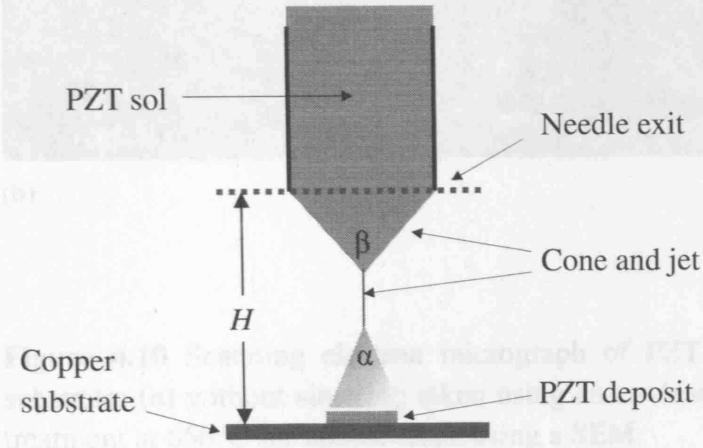

Figure 4.9 Schematic presentation illustrating the relevant processing parameters during electrohydrodynamic atomization deposition. α is the angle of spray cone, β is the angle at the cone tip and *H* is the distance between the needle exit and substrate.

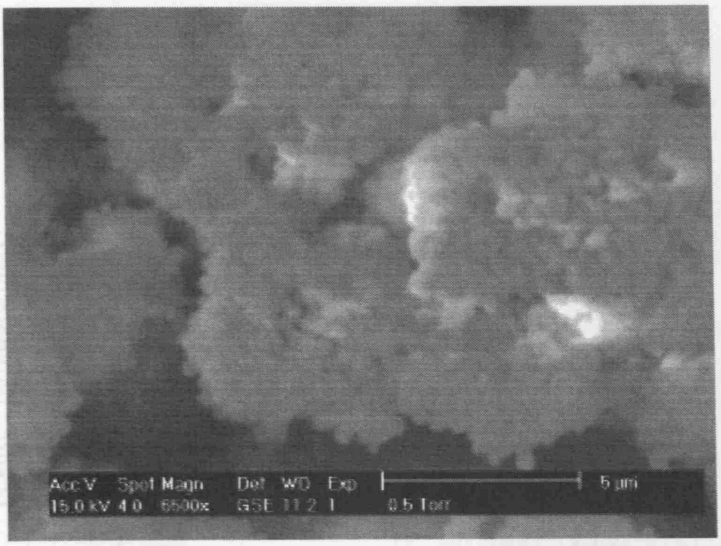

(a)

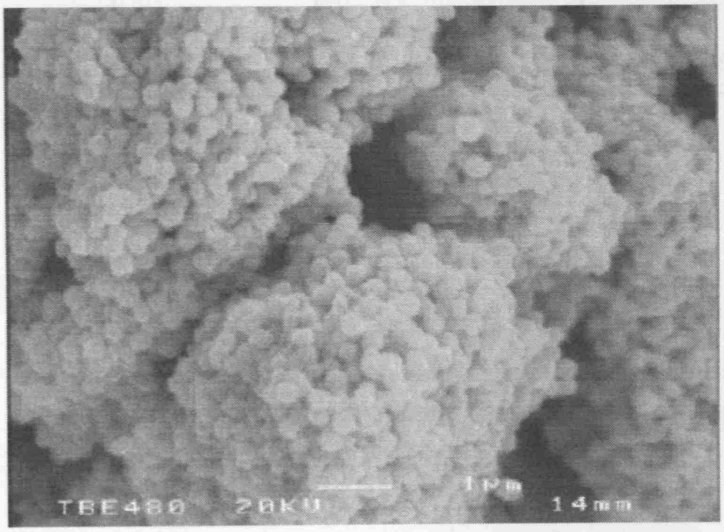

(b)

Figure 4.10 Scanning electron micrograph of PZT material deposited on copper substrate: **(a)** without sintering taken using an environmental SEM and **(b)** after heat treatment at 650°C for 3600s, taken using a SEM.

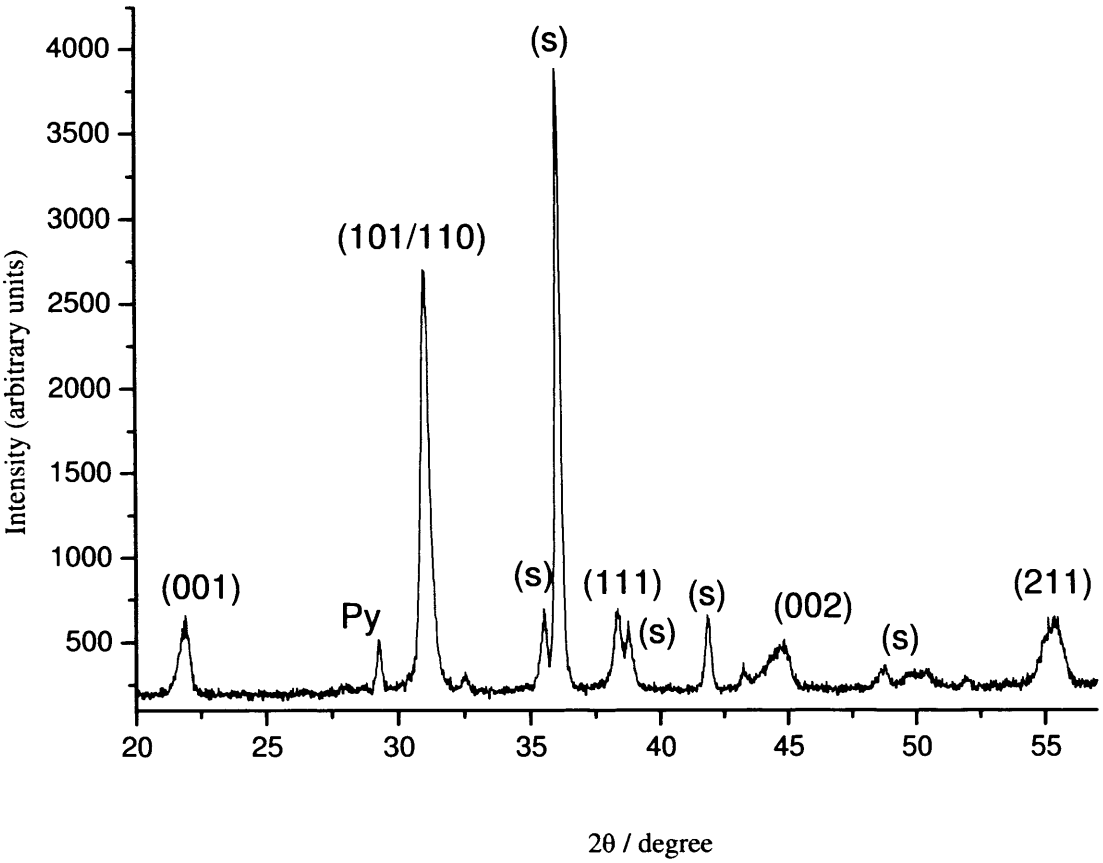

Figure 4.11 X-ray diffraction pattern of the deposited PZT on copper substrate after heating to 650°C. The pyrochlore phase is indicated by Py and the copper substrate peaks were marked as S.

CHAPTER 5 Novel Forming of Columnar PZT Structures and Continuous PZT Films

5.1 Background

In **Chapter 4**, it has been shown that it was successful to spray 0.6M PZT sol by electrohydrodynamic atomization in cone-jet mode and nano-structured PZT was generated on copper substrates, which implies that it is practical to combine sol gel solution preparation method (Schwartz 1997) with the electrohydrodynamic atomisation process to deposit ceramic layers. This derived process, namely electrohydrodynamic deposition, which can be used to generate PZT materials in columnar structures and continuous films, is investigated in this chapter.

There are several stages which can be defined during the electrohydrodynamic deposition process, and these are also discussed in this chapter. The sprayed droplets may undergo certain changes during each stage and these determine the configuration of the final deposited structure on the substrate. In this work, it has been revealed that during electrohydrodynamic deposition the concentration of the sprayed sol has a considerable effect on the configuration of the deposited structures: an agglomerated columnar structure can be generated using a high concentration sol while a continuous film can be obtained when a low concentration sol is used. The reason for this has been realized as the different droplet size obtained from different concentration sols and their evaporation during the transportation stage. Details of these factors will be discussed in this chapter.

It is well known that when using PZT materials, both the columnar structures and the continuous films are of high interest for various electrical applications. A continuous thin/thick PZT film has a wide range of applications in non-volatile random access memories for computers (Kim & Lee 2006), piezoelectric micro-sensors (Muralt 2000a; Park *et al.* 2005) and integrated circuit capacitors (Asano *et al.* 2003; Dimos & Mueller 1998) whilst a columnar PZT structures is incredibly useful when fabricated as 1-3 composites which are commonly used in sonar (Marin-Franch *et al.* 2004; Ting 1992), medical imaging technologies (Benjamin 2002) and non-destructive testing (Tseng *et al.* 2003) applications. Although there are various forming methods to process such structures in both micro and macro scales, it is believed that electrohydrodynamic deposition is suitable to form both columnar PZT structures and continuous PZT films when a proper concentration sol is used.

In this chapter, details of electrohydrodynamic deposition are described and the effect of the sol concentration on the as-deposited structures is also discussed by means of analysing the 0.01, 0.03, 0.06, 0.12, 0.3 and 0.6M sol during the spray-deposition. 0.6M and 0.06M sol are concluded as the ideal solutions for the formation of columnar PZT structures and continuous films, respectively.

When columnar PZT structures were formed, the evolution of the column was analysed by observing the cross-section of the samples deposited at different time intervals. The effect of the substrate temperature on the columnar structure was also analysed by studying the area density of the columns. Finally, a 1-3 composite was

produced by infiltrating photoresists into the columnar structures and the relative permittivity and dissipation factor of such structures were measured and discussed.

When continuous PZT films were formed, both the microstructure and phase evolution of the sample were analyzed. Dielectric properties of such film on various frequencies were analysed. The relative permittivity and dissipation factor of the sample at a particular frequency was obtained and compared with the values of columnar PZT structures. The difference in relation to the microstructure and phase presenting were compared and discussed.

During electrohydrodynamic deposition, the findings in **Chapter 4**, such as the configuration of the device set-up, the sprayed parameters according to the constructed mode selection map and the details of heat treatment for the deposited PZT, are compatible for the formation of columnar PZT structures and continuous PZT films. A detailed description of these investigations for both structures will be given in the following sections.

5.2 Electrohydrodynamic deposition process

5.2.1 Method description

The device configuration of electrohydrodynamic deposition is comparable with the one used for electrohydrodynamic atomization except for the design of the substrate/ground electrode. **Figure 5.1** is the schematic diagram showing the equipment configuration of this technique. As shown here, the precursor is syringed

out with a pump and passes through a needle that is at a high electric potential relative to the substrate. The liquid near the needle forms a stable cone under certain flow rate and applied electric field condition, which can be referred from the mode selection map constructed in **Chapter 4**. The cone-shaped liquid deforms to an elongated jet and consequently breaks-up into droplets. Different from the work in **Chapter 4**, Ti/Pt coated silicon wafer was used as the substrate to collect the deposit. A metal frame which can be altered in the z axis was used as the substrate holder and connected to the ground potential as observed in **Figure 5.1**. The same needle used in **Chapter 4** (330/640μm) was selected and the spraying parameters are given in **Table 5.1**.

Table 5.1 *Spraying parameters for PZT sol deposition*

Applied voltage	Flow rate	Needle/substrate distance
4.2 kV	2.5×10^{-11} m^3s^{-1}	10 mm

5.2.2 Main stages of electrohydrodynamic deposition

In the electrohydrodynamic deposition process, the stable cone-jet mode is expected in order to generate homogeneous droplets. The process can be defined as four different stages before the entire deposition is completed: droplet generation after jet break-up; transportation through the environment; impact and spreading on the substrate; drying and decomposition (indicated as i to iv in the enlarged image in **Figure 5.1**). Amongst those stages, droplet transportation and spreading on the substrate plays an important role in the evolution of as-deposited structures (Huang *et al.* 2004; Neagu *et al.* 2005). During droplet transportation, evaporation occurs and

this determines the solvent content in the droplets (Neagu *et al.* 2006; Wilhelm *et al.* 2003) when they arrive at the substrate, thus controlling the wetting and spreading of the droplets on the surface: particles in solvent are able to form continuous layers easily (Ferrari *et al.* 2006) whereas solvent-depleted particles tend to form a 'powdery' deposit and are exceedingly agglomerated due to their lower mobility. These agglomerations grow with the deposition time, implemented by stacking of dry particles and ultimately a number of discrete columns can be formed. In this part of work, it has been revealed that the concentration of the precursor closely relates to this feature during the process, which is believed to be a dominating factor determining the configuration of the as-deposited structure. According to this, it is believed that the electrohydrodynamic deposition technique can be utilised for generating both columnar structures and continuous films using different-concentration precursors.

5.2.3 Effect of sol concentration

In order to investigate how the concentration of the sprayed sol influences the as-deposited structures, 0.6M PZT sol was diluted using acetic acid/1-propanol solvent (introduced in **Chapter 3**) and solutions of six concentrations were obtained which is given in **Table 5.2**. The electrical conductivity of different sols was measured using a conductivity probe (introduced in **Chapter 3**), which was calibrated using standard ethanol. Samples were electrohydrodynamic deposited for 60s and then dried on a hot plate for 120s at 200°C. The as-deposited structures on the Ti/Pt coated silicon substrate were studied using scanning electron microscope.

Table 5.2 PZT sol gel solutions of different concentration

Sample ID	C1	C2	C3	C4	C5	C6
Concentration (M)	0.01	0.03	0.06	0.12	0.3	0.6

Figure 5.2 demonstrates heterogeneities in the as-deposited PZT films as the concentration of the sol gel solution is increased. There are two different kinds of structures evident as can be observed in the micrographs. For low concentration samples (C1, C2 and C3) it is clear that the deposited film is a continuous, non-agglomerated layer, while for high concentrations (C4, C5 and C6) highly agglomerated structures were observed. These observations were not obtained when spin coating or dip coating process was used and this feature is expected as characteristic of electrohydrodynamic deposition. The reason for such a characteristic feature can be explained in terms of the different droplet size produced from different concentration sols and their evaporations during the process.

It has been reported that the diameter d of the droplets produced by electrohydrodynamic deposition is related to the fluid and processing parameters as shown in *Equation 5.1*.

$$d \propto \varepsilon_r^{1/6} \cdot \left(\frac{Q}{\kappa}\right)^{1/3} \qquad \textit{Equation 5.1}$$

where ε_r is the relative permittivity of the solution, Q is the flow rate and κ is the electrical conductivity (Ganan-Calvo 1994). As evident in the equation, there are three parameters determining the droplet size, amongst which the flow rate and the relative permittivity can be considered as constants in our experiment when the

concentration of the PZT sol is changed. Flow rate (Q) is controlled by the pumping rate and was set as a constant value for the entire process. The relative permittivity of the solution (ε_r) could also be assumed as a constant for the following reasons.

Firstly, the dielectric property of the PZT sol is based on the atomic, electronic and dipolar polarization, within which the dipolar polarization is the dominating factor. In the PZT sol, the dipolar polarization in the Pb^{2+}–Ti^{4+}–Zr^{4+}–O^{2-} system is rather insignificant when compared with that in the 1-proponal solvent (H–O in C_3H_6OH). Secondly, it can be calculated that even in the 0.6M PZT sol, the volume of the metal-organic molecules is still 20 times less than that of the solvent molecules. Therefore, when the concentration of the solution is changed, the change in the relative permittivity contribution of the metal-organic molecules is insignificant and can be neglected. Thus according to *Equation 5.1*, the diameter of the droplets in our experiments can be considered as inversely proportional to the cubed root of the precursor conductivity. The electrical conductivities of the precursors with different concentrations were measured using the conductivity probe and their changing relationships are shown in **Table 5.3.**

Table 5.3 *Variation in conductivities of the precursors as a function of concentration*

Sample ID	C1	C2	C3	C4	C5	C6
Conductivity (μS/cm)	8.3±0.2	11.8±0.2	16.8±0.2	27.8±0.2	36.6±0.2	44.4±0.2

The values in **Table 5.3** demonstrate that the electrical conductivity increased when

the concentration of the PZT sol increased. Considering the inversely proportional relationship of the conductivity with the droplet diameter, the diameter of the sprayed droplets is then expected also to be inversely proportional to the cubed root of the concentration of the PZT solution.

Based on this finding, the feature in **Figure 5.2** can be explained as follows. During electrohydrodynamic deposition, the droplet transportation is a dominating factor due to the occurrence of solvent evaporation during this stage and the content of which determines whether the particles are dry or wet when they impact on the substrate. When large droplets, which are produced from low concentration sol, are transported between the nozzle and the substrate, evaporation will be less because of the large amount of solvents contained within the droplets and small volume specific surface area (surface area/volume), which will help to maintain the droplets in a viscous liquid state. Conversely, when small droplets, which are produced from high concentration sol, are transported, they will promptly dry to become solid particles/agglomerates after evaporation of the solvent which is in smaller amount when compared with that of low concentration sol. The wet relics have a high mobility and can easily spread on the surface, forming an interconnected three-dimensional structure which is necessary for continuous film formation. On the contrary, the dry solid particles cannot move when they are deposited on the surface, leaving only agglomeration and accumulation. As a result, the configuration of the as-deposit structures varies when the concentration of the sprayed sol is changed.

The relative diameter of the droplets produced from the sprayed PZT precursors with different concentrations can be deduced from *Equation 5.1* and their relationship is shown in **Figure 5.3**. It exhibits a trend where the diameter decreases rapidly as the concentration is increased up to 0.1M. Above 0.1M it shows a nearly flat curve up to 0.6M without appreciable change in the relative droplet diameter. According to this, any transition zone between continuous film and agglomerated columnar structure would be most likely expected to exist around in the zone of rapid size change (e.g. 0.1M). To the left of this demarcation (low concentration), a continuous film may be obtained while to the right of it (high concentration), a columnar structure can be obtained. This expectation correlates well with the observation of the heterogeneous structures shown in **Figure 5.2**.

As observed in **Figure 5.2** C3, the 0.06M precursor was sprayed as a continuous, non-agglomerated layer. In C4, when the concentration increased to 0.12M, the structure seems to comprise a continuous layer in which some agglomerated particles are trapped. It is believed that this structure is the transitional structure between continuous films and agglomerated columnar structures, in that layers are still three-dimensionally interconnected but the agglomerate particles could also be detected. Dramatically different from the previous ones, a columnar structure can be observed in C5 and C6. At high concentrations (above 0.3M), the droplets produced are so small that a large amount of the solvent is evaporated, forming a high concentration of low mobility particles when they arrive at the surface. The dried particles easily agglomerate and form a discrete columnar structure. In addition, the

whole procedure occurs in a high electrical field in which the particles are charged. The charged particles have a tendency to travel along the electric field and are therefore attracted more towards the curved/protruding areas, which will lead to preferential landing sites (Chen *et al.* 1996b). Therefore, once the initial particles have been deposited to produce protrusions, subsequently arriving particles will be more likely to deposit on these agglomerated sections rather than on the smooth surface. As the deposition continues, the agglomerations grow higher and larger, further intensifying the preferred deposition, and thus the columns are obtained. There is not a significant difference between the structures in C5 and C6. The reason can be deduced from **Figure 5.3**. In the high concentration region, the relative droplet diameters are not considerably different, of which the ratio between C5 and C6 is calculated as 1.08. Therefore, the droplets are of comparable size and will behave similarly, so that the configurations of the columnar structures are nearly identical.

When the sol concentration is too low, the continuous film is interrupted and there are some holes present, with an average size of approximately 50nm, which are distributed across the whole layer and can be observed in **Figure 5.2** C1 and C2, with a higher hole-distribution in C1. It is speculated that when the concentration becomes too low, the ratio of solute and solvent will be too small, and each droplet will contain insufficient material to form a continuous film. Therefore, smaller amounts of PZT will be obtained compared with those of higher concentrations at a defined spraying time. Therefore, an upper and lower limit of sol concentration needs to be developed so that a continuous film can be generated using this process.

5.3 Forming of columnar PZT structures

Columnar PZT structures are of high interest as they are remarkably valuable for the fabrication of 1-3 composites. In this section, the details of processing such structures are introduced based on the theory of column generation from high concentration sprayed sol.

5.3.1 Process description

Amongst the examined sols in section 5.2.3, it is evident that 0.6 M PZT sol is ideal for processing columnar PZT structures. Therefore, sample C6 was used to be deposited on a Ti/Pt coated silicon wafer by means of electrohydrodynamic force and the process parameters were kept as before. The as-deposited columnar structures were heat treated at 650°C for 1200s with the heating rate of 5°C per minute and furnace cooling was used to let the samples return to the ambient temperature.

5.3.2 XRD pattern of the PZT columns

The X-ray diffraction pattern for the heat treated PZT columns is shown in **Figure 5.4**. As evident in the pattern, a perovskite PZT was obtained and the second phase pyrochlore, indicated by Py, is smaller in volume when compared with the XRD result of the heat treated PZT deposit on copper substrate (see Chapter 4.5.3). It has been reported that the Ti/Pt coated silicon wafer is beneficial for the formation of the perovskite structure and the elimination of the second phase pyrochlore structure

(Duval *et al.* 2003). It is because platinum electrodes are stable in the oxidizing atmospheres which are usually used to fire the films and they act to some extent to prevent interaction between the PZT and the underlying silicon. The Ti layer between Pt and silicon is used as an adhesion layer, which is necessary when platinum is coated on silicon wafers. Therefore, it is evident that heat treatment at 650°C for 1200s can be used for the sintering of dense columnar PZT structures. This heating temperature corresponds well with the result in the previous-chapter works (Rocks *et al.* 2007; Sun *et al.* 2005).

5.3.3 Growth evolution of the PZT columns

In order to investigate the growth mechanism of the columns, the deposited structures were obtained at different time intervals, which underwent an identical heat treatment at 650°C for 1200s. The list of examined samples is given in **Table 5.4**.

Table 5.4 *Deposition time of columnar PZT obtained using 0.6M sol*

Sample ID	T1	T2	T3	T4	T5	T6
Spray time	10s	20s	40s	60s	180s	330s

The cross-sectional structures of sample T1 to T6 was studied using scanning electron microscope and the results are shown in **Figure 5.5**. The inset images show the surface morphologies of the columns when viewed with a tilt of 45°.

In T1 relatively dry particles have landed on the substrate with a low distribution

density. After that, from 20s to 40s (T2 to T3), further particles arrive and deposit on the previously deposited particles and build up. It is evident that particles are not deposited in the spaces between columns, supporting the theorized growth mechanism given earlier (section 5.2). The area and height of the agglomerates increase slightly in this period although the area density of the columns is still small. When sprayed for 60s (T4), a more defined columnar structure is observed with the area and height of the columns increasing. After 180s of spraying, the area of the columns becomes stable and only the height of the columns increases with longer spraying times (T5). Finally, columns with a height of approximately 35μm were obtained after spraying for 330s (T6).

The observations in **Figure 5.5,** T1 to T6, correlate with the results in **Figure 5.2** sample C6 where the relatively dry particles obtained from the high concentration sol impacted on the substrate (deposited for 60s). The solid particles increase the roughness of the surface which will attract further particles that agglomerate on them under the electrical field, referring to preferential landing. Lengthening deposition time will favour the build up of larger and higher columns due to the same mechanism. Therefore the growth of columnar structure with increased deposition time is reasonable. The small increase in area section at the early stages is due to the slight widening of the features as the preferential landing can still occur at the edges of the columns as well as on their tops.

A deposition model for the columnar PZT structure growth is represented by the

schematic diagram shown in **Figure 5.6**, which encourages the growth mechanism of PZT columns. The dots represent the droplets and the pillar structures represent the PZT columns. Three stages are defined as: the initial stage (**Figure 5.6 a**), where the droplets (dry particles) land on the substrate; the growing stage (**Figure 5.6 b**), where the subsequently deposited particles are highly attracted to the initial ones so that the area and height of the columns increase; and the sustained stage (**Figure 5.6 c**), where the columnar structure is formed and the height of it increases with time.

Figure 5.7 shows the variation in the thickness of the structures as a function of time. It is illustrated that throughout deposition process the thickness increases gradually with time, although there is a higher scatter at 180s. The slope is small in the initial stage, in which the droplets are landing on the surface. In this stage, it is easy for the landing particles to be distributed rather than for agglomeration to occur. This means that cluster growth is more possible in the x-y plane and the thickness increases slowly. Once the initial layer is formed by the first batch of particles, the ones following are more likely to build on top of the former layer, which is the growing stage. In this stage, the layer also grows in the z direction by agglomeration and accumulation of dry particles. In the sustained stage, the area of the columns becomes stable and the height of the layer increases with deposition time. A columnar structure with the thickness of about 35μm was obtained after being deposition over 330s.

5.3.4 Effect of substrate temperature

In order to investigate how substrate temperature affects the columnar PZT structures,

a hot plate was placed directly under the substrate. The samples were deposited with the parameters similar to that used for T6 in the last section and the substrate temperature was varied from the ambient temperature to 75°C (H1), 125°C (H2), and 175°C (H3), respectively. The as-deposited samples were also heat treated at 650°C for 1200s with the heating rate of 5°C and furnace cooled to the ambient temperature before being studied using an optical microscope.

Figure 5.8 shows micrographs of the columnar PZT structure sprayed on the substrate at different temperatures. It is evident that different columnar structures were obtained with the increase in substrate temperature. At 75°C, the area density of the columns is small, leaving a large void area where the silicon substrate is exposed. At 125°C, the area density of the columns increases, leaving gaps between the columns. At 175°C, the structure becomes denser and some of the columns start to interconnect in the x-y plane. The area density of the columns obtained at different substrate temperature was studied using an image analyse software so that the PZT column and void area fractions can be obtained for each temperature, which was then compared with the one at the ambient temperature (H0). **Figure 5.9** shows the area ratio of the PZT columns and void area of the samples obtained at individual temperature levels. It is evident that when the columns were generated on the substrate of the ambient temperature, nearly 30% of the deposited area is void where the Ti/Pt coated silicon wafer is exposed. When the temperature increased, the area density of PZT column increased gradually and at 175°C the PZT column area fraction is approximately 80%, which correlates with observations of the micrographs in **Figure 5.8**.

The observations in **Figure 5.8** and **Figure 5.9** may be explained as follows. First, it is believed that although 0.6M solution yields small droplets which have undergone significant evaporation, the incoming droplets are not completely dry when they are transported to the substrate at the ambient temperature. When the substrate temperature increases, the radiative and convective heat transfer from substrate to the droplets should be taken into account since the spatial temperature between the needle and substrate is also increased. Therefore the substrate temperature is a key factor when the droplets are transported to the surface.

At a lower substrate temperature, the incoming particles are relatively wet and still containing significant amounts of organic solvent and their reacted resultants. These "wet" particles are deposited as wet columns, which are believed to be of high conductivity due to the residual solvent in them. These conductive columns connect with the ground electrode resulting in a change of the effective profile of the ground electrode from planar to spiked. After a certain deposition time, the scale of the columns becomes large enough to disturb the electric field between the needle and the substrate. Because of the preferential landing, it is rather difficult for the particles following to deposit in the space between the columns but highly attracted to the surface of the column. However, when the substrate temperature is increased, the deposited columns are drier than those on the corresponding lower temperature substrates. These drier columns are less conductive so that they will not act as such an effective extension to the ground electrode, reducing the effect on the electric field

even when they present on a large scale. Therefore, the particles will have less of a tendency to be deposited at the sites of perturbations, leading to a finer columnar structure. Also, due to the lower conductivity, it is difficult for the electrical charges in the column to dissipate which then accumulate on the surface of the column. Thus the particles following, which contain the charges with the same polarity, will be repelled away from the column. Accordingly, it is believed that it is easier for the particles to deposit in the void area between columns due to the lower conductivity of the dry columns, resulting in the formation of interconnected structures.

Additionally, the shrinkage of the deposited structure could also be considered as a contribution to this phenomenon. The columns on the lower temperature substrate are wetter and will lose more weight due to the further decomposition at higher temperature, thus incurring a large volume reduction. When the substrate temperature is increased, the columns are drier when deposited, undergoing less shrinkage at the higher temperature; this could also help to explain why a denser structure can be obtained at a higher substrate temperature.

This effect of substrate temperature on the columnar structure is quite important in that it has possibility to realize the control of the morphology of the columns by varying the substrate temperature so that a specific columnar structure can be obtained (precise column size and distribution density). Further development on this matter will be carried out as possible future work.

5.4 Forming of 1-3 composites

The above work has revealed that using 0.6M sol, a columnar PZT structure can be generated by electrohydrodynamic deposition. Such columnar structures will be functionalised when fabricated as 1-3 composites. In this section, forming of 1-3 composites is introduced in details and the dielectric properties of this composite are also measured and discussed.

5.4.1 Process description

As mentioned in **Chapter 2**, a 1-3 composite composes of isolated PZT columns and a polymer material which prevents the columns vibrating in the x-y layer. In our experiment, a liquid photoresist (introduced in **Chapter 3**) was used to be infiltrated into the PZT columns as the polymeric second phase. The detailed processing procedure for 1-3 composites was described in **Chapter 3**. The average thickness of the prepared composite was measured using a Dektak surface profilemeter.

The measurement of the dielectric properties of such composite was realized by coating gold electrodes on top of the composite using evaporation. A Wayne Kerr 6425 Precision Component Analyser was used and the values of the capacitance and dissipation factor of the composite at 50 kHz were measured.

5.4.2 Dielectric properties of the PZT/polymer composite

The capacitance and dissipation factor of the PZT/polymer composite at 50 kHz were measured as 15.4pF and 0.021, respectively. The geometry of the coated gold

electrode was described in **Chapter 3** and the area of the electrode is calculated as 4.3×10^{-7} m^2. The thickness of the composite structure was measured as 26μm. According to *Equation 2.8* in **Chapter 2**, the relative permittivity of the composite ε_m is calculated as 105.

In the current model, the composite can be considered as a PZT and a polymer capacitor connected in parallel. As a result,

$$C_m = C_{PZT} + C_{polymer} \qquad \textit{Equation 5.2}$$

where C_m is the capacitance of the mixed composite, C_{pzt} is the capacitance of the PZT columns and $C_{polymer}$ is the capacitance of the polymer phase. If the area of the tested composite is A, and the areas of the PZT columns and the polymer phases are A_{pzt} and $A_{polymer}$, respectively, *Equation 5.2* gives

$$\varepsilon_m = \frac{\varepsilon_{PZT} \cdot A_{PZT}}{A} + \frac{\varepsilon_{polymer} \cdot A_{polymer}}{A} \qquad \textit{Equation 5.3}$$

where ε_{PZT} and $\varepsilon_{polymer}$ are the relative permittivity of the PZT columns and the polymer phase, respectively. According to the value in **Figure 5.9** that shows the image analysis of the columnar structures processed at the ambient temperature, the area fraction of PZT column and the polymer is 0.678 and 0.322 at this temperature. As a result, *Equation 5.3* gives $\varepsilon_m = \varepsilon_{PZT} \cdot 0.678 + \varepsilon_{polymer} \cdot 0.322$. The relative permittivity of the photoresist is approximately 3 thus the relative permittivity of the columnar PZT material ε_{PZT} can be calculated as 154.

Compared with homogeneous PZT films produced by other techniques (e.g. $\varepsilon_{PZT} = 400$ by spin coating), the relative permittivity of the columnar PZT

material is lower. It is believed that this is due to several factors. Firstly, the slight presence of second phase pyrochlore due to the increased loss of lead during heat treatment as a result of the high surface area may be one of the reasons. Secondly, the different crystallographic crystallization of columnar PZT with respect to planar PZT is also expected to result in a change in relative permittivity. Thirdly, the porosity within the column is higher than desired due to the preferential landing of the particles during deposition, leaving air filled pores within the structure; this is possibly another reason for the low relative permittivity. Moreover, the poor connectivity between the polymer and the PZT columns may also leave to small voids, which may increase the porosity in the matrix too. The measured value of dissipation factor is reasonable for a PZT composite. However, there is a possibility that the higher porosity may also increase the dissipation factor due to a large amount of charges accumulated near the boundary of different phases (PZT/Polymer/Air), which may induce conduction.

5.5 Forming of continuous PZT films

The previous sections have introduced the forming of columnar PZT structures for 1-3 composites applications. Apart from that, electrohydrodynamic deposition can also be utilized to generate continuous PZT films. The film can be obtained when a precursor with moderately low concentration is used during the process. This part introduces the forming of continuous PZT films using 0.06M PZT sol and the investigation of the generated structures after heat treatment. The electrical properties of the sample are also studied.

5.5.1 Process description

In order to generate continuous PZT films, 0.06M PZT sol was selected and sprayed during electrohydrodynamic deposition. The original 0.6M PZT sol that was used in the previous chapters was diluted using 11:10 (volume ratio) acetic acid/1-propanol mixed solvent to obtain the desired concentration. The procedure of electrohydrodynamic deposition for continuous films corresponds to the one for forming the columnar PZT structures and Ti/Pt coated silicon wafer was used as the substrate where the sample was deposited and the distance between the nozzle and substrate was kept as 10mm.

The process for generating the continuous films was not one-off but repeated. Dorey *et al.* (2004) has discussed that the thick films may experience shrinkage that produces significant internal stress during the heat treatment, which is the main reason for the crack formation. Therefore, a repeated spray and drying deposition procedure was used in this work. The sample was deposited for 60s and dried on a hot plate at 200°C for 120s; the dried film was coated with a second spray deposition for 60s and dried similarly; this procedure of spray and drying deposition can be repeated to further improve the thickness of the film. The advantages of this repeated deposition procedure are (1) the thin deposit obtained at each cycle will not experience high internal stress so that the possibility of crack formation can be reduced; (2) the low concentration precursor contains less amount of PZT materials and the repeated deposition is suitable to obtain the film with considerable thickness; (3) the wet deposit with excessive thickness may affect the electric field between the needle and

the substrate, which may produce an unstable cone-jet mode during spraying; the drying procedure in each cycle may reduce such an effectiveness of the columns thus eliminate the risk.

Heat treatment is necessary for the formation of continuous PZT films when using this procedure. The sample after deposited for three times was heat treated at 650°C for 1200s in order to obtain perovskite PZT material.

5.5.2 Microstructure of the PZT films

The microstructure of the PZT film produced using electrohydrodynamic deposition was studied by observing the cross-section of the samples using SEM after heat treatment at 650°C. The micrograph of the structure was shown in **Figure 5.10**. It is a laminar structure evident as can be observed in the image, which is possibly attributed to the repeated spray and drying procedure during the sample fabrication. When the deposit was heated at 200°C, the film condensed to a certain degree because the solvent in the precursor with low boiling points were evaporated or removed. The dried film was coated by the subsequent deposition and the new deposited layer was heated similarly. As a result, a laminar structure can be observed after the film was finally heat treated at 650°C.

As evident in the micrograph, a thickness of approximately 645nm was obtained after the film was deposited for three times. This value has approved the high process efficiency of electrohydrodynamic deposition technique. A comparison can be made

with the work of Miyazawa *et al.* (2000), in which PZT layers was obtained by spin coating method. In that work, only approximately 120nm thick structure can be generated in one layer, while the repeated electrohydrodynamic deposition procedure is nearly twice the efficiency than the former one. Additionally and evidently, the instruments used for electrohydrodynamic deposition are more uncomplicated when compared with the sputtering coating method where a vacuum chamber and a high energy electron beam are necessary during the process (Mohammadi *et al.* 1979).

However, it is also obvious that the film is not dense enough when compared with the structures produced by Hu *et al.* (2004), where a dense PZT layer of 3.82 μm thickness was obtained by traditional sol-gel method after 30 times process. A distribution of small holes in nanometer size can be observed within the structures. On the one hand, the lower concentration sol containing less PZT material may be one of the reasons for these holes (similar to the structure in **Figure 5.2** C1 and C2). On the other hand, the particle agglomeration and their preferential landing discussed in the previous section are also believed as a contribution to generate such a structure. This feature is believed to be characteristic of electrohydrodynamic deposition.

5.5.3 Phase detection of the PZT films

The phase development of the PZT film generated by electrohydrodynamic deposition of 0.06M sol was studied by X-ray diffraction and the pattern is shown in **Figure 5.11**. Apart from the peaks of the substrate materials (Silicon and Platinum), perovskite PZT was obtained which means heat treatment at 650°C for 1200s is suitable for the

crystallization of perovskite PZT generated by electrohydrodynamic deposition of 0.06M sol.

A very small amount of pyrochlore phase can be observed within the structure which is indicated as Py in the graph. It has been reported that when using 2-ME (2-Methoxyethanol) as the solvent in the PZT sol for sol–gel spin-on coating, the pyrochlore can not be observed (Wang 2005). However, 2-ME is a toxic solution and it is very risky when using this solvent during electrohydrodynamic deposition in which the precursor was sprayed into small droplets. Therefore, it is impractical to use such a toxic solution however a non-toxic solution 1-propanol was used instead.

5.5.4 Electrical properties of the PZT films

In this part of work, the dielectric properties of a continuous PZT film with 645nm thickness were measured. The relationship between the relative permittivity and the frequency was investigated using a precision impedance analyzer by which the relative permittivity and the dissipation factor of the film at 50 kHz was calculated particularly. Gold electrodes were firstly coated on top of the PZT film using evaporation. The detailed procedure of the electrode coating and the devices used for electrical property measurement are described in **Chapter 3**.

Figure 5.12 shows the frequency variation of the relative permittivity and the dissipation factor of the 645nm thick PZT film, measured at room temperature in the frequency range of 100 Hz to 1M Hz. The relative permittivity decreased slightly with

the increasing frequency while the dissipation factor was not changing significantly until 1 MHz after which it underwent a rapid increase. Specially, the relative permittivity and the dissipation factor at 50 kHz were 90 and 0.059.

Compared with these values of the columnar PZT structures obtained using 0.6M sol, the relative permittivity is slightly lower and the dissipation factor is higher. The lower relative permittivity of the film is possibly attributed to several reasons. First, the higher content of pyrochlore phase which was observed in the XRD patterns may reduce the dielectric property. Second, the presence of the small holes distributed in the film may reduce the homogeneity of the material and thus affect the dielectric properties. Moreover, the presence of interface between the film and the substrate is believed as another reason for the lower relative permittivity. In this work, lead can be easily infused into the substrate layer and further react with materials used to coat silicon substrates to form interfaces, which may not be a ferroelectric phase and thus affect the desired properties. The dissipation factor is also slightly higher in that the charges in the material are easily accumulated near the phase boundaries (layers and holes) which may increase the conduction of the material when it is experienced to an a.c. electrical field and thus increases the dissipation factor.

The reduced electrical properties of the obtained PZT films by electrohydrodynamic deposition remain a challenge and the mechanism is yet not fully understood. Further development and research on this matter will be carried out as possible future work.

5.6 Summary

In this chapter, it has been described that electrohydrodynamic deposition can be used as a novel technique for forming columnar PZT structures and continuous PZT films. The concentration of the precursor affects the as-deposited structures to a large degree, which attributes to the different size of the droplets formed during electrospray and the evaporation of the droplets during their transportation to the substrate. The preferential landing of charged particles is also a factor affecting the as-deposited structures. By changing the concentration from 0.06M to 0.6M, structures ranging from continuous layers to columnar structures can be obtained. It is concluded that 0.6M sol is ideal for columnar PZT structure formation while 0.06M sol is moderate for continuous PZT film formation. Heat treatment at 650°C is necessary for both of the PZT structures. A 3-stage growth process can be observed in the columnar PZT structure of which a thickness of 35μm can be obtained after 330s electrospray deposition. Substrate temperature has a significant effect on the columnar structure produced during deposition; the structure becomes smaller and denser when the substrate temperature increases. A PZT/polymer composite can be produced by infiltrating a liquid polymer among the PZT columns. The relative permittivity and the dissipation factor of such a composite is 105 and 0.021, respectively. Modelling the structures as two parallel capacitors in the composite allows the calculation of the relative permittivity of PZT column as approximately 154. A certain amount of voids are distributed throughout the PZT columns and these and the boundaries with the polymer may reduce the relative permittivity and increase the dissipation factor. A repeated deposition procedure can be used for forming continuous PZT films, by

which a film with the thickness of approximately 645nm was obtained. The electrical property measurements on such a film show a reduced dielectric property, which may be due to the slightly high porosity contained that is considered as characteristic of electrospraying. The improvement of these properties is a great challenge for the development of the electrohydrodynamic deposition technique, a possible avenue of future work.

Figures

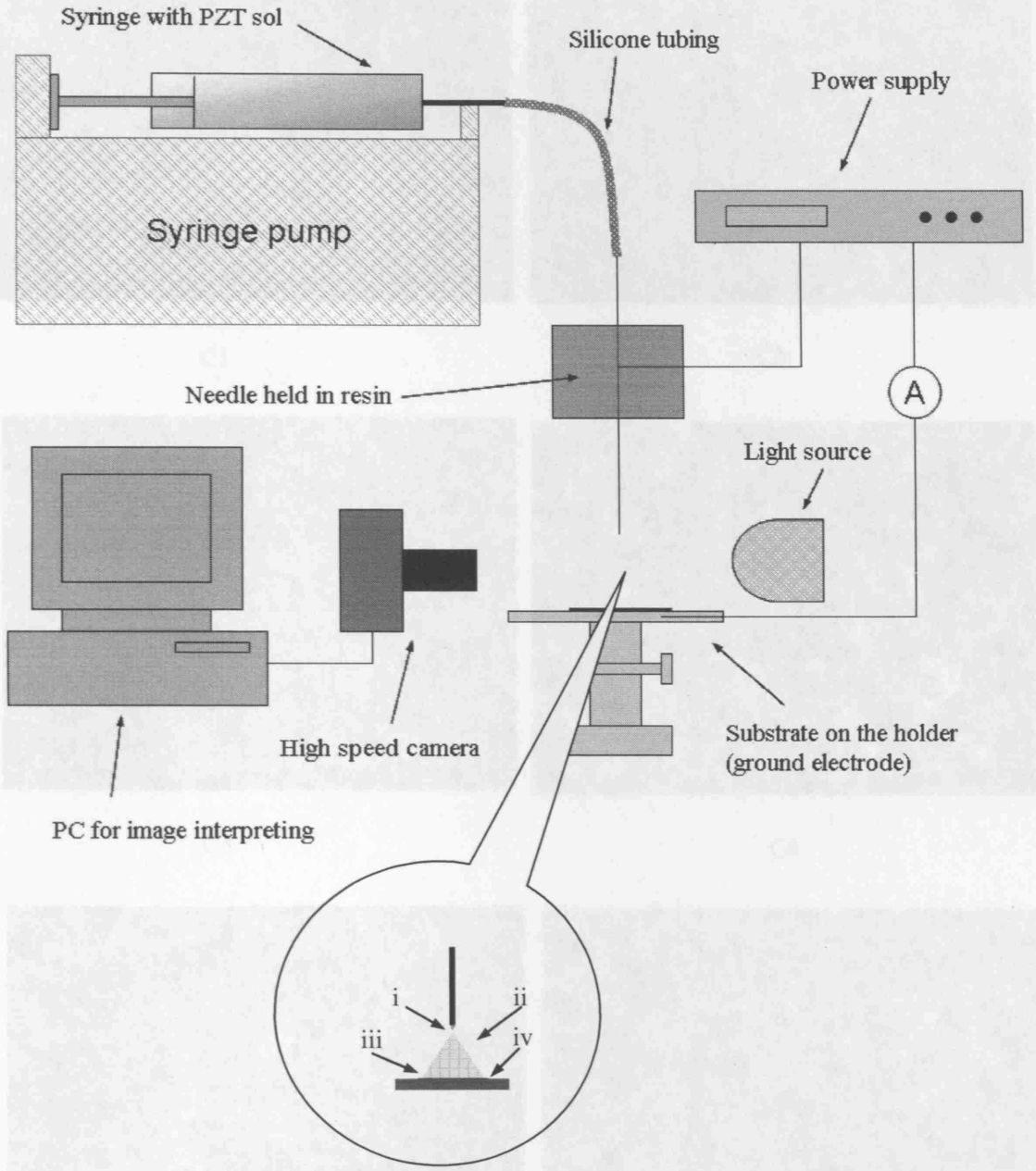

Figure 5.1 Schematic diagram of the electrohydrodynamic deposition experimental rig. The inset graph enlarged the spray-deposition region, where four stages are defined: i) droplet generation after jet break-up, ii) transportation through the environment, iii) impact and spreading on the substrate, iv) drying and decomposition.

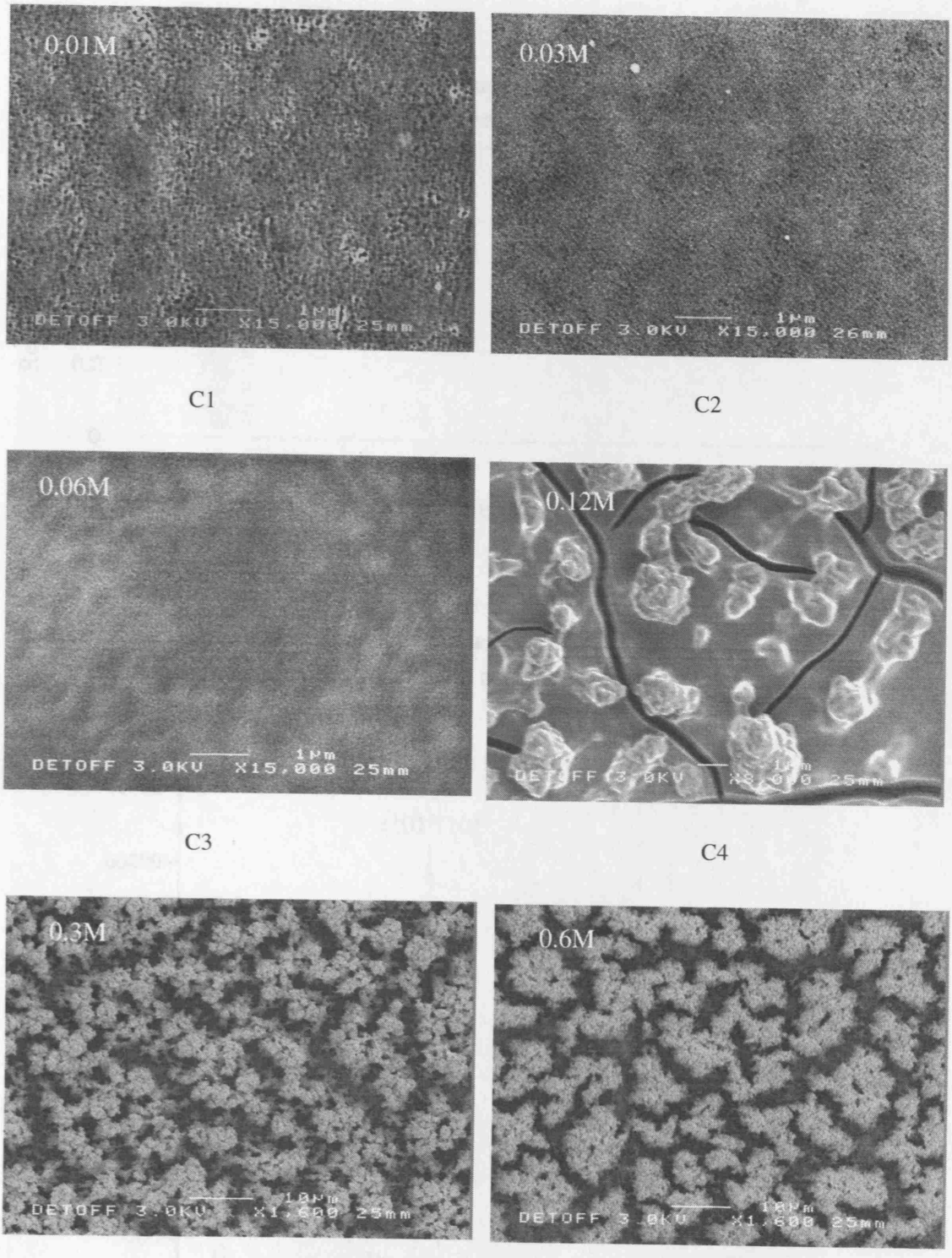

Figure 5.2 Scanning electron micrographs of as-deposited structures prepared using different concentration of PZT sol. C1: 0.01M, C2: 0.03M, C3: 0.06M, C4: 0.12M, C5: 0.3M and C6: 0.6M.

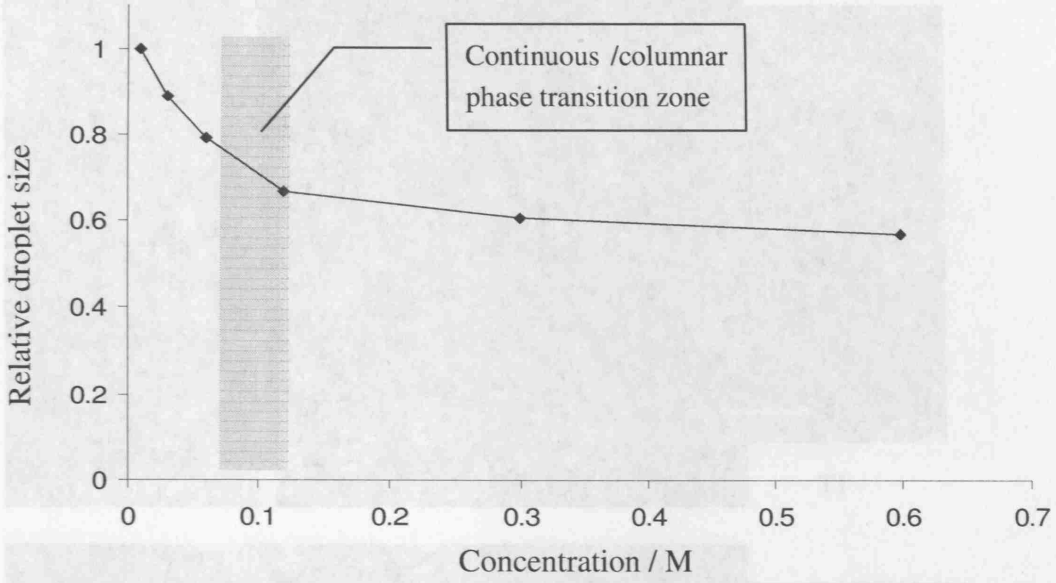

Figure 5.3 The relationship between the concentration of the sprayed sol and the relative droplet diameter deduced from *Equation 5.1*. The bar represents the continuous film to columnar structure phase transition region.

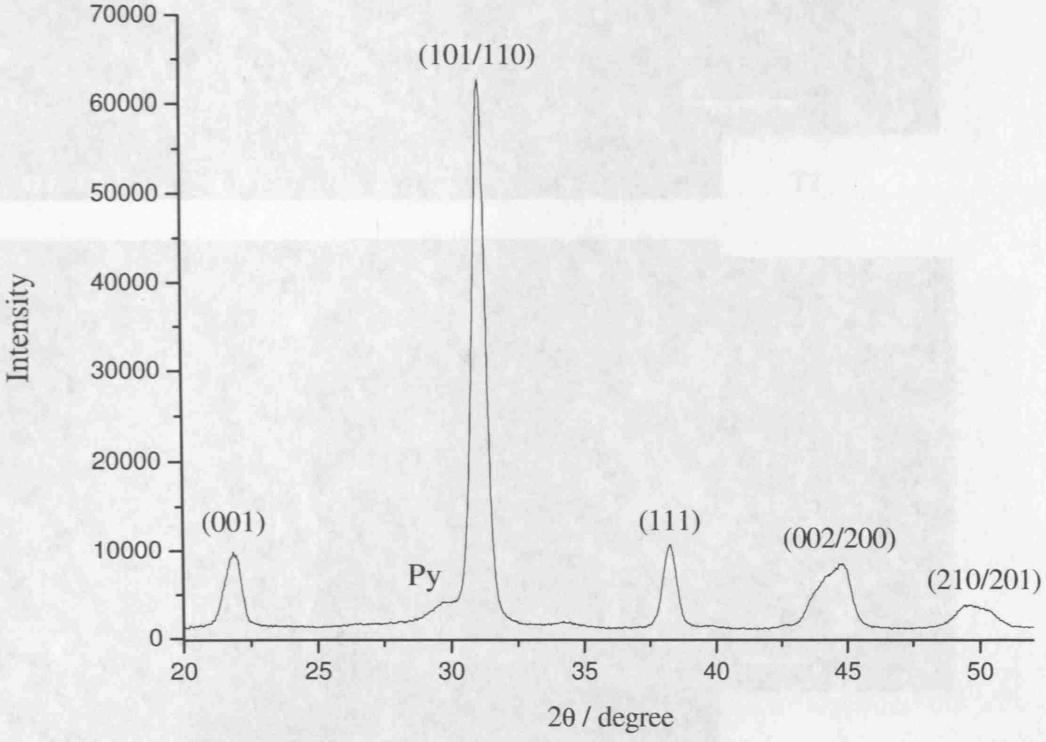

Figure 5.4 X-ray diffraction pattern of PZT columns after heat treatment at 650°C for 1200s. Very small amount of second phase pyrochlore is indicated as Py.

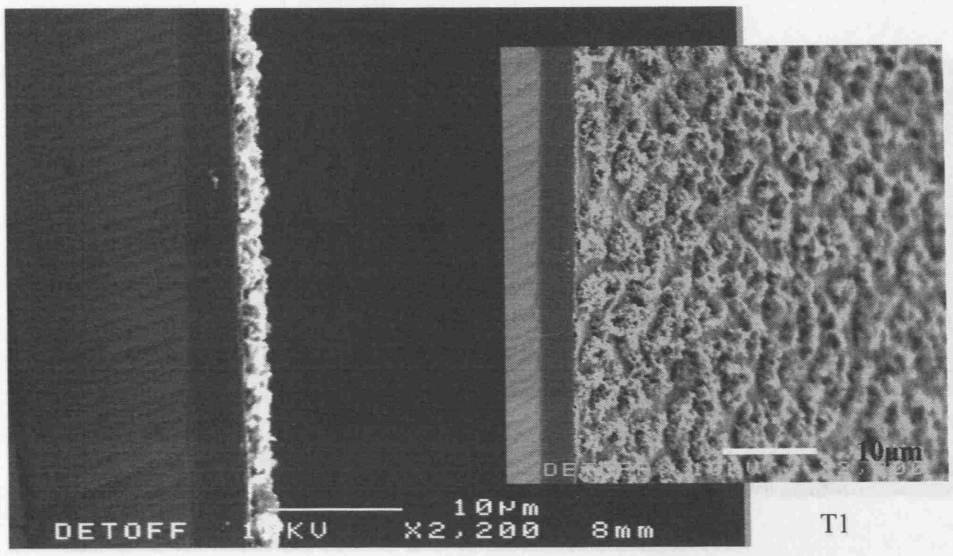

T1

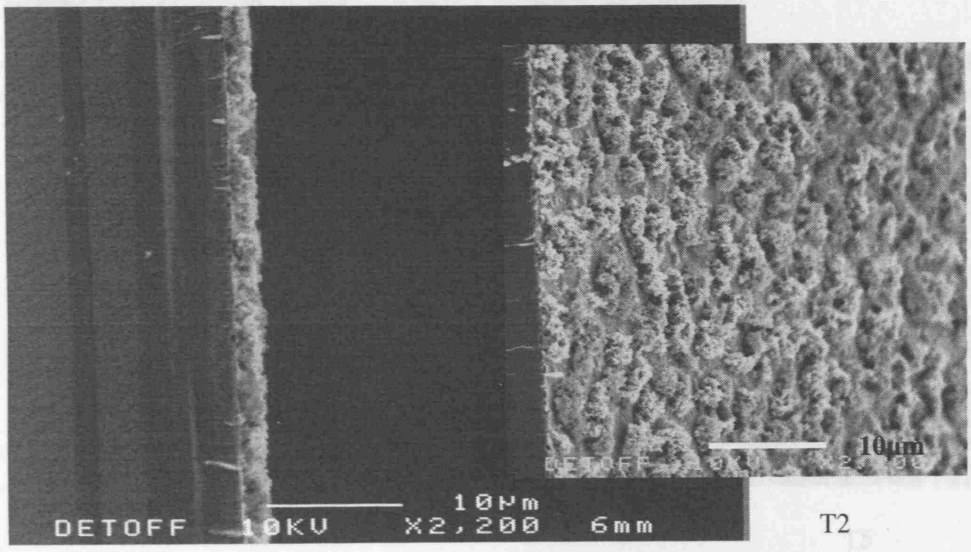

T2

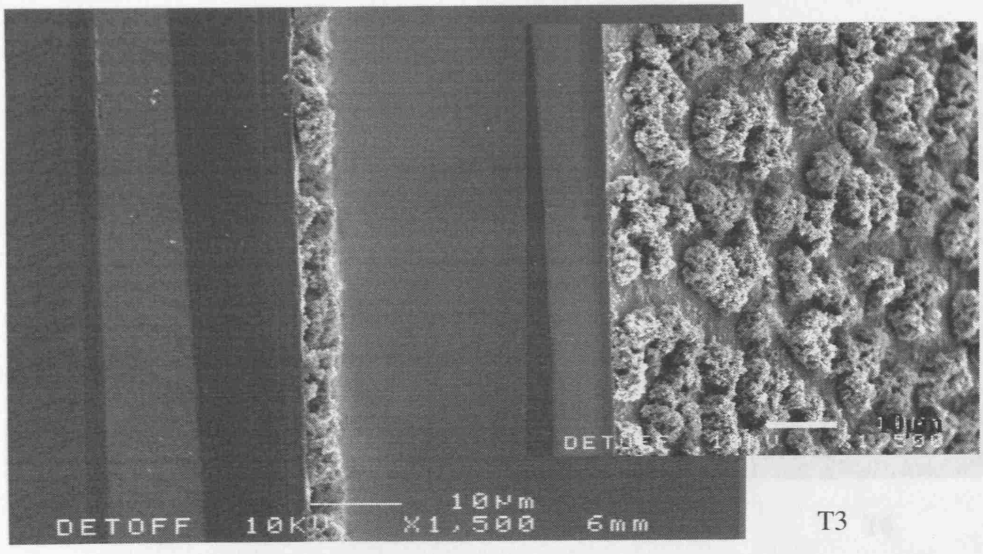

T3

Figure 5.5 Scanning electron micrographs of sintered columnar structures obtained at different deposition times T1 to T6. The inset images show the surface morphologies of each sample when viewed with a tilt of 45°.

Continued.....

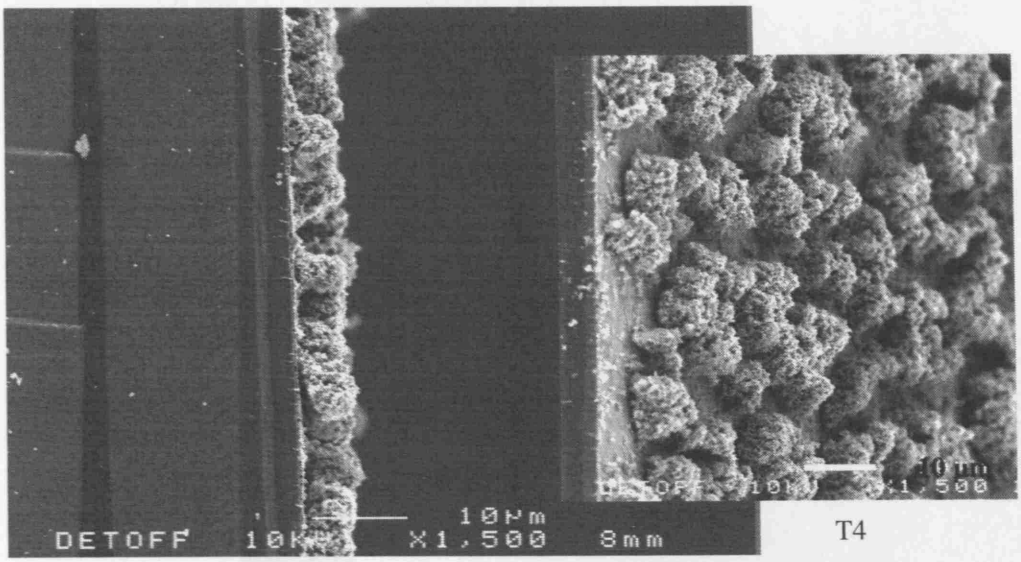

T4

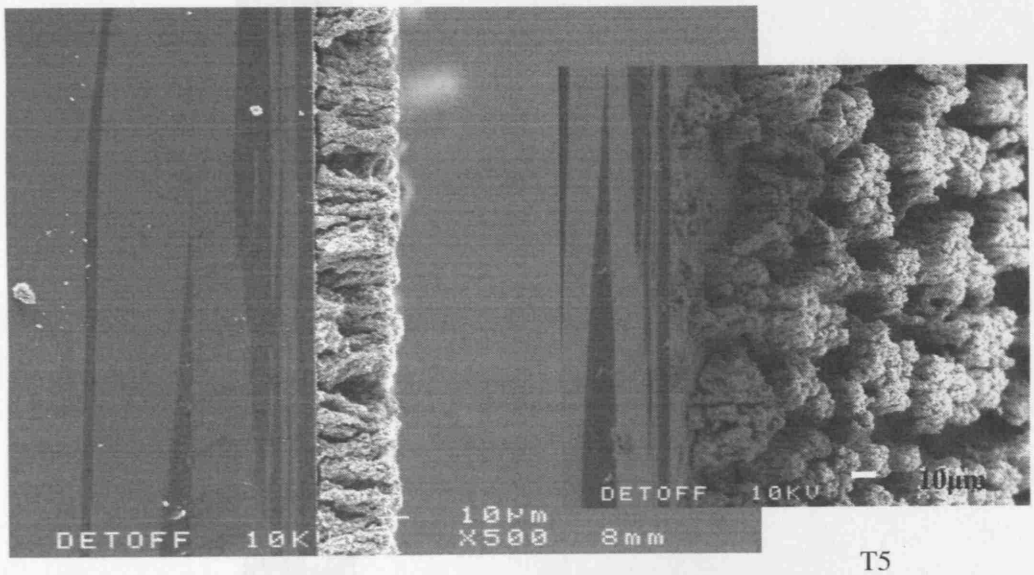

T5

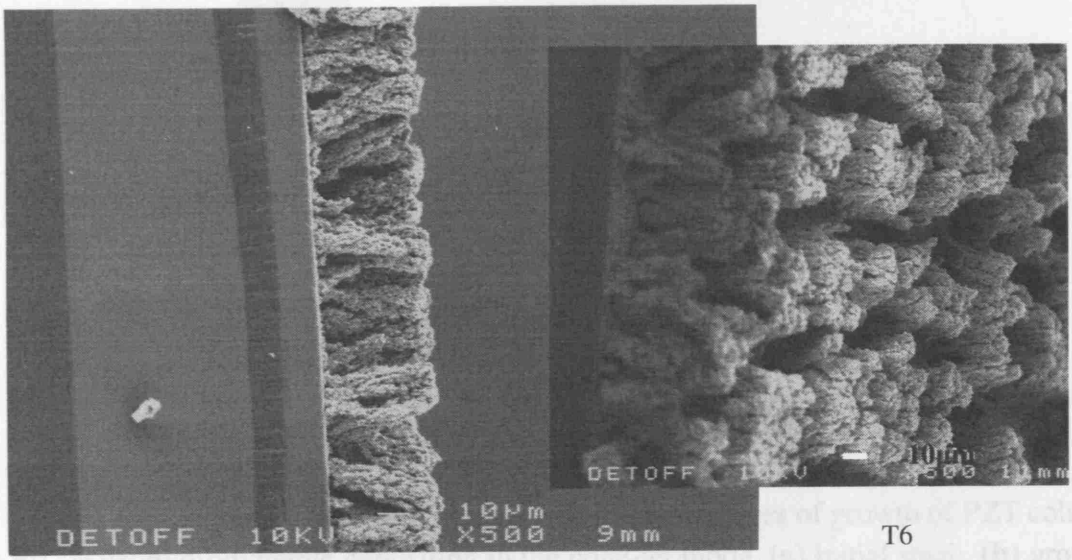

T6

Figure 5.5 All. T1: 10s, T2: 20s, T3: 40s, T4: 60s, T5: 180s and T6: 330s.

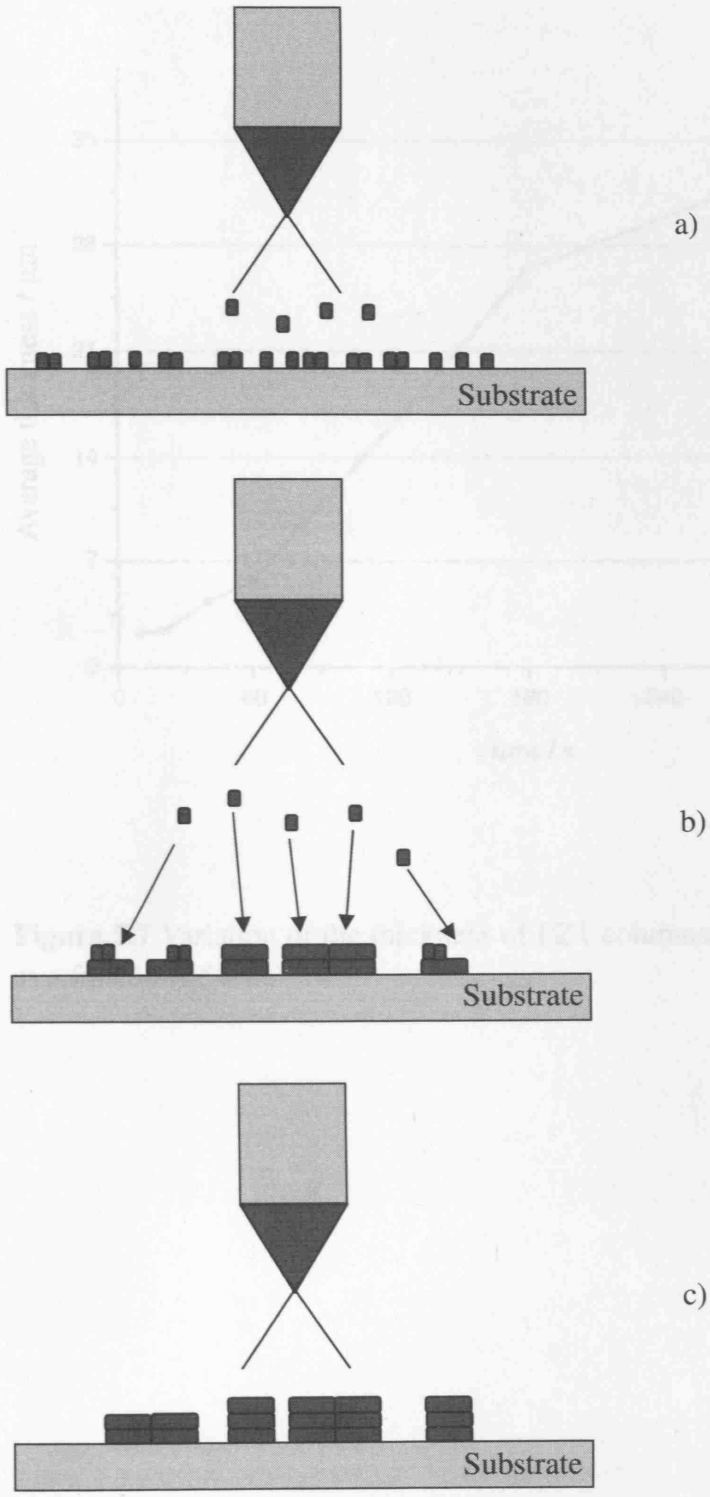

Figure 5.6 Schematic representations of the different stages of growth of PZT columns by electrohydrodynamic deposition in the cone-jet mode, **(a)** initial stage, **(b)** growing stage and **(c)** sustained stage. The small dots represent the droplet. The pillar structures represent PZT columns.

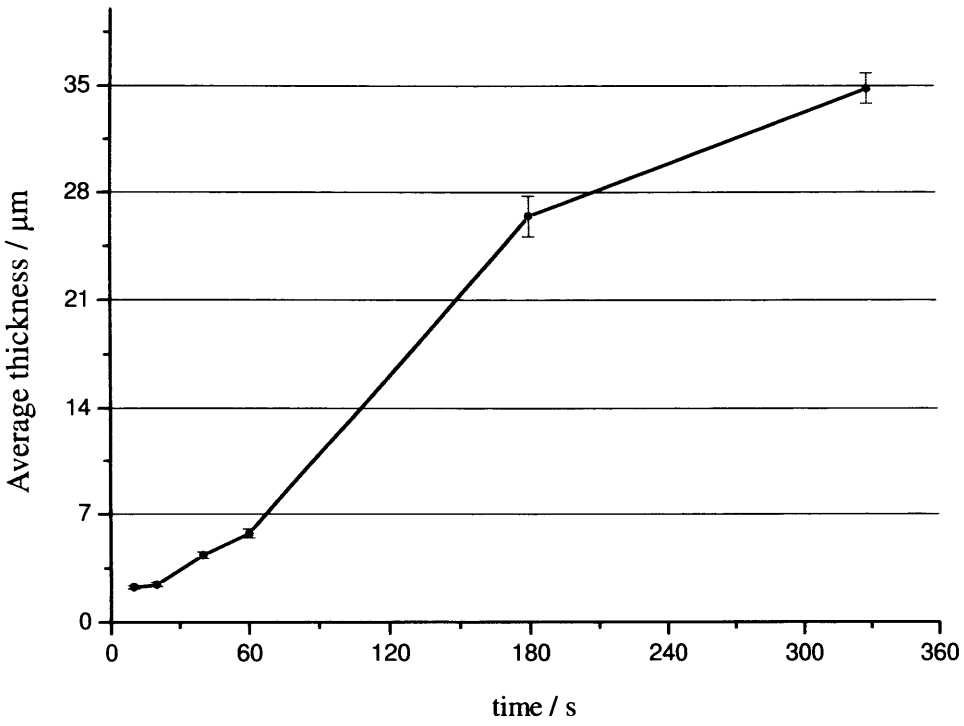

Figure 5.7 Variation of the thickness of PZT columnar structure heat-treated at 650°C as a function of time.

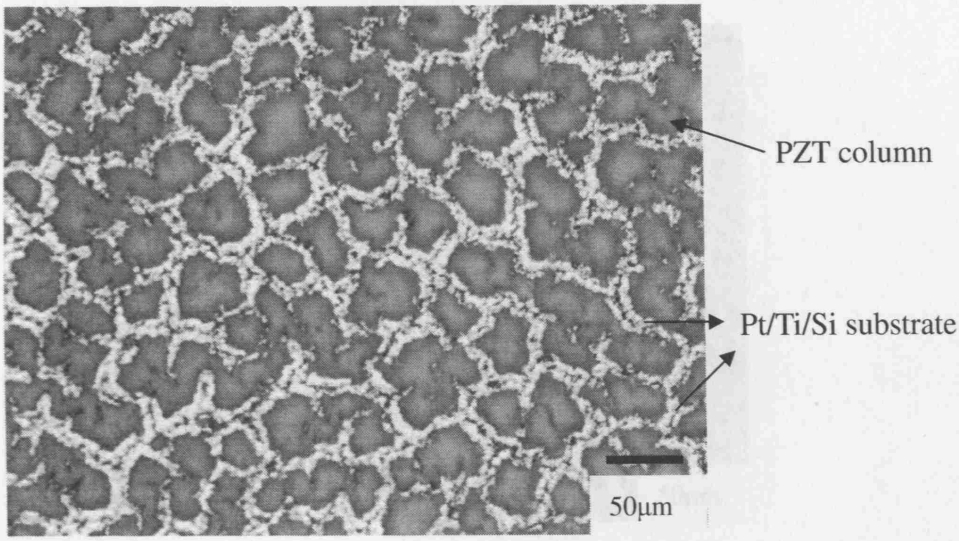

H0

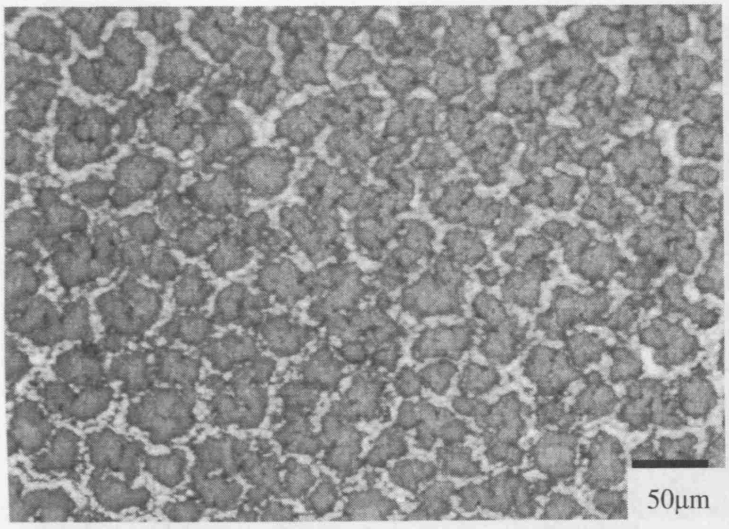

H1

Figure 5.8 Optical micrographs of columnar PZT structures sprayed at different substrate temperatures followed by heat treatment at 650°C. H0: ambient temperature and H1: 75°C.

Continued.....

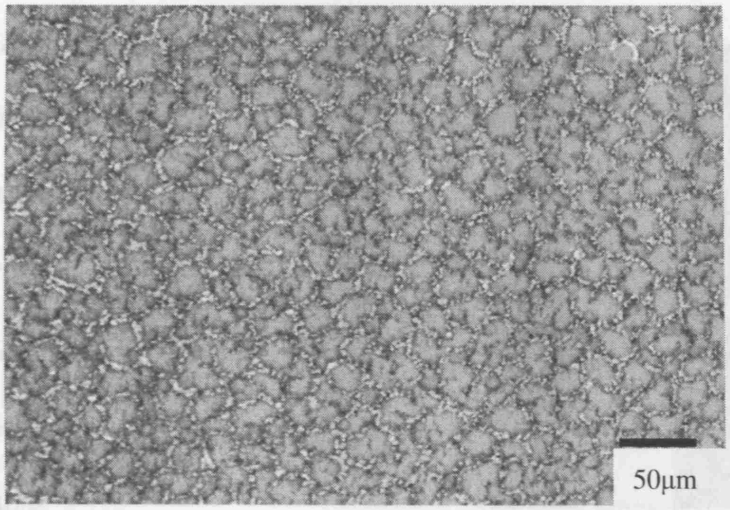

H2

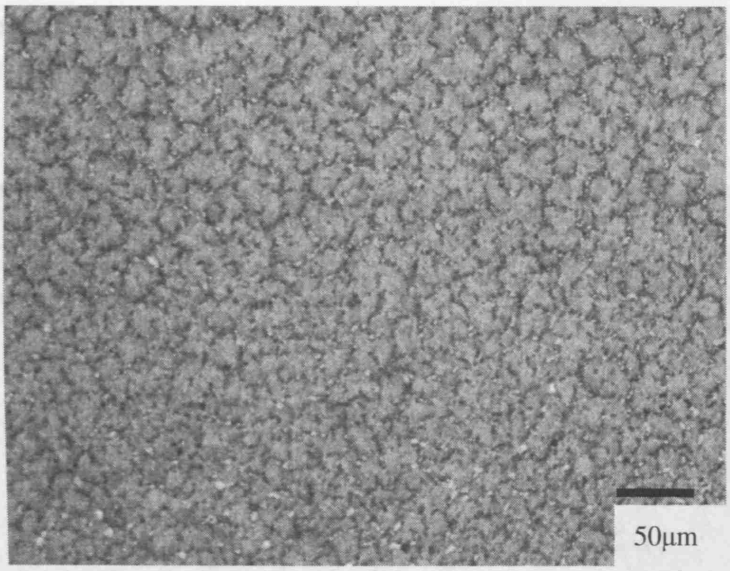

H3

Figure 5.8 All. H2: 125°C and H3: 175°C.

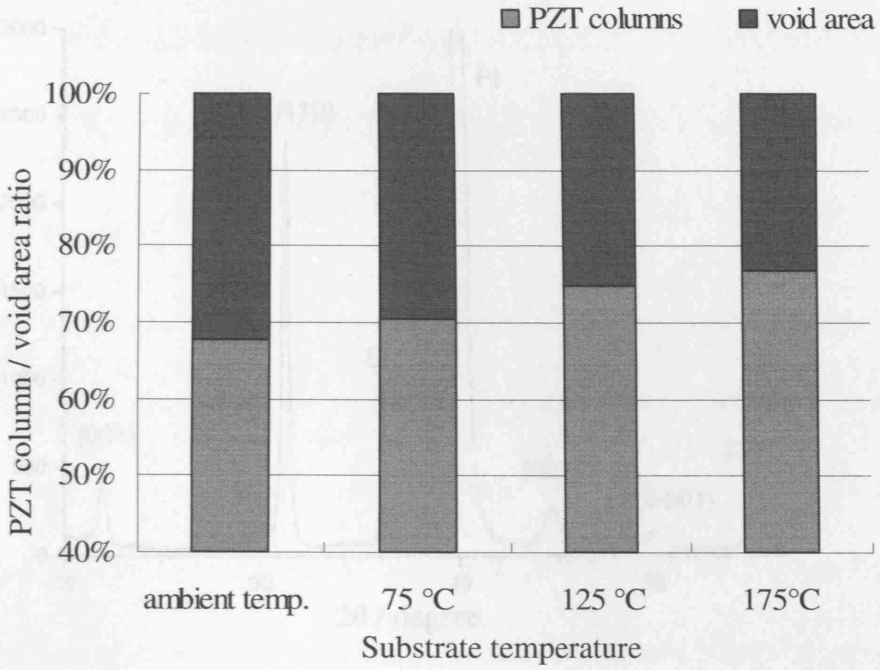

Figure 5.9 The PZT column/void area ratio obtained by analyzing the micrographs shown in **Figure 5.8**, using a common image analyse software.

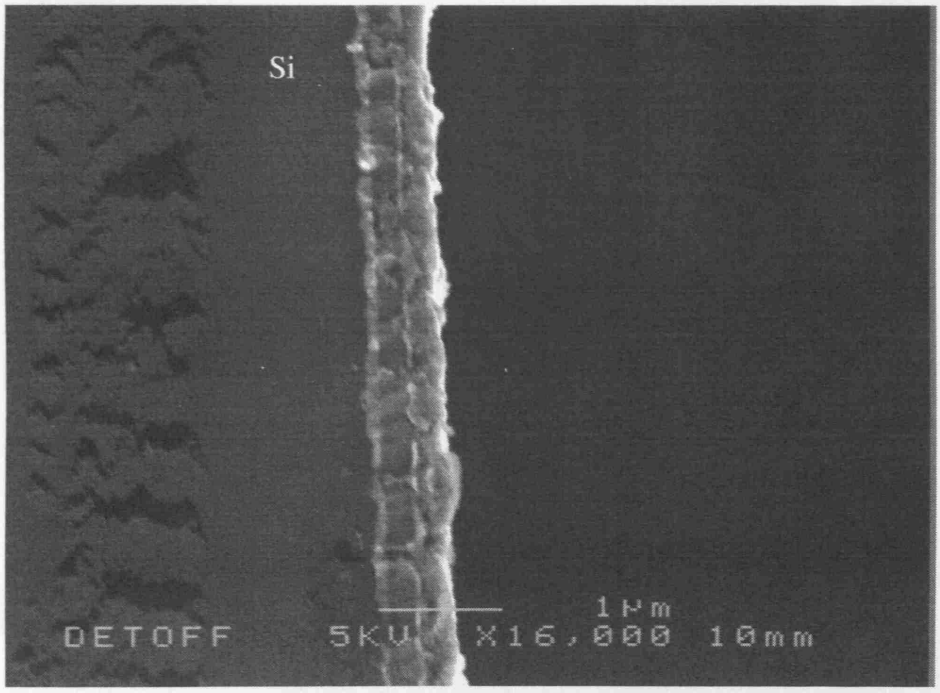

Figure 5.10 Scanning electron micrograph of cross-sectional structure of the continuous PZT film generated by electrohydrodynamic deposition, after heat treated at 650°C.

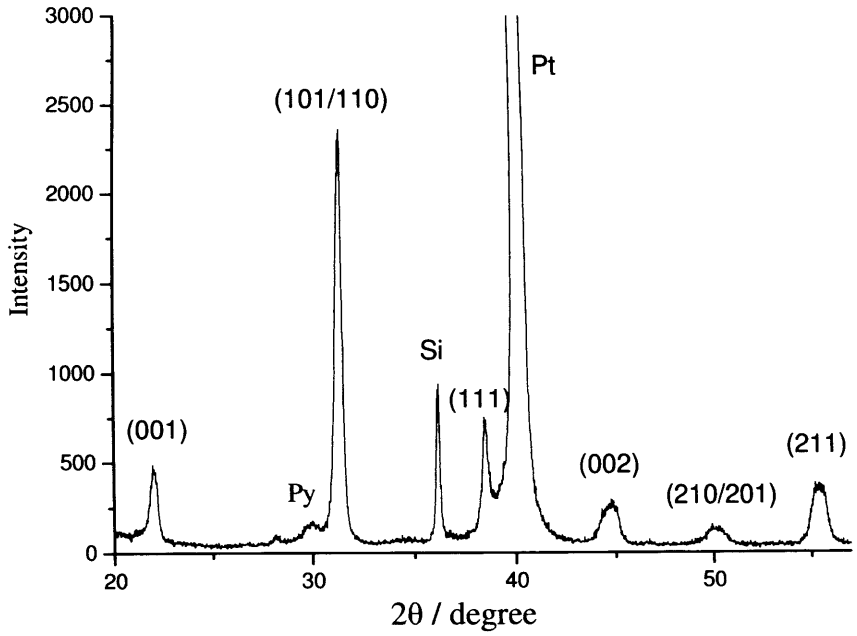

Figure 5.11 X-ray diffraction pattern of the continuous PZT film generated by electrohydrodynamic deposition, followed by heat treatment at 650°C for 1200s. Peaks of substrate materials (Silicon and Platinum) can be observed, otherwise perovskite PZT was obtained. Very small volume of second phase pyrochlore was indicated as Py.

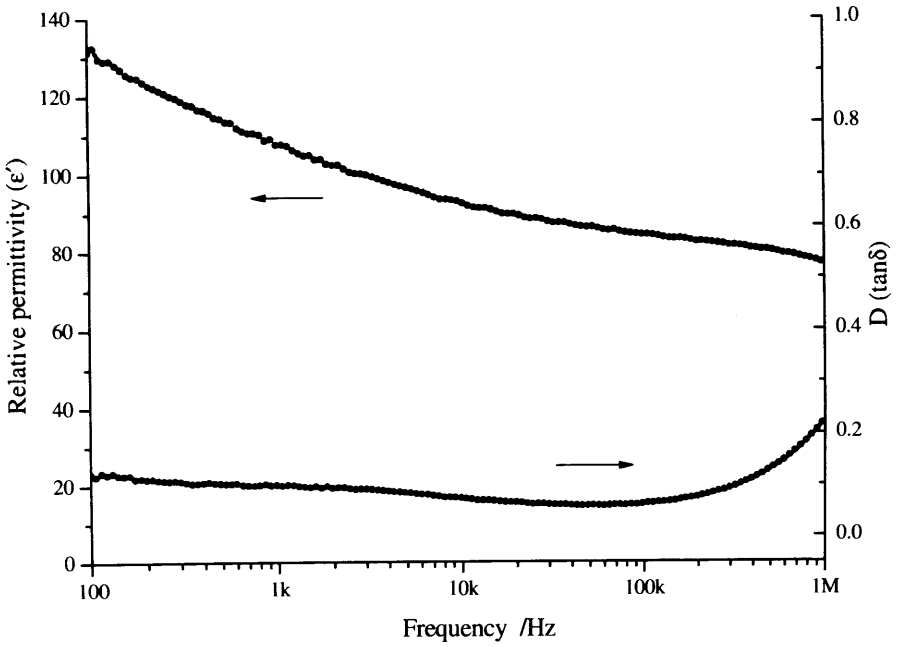

Figure 5.12 Variation of relative permittivity and the dissipation factor (D) with frequency for the continuous PZT film generated by electrohydrodynamic deposition.

CHAPTER 6 Electrohydrodynamic Printing of PZT Track-structures using PZT Sol with PVP Solution

6.1 Background

The previous two chapters have illustrated the electrohydrodynamic atomization technique and its derivative deposition process as novel methods to deposit PZT material in the form of columnar structures and continuous films. In this chapter, electrohydrodynamic printing, which is also an off-shoot of the electrohydrodynamic atomization process, is investigated. The mechanism and recent advances related to this process were described in **Chapter 2**, where other direct writing methods were also discussed. As an electrospray derived technique, electrohydrodynamic printing provides a more complex and controlled method of particulate deposition. The latter requires a multipart set-up, with a controllable collecting device and a point electrode in order to focus the jet shortly after break-up which means a small spraying distance is used between the needle and substrate.

The PZT sol used in the previous chapters was also used in this work as the printing precursor. However, the solution necessitates modification as it is known that cracking is a common feature when processing materials using sol gel solutions and it is evidently observed in the related previous work (Rocks *et al.* 2007), where 0.6M PZT sol was used directly to print straight lines. It is believed that this phenomenon is attributed to structural and chemical changes of the PZT material and its precursor on the rigid substrate during the heating and cooling processes encountered through heat treatment. This results in a large intrinsic stress, which is undoubtedly the cause of

cracking within structures. This matter is a significant challenge when using the electrohydrodynamic printing process, especially when it is utilized to pattern complex structured functional ceramics for sophisticated applications, e.g. integrated circuits, information storage devices and MEMS, where a continuous crack-free configuration is required. Thus, the objective of this chapter is to print crack-free PZT track-structures by electrohydrodynamic printing utilizing properly modified sol gel PZT solutions, which could be potentially used for such purposes.

It has been reported that the intrinsic stress can be suppressed by promoting structural relaxation or plastic flow in the material (Brinker *et al.* 1992). When using sol gel solutions, such a method can be realized by incorporating polymeric materials into the sol prior to the deposition. This is effective in reducing the cracks formed within the material when the sol undergoes structure transformation during heat treatment. Yu and coworkers have added polyethylene glycol (PEG) to a PZT sol, which resulted in a crack-free PZT film (Yu *et al.* 2003). Polyvinylpyrrolidone (PVP) can also be effectively added to PZT sol to eliminate cracks within the deposited structures, as shown by Kozuka and Kajimura (1999) for their dip coated PZT films. In this work, PVP was investigated as a capping reagent to restrain the crack formation during the printing process. The as-received PVP powder can be quite easily dissolved in the propanol-based solvent that is used to form the PZT sol. This eases the incorporation of PZT sol and PVP solution as a proper precursor for spray-printing process.

In this chapter, the preparation of PVP solution and its incorporation with PZT sol are

explained. The structure of PVP is described and the mechanism of hydrogen bonding between the molecules of PZT and PVP is shown. The solution was studied by thermogravimetric analysis (TGA) and differential thermal analysis (DTA) in order to investigate the phase evolution of both PZT and PVP. The track-structures were produced by electrohydrodynamic printing using four different PZT/PVP solutions, followed by heat treatment. The structures were examined using optical microscope and no cracks can be observed in the resultant PZT tracks. Additionally, the residue of PVP in heat-treated structures was investigated using a Fourier-transform infrared spectrometer and it was shown that the PVP polymer underwent decomposition and was completely removed after the printed structures were heat-treated at 650°C.

6.2 Characterization of PZT sol with PVP solution

6.2.1 Molecular structure of PVP

PVP is a water-soluble polymer made from the monomer vinylpyrrolidone which is schematically shown in **Figure 6.1**. The chemical components of PVP $(C_6H_9NO)_n$ are comprised of amide groups with carbon backboned molecules. It has been demonstrated that this kind of polymer can be hybridized with metalloxane polymers in sol gel solutions through strong hydrogen bonds between the C=O group of the amide structure and the OH groups of the latter (Saegusa & Chujo 1990). During the heat treatment, the hydrogen bonding between the two groups can suppress the condensation reaction and promote the structural relaxation, thus reduce stress concentration within the material (**Figure 6.2**). Based on this finding, it is speculated that when PVP solution is incorporated with PZT sol, the C=O group in PVP polymer

could work as a capping agent for the OH groups of the metal-organic molecules in the PZT sol, which can effectively restrain the crack formation in the printed structures after heat treatment.

6.2.2 PZT/PVP solutions

The PVP solution was produced by dissolving PVP powder in acetic acid/1-propanol to prepare 0.01M solution, details of which were described in **Chapter 3**. The solutions of different volumes were then mixed with 0.6M PZT sol to prepare four PZT/PVP solutions in the volume ratios of 1:1, 1:2, 1:3 and 1:4, respectively. These four solutions were used for the printing process.

6.2.3 TGA-DTA analysis of 1:1 PZT/PVP solution

In order to investigate evaporation, decomposition and phase evolution behaviour of 1:1 PZT/PVP solution, a TGA-DTA analyzer was utilized. The PZT/PVP solution was dried using a hot plate, maintained at 80°C for 1 hour. The resultant viscous gel was mechanically removed and placed into an alumina crucible. The initial mass of the test specimen was recorded (13mg) and the sample was placed into the TGA-DTA analyzer. The temperature was gradually increased from room temperature to 700°C at a constant heating rate of 10°C min^{-1} in air, with the flow rate set as 50 ml min^{-1}. The data between 120°C and 700°C were collected and studied.

Figure 6.3 shows the TGA-DTA results obtained from the 1:1 PZT/PVP solution. The

initial weight loss due to the evaporation of the solvents (propanol and acetic acid) is similar to the result obtained from 0.6M PZT sol gel solution, which has been discussed in **Chapter 4** (**Figure 4.1**). As can be observed in this graph, the weight loss persists until 600°C, after which a plateau is reached. Three major weight losses can be observed at approximately 175°C, 275°C and 350°C. As previously mentioned in **Chapter 4**, the organic solvents can react with each other to form esters, ethers, CO_2 and alcohols. These newly formed compounds react at higher temperatures and are eliminated, which may contribute to the weight loss before 300°C.

When compared with the TG curve for 0.6M PZT sol discussed in **Figure 4.1**, the relative weight loss (the loss between 130°C and 650°C) is higher for PZT/PVP gel and this was apparently caused by the addition of the PVP polymer. A considerable weight loss at around 350°C (point B) can only be observed in the curve of the PZT/PVP specimen, which is expected as the decomposition and evaporation of PVP polymer near this temperature. By comparison, the slope of this section is smaller than the one between 200°C and 300°C which is due to the initial evaporation of organic solvent (also seen in **Figure 4.1**). This slower weight loss at relatively higher temperature induced by the PVP polymer was deemed to be one of the reasons that it is effective in suppressing crack formation during the heat treatment process. Another small sloping area can be also observed in the TG curve at about 250°C (point A), which is differentiated from the feature in **Figure 4.1**. It is assumed that this weight loss relaxation stage can retard the condensation, which is also beneficial to suppress crack formation, supporting the theorized mechanism mentioned earlier.

The DTA curve in **Figure 6.3** represents the phase evolution of the PZT/PVP solution during heat treatment. There are four changes observed in the curve where the first peak (point C) is between 250°C and 300°C, which can be attributed to reactions between the organic solvents and their decomposition. This correlates with the result in the TG curve where a significant weight loss was observed in this temperature range. A minor peak can be observed near point D, which is expected as the contribution from the decomposition and evaporation of PVP polymer started at approximately 350°C. Between 450°C and 500°C there is a small peak observed (point E), which is due to the phase transition from amorphous PZT to pyrochlore structure. This temperature is comparable with the result of other researchers where the pyrochlore phase can be obtained at approximately 500°C (Chen *et al.* 2003; Tiwari *et al.* 1998). Another significant change in the DTA curve is shown as point F, which is in the temperature range of 600°C to 650°C. It is believed that this is induced by the phase transition from pyrochlore to perovskite.

According to this TGA-DTA curve, it is evident that the PZT material undergoes a similar phase development during the heat treatment regardless the presence of PVP polymer; incorporation of PVP solution into PZT sol does not change the sintering temperature of the material that used for the previous experiments (650°C).

6.2.4 Infrared absorption spectra analysis

In order to investigate the content of residual PVP within the end product after heat

treatment, Fourier transform infrared spectroscopy was used to assess for the presence of the chemical bonds in the material. 1:1 PVP/PZT solution was deposited on the Ti/Pt coated silicon wafer by electrohydrodynamic deposition, as described in **chapter 5**. The as-deposited films were heated at 150°C, 400°C and 650°C for 1200s. Infrared absorption spectra of these films were measured using a FTIR spectrometer in the wave number range of 400–4000 cm^{-1}, which was described in **Chapter 3**. The background was taken as the reference before the measurement. The presence or absence of chemical bonds associated with PVP indicated the relevance of this polymer at different temperatures.

Table 6.1 *Assignment of the infrared absorption peaks (Kozuka et al. 2002)*

Wavenumber (cm^{-1})	Assignment	Mode
890	CH_3COOH	Wagging mode (O-H)
1020	Lead acetate/alcohols	Stretching mode (C-O)
1120	$CH_3OC_2H_4OH$	Stretching mode (C-O-C)
1270	CH_3COOH	Stretching mode (C-O)
1290	PVP	Bending mode (C-N)
1420	PVP	Bending mode (C-H)
1450	PVP/CO_3^{2-}	Bending (C-H)/stretching (C-O)
1550	CH_3COO^-	Stretching mode (C-O)
1715	CH_3COOH	Stretching mode (C=O)
2950	PVP	Stretching mode (C-H)
3400	OH groups	Stretching mode (O-H)

Figure 6.4 shows the infrared absorption spectra of the films heated at 150°C, 400°C and 650°C for 1200s, respectively. The three spectra evidently indicate the presence

or absence of different vibration groups according to different compounds and these developed as the temperature increased. Kozuka *et al.* (2002) have summarized the assignments of the related absorption peaks, of which the relevant assignments for this work are shown in **Table 6.1**.

These assignments can be utilized to index the peaks in **Figure 6.4**. When the film was heated at 150°C, peaks at approximately 890, 1020, 1120, 1270, 1550 and 1715 cm^{-1} can be observed which are believed to be either wagging mode or stretching mode vibrations of the chemical bonds in the compounds of the sol such as lead acetate, alcohol, acetic acid and other organic substances which are thought to be formed by the further reaction of the original compounds. When the temperature was increased to 400°C, most of these peaks reduced or diminished, which means most of the organic compounds had decomposed and evaporated. At 650°C, none of these peaks can be observed, which means the organic compounds were completely removed at this temperature level. At 150°C and 400°C a broad peak at 3400 cm^{-1} can be observed which is assigned to the OH groups (O-H stretching mode); however it is also diminished at 650°C. Peaks at 1290, 1420, 1450 and 2950 cm^{-1} can be observed at 150°C, which are assigned to the PVP polymer. Trace amounts of PVP polymer can be observed when the temperature increased to 400°C and the alteration of such peaks could also be assigned to the decomposition of PVP to carbonaceous compounds which are typically found within the 1300-1600 cm^{-1} region, as the carbon-carbon stretching mode vibrations. When the temperature is increased to 650°C these peaks disappeared, which suggests that all the PVP and the decomposed compounds have

been eliminated, most likely due to oxidation (Kozuka & Takenaka 2002).

All temperature ranges demonstrated a peak at approximately 1050 cm^{-1} and this is possibly attributed to SiO_2 formed by the oxidation of the silicon substrate. A small unknown peak can be detected at about 560 cm^{-1}, which is possibly due to the M-O-M vibrations (M: metal) of PZT material. Peaks observed at approximately 2300 cm^{-1} could be attributed to CO_2 molecular vibrations. At the lower temperature of 150°C, the amount of CO_2 is inconsiderable. However as the temperature increased to 400°C, there is a significant increase in this peak, which could be explained by the oxidation of carbonaceous compounds obtained from the degradation of PVP at this temperature. At 650°C a shortened peak can be detected, which could be attributed to the complete oxidation of the carbonaceous compounds on the surface of the specimen and significant quantities of the carbon dioxide would have escaped as a gas at this temperature with insignificant amount left and absorbed on the surface.

From the infrared absorption spectra of the films heated at different temperature, it is deductible that (i) acetic acid and 1-propanol evaporated before 150°C but also reacted to form other organic compounds that can be removed at higher temperatures; (ii) PVP was completely decomposed after 400°C which correlates with the TGA result shown in **Figure 6.3**, where a considerable weight loss can be observed between 300°C and 450°C; (iii) at 650°C only metal oxide compounds can be observed, which confirms that PVP has been completely removed without contaminating the composition of metal oxide at 650°C.

6.3 Printing of PZT track-structures

6.3.1 Conditions of printing process

The printing system comprised an electrohydrodynamic atomization set-up and an x-y axis computer controlled motion device, both of which have been described in **Chapter 3**. Ti/Pt coated silicon wafers were selected as the collecting substrates for PZT track-structures, which was held by an A4 paper fixed between two plastic holders. A point electrode was used as the ground electrode which was aligned with the needle. Both the needle and the point-like electrode were kept ~1mm away from the substrate on either side. A high-speed camera, in combination with a fibre optic light source, was used to capture graphical data during the electrohydrodynamic printing process.

The PZT/PVP solutions of four different volume ratios were used to print track-structures. Electrohydrodynamic printing was afforded in the stable cone-jet mode for all solutions. The conditions required to print the track structures, in the stable cone-jet mode, are described in **Table 6.2**.

Table 6.2 *Printing parameters of four PZT/PVP solutions**

PZT/PVP volume ratio	1:1	1:2	1:3	1:4
Flow rate ($m^3 s^{-1}$)	1.7×10^{-11}	1.7×10^{-11}	1.7×10^{-11}	1.7×10^{-11}
Applied voltage (kV)	3.2	3.1	3.1	2.9

* The distance between the needle and the substrate was kept as ~1mm

Figure 6.5 shows the spray-printing process in the cone-jet mode, captured using the fibre-optic-light coupled high speed camera device. As shown in the image, the distance between the needle exit and substrate was kept constant. A stable cone-jet mode can be observed in which the jet breaks up in a short length and the droplets were generated and dispersed on the substrate in a small area, rather than sprayed in a large pattern, as the collecting distance is much smaller than the one used in spray-deposition process (i.e. ~10mm). The flow rate was kept as a constant and was significantly reduced (by three times) compared to the value utilized in the electrohydrodynamic deposition process (**Chapter 5**) in order to generate finer-scale structures, because it has been reported that the flow rate is an important parameter in the electrohydrodynamic printing process and plays a role in track resolution and scattering (Gupta *et al.* 2007).

A track-structure pattern program was uploaded to the motion controller system by which the substrate was moved in the straight line direction so that a track structure can be directly written onto the substrate in the stable cone-jet mode condition. The length of each printed track was approximately 20mm as set in the program.

6.3.2 Heat treatment of printed PZT track-structures

The PZT track-structures were printed on a Ti/Pt coated silicon wafer using PZT/PVP solutions of four different volume ratios. The four as-printed structures were heat treated at 650°C for 1200s, which is necessary for perovskite PZT formation. The heating ramp rate was set as 5°C per minute to allow the organic moieties to be

removed moderately and then furnace cooling was used to let the sample return to the ambient temperature. The PVP polymer constituent within the tracks can be removed by decomposition and evaporation during heat treatment, as discussed in the earlier section. The resultant four tracks, namely a, b, c and d (initially obtained from 1:1, 1:2, 1:3 and 1:4 PZT/PVP solutions, respectively), displayed no evidence of cracking under the optical microscope.

6.4 Analysis of PZT track-structures

6.4.1 Microstructures of the printed lines

The microstructure of the PZT tracks a, b, c, and d printed using four different PZT/PVP solutions were studied using an optical microscope. A segment of each track was analysed and the micrographs are shown in **Figure 6.6 (a) (b) (c)** and **(d)**.

All printed PZT track-structures possess comparable appearances after heat treatment, independent of the volume ratios of the PZT/PVP solutions. All the segments appear dense and continuous, without any break or voids within the tracks. This observation is different from the structures in other works (Rocks *et al.* 2007) where obvious cracks can be detected when using high concentration PZT sol. The generation of crack-free structures correlates well with the former findings, in which PVP polymers are expected to serve as capping agents which inhibit the condensation of the material during heat treatment and thus ultimately suppresses the crack formation within the structures.

A well defined printed edge can be observed in all the segments shown in **Figure 6.6**. This clear definition of the PZT track edge is different from the finding in other works. In Rocks *et al*'s work (referenced above), the printed lines were not continuous and the definition at the edge of the structures was decreased when the width of the structures were increased using lower concentration sol; in the work of Ahmad *et al.* (In press), significant scattering is apparent when the structures containing hydroxyapatite nano-particles were printed on a glass slide. Therefore it is believed that the additional PVP polymer has improved the quality of the printed tracks, with the reasons as follows. Firstly, the incorporation of PVP polymer solution into the parent sol increases the viscosity of the printed precursors, which can restrain the impact of the sprayed droplets on the substrate and thus diminishes the scattering of the printed structures. Secondly, the capping effect of the PVP polymers during the heat treatment may also promote the structural relaxation in the printed line, which is believed to improve the density and the definition of the structures.

6.4.2 Size of the printed lines

The average width of the printed lines was measured using Image Pro-Express software after calibration of an image with known dimensions. **Table 6.3** summaries the line width printed using the PZT/PVP solution of different volume ratios.

Table 6.3 *Geometries of printed lines*

Volume ratio (PZT:PVP)	1:1	1:2	1:3	1:4
Line width (μm)	176	166	155	135

The values in **Table 6.3** exhibit a trend where the width of the printed line decreases as the volume of the PVP solution is increased. There are two reasons for this. Firstly, the incorporation of the PVP solution reduces the concentration of the PZT sol, which means smaller amount of PZT material can be obtained compared with the one from higher concentration under the unique printing conditions (identical flow rate and printing speed). It has been confirmed that PVP is totally removed after heat treatment at 650°C, therefore the volume of the printed structures after heat treatment is smaller for the printed solution with a higher PVP ratio. Secondly, the viscosity of the mixed solution increases when the volume of the viscous PVP solution is increased. The high viscosity of the liquid constrains the fluidity of it which will remain in a small contact area when deposited on the substrate. Considering the two factors presented, the tendency shown in **Table 6.3** is appropriate.

6.5 Summary

In summary, electrohydrodynamic printing is a prospective printing technique for patterning functional ceramics such as PZT in track-structures. Incorporation of PVP polymer into PZT precursors for the printing process overcomes some limitations. Addition of PVP is effective in inhibiting crack formation which commonly arises in other works after heat treatment. This is speculated as PVP possibly promotes plastic deformation or structural relaxation in the printed structure during the heat treatment thus suppresses the cracking. The definition of the printed structures can also be improved when the PVP polymer was incorporated. The FTIR result illustrated that

PVP is completely removed after heat treatment at 650°C. The PVP polymer could decompose to carbonaceous specious which may undergo oxidation and evolve as carbon dioxide. This process may reduce the metallic elements in the PZT material and result in non-stoichiometry of the compound, forming the second phase pyrochlore. Employment of a tube furnace with extra oxygen supplementation is suggested for the development of this process, which is planned as possible future work. Under the unique processing conditions, the width of the printed structures decreased when the PVP ratio was increased, this was mainly due to the large volume shrinkage of low concentration PZT precursor, which at higher ratios may lead to cracking. Therefore an upper and lower limit of the PVP concentration needs to be developed and this has been suggested as future work too.

Figures

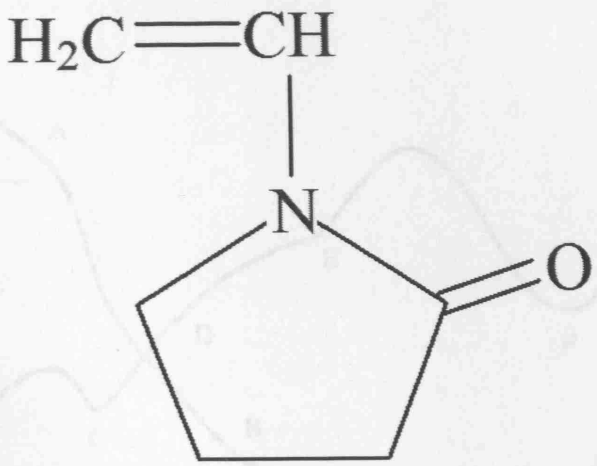

Figure 6.1 Molecular structure of PVP monomer. The amide group (-$CONH_2$) is believed to be able to hybridize with metalloxane polymers.

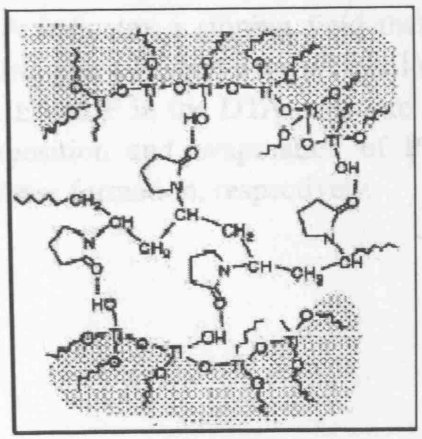

Figure 6.2 The mechanism of capping of metalloxane polymer OH groups by PVP polymer long chains (Kozuka *et al.* 2000).

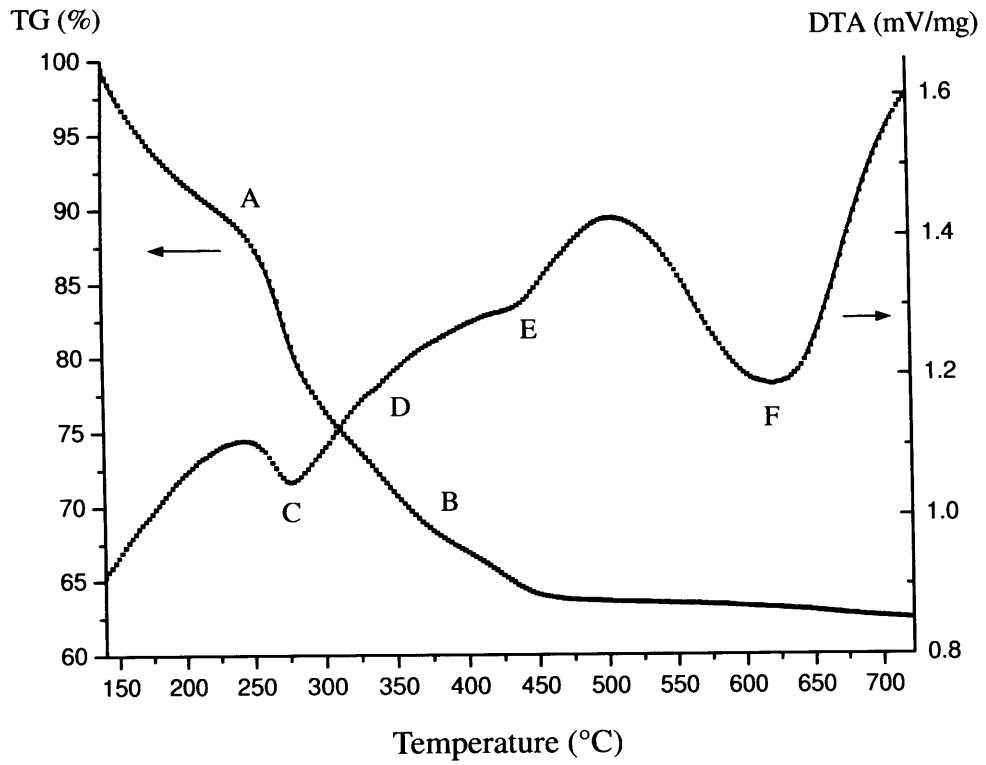

Figure 6.3 Thermogravimetric and differential thermal traces of the gel dried from 1:1 PZT/PVP solution. Point A indicates a sloping field that is believed to retard the condensation of the structure. Point B shows the weight loss due to removal of PVP. The change at point C, D, E and F in the DTA curve are induced by evaporation of organic substance, decomposition and evaporation of PVP, the pyrochlore phase formation and perovskite phase formation, respectively.

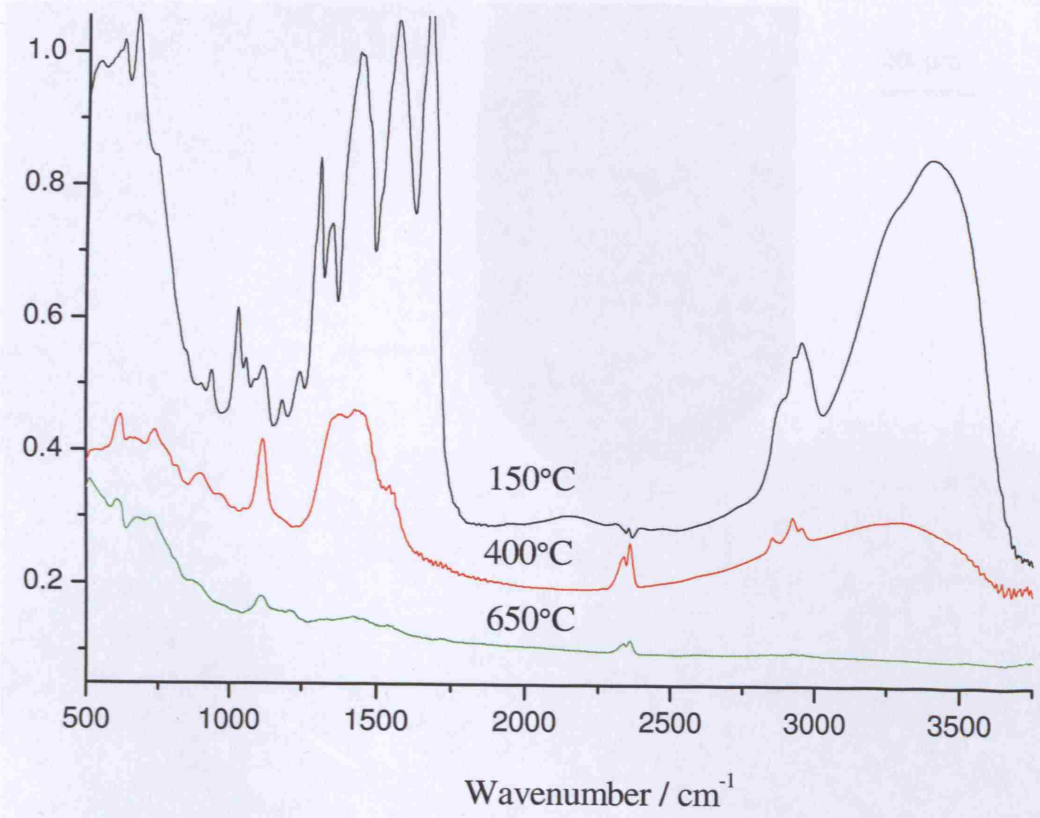

Figure 6.4 Infrared absorption spectra of the film deposited on the Ti/Pt coated silicon wafer using 1:1 PZT/PVP solution. The as-deposited structures were heated at 150°C, 400°C and 650°C for 1200s, as shown in the graph respectively.

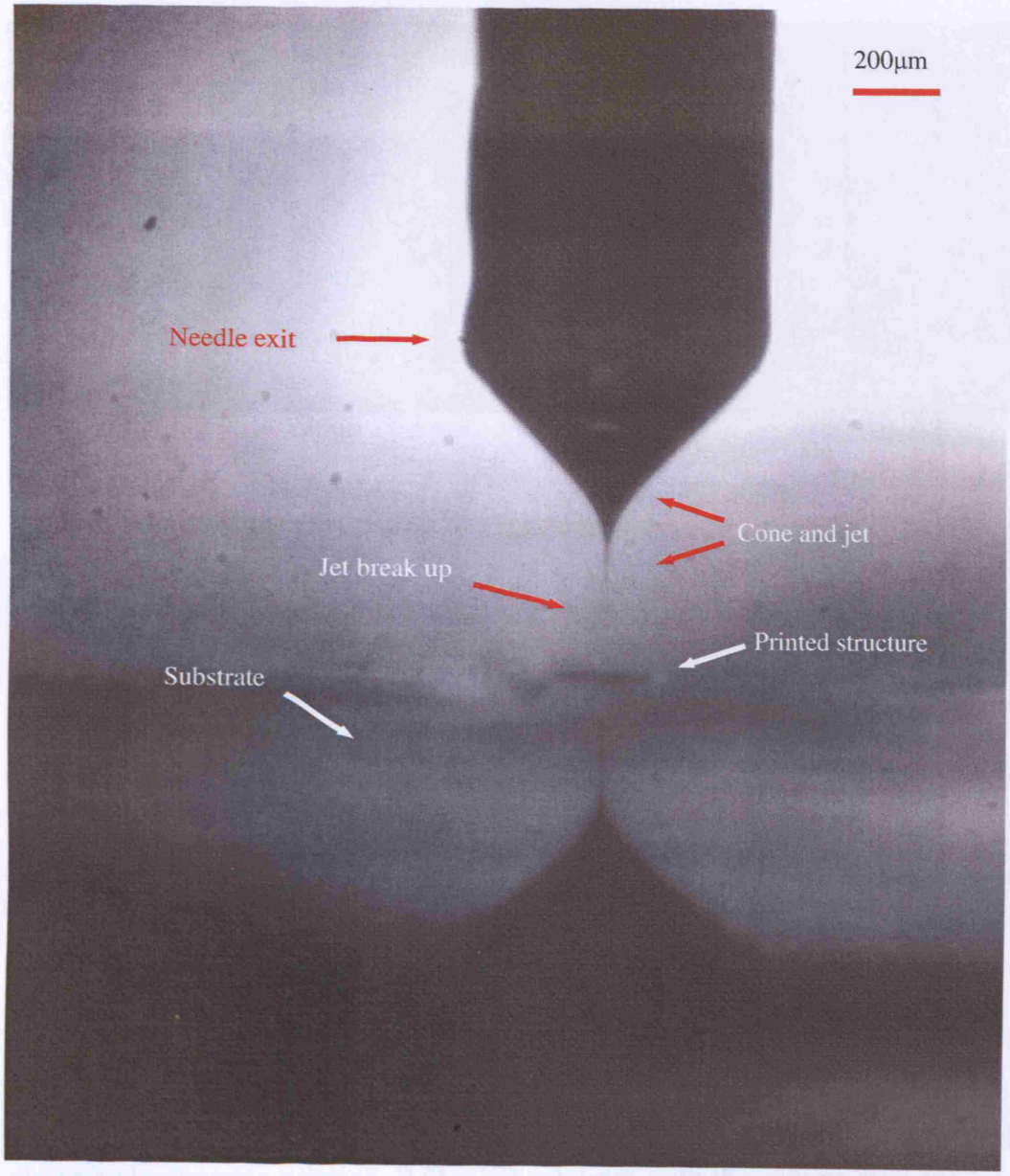

Figure 6.5 The cone-jet mode in electrohydrodynamic printing process. The distance between the needle exit and the substrate was 1mm. The track-structure was deposited after the jet break up in a short length without spraying in a large area.

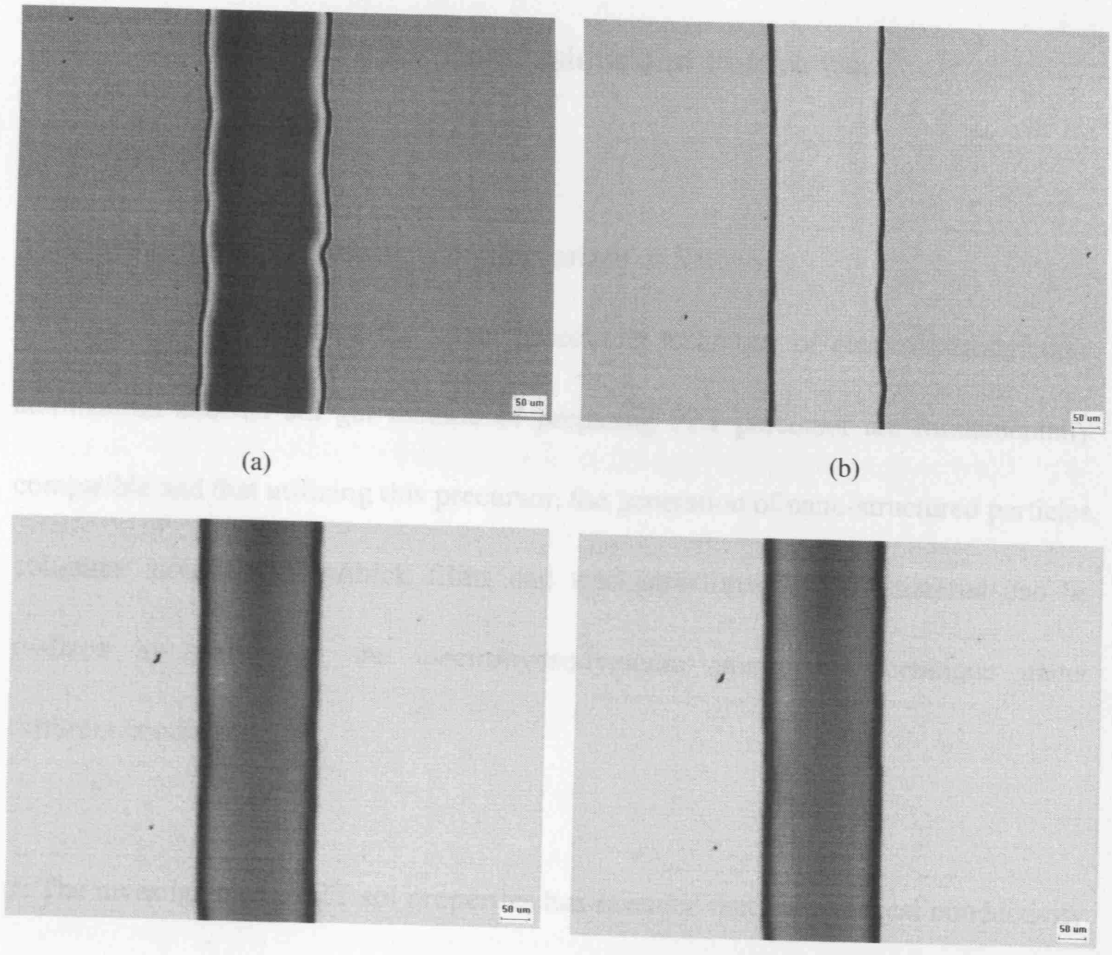

Figure 6.6 Light microscope micrographs of PZT track-structures produced by electrohydrodynamic printing. PZT/PVP solutions with the volume ratio **(a)** 1:1, **(b)** 1:2, **(c)** 1:3 and **(d)** 1:4 were used. The structures were heated at 650°C for 1200s after printed on Ti/Pt coated silicon substrate.

CHAPTER 7 Conclusions and Future work

7.1 Conclusions

The conclusions of this research are summarized as follows:

1. It has been proven that the novel processing technique of electrohydrodynamic atomization and the sol gel method of preparing PZT precursor are fundamentally compatible and that utilizing this precursor, the generation of nano-structured particles, columnar structures, thin/thick films and track-structures of PZT material can be realized by performing the electrohydrodynamic atomization technique under different conditions.

2. The investigation of PZT sol properties has revealed that the electrical conductivity of the sol is higher (4.4×10^{-3} S m^{-1}) than the value in literature, which results in the sprayed droplets being highly attractive to the ground electrode. The yield of the 0.6M PZT sol is approximately 13 wt% after heat treatment at 650°C, which is the most suitable heating temperature. Heating duration affects the PZT structures and a reduced content of second phase pyrochlore can be observed when the holding time is reduced from 3600s to 1200s, which indicates that 1200s is an ideal holding time for heat treatment of the PZT material considered in this work.

3. When using the ring electrode, 0.6M PZT sol can be sprayed in the cone-jet mode and nearly monodispersed droplets can be observed with average diameter of approximately 1μm. The mode selection map of this sol can be constructed from 5×10^{-12} m^3 s^{-1} up to the critical flow rate point (1.2×10^{-10} m^3 s^{-1}) after which the stable

cone-jet mode is not attainable. At a constant flow rate in the stable cone-jet mode regime, upper and lower limit of applied voltage can be observed, between which the cone depth is varied proportionally with the applied voltage.

4. Discrete PZT particles can be obtained on a metal substrate after spraying-deposition of PZT sol in the cone-jet mode and heat treatment at 650°C. The geometry of deposited patterns is not affected by the geometry of the substrate. The spherical particles in the deposit are of approximately 100nm in diameter and considered as characteristic of electrohydrodynamic atomization.

5. The concentration of the sol precursor has a significant effect on the as-deposited structures during electrohydrodynamic deposition, which is due to the different size of the droplets formed during electrospraying and the evaporation of them during their transportation to the substrate. The preferential landing of charged particles is also a factor that contributes to this feature.

6. 0.6M PZT sol is suitable for generating columnar PZT structures by electrohydrodynamic deposition. A 3-stage growth process can be observed in the columnar PZT structure of which a thickness of 35μm can be obtained after 330s of deposition, followed by heat treatment at 650°C for 1200s.

7. Substrate temperature has a significant effect on the columnar structure during deposition; the structure becomes smaller and denser when the substrate temperature

increases from the ambient temperature to 175°C, which is attributable to the change in electrical conductivity of the deposited columns.

8. Columnar PZT structures are of high interest when produced as 1-3 composites. In this work, PZT/polymer 1-3 composites can be produced by infiltrating a liquid polymer (photoresist) among the PZT columns that are generated using electrohydrodynamic deposition. The relative permittivity and the dissipation factor of such composites are 105 and 0.021, respectively, and the relative permittivity of the columnar PZT material can be calculated as 154.

9. Continuous PZT films can be obtained when 0.06M PZT sol is used during electrohydrodynamic deposition. A repeated procedure of spray and drying is suitable for the film generation and a PZT film with the thickness of approximately 645nm can be obtained after being processed for three times, which indicates a higher efficiency of this process when compared with other techniques. 650°C is the suitable temperature for sintering such structures. The frequency variation of the relative permittivity and the dissipation factor of the PZT film can be obtained at room temperature and these two values at 50 kHz are 90 and 0.059, respectively, which are not comparable to the values of the columnar structures. This is possibly due to the slightly higher content of second phase pyrochlore.

10. Electrohydrodynamic printing, which is another derivative technique from electrohydrodynamic atomization, is a versatile printing technique to generate PZT

track-structures. Slightly different from the deposition process, the printing is realized by collecting the droplets close to the jet break-up.

11. Incorporation of PVP polymer into PZT sol can effectively eliminate the crack formation within the printed structure after heat treatment. A more defined edge can be obtained, which improves the resolution of the printed features. More volume reduction occurs in the structures obtained using higher PVP-content solution, which implies an upper limit of the PVP content because excessive shrinkage of the structure may produce cracks again.

12. The PVP polymer in the printed structure can be removed at approximately 450°C. The polymer decomposes to carbonaceous species that subsequently react with oxygen to form carbon dioxide and escape from the structures. The presence of carbonaceous species within the structure during heat treatment can influence the metallic elements and results in a non-stiochiometry of the PZT compound, which can result in the formation of the second phase pyrochlore. According to this, a tube furnace with extra oxygen supplementation should be used during heat treatment.

7.2 Future work

Considering the experimental work carried out and the results obtained in this research, several aspects of future work are recommended and these are given below.

The mode selection map for 0.6M PZT sol should be developed from 2D to 3D, by

incorporating another parameter, spraying distance. Since it has been revealed that the droplet transportation has a considerable effect on the as-deposited structures, the distance travelled by the droplets is of importance when utilizing the electrohydrodynamic atomization technique. The varying distance could influence other parameters such as flow rate and applied voltage when the stable cone-jet mode is expected, which could subsequently change the configuration of the stable cone-jet mode map. Therefore, a 3D mode selection map composed of flow rate, applied voltage and spray distance should be constructed, from which a stable cone-jet mode triaxial space can be identified.

The discrete particles obtained on the copper substrate by electrohydrodynamic atomization are spherical and monodispersed. The mechanism of this nanoparticle formation is unknown so far. Further investigation can be carried out specifically on the droplet wetting on copper surface considering the surface tension. The kinetics of the sprayed droplets impacting on the copper surface at the initial stage should be closely observed using a high resolution camera. The dynamics of the as-sprayed droplets on both the substrate and the as-deposited ceramic layers should be modelled, which is expected to be helpful for understanding the mechanism of the spherical-nanoparticle formation.

A small amount of the second phase can be observed in the heat-treated PZT powders and deposits. It is suggested that extra lead should be incorporated into the PZT sol solution to compensate for the loss during the heat treatment (the current 0.1mole

extra lead should be increased to a more suitable content). An alternative heating process can also be attempted to restrain the lead loss at high temperatures (e.g. rapid thermal annealing).

The evaporation of sprayed droplets in the transportation stage during electrohydrodynamic deposition should be investigated exhaustively. When travelling to the substrate, the droplet size at different heights should be measured using an accurate laser detector by which the particles in micrometer or submicrometer size can be detected. Utilizing this procedure, droplets sprayed from different concentrations of precursor can be examined and various evaporation rates of the sprayed droplets from those precursors can be investigated, which may be helpful to further understand how the concentration of the sprayed sol affects the as-deposited structures.

When forming columnar PZT structures using electrohydrodynamic deposition, higher concentration of PZT sol should be investigated (currently 0.6M sol is used). The configuration of the generated columns should be investigated considering the area density and the growth rate of the columns.

The continuous PZT films processed by electrohydrodynamic deposition are not dense enough, although dense films are mostly expected when being used in electrical applications. The micro-pores present in the generated structures seem to be characteristic of this processing technique. The reason is not completely understood

but part of it may be due to the agglomeration of the produced particles during deposition (even 0.06M sol is used). Several means can be utilized to restrain the dry particle formation. A suitable suggestion is to select a second solvent to be applied during the spraying. A coaxial needle can be utilized for this method, of which the inner channel is kept as in this work and the other solvent can be ejected through the outer channel. The aim of this set-up is to reduce the evaporation degree of the droplets during spraying and keep them in a viscous liquid state which can reduce the agglomeration and allows forming an interconnected three dimensional structures on the substrate. The amount of the second solvent should be examined when using this method, since the sol of excessively low concentration may produce holes in the deposited structure due to the lower volume of PZT material obtained at a defined deposition time (similar to **Figure 5.2 C1** and **C2**).

Additionally, a vacuum chamber can also be combined with the deposition set-up, in which the droplets can be delivered to the substrate with less thermal exchange with the environment thus reduce the evaporation. This tentative plan may also be useful to stabilize the cone-jet mode during the deposition in that any air flow near the needle exit may affect the mode stability which may influence the homogeneity of the generated structures.

Effect of substrate temperature on the morphology of columnar PZT structures should be further investigated. The relationship between the substrate temperature and the area density of the columns should be established. This development could realize the

precise control of the morphology of columns by varying the substrate temperature, which is valuable for the PZT fabrication when a specific column size and density are in demand.

Electrohydrodynamic printing is a novel and pospective technique, which should be developed for processing MEMS fabrications. The printing structures need to be improved from single track-structures to more complex ones (e.g. curvilinear, circular and square structures). These curves, angles and corners should be printed accurately by adjusting the acceleration and deceleration of the printer, the flow rate of the liquid and also the applied voltage, so that the capillary can remain in the stable cone-jet mode during the entire printing process.

It has been revealed that it is successful to incorporate PVP polymer into PZT sol to eliminate the crack formation during the printing process. However, an upper limit of the PVP content needs to be investigated since excessive shrinkage of the structure due to the removal of PVP may induce cracking again. It is recommended that more volume ratios of PZT and PVP solutions should be examined, amongst which an ideal ratio can be identified.

When heat treating the PVP contained PZT printed structures, a tube furnace with oxygen supplementation should be used because of the formation of carbon spacious during the PVP polymer decomposition. The tube can be designed with two channels at both ends for the passage of the air with a valve to control the flow rate of it. The

extra oxygen is not only necessary for the perovskite PZT formation but also beneficial for the removal of PVP polymer during its decomposition.

The cross-sectional structures of the printed tracks should be investigated using scanning electron microscope. The relationship between the structure thickness and the flow rate, the volume ratio of precursor and the printing speed should be examined. Piezoelectric properties of the tracks should be investigated, such as piezoelectric coefficient and relative permittivity.

Electrohydrodynamic printing technique should be developed to produce PZT structures in three dimensions. The architectures should be built up in z direction by the add-on process (layer by layer). The hollow parts within the structure can be occupied by some sacrificial materials which can be removed after subsequent heat treatment. Some organic binders are possibly necessary to enhance the mechanical property of the architecture and such organic materials should be examined when used in terms of the residual content, volume shrinkage and so on.

It is also recommended that further exploration should be carried out for the development of drop-on-demand 2D and 3D electrohydrodynamic printing technique, similar to the one in the ink-jet printing process. This will enable the direct writing of more complex patterns in high resolution using electrohydrodynamic jetting.

REFERENCES

Adachi, H., Mitsuyu, T., Yamazaki, O., & Wasa, K. 1986, "Ferroelectric (Pb,La)(Zr,Ti)O_3 epitaxial thin-films on sapphire grown by RF-planar magnetron sputtering", *Journal of Applied Physics*, vol. 60, no. 2, pp. 736-741.

Ahmad, Z., Thian, E., Huang, H., Edirisinghe, M., Jayasinghe, S., Best, S., Bonfield, W., Brooks, R., & Rushton, N, "Deposition of nano-hydroxyapatite utilising direct and transitional electrohydrodynamic processes", *Journal of Materials Science: Materials in Medicine*, In press.

Alguero, M., Bushby, A. J., Reece, M. J., Calzada, M. L., & Pardo, L. 2001, "Mechanical characterisation of ferroelectric thin films for MEMS", *Integrated Ferroelectrics*, vol. 32, no. 1-4, pp. 775-784.

Allen, S. D. 1981, "Laser chemical vapor-deposition - A technique for selective area deposition", *Journal of Applied Physics*, vol. 52, no. 11, pp. 6501-6505.

Anderson, J. C., Leaver, K. D., Rawlings, R. D., & Alexander, J. M. 1990, *Materials Science, Forth edition* Thomson Learning.

Asano, G., Morioka, H., Funakubo, H., Shibutami, T., & Oshima, N. 2003, "Fatigue-free RuO_2/Pb(Zr,Ti)O_3/RuO_2 capacitor prepared by metalorganic chemical vapor deposition at 395 degrees C", *Applied Physics Letters*, vol. 83, no. 26, pp. 5506-5508.

Auciello, O., Foster, C. M., & Ramesh, R. 1998, "Processing technologies for ferroelectric thin films and heterostructures", *Annual Review of Materials Science*, vol. 28, pp. 501-531.

Ben Ali, M., Ondarcuhu, T., Brust, M., & Joachim, C. 2002, "Atomic force microscope tip nanoprinting of gold nanoclusters", *Langmuir*, vol. 18, no. 3, pp. 872-876.

Benjamin, K. C. 2002, "Recent advances in 1-3 piezoelectric polymer composite transducer technology for AUV/UUV acoustic imaging applications", *Journal of Electroceramics*, vol. 8, no. 2, pp. 145-154.

Berlincourt, D. 1959, "Transducer properties of lead titanate zirconate ceramics", *Proceedings of the IRE*, vol. 47, no. 3, pp. 482-485.

Berlincourt, D. 1960, "Piezoelectric properties of polycrystalline lead titanate zirconate compositions", *Proceedings of the IRE*, vol. 48, no. 2, pp. 220-229.

Beuth, J. & Klingbeil, N. 2001, "The role of process variables in laser-based direct metal solid freeform fabrication", *JOM-Journal of the Minerals Metals & Materials Society*, vol. 53, no. 9, pp. 36-39.

Bhatti, A. R., Mott, M., Evans, J. R. G., & Edirisinghe, M. J. 2001, "PZT pillars for 1-3 composites prepared by ink-jet printing", *Journal of Materials Science Letters*, vol. 20, no. 13, pp. 1245-1248.

Boughaba, S. 2000, "Synthesis of tantalum pentoxide films by pulsed laser deposition: material characterization and scale-up", *Thin Solid Films*, vol. 358, no. 1-2, pp. 104-113.

Bourell, D. L., Marcus, H. L., Barlow, J. W., & Beaman, J. J. 1992, "Selective Laser Sintering of Metals and Ceramics", *International Journal of Powder Metallurgy*, vol. 28, no. 4, pp. 369-381.

Braccini, V., Marre, E., Ferdeghini, C., Malagoli, A., Mollica, A., Putti, M., Balestrino, G., Lavanga, S., Medaglia, P. G., & Siri, A. S. 2001, "Transport property characterization of (Ba,La)CuO_2/$CaCuO_2$ superconducting multilayers deposited by pulsed laser ablation", *Superconductor Science & Technology*, vol. 14, no. 8, pp. 561-566.

Bradley, D. C. 1989, "Metal alkoxides as precursors for electronic and ceramic materials", *Chemical Reviews*, vol. 89, no. 6, pp. 1317-1322.

Brinker, C. J., Hurd, A. J., Schunk, P. R., Frye, G. C., & Ashley, C. S. 1992, "Review of sol-gel thin-film formation", *Journal of Non-Crystalline Solids*, vol. 147, pp. 424-436.

Budhani, R. C., Prakash, S., Doerr, H. J., & Bunshah, R. F. 1987, "Structural order in Si-N and Si-N-O films prepared by plasma assisted chemical vapor-deposition process", *Journal of Vacuum Science & Technology A-Vacuum Surfaces and Films*, vol. 5, no. 4, pp. 1644-1648.

Burianova, L., Hana, P., Panos, S., Furman, E., Zhang, S., & Shrout, T. R. 2004, "Hydrostatic piezoelectric coefficient d_h of PZT ceramics and PZN-PT and PYN-PT single crystals", *Journal of Electroceramics*, vol. 13, no. 1-3, pp. 443-448.

Busch, G. 1987, "History of ferroelectricity: 1. Early history of ferroelectricity", *Ferroelectrics*, vol. 74, no. 3-4, pp. 267-284.

Calvert, P. 2001, "Inkjet printing for materials and devices", *Chemistry of Materials*, vol. 13, no. 10, pp. 3299-3305.

Carrin, A. 1997, "Technology forecast on ink-jet head technology applications in rapid prototyping", *Rapid Prototyping Journal*, vol. 3, no. 17, pp. 99-115.

Chen, C. H., Emond, M. H. J., Kelder, E. M., Meester, B., & Schoonman, J. 1999a, "Electrostatic sol-spray deposition of nanostructured ceramic thin films", *Journal of Aerosol Science*, vol. 30, no. 7, pp. 959-967.

Chen, C. H., Kelder, E. M., Jak, M. J. G., & Schoonman, J. 1996a, "Electrostatic spray deposition of thin layers of cathode materials for lithium battery", *Solid State Ionics*,

vol. 86-8, pp. 1301-1306.

Chen, C. H., Kelder, E. M., & Schoonman, J. 1996, "Unique porous $LiCoO_2$ thin layers prepared by electrostatic spray deposition", *Journal of Materials Science*, vol. 31, no. 20, pp. 5437-5442.

Chen, C. H., Kelder, E. M., & Schoonman, J. 1999b, "Electrostatic sol-spray deposition (ESSD) and characterisation of nanostructured TiO_2 thin films", *Thin Solid Films*, vol. 342, no. 1-2, pp. 35-41.

Chen, C. H., Kelder, E. M., vanderPut, P. J. J. M., & Schoonman, J. 1996b, "Morphology control of thin $LiCoO_2$ films fabricated using the electrostatic spray deposition (ESD) technique", *Journal of Materials Chemistry*, vol. 6, no. 5, pp. 765-771.

Chen, D. R., Pui, D. Y. H., & Kaufman, S. L. 1995, "Electrospraying of conducting liquids for monodisperse aerosol generation in the 4 nm to 1.8 μm diameter range", *Journal of Aerosol Science*, vol. 26, no. 6, pp. 963-977.

Chen, F., Yang, S. Y., Wang, J. X., He, H. L., & Wang, G. C. 2007, "Effect of cylindrical shock synthesis on properties and sintering behavior of PZT 95/5 powder", *Journal of Inorganic Materials*, vol. 22, no. 5, pp. 827-832.

Chen, S. Y. & Chen, I. W. 1998, "Texture development, microstructure evolution, and crystallization of chemically derived PZT thin films", *Journal of the American Ceramic Society*, vol. 81, no. 1, pp. 97-105.

Chen, Y. Z., Ma, J., & Zhang, J. X. 2003, "Thermal analysis of the seeded lead zirconate titanate sol-gel system", *Materials Letters*, vol. 57, no. 22-23, pp. 3392-3396.

Chiang, Y.-M., Birnie, D. P., & Kingery, W. D. 1996, *Physical Ceramics: Principles for Ceramic Science and Engineering* John Wiley & Sons.

Choi, J. J., Park, G. T., Park, C. S., & Kim, H. E. 2005, "Ferroelectric and piezoelectric properties of highly oriented $Pb(Zr,Ti)O_3$ film grown on $Pt/Ti/SiO_2/Si$ substrate using conductive lanthanum nickel nitrate buffer layer", *Journal of Materials Research*, vol. 20, no. 3, pp. 726-733.

Choy, K. L. 2003, "Chemical vapour deposition of coatings", *Progress in Materials Science*, vol. 48, no. 2, pp. 57-170.

Chrisey, D. B., Pique, A., Modi, R., Wu, H. D., Auyeung, R. C. Y., & Young, H. D. 2000, "Direct writing of conformal mesoscopic electronic devices by MAPLE DW", *Applied Surface Science*, vol. 168, no. 1-4, pp. 345-352.

Cloupeau, M. & Prunetfoch, B. 1989, "Electrostatic spraying of liquids in cone-jet mode", *Journal of Electrostatics*, vol. 22, no. 2, pp. 135-159.

Cloupeau, M. & Prunetfoch, B. 1990, "Electrostatic spraying of liquids - main functioning modes", *Journal of Electrostatics*, vol. 25, no. 2, pp. 165-184.

Cloupeau, M. & Prunetfoch, B. 1994, "Electrohydrodynamic spraying functioning modes - A critical-review", *Journal of Aerosol Science*, vol. 25, no. 6, pp. 1021-1036.

Cuk, T., Troian, S. M., Hong, C. M., & Wagner, S. 2000, "Using convective flow splitting for the direct printing of fine copper lines", *Applied Physics Letters*, vol. 77, no. 13, pp. 2063-2065.

Damjanovic, D. 1998, "Ferroelectric, dielectric and piezoelectric properties of ferroelectric thin films and ceramics", *Reports on Progress in Physics*, vol. 61, no. 9, pp. 1267-1324.

Demartin, M. & Damjanovic, D. 1996, "Dependence of the direct piezoelectric effect in coarse and fine grain barium titanate ceramics on dynamic and static pressure", *Applied Physics Letters*, vol. 68, no. 21, pp. 3046-3048.

Demers, L. M., Ginger, D. S., Park, S. J., Li, Z., Chung, S. W., & Mirkin, C. A. 2002, "Direct patterning of modified oligonucleotides on metals and insulators by dip-pen nanolithography", *Science*, vol. 296, no. 5574, pp. 1836-1838.

Dimos, D. & Mueller, C. H. 1998, "Perovskite thin films for high-frequency capacitor applications", *Annual Review of Materials Science*, vol. 28, pp. 397-419.

Dorey, R. A., Stringfellow, S. B., & Whatmore, R. W. 2002, "Effect of sintering aid and repeated sot infiltrations on the dielectric and piezoelectric properties of a PZT composite thick film", *Journal of the European Ceramic Society*, vol. 22, no. 16, pp. 2921-2926.

Dorey, R. A. & Whatmore, R. W. 2004, "Electroceramic thick film fabrication for MEMS", *Journal of Electroceramics*, vol. 12, no. 1-2, pp. 19-32.

Du, X. H., Zheng, J. H., Belegundu, U., & Uchino, K. 1998, "Crystal orientation dependence of piezoelectric properties of lead zirconate titanate near the morphotropic phase boundary", *Applied Physics Letters*, vol. 72, no. 19, pp. 2421-2423.

Duval, F. F. C., Dorey, R. A., Haigh, R. H., & Whatmore, R. W. 2003, "Stable TiO_2/Pt electrode structure for lead containing ferroelectric thick films on silicon MEMS structures", *Thin Solid Films*, vol. 444, no. 1-2, pp. 235-240.

Edirisinghe, M. J. & Jayasinghe, S. N. 2004, "Electrohydrodynamic atomization of a concentrated nano-suspension", *International Journal of Applied Ceramic Technology*, vol. 1, no. 2, pp. 140-145.

Eyett, M., Bauerle, D., Wersing, W., & Thomann, H. 1987, "Excimer-laser-induced etching of ceramic $PbTi_{1-x}Zr_xO_3$", *Journal of Applied Physics*, vol. 62, no. 4, pp. 1511-1514.

Ferrari, M., Ravera, F., Rao, S., & Liggieri, L. 2006, "Surfactant adsorption at superhydrophobic surfaces", *Applied Physics Letters*, vol. 89, no. 5, p. 053104.

Foster, C. M., Li, Z., Buckett, M., Miller, D., Baldo, P. M., Rehn, L. E., Bai, G. R., Guo, D., You, H., & Merkle, K. L. 1995, "Substrate effects on the structure of epitaxial $PbTiO_3$ thin-films prepared on MgO, $LaAlO_3$, and $SrTiO_3$ by metalorganic chemical-vapor-deposition", *Journal of Applied Physics*, vol. 78, no. 4, pp. 2607-2622.

Ganan-Calvo, A. M., Barrero, A., & Pantano-Rubino, C. 1993, "The electrohydrodynamics of electrified conical menisci", *Journal of Aerosol Science*, vol. 24, no. Supplement 1, pp. S19-S20.

Ganan-Calvo, A. M. 1994, "The size and charge of droplets in the electrospraying of polar liquids in cone-jet mode, and the minimum droplet size", *Journal of Aerosol Science*, vol. 25, no. Supplement 1, pp. 309-310.

Ganan-Calvo, A. M., Davila, J., & Barrero, A. 1997, "Current and droplet size in the electrospraying of liquids. Scaling laws", *Journal of Aerosol Science*, vol. 28, no. 2, pp. 249-275.

Gao, Y., Bai, G., Merkle, K. L., Shi, Y., Chang, H. L. M., Shen, Z., & Lam, D. J. 1993, "Microstructure of $PbTiO_3$ thin-films deposited on (001)MgO by MOCVD", *Journal of Materials Research*, vol. 8, no. 1, pp. 145-153.

Garno, J. C., Yang, Y. Y., Amro, N. A., Cruchon-Dupeyrat, S., Chen, S. W., & Liu, G. Y. 2003, "Precise positioning of nanoparticles on surfaces using scanning probe lithography", *Nano Letters*, vol. 3, no. 3, pp. 389-395.

Geissler, M. & Xia, Y. N. 2004, "Patterning: Principles and some new developments", *Advanced Materials*, vol. 16, no. 15, pp. 1249-1269.

Ginger, D. S., Zhang, H., & Mirkin, C. A. 2004, "The evolution of dip-pen nanolithography", *Angewandte Chemie-International Edition*, vol. 43, no. 1, pp. 30-45.

Grace, J. M. & Marijnissen, J. C. M. 1994, "A review of liquid atomization by electrical means", *Journal of Aerosol Science*, vol. 25, no. 6, pp. 1005-1019.

Griffith, L. G. & Naughton, G. 2002, "Tissue engineering - Current challenges and expanding opportunities", *Science*, vol. 295, no. 5557, p. 1009-1014.

Gupta, A., Seifalian, A. M., Ahmad, Z., Edirisinghe, M. J., & Winslet, M. C. 2007, "Novel electrohydrodynamic printing of nanocomposite biopolymer scaffolds", *Journal of Bioactive and Compatible Polymers*, vol. 22, no. 3, pp. 265-280.

Haaheim, J., Eby, R., Nelson, M., Fragala, J., Rosner, B., Zhang, H., & Athas, G. 2005, "Dip Pen Nanolithography (DPN): process and instrument performance with NanoInk's NSCRIPTOR system", *Ultramicroscopy*, vol. 103, no. 2, pp. 117-132.

Haertling, G. H. 1999, "Ferroelectric ceramics: History and technology", *Journal of the American Ceramic Society*, vol. 82, no. 4, pp. 797-818.

Hartman, R. P. A., Borra, J. P., Brunner, D. J., Marijnissen, J. C. M., & Scarlett, B. 1999a, "The evolution of electrohydrodynamic sprays produced in the cone-jet mode, a physical model", *Journal of Electrostatics*, vol. 47, no. 3, pp. 143-170.

Hartman, R. P. A., Brunner, D. J., Camelot, D. M. A., Marijnissen, J. C. M., & Scarlett, B. 1999b, "Electrohydrodynamic atomization in the cone-jet mode physical modeling of the liquid cone and jet", *Journal of Aerosol Science*, vol. 30, no. 7, pp. 823-849.

Hartman, R. P. A., Brunner, D. J., Camelot, D. M. A., Marijnissen, J. C. M., & Scarlett, B. 2000, "Jet break-up in electrohydrodynamic atomization in the cone-jet mode", *Journal of Aerosol Science*, vol. 31, no. 1, pp. 65-95.

Hayati, I., Bailey, A. I., & Tadros, T. F. 1987, "Investigations into the mechanisms of electrohydrodynamic spraying of liquids", *Journal of Colloid and Interface Science*, vol. 117, no. 1, pp. 205-230.

Heinzl, J. & Hertz, C. H. 1985, "Ink-jet printing", *Advances in Imaging and Electron Physics*, vol. 65, pp. 91-171.

Hohman, M. M., Shin, M., Rutledge, G., & Brenner, M. P. 2001, "Electrospinning and electrically forced jets", *Physics of Fluids*, vol. 13, no. 8, pp. 2201-2236.

Hu, S. H., Meng, X. J., Wang, G. S., Sun, J. L., & Li, D. 2004, "Preparation and characterization of multi-coating PZT thick films by sol-gel process", *Journal of Crystal Growth*, vol. 264, no. 1-3, pp. 307-311.

Huang, H., Yao, X., Wu, X. Q., Wang, M. Q., & Zhang, L. Y. 2004, "Morphology control of ferroelectric lead titanate thin films prepared by electrostatic spray deposition", *Thin Solid Films*, vol. 458, no. 1-2, pp. 71-76.

Izyumskaya, N., Alivov, Y., Cho, S. J., Morkoc, H., Lee, H., & Kang, Y. S. 2007, "Processing, structure, properties, and applications of PZT thin films", *Critical Reviews in Solid State and Materials Sciences*, vol. 32, pp. 111-202.

Jackman, R. J., Brittain, S. T., Adams, A., Prentiss, M. G., & Whitesides, G. M. 1998, "Design and fabrication of topologically complex, three-dimensional microstructures", *Science*, vol. 280, no. 5372, pp. 2089-2091.

Jaffe, B. 1971, *Piezoelectric Ceramics* Academic Press Inc.

Jaffe, B. 1954, "Piezoelectric properties of lead zirconate-lead titanate solid-solution ceramics", *Journal of Applied Physics*, vol. 25, no. 6, pp. 809-810.

Janas, V. F. & Safari, A. 1995, "Overview of fine-scale piezoelectric ceramic/polymer composite processing", *Journal of the American Ceramic Society*, vol. 78, no. 11, pp. 2945-2955.

Jaworek, A. & Krupa, A. 1998, "Main modes of electrohydrodynamic spraying of liquids", *Third International Conference on Multiphase Flow. Lyon, France.* pp. 8-12.

Jaworek, A. & Krupa, A. 1999a, "Classification of the modes of EHD spraying", *Journal of Aerosol Science*, vol. 30, no. 7, pp. 873-893.

Jaworek, A. & Krupa, A. 1999b, "Jet and drops formation in electrohydrodynamic spraying of liquids. A systematic approach", *Experiments in Fluids*, vol. 27, no. 1, pp. 43-52.

Jayadevan, K. P. & Tseng, T. Y. 2002, "Composite and multilayer ferroelectric thin films: processing, properties and applications", *Journal of Materials Science-Materials in Electronics*, vol. 13, no. 8, pp. 439-459.

Jayasinghe, S. N. & Edirisinghe, M. J. 2002a, "Effect of viscosity on the size of relics produced by electrostatic atomization", *Journal of Aerosol Science*, vol. 33, no. 10, pp. 1379-1388.

Jayasinghe, S. N. & Edirisinghe, M. J. 2002b, "Obtaining fine droplet relics by electrostatic atomization of viscous liquids", *Journal of Materials Science Letters*, vol. 21, no. 5, pp. 371-373.

Jayasinghe, S. N. & Edirisinghe, M. J. 2003, "A novel process for simulataneous printing of multiple tracks from concentrated suspensions", *Materials Research Innovations*, vol. 7, no. 2, pp. 62-64.

Jayasinghe, S. N. & Edirisinghe, M. J. 2004, "Electrostatic atomisation of a ceramic suspension", *Journal of the European Ceramic Society*, vol. 24, no. 8, pp. 2203-2213.

Jayasinghe, S. N. & Edirisinghe, M. J. 2005, "Electrostatic atomization of a ceramic suspension at pico-flow rates", *Applied Physics A-Materials Science & Processing*, vol. 80, no. 2, pp. 399-404.

Jayasinghe, S. N., Edirisinghe, M. J., & De Wilde, T. 2002, "A novel ceramic printing technique based on electrostatic atomization of a suspension", *Materials Research Innovations*, vol. 6, no. 3, pp. 92-95.

Jayasinghe, S. N., Edirisinghe, M. J., & Wang, D. Z. 2004, "Controlled deposition of nanoparticle clusters by electrohydrodynamic atomization", *Nanotechnology*, vol. 15, no. 11, pp. 1519-1523.

Jia, Q. X., Chang, L. H., & Anderson, W. A. 1995, "Low leakage current $BaTiO_3$ thin-film capacitors using a multilayer construction", *Thin Solid Films*, vol. 259, no. 2, pp. 264-269.

Jung, H., Kulkarni, R., & Collier, C. P. 2003, "Dip-pen nanolithography of reactive alkoxysilanes on glass", *Journal of the American Chemical Society*, vol. 125, no. 40, pp. 12096-12097.

Kidoh, H., Ogawa, T., Morimoto, A., & Shimizu, T. 1991, "Ferroelectric properties of lead-zirconate-titanate films prepared by laser ablation", *Applied Physics Letters*, vol. 58, no. 25, pp. 2910-2912.

Kim, K. & Lee, S. 2006, "Integration of lead zirconium titanate thin films for high density ferroelectric random access memory", *Journal of Applied Physics*, vol. 100, no. 5, p. 051604.

Kim, K. & Turnbull, R. J. 1976, "Generation of charged drops of insulating liquids by electrostatic spraying", *Journal of Applied Physics*, vol. 47, no. 5, pp. 1964-1969.

Kipkoech, E. R., Azough, F., & Freer, R. 2005, "Domain structures in perovskite-type lanthanum magnesium titanate ceramics", *Journal of the American Ceramic Society*, vol. 88, no. 3, pp. 768-772.

Klissurska, R. D., Tagantsev, A. K., Brooks, K. G., & Setter, N. 1995, "Effect of Nb doping on the hysteresis parameters of sol-gel derived $Pb_{1.1-x/2}(Zr_{0.53}TiO_{0.47})_{(1-x)}Nb_xO_3$ thin films", *Microelectronic Engineering*, vol. 29, no. 1-4, pp. 271-274.

Kozuka, H. & Kajimura, M. 1999, "Achievement of crack-free $BaTiO_3$ films over 1 μm in thickness via non-repetitive dip-coating", *Chemistry Letters* no. 10, pp. 1029-1030.

Kozuka, H., Kajimura, M., Hirano, T., & Katayama, K. 2000, "Crack-free, thick ceramic coating films via non-repetitive dip-coating using polyvinylpyrrolidone as stress-relaxing agent", *Journal of Sol-Gel Science and Technology*, vol. 19, no. 1-3, pp. 205-209.

Kozuka, H. & Takenaka, S. 2002, "Single-step deposition of gel-derived lead zirconate titanate films: Critical thickness and gel film to ceramic film conversion", *Journal of the American Ceramic Society*, vol. 85, no. 11, pp. 2696-2702.

Kukla, R. 1997, "Magnetron sputtering on large scale substrates: an overview on the state of the art", *Surface and Coatings Technology*, vol. 93, no. 1, pp. 1-6.

Kwok, C. K. & Desu, S. B. 1992, "Pyrochlore to perovskite phase-transformation in sol-gel derived lead-zirconate-titanate thin-films", *Applied Physics Letters*, vol. 60, no. 12, pp. 1430-1432.

Lange, F. F. 1984, "Sinterability of agglomerated powders", *Journal of the American Ceramic Society*, vol. 67, no. 2, pp. 83-89.

Le Dren, S., Simon, L., Gonnard, P., Troccaz, M., & Nicolas, A. 2000, "Investigation of factors affecting the preparation of PZT thick films", *Materials Research Bulletin*, vol. 35, no. 12, pp. 2037-2045.

Le, H. P. 1998, "Progress and trends in ink-jet printing technology", *Journal of Imaging Science and Technology*, vol. 42, no. 1, pp. 49-62.

Lee, Y. J. & Braun, P. V. 2003, "Tunable inverse opal hydrogel pH sensors", *Advanced Materials*, vol. 15, no. 7-8, pp. 563-566.

Lercel, M. J., Craighead, H. G., Parikh, A. N., Seshadri, K., & Allara, D. L. 1996, "Sub-10 nm lithography with self-assembled monolayers", *Applied Physics Letters*, vol. 68, no. 11, pp. 1504-1506.

Lewis, J. A. & Gratson, G. M. 2004, "Direct writing in three dimensions", *Materials Today*, vol. 7, no. 7-8, pp. 32-39.

Li, P. F., Jin, C. Q., Xiao, C. J., Wang, F. P., Wang, X. H., & Li, L. T. 2007, "Effect of annealing on ferroelectric properties of nanometre $BaTiO_3$ ceramics prepared by high pressure sintering method", *Chinese Physics Letters*, vol. 24, no. 1, pp. 244-247.

Li, Y., Maynor, B. W., & Liu, J. 2001, "Electrochemical AFM "Dip-Pen" Nanolithography", *Journal of the American Chemical Society*, vol. 123, no. 9, pp. 2105-2106.

Li, Y. Y., Cunin, F., Link, J. R., Gao, T., Betts, R. E., Reiver, S. H., Chin, V., Bhatia, S. N., & Sailor, M. J. 2003, "Polymer replicas of photonic porous silicon for sensing and drug delivery applications", *Science*, vol. 299, no. 5615, pp. 2045-2047.

Lim, D., Kamotani, Y., Cho, B., Mazumder, J., & Takayama, S. 2003, "Fabrication of microfluidic mixers and artificial vasculatures using a high-brightness diode-pumped Nd:YAG laser direct write method", *Lab on a Chip*, vol. 3, no. 4, pp. 318-323.

Lim, J. H. & Mirkin, C. A. 2002, "Electrostatically driven dip-pen nanolithography of conducting polymers", *Advanced Materials*, vol. 14, no. 20, pp. 1474-1477.

Liu, X. G., Fu, L., Hong, S. H., Dravid, V. P., & Mirkin, C. A. 2002, "Arrays of magnetic nanoparticles patterned via "dip-pen" nanolithography", *Advanced Materials*, vol. 14, no. 3, pp. 231-234.

Liu, X. G., Guo, S. W., & Mirkin, C. A. 2003, "Surface and site-specific ring-opening metathesis polymerization initiated by dip-pen nanolithography", *Angewandte Chemie-International Edition*, vol. 42, no. 39, pp. 4785-4789.

Livage, J., Henry, M., & Sanchez, C. 1988, "Sol-gel chemistry of transition metal oxides", *Progress in Solid State Chemistry*, vol. 18, no. 4, pp. 259-341.

Lohse, O., Grossmann, M., Boettger, U., Bolten, D., & Waser, R. 2001, "Relaxation mechanism of ferroelectric switching in $Pb(Zr,Ti)O_3$ thin films", *Journal of Applied Physics*, vol. 89, no. 4, pp. 2332-2336.

Lucovsky, G. & Tsu, D. V. 1987, "Plasma enhanced chemical vapor-deposition - Differences between direct and remote plasma excitation", *Journal of Vacuum Science & Technology A-Vacuum Surfaces and Films*, vol. 5, no. 4, pp. 2231-2238.

Lucovsky, G., Tsu, D. V., Kim, S. S., Markunas, R. J., & Fountain, G. G. 1989,

"Formation of thin-film dielectrics by remote plasma-enhanced chemical-vapor deposition (remote PECVD)", *Applied Surface Science*, vol. 39, no. 1-4, pp. 33-56.

Mackenzie, J. D. & Xu, Y. H. 1997, "Ferroelectric materials by the sol-gel method", *Journal of Sol-Gel Science and Technology*, vol. 8, no. 1-3, pp. 673-679.

Marin-Franch, P., Cochran, S., & Kirk, K. 2004, "Progress towards ultrasound applications of new single crystal materials", *Journal of Materials Science-Materials in Electronics*, vol. 15, no. 11, pp. 715-720.

Maynor, B. W., Filocamo, S. F., Grinstaff, M. W., & Liu, J. 2002, "Direct-writing of polymer nanostructures: Poly(thiophene) nanowires on semiconducting and insulating surfaces", *Journal of the American Chemical Society*, vol. 124, no. 4, pp. 522-523.

Mayo, M. J. 1986, "Photodeposition - Enhancement of deposition reactions by heat and light", *Solid State Technology*, vol. 29, no. 4, pp. 141-144.

Meesters, G. M. H., Vercoulen, P. H. W., Marijnissen, J. C. M., & Scarlett, B. 1992, "Generation of micron-sized droplets from the Taylor cone", *Journal of Aerosol Science*, vol. 23, no. 1, pp. 37-49.

Miao, P., Balachandran, W., & Xiao, P. 2001, "Characterization of ZrO_2 and SiC ceramic thin films prepared by electrostatic atomization", *Journal of Materials Science*, vol. 36, no. 12, pp. 2925-2930.

Miyazawa, K., Ito, K., & Maeda, R. 2000, "Structure and electrical properties of multilayer PZT films prepared by sol-gel processing", *Ceramics International*, vol. 26, no. 5, pp. 501-506.

Mohammadi, F., Saraswat, K. C., & Meindl, J. D. 1979, "Kinetics of the thermal oxidation of WSi_2", *Applied Physics Letters*, vol. 35, no. 7, pp. 529-531.

Moon, J., Grau, J. E., Cima, M. J., & Sachs, E. M. 2000, "Slurry chemistry control to produce easily redispersible ceramic powder compacts", *Journal of the American Ceramic Society*, vol. 83, no. 10, pp. 2401-2408.

Moon, J., Grau, J. E., Knezevic, V., Cima, M. J., & Sachs, E. M. 2002, "Ink-jet printing of binders for ceramic components", *Journal of the American Ceramic Society*, vol. 85, no. 4, pp. 755-762.

Moulson, A.J. & Herbert, J.M. 2003, *Electroceramics: Materials, Properties, Applications, Second Edition* Wiley.

Muralt, P. 1997, "Piezoelectric thin films for MEMS", *Integrated Ferroelectrics*, vol. 17, no. 1-4, pp. 297-307.

Muralt, P. 2000a, "Ferroelectric thin films for micro-sensors and actuators: A review", *Journal of Micromechanics and Microengineering*, vol. 10, no. 2, pp. 136-146.

Muralt, P. 2000b, "PZT thin films for microsensors and actuators: Where do we stand?", *Ieee Transactions on Ultrasonics Ferroelectrics and Frequency Control*, vol. 47, no. 4, pp. 903-915.

Neagu, R., Perednis, D., Princivalle, A., & Djurado, E. 2006, "Zirconia coatings deposited by electrostatic spray deposition - A chemical approach", *Solid State Ionics*, vol. 177, no. 17-18, pp. 1451-1460.

Neagu, R., Perednis, D., Princivalle, A. S., & Djurado, E. 2005, "Initial stages in zirconia coatings using ESD", *Chemistry of Materials*, vol. 17, no. 4, pp. 902-910.

Nguyen, T. & Djurado, E. 2001, "Deposition and characterization of nanocrystalline tetragonal zirconia films using electrostatic spray deposition", *Solid State Ionics*, vol. 138, no. 3-4, pp. 191-197.

Nielsen, M. C., Kim, J. Y., Rymaszewski, E. J., Lu, T. M., & Bakhru, H. 1998, "Composite and multilayered TaO_x-TiO_y high dielectric constant thin films", *Ieee Transactions on Components Packaging and Manufacturing Technology Part B-Advanced Packaging*, vol. 21, no. 3, pp. 274-280.

Noguera, R., Lejeune, M., & Chartier, T. 2005, "3D fine scale ceramic components formed by ink-jet prototyping process", *Journal of the European Ceramic Society*, vol. 25, no. 12, pp. 2055-2059.

Noheda, B., Gonzalo, J. A., Cross, L. E., Guo, R., Park, S. E., Cox, D. E., & Shirane, G. 2000, "Tetragonal-to-monoclinic phase transition in a ferroelectric perovskite: The structure of $PbZr_{0.52}Ti_{0.48}O_3$", *Physical Review B*, vol. 61, no. 13, pp. 8687-8695.

Nomura, M., Meester, B., Schoonman, J., Kapteijn, F., & Moulijn, J. A. 2003, "Improvement of thermal stability of porous titania films prepared by electrostatic sol-spray deposition (ESSD)", *Chemistry of Materials*, vol. 15, no. 6, pp. 1283-1288.

Nouwen, R., Mullens, J., Franco, D., Yperman, J., & VanPoucke, L. C. 1996, "Use of thermogravimetric analysis Fourier transform infrared spectroscopy in the study of the reaction mechanism of the preparation of $Pb(Zr,Ti)O_3$ by the sol-gel method", *Vibrational Spectroscopy*, vol. 10, no. 2, pp. 291-299.

Ohara, Y., Miyayama, M., Koumoto, K., & Yanagida, H. 1993, "Partially-stabilized zirconia polymer composites fabricated with an ultrasonic cutter", *Journal of Materials Science Letters*, vol. 12, no. 16, pp. 1279-1282.

Ohara, Y., Miyayama, M., Koumoto, K., & Yanagida, H. 1994, "PZT-polymer composites fabricated with YAG laser cutter", *Sensors and Actuators A-Physical*, vol. 40, no. 3, pp. 187-190.

Park, J. H., Kwon, T. Y., Yoon, D. S., Kim, H., & Kim, T. S. 2005, "Fabrication of microcantilever sensors actuated by piezoelectric $Pb(Zr_{0.52}Ti_{0.48})O_3$ thick films and determination of their electromechanical characteristics", *Advanced Functional Materials*, vol. 15, no. 12, pp. 2021-2028.

Peng, C. H. & Desu, S. B. 1994, "Metalorganic chemical-vapor-deposition of ferroelectric Pb(Zr,Ti)O_3 thin-films", *Journal of the American Ceramic Society*, vol. 77, no. 7, pp. 1799-1812.

Perkins, F. K., Dobisz, E. A., Brandow, S. L., Calvert, J. M., Kosakowski, J. E., & Marrian, C. R. K. 1996, "Fabrication of 15 nm wide trenches in Si by vacuum scanning tunneling microscope lithography of an organosilane self-assembled film and reactive ion etching", *Applied Physics Letters*, vol. 68, no. 4, pp. 550-552.

Pham, D. T. & Wang, X. 2000, "Prediction and reduction of build times for the selective laser sintering process", *Proceedings of the Institution of Mechanical Engineers Part B-Journal of Engineering Manufacture*, vol. 214, no. 6, pp. 425-430.

Piner, R. D. & Mirkin, C. A. 1997, "Effect of water on lateral force microscopy in air", *Langmuir*, vol. 13, no. 26, pp. 6864-6868.

Piner, R. D., Zhu, J., Xu, F., Hong, S. H., & Mirkin, C. A. 1999, ""Dip-pen" nanolithography", *Science*, vol. 283, no. 5402, pp. 661-663.

Reading, J., Gordeev, S., & Weller, M. T. 2002, "The synthesis, structure and properties of $Hg_2Os_2O_7$", *Journal of Materials Chemistry*, vol. 12, no. 3, pp. 646-650.

Reuter, H. 1991, "Sol-gel processes", *Advanced Materials*, vol. 3, no. 5, pp. 258-259.

Richard, P. D., Markunas, R. J., Lucovsky, G., Fountain, G. G., Mansour, A. N., & Tsu, D. V. 1985, "Remote plasma enhanced CVD deposition of silicon nitride and oxide for gate insulators in (In, Ga)As FET devices", *Journal of Vacuum Science & Technology A-Vacuum Surfaces and Films*, vol. 3, no. 3, pp. 867-872.

Rocks, S., Wang, D., Sun, D., Jayasinghe, S., Edirisinghe, M., & Dorey, R. 2007, "Direct writing of lead zirconate titanate piezoelectric structures by electrohydrodynamic atomisation", *Journal of Electroceramics*, vol. 19, pp. 287-293.

Roda, A., Guardigli, M., Russo, C., Pasini, P., & Baraldini, M. 2000, "Protein microdeposition using a conventional ink-jet printer", *Biotechniques*, vol. 28, no. 3, pp. 492-496.

Rosler, R. S. 1991, "The evolution of commercial plasma enhanced CVD systems", *Solid State Technology*, vol. 34, no. 6, pp. 67-71.

Rossnagel, S. M. & Hopwood, J. 1994, "Metal-ion deposition from ionized magnetron sputtering discharge", *Journal of Vacuum Science & Technology B*, vol. 12, no. 1, pp. 449-453.

Sachs, E., Cima, M., Williams, P., Brancazio, D., & Cornie, J. 1992, "3-Dimensional printing - Rapid tooling and prototypes directly from a CAD model", *Journal of Engineering for Industry-Transactions of the Asme*, vol. 114, no. 4, pp. 481-488.

Saegusa, T. & Chujo, Y. 1990, "An organic inorganic hybrid polymer", *Journal of*

Macromolecular Science-Chemistry, vol. A27, no. 13-14, pp. 1603-1612.

Samarasinghe, S. R., Pastoriza-Santos, I., Edirisinghe, M. J., Reece, M. J., & Liz-Marzan, L. M. 2006, "Printing gold nanoparticles with an electrohydrodynamic direct-write device", *Gold Bulletin*, vol. 39, no. 2, pp. 48-53.

Sato, M. 1984, "The production of essentially uniform-sized liquid droplets in gaseous or immiscible liquid-media under applied ac potential", *Journal of Electrostatics*, vol. 15, no. 2, pp. 237-247.

Schwartz, R. W. 1997, "Chemical solution deposition of perovskite thin films", *Chemistry of Materials*, vol. 9, no. 11, pp. 2325-2340.

Scott, J. F., Dearaujo, C. A. P., Mcmillan, L. D., Yoshimori, H., Watanabe, H., Mihara, T., Azuma, M., Ueda, T., Ueda, T., Ueda, D., & Kano, G. 1992, "Ferroelectric thin-films in integrated microelectronic devices", *Ferroelectrics*, vol. 133, no. 1-4, pp. 47-60.

Setter, N. 2001, "Electroceramics: looking ahead", *Journal of the European Ceramic Society*, vol. 21, no. 10-11, pp. 1279-1293.

Shirane, G. & Suzuki, K. 1952, "Crystal structure of Pb(Zr-Ti)O_3", *Journal of the Physical Society of Japan*, vol. 7, no. 3, pp. 333-333.

Shiryaeva, S. O. & Grigorev, A. I. 1995, "The semiphenomenological classification of the modes of electrostatic dispersion of liquids", *Journal of Electrostatics*, vol. 34, no. 1, pp. 51-59.

Sirringhaus, H., Kawase, T., Friend, R. H., Shimoda, T., Inbasekaran, M., Wu, W., & Woo, E. P. 2000, "High-resolution inkjet printing of all-polymer transistor circuits", *Science*, vol. 290, no. 5499, pp. 2123-2126.

Smith, D. L., Alimonda, A. S., Chen, C. C., Ready, S. E., & Wacker, B. 1990, "Mechanism of SiN_xH_y deposition from NH_3-SiH_4 plasma", *Journal of the Electrochemical Society*, vol. 137, no. 2, pp. 614-623.

Smith, D. P. H. 1986, "The electrohydrodynamic atomization of liquids", *Ieee Transactions on Industry Applications*, vol. 22, no. 3, pp. 527-535.

Song, J. H., Edirisinghe, M. J., & Evans, J. R. G. 1999, "Formulation and multilayer jet printing of ceramic inks", *Journal of the American Ceramic Society*, vol. 82, no. 12, pp. 3374-3380.

Srinivasan, R. & Braren, B. 1989, "Ultraviolet laser ablation of organic polymers", *Chemical Reviews*, vol. 89, no. 6, pp. 1303-1316.

Su, M., Liu, X., Li, S. Y., Dravid, V. P., & Mirkin, C. A. 2002, "Moving beyond molecules: Patterning solid-state features via dip-pen nanolithography with sol-based inks", *Journal of the American Chemical Society*, vol. 124, no. 8, pp. 1560-1561.

Subramanian, P. K. & Marcus, H. L. 1995, "Selective laser sintering of alumina using aluminum binder", *Materials and Manufacturing Processes*, vol. 10, no. 4, pp. 689-706.

Sun, D., Rocks, S. A., Edirisinghe, M. J., Dorey, R. A., & Wang, Y. 2005, "Electrohydrodynamic deposition of nanostructured lead zirconate titanate", *Journal of Nanoscience and Nanotechnology*, vol. 5, no. 11, pp. 1846-1851.

Suzuki, H., Koizumi, T., Kondo, Y., & Kaneko, S. 1999, "Low-temperature processing of $Pb(Zr_{0.53}Ti_{0.47})O_3$ thin film from stable precursor sol", *Journal of the European Ceramic Society*, vol. 19, no. 6-7, pp. 1397-1401.

Tagantsev, A. K., Landivar, M., Colla, E., & Setter, N. 1995, "Identification of passive layer in ferroelectric thin-films from their switching parameters", *Journal of Applied Physics*, vol. 78, no. 4, pp. 2623-2630.

Tay, B. Y., Evans, J. R. G., & Edirisinghe, M. J. 2003, "Solid freeform fabrication of ceramics", *International Materials Reviews*, vol. 48, no. 6, pp. 341-370.

Taylor, G. 1964, "Disintegration of water drops in electric field", *Proceedings of the Royal Society of London Series A-Mathematical and Physical Sciences*, vol. 280, no. 138, pp. 383-397.

Ting, R. Y. 1992, "A review on the development of piezoelectric composites for underwater acoustic transducer applications", *Ieee Transactions on Instrumentation and Measurement*, vol. 41, no. 1, pp. 64-67.

Tiwari, V. S., Kumar, A., Wadhawan, V. K., & Pandey, D. 1998, "Kinetics of formation of the pyrochlore and perovskite phases in sol-gel derived lead zirconate titanate powder", *Journal of Materials Research*, vol. 13, no. 8, pp. 2170-2173.

Tsaur, J., Wang, Z. J., Zhang, L. L., Ichiki, M., Wan, J. W., & Maeda, R. 2002, "Preparation and application of lead zirconate titanate (PZT) films deposited by hybrid process: Sol-gel method and laser ablation", *Japanese Journal of Applied Physics Part 1-Regular Papers Short Notes & Review Papers*, vol. 41, no. 11B, pp. 6664-6668.

Tseng, K. K., Tinker, M. L., Lassiter, J. O., & Peairs, D. M. 2003, "Temperature dependency of impedance-based nondestructive testing", *Experimental Techniques*, vol. 27, no. 5, pp. 33-36.

Tsu, D. V. & Lucovsky, G. 1987, "Properties of the Si-H bond-stretching absorption band in a-Si:H grown by remote plasma enhanced CVD (RPECVD)", *Journal of Non-Crystalline Solids*, vol. 97-98, pp. 839-842.

Tuncer, E., Serdyuk, Y. V., & Gubanski, S. M. 2002, "Dielectric mixtures: Electrical properties and modeling", *Ieee Transactions on Dielectrics and Electrical Insulation*, vol. 9, no. 5, pp. 809-828.

Verardi, P., Dinescu, M., & Craciun, F. 2000, "Pulsed laser deposition and characterization of PZT thin films", *Applied Surface Science*, vol. 154, pp. 514-518.

Wang, D. Z., Edirisinghe, M. J., & Jayasinghe, S. N. 2006, "Solid freeform fabrication of thin-walled ceramic structures using an electrohydrodynamic jet", *Journal of the American Ceramic Society*, vol. 89, no. 5, pp. 1727-1729.

Wang, D. Z., Jayasinghe, S. N., & Edirisinghe, M. J. 2005a, "High resolution print-patterning of a nano-suspension", *Journal of Nanoparticle Research*, vol. 7, no. 2-3, pp. 301-306.

Wang, D. Z., Jayasinghe, S. N., & Edirisinghe, M. J. 2005b, "Instrument for electrohydrodynamic print-patterning three-dimensional complex structures", *Review of Scientific Instruments*, vol. 76, no. 7, p. 075105.

Wang, D. Z., Jayasinghe, S. N., Edirisinghe, M. J., & Luklinska, Z. B. 2007, "Coaxial electrohydrodynamic direct writing of nano-suspensions", *Journal of Nanoparticle Research*, vol. 9, no. 5, pp. 825-831.

Wang, Q. M. 2005, "Crystalline orientation dependence of nanomechanical properties of $Pb(Zr_{0.52}Ti_{0.48})O_3$ thin films", *Applied Physics Letters*, vol. 86, no. 16, p. 162903.

Wang, X., Ryu, K. S., Bullen, D. A., Zou, J., Zhang, H., Mirkin, C. A., & Liu, C. 2003, "Scanning probe contact printing", *Langmuir*, vol. 19, no. 21, pp. 8951-8955.

Wilhelm, O., Madler, L., & Pratsinis, S. E. 2003, "Electrospray evaporation and deposition", *Journal of Aerosol Science*, vol. 34, no. 7, pp. 815-836.

Wilhelm, O., Pratsinis, S. E., Perednis, D., & Gauckler, L. J. 2005, "Electrospray and pressurized spray deposition of yttria-stabilized zirconia films", *Thin Solid Films*, vol. 479, no. 1-2, pp. 121-129.

Wu, A. Y., Salvado, I. M. M., Vilarinho, P. M., & Baptista, J. L. 1998, "Lead zirconate titanate prepared from different zirconium and titanium precursors by sol-gel", *Journal of the American Ceramic Society*, vol. 81, no. 10, pp. 2640-2644.

Yoo, J., Cho, K. M., Bae, W. S., Cima, M., & Suresh, S. 1998, "Transformation-toughened ceramic multilayers with compositional gradients", *Journal of the American Ceramic Society*, vol. 81, no. 1, pp. 21-32.

Yu, S., Yao, K., Shannigrahi, S., & Hock, F. T. E. 2003, "Effects of poly(ethylene glycol) additive molecular weight on the microstructure and properties of sol-gel-derived lead zirconate titanate thin films", *Journal of Materials Research*, vol. 18, no. 3, pp. 737-741.

Zahi, S., Bouaziz, R., Abdessalem, N., & Boutarfaia, A. 2003, "Dielectric and piezoelectric properties of $PbZrO_3$-$PbTiO_3$-Pb $(Ni_{1/3}, Sb_{2/3})O_3$ ferroelectric ceramic system", *Ceramics International*, vol. 29, no. 1, pp. 35-39.

Zeleny, J. 1914, "The electrical discharge from liquid points, and a hydrostatic method of measuring the electric intensity at their surfaces", *Physical Review*, vol. 3, no. 2, pp. 69-91.

Zhang, M., Bullen, D., Chung, S. W., Hong, S., Ryu, K. S., Fan, Z. F., Mirkin, C. A., & Liu, C. 2002, "A MEMS nanoplotter with high-density parallel dip-pen manolithography probe arrays", *Nanotechnology*, vol. 13, no. 2, pp. 212-217.

Zou, J., Bullen, D., Wang, X. F., Liu, C., & Mirkin, C. A. 2003, "Conductivity-based contact sensing for probe arrays in dip-pen nanolithography", *Applied Physics Letters*, vol. 83, no. 3, pp. 581-583.